Parametric study and simulation of Titanium Carbide (TiC) supported, Platinum doped tetrahedral Carbon (taC) electrodes for Hydrogen Evolution Reactions (HER)

Harunal Rejan Ramji

Thèse de doctorat

Université de Limoges

Université de Limoges
ED 653 - Sciences et Ingénierie (SI)
IRCER

Thèse pour obtenir le grade de
Docteur de l'Université de Limoges
Matériaux céramiques et traitements de surface

Présentée et soutenue par
Harunal Rejan b Ramji

Le 3 juillet 2023

Étude paramétrique et simulation d'électrodes en carbone tétraédrique (taC) supportées par du carbure de titane(TiC) pour les réactions d'évolution de l'hydrogène (HER)

Thèse dirigée par JOSEPH ABSI et Soh Fong LIM

JURY :

Président du jury
M. **Mohammad Omar ABDULLAH, Professeur des universités, Universiti Malaysia Sarawak**

Rapporteurs
M. M. Kouakou Boniface KOKOH, Professeur des universités, Université de Poitiers
M. M. Abdul Aziz ABDUL RAMAN, Professeur des universités, Universiti Malaya

Examinateurs
M. M. Nicolas GLANDUT, Maître de conferences, Université de Limoges

Corrections from examiners Prof Abdul Aziz ABDUL RAMAN

Remarks and Suggestions	Changes and corrections
Pg: 17 “conduct study” is not a suitable verb. Perhaps the candidate may consider “to evaluate effect of various parameter on hydrogen evaluation”.	Pg: 17 Evaluate the effect of various parameters of HER using the Volmer-Heyrovsky-Tafel mechanism
Objective number 4, the practically aspect should be dropped as it is not carried out.	Pg: 17 Compare the simulation and experimental results to justify the developed system
The candidate should provide a list of abbreviations and symbols.	Added in pg
The thesis should be free of expressive and unsubstantiated terms such as greatly, unfortunately, extremely, recently, etc.	Pg iv. Surface diffusion was rendered negligible because negligible compared to the high kinetic parameters on the edge in comparison to the TiC and taC:Pt surface. Pg 22 Therefore, water electrolysis was either performed in acidic (pH 0) electrolytes that have anodically inert anions such as sulfate and perchlorate or with basic (pH 14) electrolytes such as KOH and NaOH with concentrations equal to 1 m or higher (eg: Anantharaj and Noda, 2020). Pg 36: Graphene's unique band structure means that electrons move through it at high speeds (about 1/300 the speed of light), giving it fascinating properties - such as unparalleled thermal conductivity. Optically transparent, graphene absorbs only 2% of incident visible light and has the highest tensile strength of any material (Lee et al. 2008). Pg 168: Surface diffusion was rendered negligible because of the high kinetic parameters on the edge in comparison to the TiC and taC:Pt surface. Pg 170: Surface diffusion was rendered negligible because of the high kinetic parameters on the edge in comparison to the TiC and taC:Pt surface (discussed in Chapter 6).
Expressive terms such as us, we, our should be replaced with technical expression (Example: “we” to “in this work”)	Pg 16: **This work** hope to provide readers with an approximation of the time taken to complete one simulation dealing with simple electrochemistry using COMSOL. Pg 16: Hence, **this work** would like to fill the gap on comparative 3D simulation on an identical work with three different dimensions discussing on the effect of meshing directly on the t_{com}. Pg: 16: Closely approximated models like this verifies the simulation across all models. Pg 169: In this chapter, this work would like to conclusively summarize the objectives that were outlined at the beginning of the thesis

This work should be either referred as this “work” or “study” and should be maintained throughout the thesis. Term such as “paper” should be avoided.	Pg iii: This study proved the software's consistency to produce less than 3% error between simulation and analytical results across all dimensions. Pg 56: Both studies show the accuracies of simulations for different meshing configurations on a 2D axisymmetric model Pg 57: Several published works described the algorithms behind adaptive meshing to increase accuracy and precision to the developed model (Gavaghan et al. 2006; Harriman et al. 2000)… Pg 59: The utilization of well-known simulation techniques such as FEM and DFT were elaborated by providing figures and quotes from previous notable work

Corrections from examiners Prof Mohammad Omar ABDULLAH

Remarks and Suggestions	**Changes and corrections**
On page iii, “This paper….” replace “paper” with “thesis”.	Pg iii: This study proved the software's consistency to produce less than 3% error between simulation and analytical results across all dimensions.
On page iii, 3rd bottom line. “.. implement near similar application.” What is “near similar” here? Please revise.	Pg iii: Given the reliability of COMSOL presented in the first study, the second study implement similar approach to model the experiment by Glandut et. al (2015) on Titanium carbide (TiC) support, tetrahedral amorphous carbon doped platinum (taC:Pt) electrode for hydrogen evolution reaction
On page iv, the last sentence “Surface diffusion was rendered negligible because negligible compared to the extremely high kinetic parameters on the edge in comparison to the TiC and taC:Pt surface.”. Please rephrase the sentence.	Pg iv: Surface diffusion was rendered negligible because of the high kinetic parameters on the edge in comparison to the TiC and taC:Pt surface
On page 2, Second paragraph: “The prime minister of Malaysia, Tan Sri Muhyiddin Yassin in recent events..”. Insert “pass” before “prime minister of Malaysia..	Pg 2: The 9th prime minister of Malaysia, Tan Sri Muhyiddin Yassin…
On page 12, “by a process called electrolysis as made example by Kelly et al. (2014)” suggest change “as made example” to “see for example”.	Pg 12: Consequently, an electrolyzer is a device that combines an oxidation and a reduction reaction, driven by electricity, to produce separate streams of hydrogen gas and oxygen gas by a process called electrolysis see for example by Kelly et al. (2014)
On page 13, second paragraph, “finding suitable electrocatalysts” or “more efficient electrocatalysts”?	Pg 13: While hydrogen has been gaining attention as a cleaner and more sustainable energy resource, there are still challenges in finding more efficient electrocatalysts for the electrolysis process, and the…

ACKNOWLEDGEMENT

I would like to take this opportunity to thank Assoc. Prof. Dr Nicolas Glandut and Prof Dr Joseph Absi in University of Limoges for their guidance in understanding electrochemistry and mastering COMSOL for the purpose of this research. My thanks also to Prof Dr Amir Azam Khan and Assoc. Prof. Dr Lim Soh Fong for arranging this dual PhD programme and making it possible for the collaboration to happen.

My sincere gratitude to UNIMAS and UNILIM for giving me the opportunity to conduct my research and complete my study in Limoges and Kota Samarahan, and for all the support given during my period of study.

Finally, I would like to thank my dearest parents Ramji Sedek and Jamilah Razali for their endless support for me in pursuing knowledge. To my beloved wife and daughter Nur Ain Farhanah and Airina Madina for being there for me throughout my journey in completing this thesis. Last but not least to those who have contributed directly or indirectly to this thesis. Thank you all.

ABSTRACT

This work presented the use of commercial software COMSOL Multiphysics to simulate and solve the Volmer - Heyrovsky –Tafel mechanistic steps for hydrogen evolution reaction (HER). The first study will address the reliability of COMSOL to provide accurate and precise results for electrochemistry problem. The developed model is for classical cyclic voltammetry of redox reaction (E). In this study, mesh refinement with its consequent number of elements (*noe*), computation time (t_{com}), and current, $I_{(t)}$ was compared on the 1-dimension (1D), 2-dimension (2D) axisymmetric, and 3-dimension (3D) model. This study proved the software's consistency to produce less than 3% error between simulation and analytical results across all dimensions. By using a relative tolerance (*rtol*) value of 1×10^{-8} with very concentrated custom meshing, a 3D model yielded a result with an error of 2.5% compared to analytical solution. It has the drawback of taking 40 times longer to complete. A slight discrepancy between 2D axisymmetric and 3D simulation results on finest meshing recorded to have less than 3% difference due to CPU memory limit. The use of adaptive meshing on 2D axisymmetric and 3D model with coarse initial mesh reduces the error significantly by 32% and 50%, respectively. At the same time, the computation time, t_{com} increased by nearly ten times on the 2D axisymmetric model and five times on the 3D model. On the “finer” initial mesh, the simulation has reduced the error to near 0%. The *rtol* study shows that the value of 1×10^{-4} is adequate for 2D axisymmetric and 1×10^{-5} for both 1D and 3D. Further investigations on complex electrochemistry using this platform are well justified and highly recommended. Given the reliability of COMSOL presented in the first study, the second study implement similar approach to model the experiment by Glandut et. al (2015) on Titanium carbide (TiC) support, tetrahedral amorphous carbon doped platinum (taC:Pt) electrode for hydrogen evolution reaction. The developed model was tested for surface

diffusion in 2D and surface diffusion with edge effect in 3D. The simulation results show that kinetic parameters permutation with surface diffusivity shows some increased in current output but was unable to achieve the current output obtained from the experiment. However, the introduction of edge effect on the side of taC:Pt on TiC support would significantly increase the current output with great coherency to the experimental result. The edge exhibits kinetic properties unlike both TiC or taC:Pt. The kinetic parameters were determined using the simulation and a dataset was found to show great coherency with the experimental result. Surface diffusion was rendered negligible because of the high kinetic parameters on the edge in comparison to the TiC and taC:Pt surface.

Keywords: simulation, COMSOL, redox reaction, mesh refinement, hydrogen evolution reaction (HER), surface diffusion, edge effect.

Kajian parametrik dan simulasi Titanium Karbida (TiC) disokong, elektrod tetrahedral amorfus Karbon (taC) dop Platinum untuk Reaksi Evolusi Hidrogen (HER)

ABSTRAK

Kerja ini membentangkan penggunaan perisian komersial COMSOL Multiphysics untuk mensimulasikan dan menyelesaikan langkah mekanistik Volmer - Heyrovsky -Tafel untuk tindak balas evolusi hidrogen (HER).

Kajian pertama akan menangani kebolehpercayaan COMSOL untuk memberikan keputusan yang jitu dan tepat untuk menyelesaikan masalah elektrokimia. Model yang dibangunkan adalah untuk voltammetri kitaran. Dalam kajian ini, penghalusan jejaring dengan bilangan unsur (noe), masa pengiraan (t_{com}), dan arus, $I_{(t)}$ telah dibandingkan pada paksisimetrik 1-dimensi (1D), 2-dimensi (2D), dan 3 -model dimensi (3D). Kertas kerja ini membuktikan ketekalan perisian untuk menghasilkan ralat kurang daripada 3% antara simulasi dan keputusan analisis merentas semua dimensi. Dengan menggunakan nilai toleransi relatif (rtol) 1×10^{-8} dengan jejaring tersuai yang sangat padat, model 3D menghasilkan keputusan dengan ralat 2.5%. Ia mempunyai kelemahan iaitu mengambil masa 40 kali lebih lama untuk disiapkan. Sedikit percanggahan antara paksisimetri 2D dan simulasi 3D menghasilkan jalinan terbaik yang direkodkan mempunyai perbezaan kurang daripada 3% disebabkan oleh had memori CPU. Penggunaan jejaring adaptif pada model axisymmetric 2D dan 3D dengan jejaring awal kasar mengurangkan ralat dengan ketara masing-masing sebanyak 32% dan 50%. Pada masa yang sama, tcom meningkat hampir sepuluh kali ganda pada model axisymmetric 2D dan lima kali pada model 3D. Pada jaringan awal yang "lebih halus", simulasi telah mengurangkan ralat kepada hampir 0%. Kajian rtol menunjukkan bahawa nilai 1×10^{-4} adalah memadai untuk axisymmetric 2D dan 1×10^{-5} untuk kedua-dua

1D dan 3D. Siasatan lanjut mengenai elektrokimia kompleks menggunakan platform ini adalah wajar dan sangat disyorkan

Memandangkan kebolehpercayaan COMSOL yang dibentangkan dalam kajian pertama, kajian kedua melaksanakan aplikasi yang hampir serupa untuk memodelkan eksperimen oleh Glandut et. al (2015) mengenai sokongan Titanium karbida (TiC), elektrod platinum dop karbon amorfus tetrahedral (taC:Pt) untuk tindak balas evolusi hidrogen. Model yang dibangunkan telah diuji untuk resapan permukaan dalam 2D dan resapan permukaan dengan kesan tepi dalam 3D. Keputusan simulasi menunjukkan bahawa pilihatur parameter kinetik dengan keresapan permukaan menunjukkan beberapa peningkatan dalam arus litar tetapi tidak dapat mencapai arus yang diperolehi daripada eksperimen. Walau bagaimanapun, pengenalan kesan tepi pada sisi taC:Pt pada sokongan TiC akan meningkatkan arus litar dengan ketara dengan keselarasan yang besar kepada hasil eksperimen. Tepi mempamerkan sifat kinetik tidak seperti kedua-dua TiC atau taC:Pt. Parameter kinetik ditentukan menggunakan simulasi dan set data didapati menunjukkan keselarasan yang besar dengan keputusan eksperimen. Penyebaran permukaan tidak berguna kerana parameter kinetik yang sangat tinggi di tepi berbanding dengan permukaan TiC dan taC: Pt.

Kata kunci: *simulasi, COMSOL, reaksi redox, penghalusan jejaring, reaksi evolusi hidrogen, keresapan permukaan, kesan tepi.*

Étude paramétrique et simulation d'électrodes en carbone tétraédrique (taC) supportées par du carbure de titane (TiC) pour les réactions d'évolution de l'hydrogène (HER)

RÉSUMÉ

Ce travail a présenté l'utilisation du logiciel commercial COMSOL Multiphysics pour simuler et résoudre les étapes mécanistes Volmer - Heyrovsky –Tafel pour la réaction d'évolution de l'hydrogène (HER).

La première étude portera sur la fiabilité de COMSOL à fournir des résultats exacts et précis pour un problème d'électrochimie. Le modèle développé est pour la voltamétrie cyclique sous diffusion sphérique semi-infinie. Dans cette étude, le raffinement du maillage avec son nombre conséquent d'éléments (noe), son temps de calcul (t_{com}) et son courant, $I_{(t)}$ a été comparé sur la 1 dimension (1D), la 2 dimension (2D) axisymétrique et la 3 modèle tridimensionnel (3D). Cet article a prouvé la cohérence du logiciel pour produire moins de 3% d'erreur entre la simulation et les résultats analytiques dans toutes les dimensions. En utilisant une valeur de tolérance relative (rtol) de 1×10^{-8} avec un maillage personnalisé très concentré, un modèle 3D a donné un résultat avec une erreur de 2,5 %. Il a l'inconvénient de prendre 40 fois plus de temps à compléter. Un léger écart entre les résultats de simulation 2D axisymétrique et 3D sur le maillage le plus fin enregistré a moins de 3 % de différence en raison de la limite de mémoire CPU. L'utilisation du maillage adaptatif sur le modèle 2D axisymétrique et 3D avec un maillage initial grossier réduit l'erreur de manière significative de 32 % et 50 %, respectivement. Dans le même temps, le t_{com} a été multiplié par près de dix sur le modèle axisymétrique 2D et par cinq sur le modèle 3D. Sur le maillage initial "plus fin", la simulation a réduit l'erreur à près de 0%. L'étude rtol montre que la valeur de 1×10^{-4} est adéquate pour le 2D axisymétrique et 1×10^{-5} pour le 1D et le 3D. D'autres

investigations sur l'électrochimie complexe utilisant cette plate-forme sont bien justifiées et fortement recommandées.

Compte tenu de la fiabilité de COMSOL présentée dans la première étude, la seconde étude met en œuvre une application quasi similaire pour modéliser l'expérience de Glandut et. al (2015) sur support en carbure de titane (TiC), électrode en platine dopé au carbone amorphe tétraédrique (taC:Pt) pour la réaction de dégagement d'hydrogène. Le modèle développé a été testé pour la diffusion de surface en 2D et la diffusion de surface avec effet de bord en 3D. Les résultats de la simulation montrent que la permutation des paramètres cinétiques avec la diffusivité de surface montre une certaine augmentation de la sortie de courant mais n'a pas été en mesure d'atteindre la sortie de courant obtenue à partir de l'expérience. Cependant, l'introduction d'un effet de bord du côté de taC:Pt sur le support TiC augmenterait considérablement la sortie de courant avec une grande cohérence avec le résultat expérimental. Le bord présente des propriétés cinétiques contrairement à TiC ou taC:Pt. Les paramètres cinétiques ont été déterminés à l'aide de la simulation et un ensemble de données a été trouvé pour montrer une grande cohérence avec le résultat expérimental. La diffusion de surface a été rendue inutile en raison des paramètres cinétiques extrêmement élevés sur le bord par rapport à la surface TiC et taC:Pt

Mots clés: *simulation, COMSOL, réaction redox, raffinement de maillage, réaction de dégagement d'hydrogène (HER), diffusion de surface, effet de bord.*

TABLE OF CONTENTS

LIST OF TABLES

LIST OF FIGURES

LIST OF ABBREVIATIONS

UNIMAS	Universiti Malaysia Sarawak
UNILIM	Universite de Limoges
noe	Nombor of elements
t_{com}	Computational time
TiC	Titanium carbide
taC	Tetrahedral amorphous carbon
PETRONAS	Petroliam Nasional Bhd
SEB	Sarawak Energy Berhad
R&D	R
D	Diffusivity
PDE	Partial differential equation
UI	User interface
rtol	Relative tolerance
VHT	Volmer-Heyrovsky-Tafel
OER	Oxygen evolution reaction
HER	Hydrogen evolution reaction
HOR	Hydrogen oxidation reaction
HAR	Hydrogen adsorption reaction
Hs	Hydride surface
tds	Transport of diluted species

CHAPTER 1

INTRODUCTION

1.1 Recent development of hydrogen in Malaysia

As one of the key players in Southeast Asia, Malaysia has put on great strides to be on par with developed nations and provide market opportunity to investors. Through collaborations, various technology has been brought into the region, giving ways for further knowledge sharing and advancement in manufacturing technology. With the ever-growing concerns on the environmental impact from industrialization, Malaysia has put forth The National Green Technology Policy that was issued in 2009. It recognizes the importance of green technologies to achieve progress. "Green Technology as a driver to accelerate the national economy and promote sustainable development". The National Green Technology Policy is built on four pillars:

(1) Energy: Seek to attain energy independence and promote efficient utilization.

(2) Environment: Conserve and minimize the impact on the environment.

(3) Energy Supply Sector: Application of Green Technology in power generation and in the energy supply side management, including co-generation by the industrial and commercial sectors.

(4) Energy Utilization Sector: Application of Green Technology in all energy utilization sectors and in demand side management programs.

In recent efforts, Petroliam Nasional Bhd (Petronas) and Universiti Kebangsaan Malaysia's (UKM) collaboration on hydrogen energy has yielded positive outcomes since the tie-up began in July 2019. The two parties are looking into the production of hydrogen gas from water through electrolysis technology, covering five areas – bipolar plate design, membrane

electrode assembly, coating materials, construction materials and economy of scale (Bernama, 2021). This initiative is seen as a good example in promoting the transition towards green energy by harnessing hydrogen as power source.

The 9th prime minister of Malaysia, Tan Sri Muhyiddin Yassin in recent events, speak after officiating the 12th International Greentech and Eco Products Exhibition and Conference Malaysia (IGEM) 2021 was quoted saying “The government will continue to adopt a 'whole-of-nation' approach to ensure that its policies are clear and conducive, for a sustainable economic development (referring to the National Green Technology Policy). It was crucial to continue to engage with all industry players and stakeholders to ensure perpetual environmental sustainability. Innovating products and services and offer solutions that can help minimize environmental impacts to ensure the (environment) sustainability for the community (Yunus, 2021).

In a press statement by Environment and Water Minister Datuk Seri Tuan Ibrahim Tuan Man mentioned that as a signatory to the Paris Agreement, Malaysia is committed to achieving its target to reduce carbon emissions, adding that the hydrogen economy can help reduce the intensity of the country’s greenhouse gas emissions by 45 percent by 2030 (Bernama, 2021). At the event, Tuan Ibrahim and the Japanese Ambassador to Malaysia Oka Hiroshi witnessed the exchange of memoranda of cooperation between Malaysian Green Technology and Climate Change Corporation (MGTC) and several strategic partners for the development of the hydrogen economy in Malaysia. The partners include UMW Innovation and R&D Centre Sdn Bhd; Mitsui & Co Ltd; Sarawak Economic Development Cooperation (SEDC); and Vizione Energy Sdn Bhd.

In Sarawak, the state aspired to be one of the major hydrogen exporters by 2050. The Sarawak Chief Minister Datuk Patinggi Abang Johari Openg said and was quoted “It seems

that other countries are monitoring Sarawak. Lately, we have received interest by Japanese companies, Sumitomo Corp and Eneos Globe Corp, a subsidiary of Nippon Oil Corp, to set up a hydrogen plant in Bintulu." (Bernama, 2020). Sarawak had initiated a prototype project after studying the methods that have been employed in other countries that are already producing hydrogen as fuel, such as in Germany, Italy, France, South Korea and Scotland.

Local energy company such as Petroliam Nasional Bhd (PETRONAS), had embarked on a collaboration with Sarawak Energy Bhd (SEB) to carry out the R&D activities for hydrogen production. The tie-up marks a major milestone in Sarawak's efforts to scale up and venture into energy export with hydrogen as an energy carrier. This is to meet global clean energy demand and to position Sarawak as the hub for the hydrogen value chain. SEB, in collaboration with Linde EOX Sdn Bhd had also launched South-East Asia's first integrated hydrogen production plant and refuelling station in Kuching (Figure 1.1). The plant, which uses water to produce carbon-free hydrogen via electrolysis (Figure 1.2), is the Sarawak government's first initiative towards creating a hydrogen-based economy (Wong, 2020). The hydrogen plant is capable of refueling up five fuel cell buses and 10 fuel cell cars per day. Figure 1.3 showing the hydrogen powered car owned by the SEB.

Figure 1.1: Sarawak first integrated hydrogen refueling station and hydrogen bus (Sarawak Energy, 2020)

Figure 1.2: Two electrolyzers are used to produce hydrogen via electrolysis (The Borneo Post, 2020)

State player SEB and Pestech International Bhd had struck an agreement on a research project to explore clean alternative energy where both parties to conduct research, design, and develop a self-recharging autonomous hydrogen solution to be deployed at rural

Sarawak, over the next 15 months as an initiative to explore the potential of hydrogen storage solutions for rural electrification (Bernama, 2021).

Figure 1.3: Hydrogen car, Hyundai Nexos owned by Sarawak Energy (Sarawak Energy, 2020)

All of the efforts made by Sarawak government as described in the previous paragraph underlines the importance of hydrogen economy and how the Sarawak state value the resources. On the 22nd of July 2021, the Sarawak government has launched its Post Covid-19 Development Strategy (PCDS) 2030, aspiring to be a thriving society driven by data and innovation to enjoy economic prosperity, social inclusivity and sustainable environment. The seven strategic thrusts to accelerate the economic development are as follows (Lim, 2021):

(a) Transforming Sarawak into a competitive economy by increasing productivity level, developing more high value downstream activities and creating new industries through active private sector involvement. For example, precision farming to increase quantity and quality of produce for high value downstream food processing products for domestic consumption and export market.

(b) Improving ease of doing business to facilitate domestic investment (DDI) and making Sarawak an investment destination of choice for foreign investors (FDI). For example, by establishing Sarawak Invest as a one-stop agency for investment.

(c) Spending on areas that yield the most economic, social and environmental impact. For example, environmental-friendly construction (design and materials) of access road to social and economic hubs that will stimulate socio-economic activities and improve standard of living of the community.

(d) Optimizing use of assets and government funding and developing human capital to support socio-economic development. For example, rather than constructing new buildings, Sarawak should optimize the use of existing building spaces for productive activities. Human capital investment should focus on the right training to meet industrial needs of the state to progress.

(e) Accelerating digital adoption and data utilization to generate outcomes. This will include establishing a state-wide network coverage of telecommunication infrastructure and services that will enable the adoption of digital technology in agriculture for precision farming, industry 4.0, e-learning and telemedicine to support Sarawak's digital economy initiatives towards high income and developed state by 2030.

(f) Driving economic and social benefits for all Sarawakians, focusing on impoverished segment of the population. This include providing the society with access to basic infrastructure and implementing concerted initiatives to help increase household income.

(g) Balancing economic growth with environmental sustainability. Sarawak aims to balance economic growth with a responsible approach towards utilization of natural

resources and integration of climate adaptation and mitigation plans. This approach prioritizes the sustainable use of land and ocean resources for economic growth, improved livelihoods and jobs while preserving the health of the land and ocean ecosystem.

The development of hydrogen technology is very much in line with the Sarawak state aspiration and their development strategy in the near future.

1.2 Recent development of hydrogen in France and Europe

France aims to produce hydrogen without creating any CO_2 emissions using electrolysis, a process by which an electric current extracts hydrogen from the H_2O water molecule. 90% of hydrogen production still generates greenhouse gas emissions, amounting to 9 million tons of CO_2 per year, according to the French government.

The French government is aiming by 2030 to develop the industrial potential of electrolysis to a capacity of 6.5GW. In line with its hydrogen strategy, France is aiming to decarbonise its transport sector – currently the country's first source of CO_2 emissions (30.1%), before agriculture (19.6%), housing (18.5%) and industry (18%) [Pistorius. M, 2021]

Europe

On May 2008, The first Fuel Cells and Hydrogen Joint Undertaking (FCH-JU) was created as a public private partnership (PPP) supporting research, technological development and demonstration activities in fuel cell and hydrogen energy technologies in Europe (Figure

1.4). Its aim is to accelerate the market introduction of these technologies, realizing their potential as an instrument in achieving a carbon-lean energy system.

Since the introduction of the project, nearly 2.277 billion EUR was channeled to numerous beneficiaries to support research and technology developments (RTD) within the period 2007-2020. Half of the budget was covered by contributions from industrial legal entities and private members [Cuevas et. al., 2021].

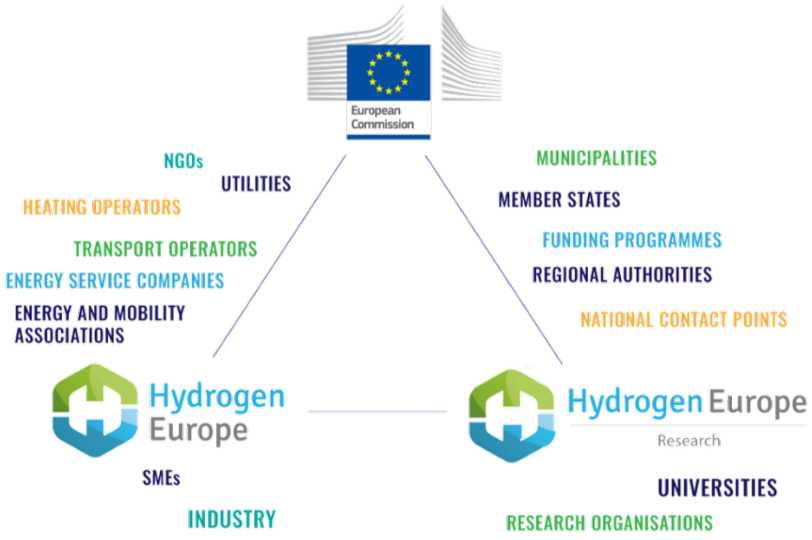

Figure 1.4: The Fuel Cells and Hydrogen Joint Undertaking (FCH-JU) public private partnership (PPP) (www.fcu.europa.eu).

Within the 13 years' span, the first phase (FCH-JU) was concluded in 2013 while the second phase (FCH 2 JU) kick started in 2014 until 2020 with further extension. The core objectives of the second phase are described in Figure 1.5.

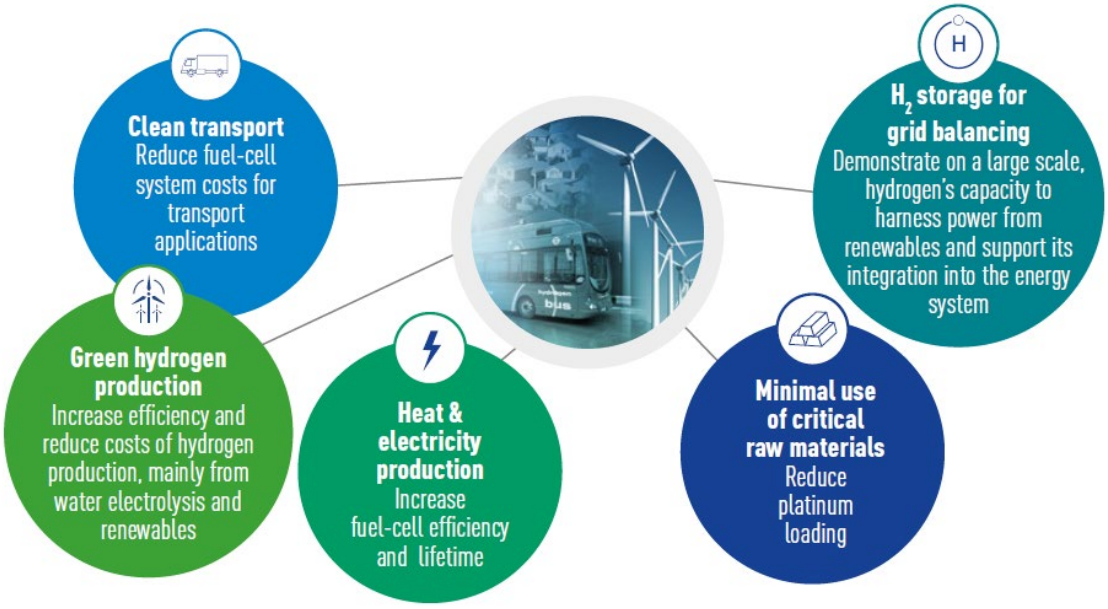

Figure 1.5: FCH 2 JU core objectives (www.fcu.europa.eu).

1.3 Recent technologies utilizing hydrogen energy

Japan hosting the Olympics in 2021 (Tokyo 2020) is meant to be the 'hydrogen Olympics'. Showcasing Japan's aspiration towards zero carbon emissions by making Hydrogen the fuel of the 21st century and the central technology. The Olympic flame is burning hydrogen. Quoting the former Japan prime minister Shinzo Abe in March 2020 "During the Olympics and Paralympics, cars and buses will run through the city powered by hydrogen and the athlete's village will run on electricity made from hydrogen (Harding, 2021).

In automotive industries, Toyota Motor Corporation a multinational automotive manufacturer had claim a new record for distance traveled in a hydrogen –powered vehicle without refueling, with its new Mirai. The Mirai is driven by electric motors, fed by a hydrogen fuel-cell instead of battery power. The official Guinness World Record was 1360

km achieved during a round trip tour of Southern California on August 23 and 24, 2021 [Pattni V., 2021]. The car consumed 5.65 kg of hydrogen.

Figure 1.6: Examples of developed hydrogen technology in automotive, aviation and naval engineering.

In Norway, the world's first operational hydrogen powered ferries were developed by Norled (F. Bahtic., 2021). The ferry operator struck a deal with gas giant Linde for the supply of liquid hydrogen from 24 MW electrolyser utilizing the PEM technology at Leuna Chemical complex in Germany. In aviation, Airbus has state its commitment to developed the world's first zero-emission commercial aircraft by 2035 (Airbus. Read online on 2022 April 25). Powered using liquid hydrogen for combustion with oxygen in a modified gas turbines engines. Hydrogen fuel cells will complement the gas turbine by creating electrical power resulting in a highly efficient hybrid electric propulsion systems.

It is very clear that the transition towards cleaner and sustainable energy with the use of hydrogen power in transportation to displaced our over reliance on the fossil fuels. The examples given in this section shows the trends are moving very rapidly from small hydrogen

technologies to more complex systems that will utilize hydrogen as a reliable renewable energy source.

1.4 Problem Statement

The global outlook on energy resources has shown a great shift from fossil fuels to cleaner and more sustainable resources. Among the option that has been gaining serious attention is hydrogen. Hydrogen was a proven resource because it has the highest gravimetric energy density of any known fuel (as shown in Table 1) and is compatible with electrochemical processes for energy conversion free of CO_2 emissions eg by: (Bicelli, 1986; Mazloomi and Gomes, 2012).

Table 1.1: Volumetric and gravimetric energy densities of common fuels (Mazloomi and Gomes, 2012).

Material	Energy per kilogram (MJ/kg)	Energy per litre (MJ/L)
H_2 (L)	143	10.1
H_2 (comp. 700 bar)	143	5.6
H_2 (ambient temperature)	143	0.0107
CH_4 (ambient pressure)	55.6	0.0378
Natural gas (L)	53.6	22.2
Natural gas (comp. 250 bar)	53.6	9
Natural gas	53.6	0.0364
LPG propane	49.6	25.3
LPG butane	49.1	27.7
Gasoline (petrol)	46.4	34.2
Biodiesel oil	42.2	33
Diesel	45.4	34.6

Hydrogen production via electrolysis has been discussed heavily in multiple literatures ever since the 19th century. Work on electrochemistry can be found as early as 1932 by E.W Washburn and H.C Urey (Washburn and Urey, 1932). More recent progress

on the electrolysis methodology are described by various researchers. Electrolysis is a technique that uses a direct electric current (DC) to drive an otherwise non-spontaneous chemical reaction. Consequently, an electrolyzer is a device that combines an oxidation and a reduction reaction, driven by electricity, to produce separate streams of hydrogen gas and oxygen gas by a process called electrolysis, see for example by Kelly et al. (2014).

In this complex system, one of the core components in the electrolyzer is the electrocatalyst. The electrocatalyst predominantly determines the ability of the system to effectively generate H_2 (at anode) or O_2 (at cathode) from water splitting (Figure 1.7) via electrochemical reactions that occur on its surface. Throughout the years, in-depth discussions on the approaches and challenges of electrocatalyst in wide range of engineering aspect has been presented by various electrochemist for example by Debe (2012), Birdja et al. (2019) and Liu et al. (2020).

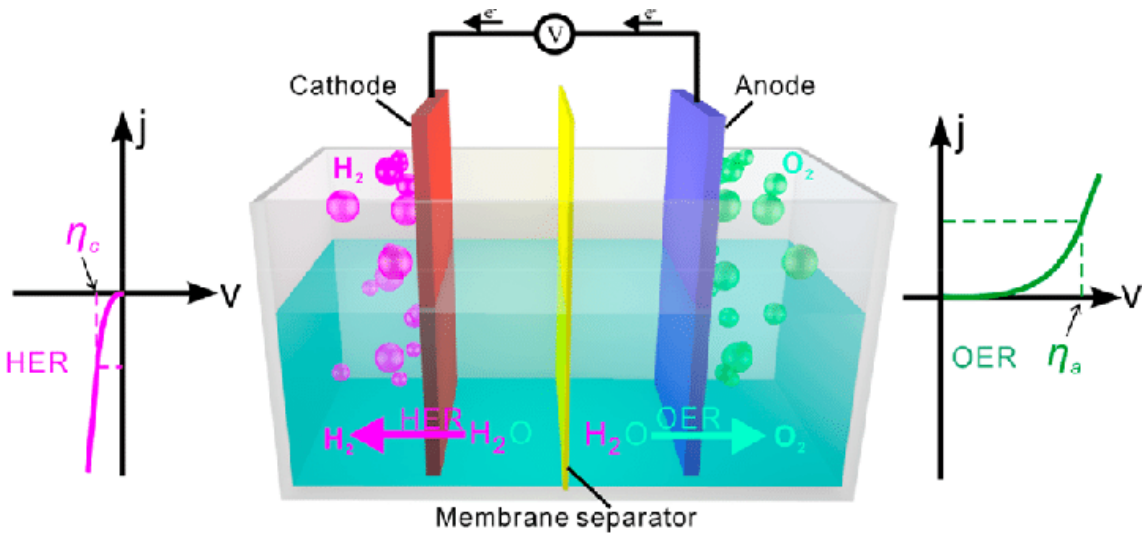

Figure 1.7: HER and OER of electrocatalytic water splitting. (Zhu et al., 2019)

Platinum was proven to have an outstanding catalytic performances with great chemical and mechanical stability and durability. Recent advances in this field has been

seeking new materials as substitutes to Pt as an efficient electrocatalyst. This advancement includes new way to synthesize and fabricate metal and/or non-metal with high catalytic activity with great durability.

The main problem implied in this statement is the lack of a practical, safe, highly efficient, economically feasible, and sustainable system for hydrogen production via electrolysis. While hydrogen has been gaining attention as a cleaner and more sustainable energy resource, there are still challenges in finding more efficient electrocatalysts for the electrolysis process, and the development of a practical system for hydrogen production remains elusive. Further research and experimentation are needed to improve the efficiency and sustainability of hydrogen production via electrolysis. In this thesis, the works were focused on problems given with specific details in sub chapter 1.4.1 and 1.4.2.

1.4.1 TiC/taC:Pt experimental background

Tetrahedral amorphous carbon is among new carbonaceous materials attracting a lot of attention in recent years. This material is characterized by preferential sp^3 hybridization of the C-C bonds. A work presented by Glandut et al. (2015) on thin films of tetrahedral amorphous carbon doped with 10 % platinum, ta-C:Pt, were deposited by pulsed laser deposition on several substrates (namely silicium and titanium carbide). These materials have been tested as potential electrodes for dihydrogen evolution reaction, HER. When these films had a cracked-mud morphology on TiC, it was observed that the kinetics of HER was much higher than when the same films were not cracked. Hence, to improve on this findings, an array of electrodes made of ca. 100 nm thick, 100 x 100μm^2 squares of ta-C:Pt was deposited on TiC electrodes. The space between the squares has been set at 75 µm.

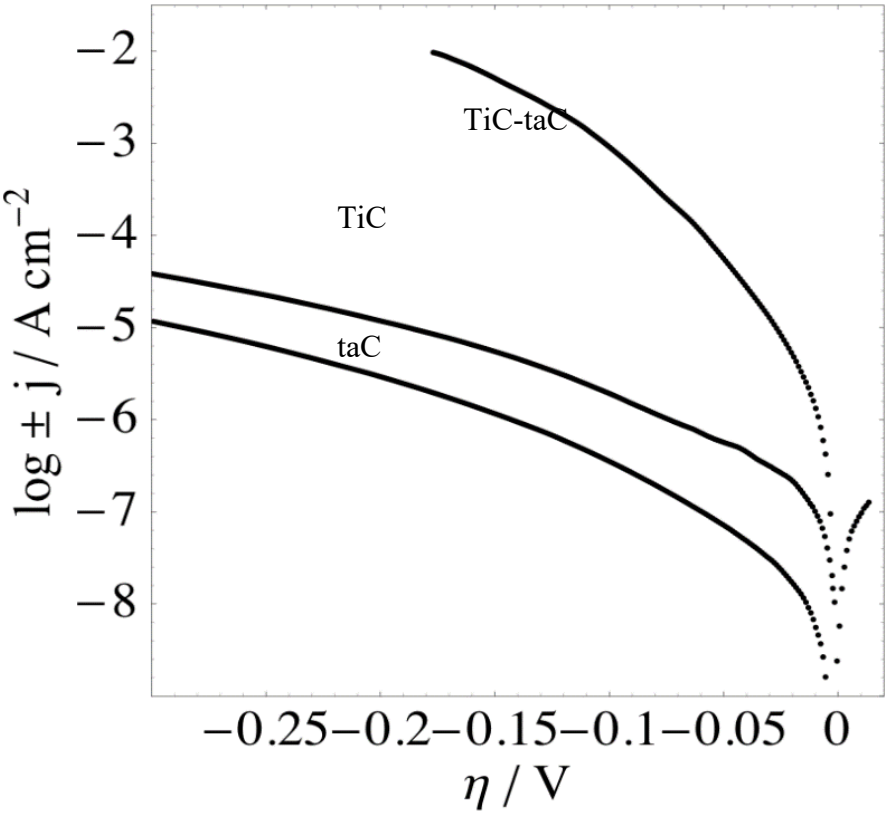

Figure 1.8: Tafel plots for taC only, TiC only and TiC-taC array. (Glandut et al., 2015).

The results in Figure 1.8 showed that the electrochemical response of these array electrodes is higher of several order of magnitude compared to the two components, taken separately (synergetic effect). The exchange current density, j_0, has been estimated at 10 μA/cm^2, compared to ca. 0.1 and 0.01 μA/cm^2 for pure TiC and ta-C:Pt, respectively.

Considering the geometrically arrayed design of the TiC/taC electrocatlyst, COMSOL was selected as it is an exceptionally powerful tools in modelling problem involving diffusivity via the usage of customizable PDE. This study is an extension of the experimental work by Glandut et al. (2015) to explain the improved HER using the mechanistic steps with effect of surface diffusion using the Butler-Volmer estimation via

FEM. This will theoretically explain the TiC/taC:Pt intrinsic activity by presenting the necessary electrochemical system modelling.

1.4.2 COMSOL Multiphysics as a reliable tool in electrochemistry

It was generally known that a complicated modelling and simulation works could take an extensive amount of time to complete. The simulation time with regards to meshing quality and results accuracy were rarely explicitly explained. Longer computation time on 3D simulation was stated in plenty of literatures subjectively but a definite timeframe was rarely given. This works will give an approximation of the time taken to complete one simulation dealing with simple electrochemistry using COMSOL. This work would also like to address the data accuracy of these different geometry on a similar working model. This is considered important for project management and time planning in working with computational simulation while providing reliable outcome.

There are no shorts of literature presenting works on 3D simulations for e.g. Lakshmi et al. (2017) and Li et al. (2016). But many of the works discuss a particular scenario. For e.g. case study by (Somasundaram et al. 2011) of an electrochemical capacitor and by (Almazán-Ruiz et al. 2012) on a rotating cylinder in an electrochemical reactor. The software is often used to visualize physical phenomena and justify experimental findings. Few correlations are made on to 1D or 2D models problems or vice-versa. Lakshmi et al. (2017) did present a comparative analysis between 2D and 3D models of proton exchange membrane fuel-cell showing the variances in the simulation results. However, scarcely available literature on a direct comparison with mesh analysis was to be found. Hence, this study presented substantial work in finite element analysis for three models of varying sizes on transient redox reactions. By referring to some closely relevant articles namely (Cutress

et al. 2010; Dickinson et al. 2014; Trinh et al. 2014; Lavacchi et al. 2009), selected parameters to be elaborated in this study includes current, $I_{(t)}$, *noe* or domains (related to meshing quality), the relative tolerance (*rtol*) value and the computation time, t_{com}.

This work hope to provide readers with an approximation of the time taken to complete one simulation dealing with simple electrochemistry using COMSOL. This work would also like to address the data accuracy of these different geometry on a similar working model. This is considered important for project management and time planning in working with computational simulation while providing reliable outcome.

Cutress et al. (2010) revealed an overview of the general precision of the software on a 3D microdisk model with an error of 18.54%. Limitations due to available CPU memory become a hindrance to achieving desirable granularity. Hence, this work would like to fill the gap on comparative 3D simulation on an identical work with three different dimensions discussing on the effect of meshing directly on the t_{com}. Closely approximated models like this verifies the simulation across all models. The comparative study on a simplified model is to give confidence and assurance on the simulated results to produce reasonable approximation on the advance works in the previous works.

1.5 Objectives

This research aims to present using COMSOL Multiphysics® a Hydrogen Evolution Reaction (HER) of Titanium Carbide (TiC) and tetrahedral amorphous carbon doped with platinum (taC-Pt). This is achieved via the objectives set below;

i. Design a robust electrochemical reaction on 1D, 2D and 3D models and verify the data precision and accuracy acquired from COMSOL Multiphysics® simulations.

ii. Design and simulate the electrode on 1D for TiC only and taC only and 2D and 3D for TiC-taC combination.

iii. Evaluate the effect of various parameters of HER using the Volmer-Heyrovsky-Tafel mechanism.

iv. Compare the simulation and experimental results to justify the developed system.

1.6 Chapter Summary

This chapter describe the current and ongoing activities on hydrogen technologies in Malaysia particularly in Sarawak. The elaboration includes the implemented government policies and the collaboration of the main players in developing the advancement that could spur the hydrogen economy. Additionally, a quick look on the EU and France in particular through their initiative of bridging the industries and the universities under one huge project that would tackle the issue of greenhouse emission in multiple sectors. The utilization of hydrogen energy in recent years was briefly described through its implementation in automotive, aviation and naval engineering.

Finally, in the problem statements the general overview of the electrocatalyst's function in an electrolyzer were presented. The study consist of into two main parts where (a) a modelling and simulation work via COMSOL based on the original experimentation on a novel electrocatalyst dubbed TiC/taC:Pt and (b) a modelling and simulation analysis of a simple electrochemical reaction on various dimensions with consideration of meshing quality and results accuracy. The objectives were listed in 1.5 based on the issues raised in the problem statement.

CHAPTER 2

LITERATURE REVIEW

2.1 Hydrogen production

This past decade had seen hydrogen emerges as the energy of choice. Hydrogen production technology was studied and rapidly developed by researchers and industry players to harness this clean energy resource. In global market, hydrogen was identified based on their colours (Figure 2.1) that refers to the hydrogen resources and its production processes. Categorically, hydrogen is divided into 7 colours as shown in Table 2.1.

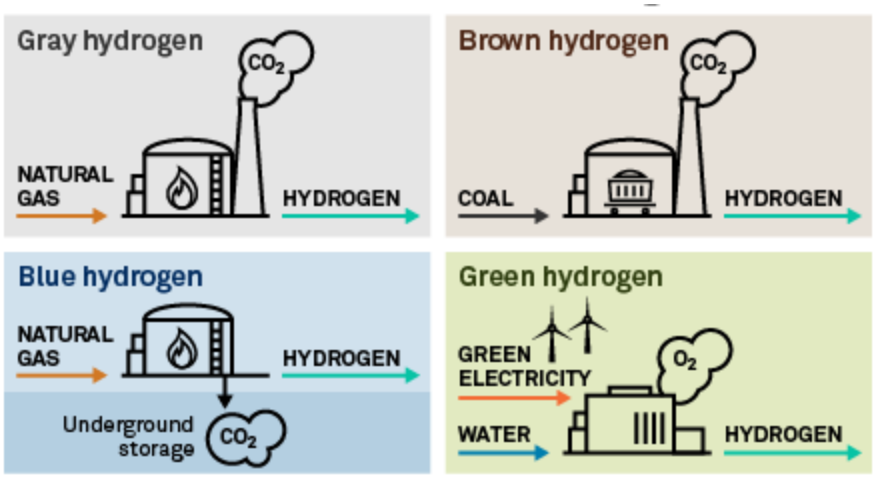

Figure 2.1: Examples of four main sources of hydrogen (DiChristopher, 2021)

Table 2.1: Hydrogen colours and methods of production.

Colour	Production resources	Examples	Ref.
	Renewable energy and electricity	Water splitting $4H_2O \rightleftharpoons 4H^+ + 4OH^-$ (Figure 2.1)	Azizian et al. (2021)
	Thermal splitting of methane	$CH_4 \rightarrow C + 2H_2$ at >1000°C	Malek et al. (2021)
	Carbon capture and storage	Methyl diethanolamine as solvent for capturing CO_2 in high pressure gaseous stream (Figure 2.2)	Antonini et al. (2020)

	Fossil hydrocarbons	$C_{12}H_{24} + 6O_2 \rightarrow 12CO + 12H_2$ (Figure 2.1)	
	Coal	$Coal + O_2 + H_2O \rightarrow H_2 + 3CO$ (Figure 2.1)	Madili et al. (2021)
	Nuclear power	Nuclear water splitting pathways in Figure 2.3	Naterer et al. (2013)
	Solar power	Outline in Figure 2.4	Ngoh and Njomo (2012)

The examples for each of the hydrogen resources are illustrated in Figure 2.2 for hydrogen production via carbon capture and storage (Antonini et al., 2021), Figure 2.3 for hydrogen obtained via nuclear power (Naterer et al., 2013) and Figure 2.4 for hydrogen produced via solar power (Ngoh and Njomo, 2012). Noticeably, there were some repeating for different types of resources. This arises due to the methods of obtaining hydrogen or the hydrogen technologies used for production (see Table 2.2).

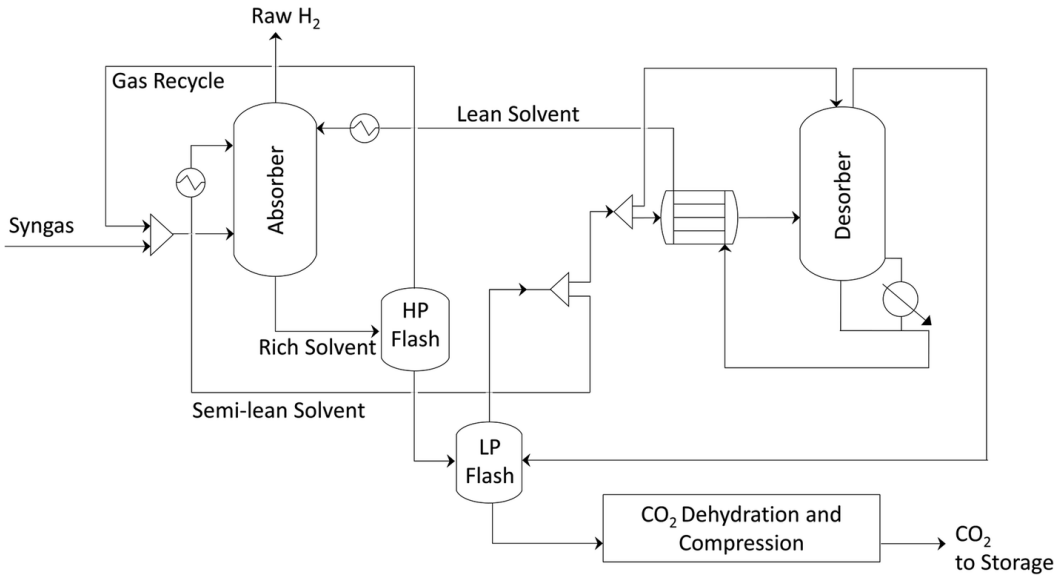

Figure 2.2: Schematic of CO_2 capture process using methyl diethanolamine solvent (Antonini et al., 2021)

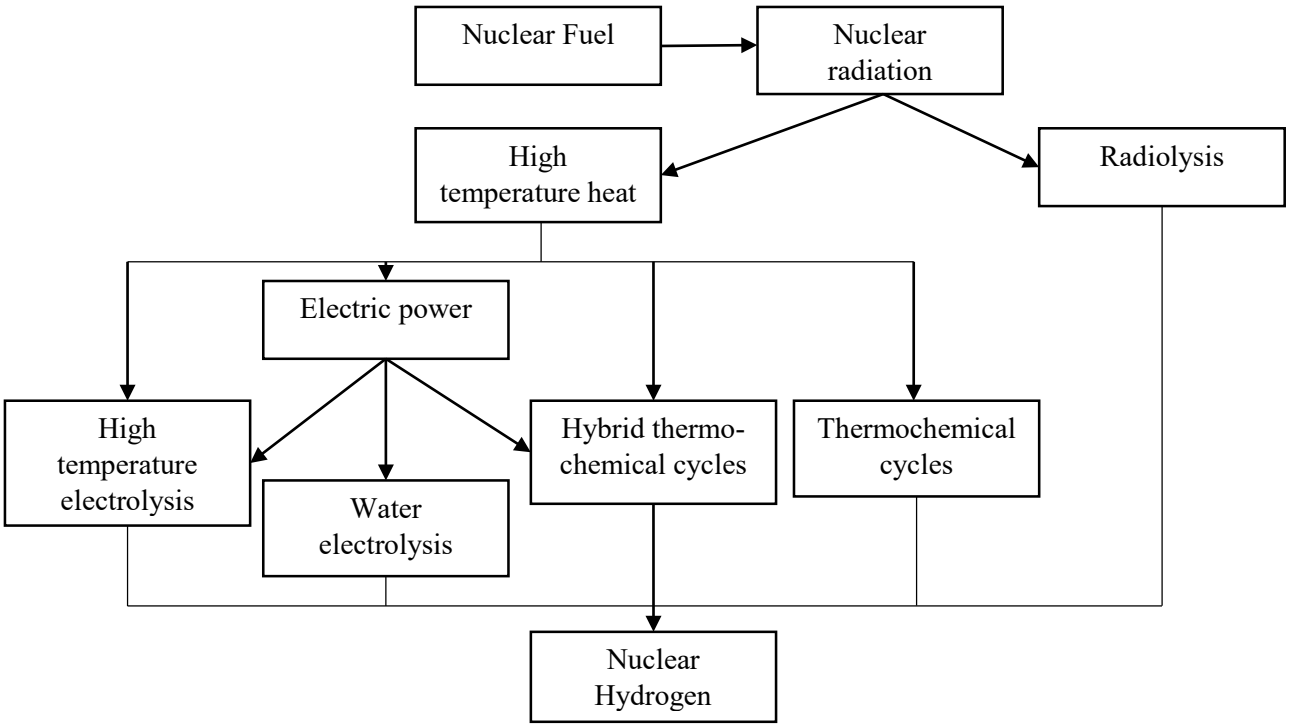

Figure 2.3: Nuclear water splitting pathways (Naterer et al., 2013)

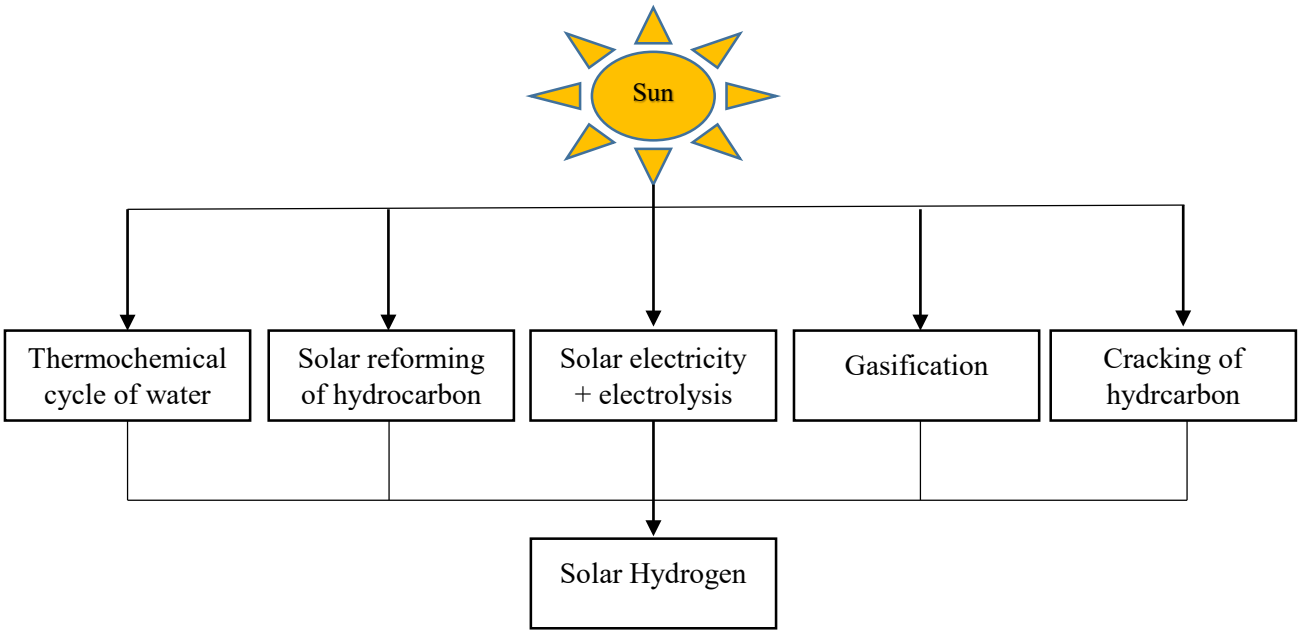

Figure 2.4: Outline of hydrogen production via solar energy (Ngoh and Njomo, 2021)

Over 95% of hydrogen is produced from fossil fuels via various methods for example steam reforming, auto-thermal reforming and partial oxidation (Holladay, J.D., 2009) and (Liu et al., 2010). Holladay (2009) had summarized the hydrogen production technologies, with its related feed stock, estimated efficiency and maturity for the market. The brief review did a very good job in detailing the current progress and situation of the hydrogen industry both in research level and commercial production.

Table 2.2: Summary of hydrogen production technologies (Holladay, J.D., 2009).

Technology	Feed stock	Efficiency	Maturity
Steam reforming	Hydrocarbons	70-85%	Commercial
Partial oxidation	Hydrocarbons	60-75%	Commercial
Autothermal reforming	Hydrocarbons	60-75%	Near term
Plasma reforming	Hydrocarbons	9-85%	Long term
Aqueous phase reforming	Carbohydrates	35-55%	Med. term
Ammonia reforming	Ammonia	NA	Near term
Biomass gasification	Biomass	35-50%	Commercial
Photolysis	Sunlight + water	0.50%	Long term
Dark fermentation	Biomass	60-80%	Long term
Photo fermentation	Biomass + sunlight	0.10%	Long term
Microbial electrolysis cells	Biomass + electricity	78%	Long term
Alkaline electrolyzer	H_2O + electricity	50-60%	Commercial
PEM electrolyzer	H_2O + electricity	55-70%	Near term
Solid oxide electrolysis cells	H_2O + electricity + heat	40-60%	Med. term
Thermochemical water splitting	H_2O + heat	NA	Long term
Photoelectrochemical water splitting	H_2O + sunlight	12.40%	Long term

Based on Table 2.2, it shows that water splitting technologies exhibits great efficiency of more than 50% with PEM and solid oxide electrolyzers to high 70% with alkaline electrolyzer. Over the years this technology is being improved and refined further for commercialization. As discussed in chapter 1.4.1 the study of the electrodes would be one of the essential part to have an efficient water splitting mechanism in an electrolyzer.

This will be elaborated in the next part that includes HER (mechanistic steps) and electrocatalyst.

2.1.1 Electrolyzers and electrochemical water splitting mechanism

Electrolyzer is define as a system that break water into hydrogen and oxygen using electricity. This was called as electrochemical water splitting mechanism or in short electrolysis. A working electrolyzer can be as simple as electrolysis setup shown in Fig 1.7. There are various types of electrolyzer and based on Table 2.2, there are 5 distinct methods for water splitting (1) Alkaline electrolyzer, (2) Proton exchange membrane (PEM) electrolyzer, (3) solid oxide electrolyzers, (4) thermochemical water splitting, and (5) photoelectrochemical water splitting.

Splitting pure water electrochemically requires huge input electrical energy. Unfortunately, due to redox active impurity ions, conducting water splitting on tap and seawater are not energy-efficient as that would take up the part of applied energy for side reactions. Therefore, water electrolysis was either performed in acidic (pH 0) electrolytes that have anodically inert anions such as sulfate and perchlorate or with basic (pH 14) electrolytes such as KOH and NaOH with concentrations equal to 1 m or higher (eg: Anantharaj and Noda, 2020).

Equations (2.1) at cathode and (2.2) at anode are the half-cell reactions (HER and OER, respectively) in acidic conditions. Similarly, equations (2.3) at cathode and (2.4) at anode are the half-cell reactions (HER and OER, respectively) in basic conditions.

$$4H^+ + 4e^- \rightarrow 2H_2 \qquad E^o = 0.0V \qquad (2.1)$$

$$2\mathrm{H_2O} \rightarrow \mathrm{O_2} + 4\mathrm{H^+} + 4\mathrm{e^-} \qquad E^o = +1.23V \qquad (2.2)$$

$$4H_2O + 4e^- \rightarrow 2H_2 + 4OH^- \qquad E^o = -0.828V \qquad (2.3)$$

$$4OH^- \rightarrow O_2 + H_2O + 4e^- \qquad E^o = +0.401V \qquad (2.4)$$

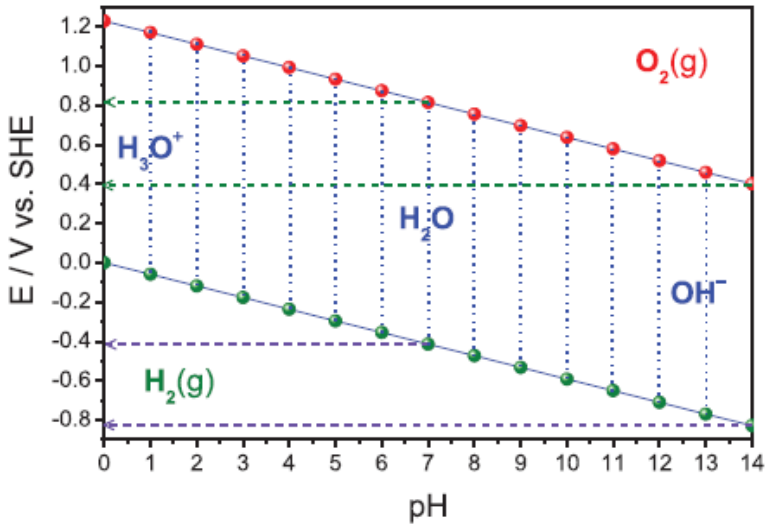

Figure 2.5: Pourbaix diagram of water showing the pH dependence of OER and HER. Left-faced arrows indicate the respective potential of OER and HER in neutral (pH 7) and in alkaline (pH 14) solution. (Anantharaj and Noda, 2020)

Based on experimental findings the Pourbaix diagram (Figure 2.5) was plotted showing the equilibrium potential of electrochemical reactions against pH. The focus of this work will be on HER under acidic condition and the detail mechanism under this sub topic will be explained further in the next section.

2.2 Hydrogen Evolution Reaction (HER)

Hydrogen evolution reaction (HER) known to be the cleanest technique to produce hydrogen. The hydrogen obtained via this method is very high purity and nonpolluting. But it is not the least expensive or the most efficient way of producing hydrogen. HER occurs on the cathodic side of electrode producing H_2 while OER occurs on the anodic side of

electrode producing O_2 as shown in eq. (1)-(4). Extensive studies on this topic were carried out by various researchers seeking ways to maximize H_2 produced (improving efficiency) while maintaining stability and be cost effective.

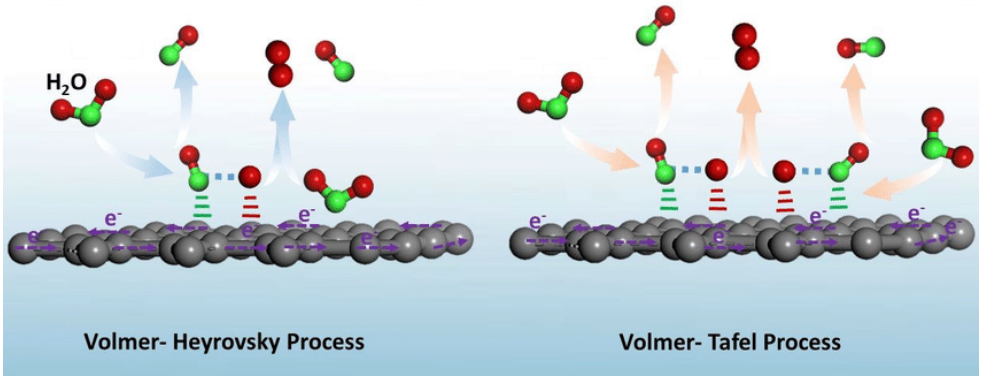

Figure 2.6: Schematic diagram of Volmer-Heyrovsky and Volmer-Tafel steps on catalyst surface (Chen et. al (2019))

Mathematical representation of the HER (in Chapter 2.2.1) was model using the mechanistic step of Volmer Heyrovsky and Tafel (Figure 2.6). This area of the HER are heavily discussed and are debatable as some estimation are far from perfect. But it serves as a good model in verifying certain behaviour in electrocatalytic activity.

2.2.1 Volmer–Heyrovsky–Tafel mechanisms

The role of the adsorbed intermediate in the Volmer-Heyrovsky-Tafel (VHT) steps for the hydrogen evolution reaction (HER) on metallic electrodes has been extensively studied by prominently Lasia since the early 80s (eg: Lasia, 1974; Lasia et. al., 2019) and Chialvo since the early 90s (eg: Chialvo et al, 1991) to date. Relationships between the Tafel slope, the rate-determining step (RDS) and the surface coverage were derived to fit different types of metals in various conditions. They are widely used to analyze the experimental

kinetic results. To provide the readers with the general consensus in VHT mechanism, Vilekar et. al. (2010) presented an approach that provides explicit rate expression involving kinetics of all three steps (Volmer-Heyrovsky-Tafel) simultaneously shown by eqs. (2.5-2.7).

$$H^+ + s + e^- \rightleftarrows Hs \tag{2.5}$$

$$H^+ + Hs + e^- \rightleftarrows H_2 + s \tag{2.6}$$

$$Hs + Hs \rightleftarrows H_2 + 2s \tag{2.7}$$

Given the Volmer and Heyrovsky are electrochemical reactions and are potential dependent, the rate constant for the forward reaction and the backward reaction are expressed as eq. (2.8-2.11).

$$K_V = \left(k_V e^{\left(-\frac{\beta_V nF}{RT}\right)\left(E_{(t)}-E_o\right)}\right) \tag{2.8}$$

$$K_{-V} = \left(k_{-V} e^{\left(-\frac{(1-\beta_V)nF}{RT}\right)\left(E_{(t)}-E_o\right)}\right) \tag{2.9}$$

$$K_H = \left(k_H e^{\left(-\frac{\beta_H nF}{RT}\right)\left(E_{(t)}-E_o\right)}\right) \tag{2.10}$$

$$K_{-H} = \left(k_{-H} e^{\left(-\frac{(1-\beta_H)nF}{RT}\right)\left(E_{(t)}-E_o\right)}\right) \tag{2.11}$$

Assuming the Langmuir adsorption isotherm, the reaction rates are presented in eq. (2.12-2.14) for Volmer, Heyrovsky and Tafel respectively.

$$R_V = (K_v c_{H^+} c_s) - (K_{-v} c_{Hs}) \tag{2.12}$$

$$R_H = (K_H c_{H^+} c_{Hs}) - \left(K_{-H} c_{H_2} c_{Hs}\right) \tag{2.13}$$

$$R_T = \left(K_T ({c_{Hs}}^2)\right) - \left(K_{-v} {c_{H^2}} ({c_s}^2)\right) \tag{2.14}$$

Figure 2.7 shows the semilog plot of overpotential and kinetic current for multiple combinations of VHT steps. This figure provides a clear picture of the expected curve from each of the VHT steps. The curve will definitely differ with the change of the kinetics values accompanying the rate expression. The author did prove that Heyrovsky-Tafel is not a significant contributor in their electrochemical system. They also shown that the steps are potential dependent and only work under certain overpotential.

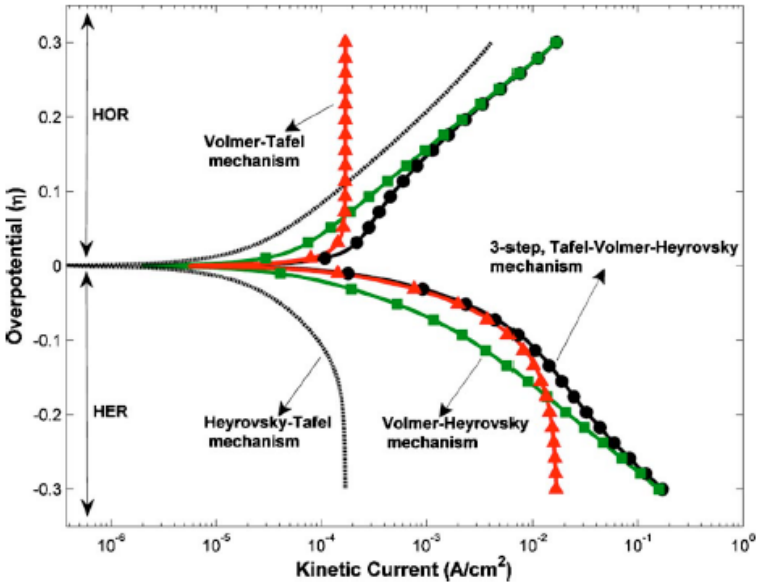

Figure 2.7: Overpotential against kinetic current for 2-steps of Volmer-Heyrovsky (VH), Volmer-Tafel (VT), Heyrovsky-Tafel (HT) and 3-steps of Tafel-Volmer-Heyrovsky (TVH) in quasi steady-state (Vilekar et. al., 2010).

Watzele et al. (2018) show that it is possible to distinguish different reaction pathways experimentally at each electrode potential, using impedance measurements and demonstrate that the relative contributions of the Volmer-Heyrovsky and Volmer-Tafel pathways are in most cases comparable. Both mechanisms contribute differently to the total current at different electrode potentials and none of them can be considered as absolutely dominating at a given time.

Koster et al. (2019) presented a model that assumed H_2 generation exclusively follows the Volmer-Tafel mechanism. To distinguish between Volmer-Tafel and Volmer-Heyrovsky mechanism, it was necessary to look at the dependence of the parameters on the potential. The extracted parameters show similar dependence on the potential, independently from the electrolyte concentration. Particularly interesting features were: 1) Volmer and Tafel step have comparable rates in diluted electrolytes, opposite to usual perception that HER on Pt in acidic media is controlled by Tafel step; 2) Can exhibits drastic change in proximity of reversible potential for HER, which indicates some unknown reconstruction of the interfacial region.

In 2015, Kichigin and Shein describes the HER on cobalt silicides in alkaline solution of (0.5 - 2.0) M KOH. It was shown that the current densities on Co_2Si is 10 times higher compared to Co electrode. The author presented the atomic hydrogen adsorption on the surface of cobalt silicides using the Langmuir isotherm, and hydrogen evolution proceeds through the Volmer–Heyrovsky mechanism. The Heyrovsky reaction is then assumed to be the rate-determining step.

A brief summary in Table 2.3 shows the research and findings on single element electrocatalyst along with the proposed HER mechanistic steps. This table indicates that there are different interpretations of VH or VT by different literatures that could probably be due to the differences in the electrocatalysts or the experimental setup and the operating conditions.

What has becoming more apparent on HER studies is that the determination of the mechanistic step of either VH, VT or VHT are not resolute and are interchangeable based on the conditions. Though the model prove itself as a great approximation of the presented

system and helps researchers in understanding the phenomena that is the hydrogen evolution reaction.

Table 2.3: Summary of VHT elementary steps for HER/HOR on single element electrodes and systems

Mechanisms	Systems and materials	References
HOR (Volmer-Tafel) HER (Volmer-Heyrovsky)	Electrochemical hydrogen pump	Hao. et al (2019)
HOR (Volmer-Tafel)	Pt in alkaline and acidic	Durst et. al (2015)
HOR (Volmer-Tafel) HER (Volmer-Heyrovsky)	Pt in 0.5M NaOH at 296K	Vilekar et al (2010)
HOR (Tafel-Volmer) HER (Volmer-Tafel)	Pt (111)	Skúlason et al. (2010)
HER (Volmer-Heyrovsky)	Pt (100) and polycrystalline Pt	Wang et al. (2006)
HOR at low η(Volmer-Tafel) at high η (Volmer-Heyrovsky)	Pt	Wang et al. (2006)
HOR (Volmer-Tafel) with slow H_2 adsorption	Porous Pt	Vogel et al. (2017)
HER (Volmer- Heyrovsky with surface diffusion)	Gold in mild acidic solution	Kahyarian et al. (2017)
HER (Volmer– Heyrovsky mechanism with a simultaneous slow desorption of anions)	Silver in acidic solution	Ruderman et al. (2013)
HER (Volmer-Heyrovsky)	Rough Pd in acidic solution	Lin and Lasia (2016)
HER (Volmer-Heyrovsky)	Tin in 0.1 M H_2SO_4	Azizi et al. (2007)
HER (Volmer-Heyrovsky)	Nb in acidic solution	Nady et al. (2021)
HER (Volmer-Heyrovsky)	Cobalt Silicides in alkaline solution (1M KOH)	Kichigin and Shein (2015)

2.2.2 Simultaneous reactions

In the previous section (Ch. 2.2.1), it can be observed that the HER model based on VHT mechanistic steps provide insight on different types of electrocatalysts activity. The examples given in Table 2.3 shows that even the same material could possibly exhibit either VH or VT. This is proven by Skúlason et al. (2010) for Pt (111) displaying VT trend while

most literatures for eg: (Durst et al. 2015 and Wang et al. 2006) shows that Pt displays VH trends.

The introduction of more complex electrocatalysts had seen that by simply employing the VHT mechanistic steps is not enough to model the electrocatalytic activity in HER. Hence subsequent reactions were added with justifications to reinforced the findings.

For example, Lin and Lasia (2016) presented their work on rough Pd as catalyst in acidic solution. They tried to approximate simultaneously current and impedance parameters to determine the rate constants of the Volmer-Heyrovsky reaction mechanism with Langmuir adsorption isotherm. However, no good approximation could be found. They suggest that it might indicate that the hydrogen adsorption isotherm is more complex. The findings presented by these researchers shows the different of opinion on the HER/HOR mechanism and this topic is still under heavy discussion.

In recent research, it is becoming more apparent that VHT reactions are not sufficient in describing HER. This was presented by researchers that worked both on the experimental design and the theoretical science behind it. The next part discusses a number of steps that were taken by some notable research in addition to the VHT mechanistic steps to further explain HER on more elaborate electrocatalyts.

2.2.2.1 VHT with surface diffusion step

Kahyarian et al. (2017) presented the plausible mechanisms of gold in mild acid based on the VHT elementary steps. The mechanisms included a surface diffusion step analyzed via a parametric study of the kinetic parameters. They suggest that the polarization behavior of HER on gold over an extended pH range was explained best when a surface

diffusion (eq. 2.16) step preceding the Tafel recombination reaction (eq. 2.17) was considered, along with the VH steps (eq. 2.15 and 2.18). Where A and B are distinct adsorption and desorption site.

$$H^+ + e^- \leftrightarrow H_{ads,A} \quad (2.15)$$

$$H_{ads,A} \rightarrow H_{ads,B} \quad (2.16)$$

$$2H_{ads,B} \rightarrow H_2 \quad (2.17)$$

$$H^+ + H_{ads,A\ or\ B} + e^- \rightarrow H_2 \quad (2.18)$$

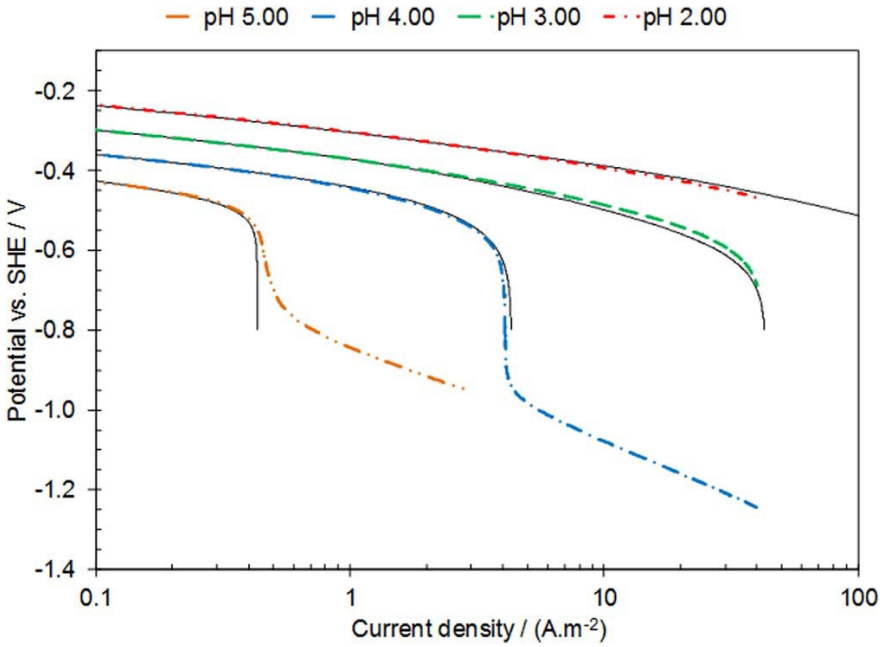

Figure 2.8: Comparison of the linear sweep voltammograms obtained experimentally (bold curve) and the results from simulation (dotted line) of gold RDE at 2000 rpm, 30 °C and 0.1M $NaClO_4$ for different pH (Kahyarian et al., 2017).

The study was carried out experimentally and by simulation via Microsoft Visual Studio 2012 and Intel Visual Fortran Compiler 13.0 for coding while using MATLAB 2012 GUI for operation of simplification. Figure 2.8 shows the comparison between the results

obtained from the experiment and simulation of gold RDE at 2000 rpm, 30 ºC and 0.1M $NaClO_4$.

The proposed mechanism suggests that at low current densities, the HER rate was limited by the surface diffusion of H_{ads}, regardless of the solution pH. At higher current densities and more acidic solutions, where a 120 mV Tafel slopes were observed, the rate-limiting step was the slow electrochemical desorption reaction (Heyrovsky step). This proposed mechanism was incorporated into a comprehensive mathematical model. The simulated polarization curves showed a reasonable agreement with both the lower and the higher Tafel slopes and the apparent reaction order, further supporting the proposed mechanism.

2.2.2.2 VHT with co-desorption mechanism

Ruderman et al. (2013) investigated the kinetics of HER on Ag (100). The authors found that within the entire range of overpotentials investigated, the reaction proceeds via the Volmer – Heyrovsky mechanism with simultaneous slow desorption of anions specifically adsorbed during the pre-treatment at potentials in the double layer region. The justification is that the co-adsorption of hydronium stabilizes these anions. The rate-determining step is the Volmer reaction, although the Heyrovsky step is only slightly faster. This fact is the reason why the anion effect is so strong. This was shown in their result in Figure 2.9 plotting results from both experiment and simulation.

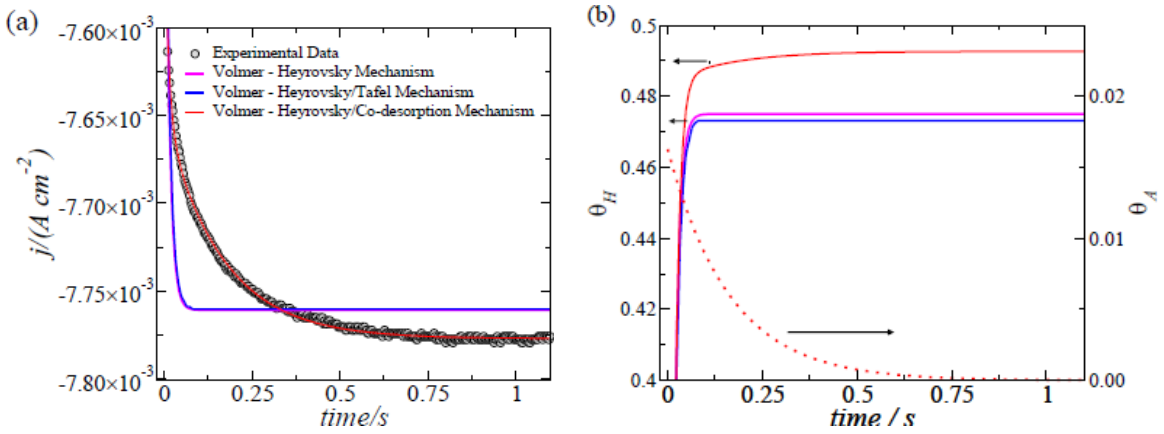

Figure 2.9: Plots of experimental and best fits lines form model of Ag(100) at 1.2V, in 0.03 mol/dm^3 H_2SO_4 solution (a) potentiostatic current transient for HER (b) Hydrogen and anions coverages against time, s (Ruderman et al., 2013).

The model proposed by Ruderman et al. (2013) initially considers VHT steps with the assumptions of no double layer charging, transport contribution and the reverse reactions. The employed equations for the current and hydrogen coverage by Gerischer and Mehl (1955) as given in eq. (2.19-2.25). Then, the co-desorption effect was included to analyze the effect when previously adsorbed species A desorbs simultaneously during HER with the rate constant k_D (eq. 2.26-2.27). Q^o_H is the charge density corresponding to a monolayer of hydrogen for Ag (100), 1.92 x 10^{-4} C/cm^2.

$$j(t) = nFk_v\big(1 - \theta_H(t) - \theta_A(t)\big) + nFk_H\big(\theta_H(t)\big) \tag{2.19}$$

$$\theta_H = P\frac{1-Se^{-\lambda_G t}}{1+Se^{-\lambda_G t}} - R \tag{2.20}$$

$$P = \frac{\sqrt{(k_V+k_H)^2+4k_Vk_H}}{2k_T} \tag{2.21}$$

$$R = \frac{k_V+k_H}{2k_T} \tag{2.22}$$

$$S = \frac{\sqrt{1+X}-1}{\sqrt{1+X}+1} \tag{2.23}$$

$$X = \frac{4k_Vk_T}{(k_T+k_H)^2} \tag{2.24}$$

$$\lambda_G = 2nF\frac{k_V P}{Q_H^o} \quad (2.25)$$

$$\theta_A(t) = \theta_A^o e^{-\lambda_A t} \quad (2.26)$$

$$\lambda_A = nF\frac{k_D}{Q_H^o} \quad (2.27)$$

The small values of the anion desorption constant have a significant consequence in the transients' shape even if the anion coverage is not substantial. The rate constants for the anions desorption process are considerably lower than the kinetics of the HER. Therefore, the HER could reach the stationary state quickly if the anions were absent. However, there are adsorption sites that the anions must release in order for the HER to take place. About 95% of the transient is determined by the kinetics of the anions desorption process.

This was further proven by Ruderman et al. (2016) in their study on the kinetics of silver. It mentioned that thermodynamics is not enough to explain the reactivity of the metal. The study compares the reactivity at the hollow sites of the flat Ag(1 0 0) surface and the vicinal Ag(1 1 5) surface. Although the adsorption energy calculated by Density Functional Theory (DFT) is similar for both systems, they found a substantially higher value for the activation energy in the case of the (1 1 5) crystal orientation. The analysis shows other essential factors, such as the electronic interactions between reactant and substrate at the transition state. A review by Zhao et al. (2018) commented that the catalytic performance of the catalysts varies very significantly, even for catalysts with similar compositions and nanostructures.

2.2.2.3 VHT with hydrogen absorption reaction (HAR)

While some researchers state that there could be other reactions along with Volmer-Heyrovsky-Tafel elementary steps during HER/HOR. Kichigin and Shein (2020) presented

a parallel hydrogen adsorption reaction (HAR) along with a hydrogen evolution reaction (HER). The HER+HAR model is considered using the concept of hydrogen adsorbed in the subsurface, an intermediate state between atomic hydrogen adsorbed on a surface and hydrogen dissolved in a surface metal layer. This is represented in terms of the reactions written in eqs. (2.28-2.32)

$H^+ + e^- \leftrightarrow H_{ad}$ (Volmer reaction) (2.28)

$H_{ad} + e^- \leftrightarrow H_2$ (Heyrovsky reaction) (2.29)

$H_{ad} \leftrightarrow H_{adss}$ (adsorbed on subsurface) (2.30)

$H_{adss} \leftrightarrow H_{abs(x=0)}$ (hydrogen near metal surface) (2.31)

$H_{abs(x=0)} \rightarrow H_{abs(bulk)}$ (diffusion) (2.32)

Where the inclusion of a new adsorbed intermediate H_{adss} and the step of desorption of H_{adss} from the subsurface to the $H_{abs(x=0)}$, a state that represents hydrogen in metal near the metal surface but deeper than the first subsurface layer in which H_{adss} is located (reaction 30). The assumption made by the authors are (1) the existence of indirect hydrogen absorption, (2) the interactions between hydrogen atoms on the electrode surface and in the subsurface are not taken into account and (3) the kinetics with Langmuir adsorption isotherm is considered. Figure 2.10 shows the Tafel plots for the HER at different HAR kinetics.

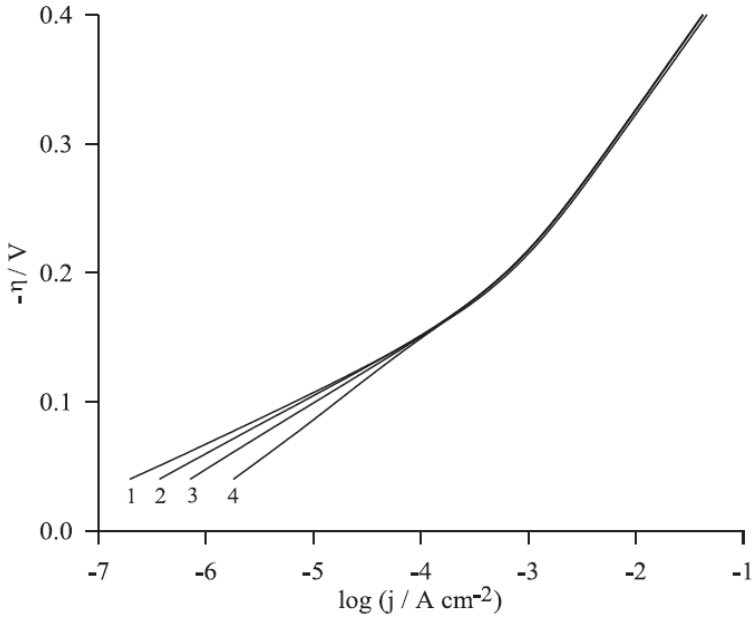

Figure 2.10: Simulated current-overpotentials curves when the HER proceeds through VH mechanism. (1) no HAR (2) 1×10^{-8} (3) 3×10^{-8} (4) 1×10^{-7} with all rate constant in mol/cm^2.(Kichigin and Shein, 2020)

A hydrogen absorption reaction can have a noticeable effect on the shape of the cathodic polarization curve at low current densities. The occurrence of the HAR leads to an increase in the slope at small overpotential. The value of the slope can become noticeably more significant than the diagnostic values by which it would be possible to discuss the mechanism of the HER. The effect of HAR is considered important for (i) studies of HER at metallic membranes on the rear side of zero concentration of hydrogen by potentiostatic anodic polarization and (ii) HER on thick electrodes.

2.3 Electrocatalysts

For any given electrocatalyst, the most desired characteristics are high activity (both thermodynamic and kinetic), reasonable stability and high selectivity. The same is applicable

to the electrocatalysts of OER and HER too. Lasia (2010) list out the general requirements for a good metal for hydrogen electrode;

a. The metal must be noble and must not itself react or dissolve in the solution
b. The metal must be a good catalyst for the hydrogen dissociation reaction; that is the metal can absorb hydrogen atoms on the surface but will not react with them to form a stable hydride.
c. The metal surface should be made by finely divided deposits. Because the catalytic activity of the metal surface is associated with crystal imperfections, the metal surface made by finely divided deposits increases not only the real surface but also the active catalytic sites.
d. In non-aqueous or partly aqueous solutions, the metal must not promote undesired non-electrochemical hydrogenation reactions.

The most widely used catalyst as a support/matrix is graphene. In its purest form, graphene is a chemically inert surface, because there are no free chemical bonds. However, the addition of strain, defects, or functional groups radically changes the chemical properties of graphene and makes it suitable as catalytic support.

Graphene is a covalently-bonded hexagonal lattice of carbon atoms just one atom thick (about 0.14 nm). It is a semimetal (its conduction and valence bands both touch). Graphene's unique band structure means that electrons move through it at high speeds (about 1/300 the speed of light), giving it fascinating properties - such as unparalleled thermal conductivity. Optically transparent, graphene absorbs only 2% of incident visible light and has the highest tensile strength of any material (Lee et al. 2008).

In the advancement of electrocatalysts field, the ranges of complexity vary including the sizes and dimensions. For example; a fabricated electrocatalyst could be in the form of visibly bulk object to a nanoscopic level that was called the quantum dots. Table 2.4 break downs the nanoscopic dimensions of a material or compound while figure 2.11 provides illustrations on given nanoscopic dimensions.

Table 2.4: Materials nanoscopic dimensions and classification

No. of nanoscopic dimensions	Classification	Example
0	Bulk	Anything visible
1	2D (nanosheet)	Graphene
2	1D (nanotube or nanowire)	Carbon nanotube
3	0D (nanoparticle)	Quantum dot

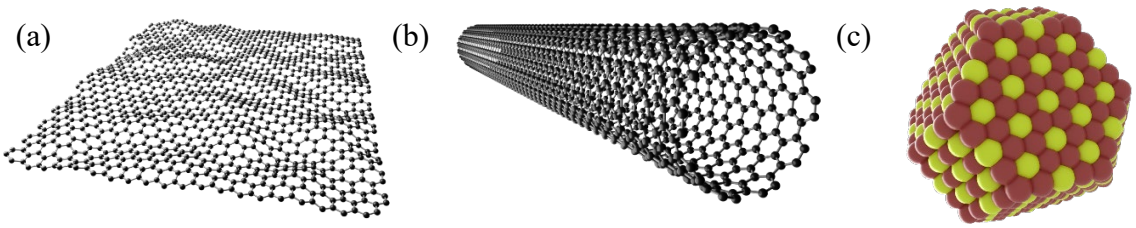

Figure 2.11: Illustrative figure of a (a) 2D graphene sheet (b) 1D carbon nanotube and (c) 0D quantum dot.

Noble metal known to be a good electrocatalyst specifically Pt, but due to the market price and rarity the use of transitional metal as an efficient substitute were explored by many (for eg: a review on self-supported TMs electrocatalyst by Sun et al. (2020) and TMs based electrocatalyst by Han et al. (2016). Transition metal dichalcogenides in particular was cited by many shows great potential. Commonly referred to as TMDCs, the chemical formula was written as MX_2, where M is a transition metal (such as molybdenum (Mo) or tungsten (W)) and X is a chalcogen such as sulfur (S), selenium (Se) or Tellurium (Te). Bulk TMDCs are

van der Waals materials with each layer being three atoms thick, consisting of the metal layer sandwiched between two chalcogenide layers.

TDMCs can take various crystal structures. The most common is the 2H-phase with trigonal symmetry, which results in semiconducting characteristics such as possessed by MoS_2, WS_2, $MoSe_2$. These semiconductors have an indirect bandgap when in the bulk. For monolayers, the bandgap becomes direct and in the visible spectrum, making them attractive for optoelectronics. Charge mobilities of ~100-1000 $cm^2V^{-1}s^{-1}$ make them a popular choice for 2D transistors. Another possible structure is the metallic 1T phase, which is the most stable polymorph of WTe_2.

Monolayers of silicon (silicene), germanium (germanene) and tin (stanene), are collectively known as Xenes (following the naming convention of graphene). They have a hexagonal structure similar to graphene, but are buckled to varying degrees. Unlike graphene, they cannot be exfoliated from bulk material and must be epitaxially grown on a substrate, and generally retain a strong interaction with that substrate. While still very much in their infancy, potential applications range from field-effect transistors to topological insulators.

2.3.1 Doped/undoped graphene, carbon, amorphous carbon (G, C, aC)

Studies on amorphous diamond-like carbon has literally proven the tremendous potential of the carbonaceous materials in electrochemistry due to its corrosion resistance. This material characterized by preferential sp^3 hybridization of the C–C bonds is inferior to diamond in its electrochemical parameters yet it is simpler to manufacture and are less expensive and easily available. Amorphous carbon on itself is considered inert or inactive.

But it can be deposited onto conducting substrates using chemical vapor deposition (CVD) or various modifications of ion-plasma (PVD) methods. In many occasions, amorphous electrocatalysts had outperformed their crystalline counterparts in electrolysis (Indra et al., 2014). One of its many possible reason is due to the flexibility (Liu et al., 2018) that allows it to adapt to the electrocatalytic conditions and provide means for both volume and surface confined electrocatalysis (Figure 2.12).

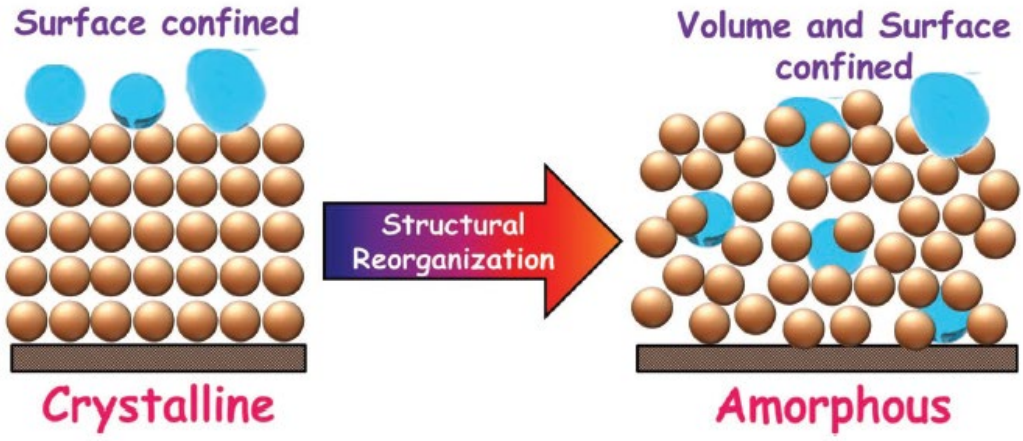

Figure 2.12: Graphical sketch showing the difference in a crystalline and amorphous materials during electrolysis (Anantharaj and Noda, 2019).

Though there is a very distinctive different between amorphous hydrogenated diamond-like carbon with a high hydrogen content(a-C:H) and the so-called tetrahedral amorphous carbon containing no hydrogen (ta-C).

An extensive study by Laurila et al. (2018) presented the electrochemistry special features of an undoped taC. It was stated that the electrical properties of the ta-C thin films are heavily dependent on the thickness of the films and consequently on the overall sp^2 fraction. The surface of the ta-C thin films is always sp^2 rich despite the sp^3 fraction of the underlying material.

Throughout the past decade, doped taC has been studied extensively in electrochemistry. Vast majority are working on nitridation and hydrogenation of taC. In a study on doped taC, Etula et al. (2021) shows that nitrogen disrupting the sp^3 C–C structure of the reference ta-C. The surface roughness increases. These changes are linked to significant increases in the hydrogen and oxygen content of the films by utilizing time-of-flight elastic recoil detection analysis. Zhao et al. (2014) shows that aC inhibits the aggregation of MoS_2 nanosheets, expose abundance catalytic edge sites and render MoS_2/AC excellent conductivity, thus effectively enhanced the catalytic performance of MoS_2 based HER electrocatalyst

As early as 1999, Yoo et al. presented their work on Nitrogen-incorporated tetrahedral amorphous carbon (taC:N) as a thin film electrocatalytic material showing its diamond-like stability. Their experiments conclude that taC:N have the characteristics of (i) a wider potential window in aqueous system sat both extremes than CVD B-diamond; (ii) reversible behavior with outer sphere couples; (iii) electron-transfer kinetics intermediate between polished pyrolytic graphite and B-diamond for the quinone/hydroquinone couple and excellent analytical behavior; and (iv) considerably higher catalytic activity for Cl_2/Cl- than B-diamond as well as durability to high anodic potential.

2.3.2 Titanium carbide

Titanium carbide (TiC) is gaining a lot of attention as an efficient electrocatalysts. In 2007, Ferri et al. had presented a comprehensive study on the electrocatalyst performances of thin film and bulk TiC. Conclusively placing TiC as a better material compared to Palladium (Pd). Which according to Shao M., (2011) Palladium is considered as a good catalyst.

Song et al. (2021) presented a relatively easy method to produce a single crystalline TiC with fully exposed {100} crystal planes with impressive catalytic activity in HER. It was explained that the improve catalytic behavior is due to the partially graphitized carbon shell promotes reduction of the Gibbs free energy for atomic hydrogen adsorption (ΔG) (synergy of C and TiC) to a moderate value. The use of TiC as support material was also widely discussed as it shows great potential particularly in HER. Sahoo et al. (2018) studied TiC as support to single metal atom found that Pt/TiC showed 6.5 times and 3.5 times higher mass activity at a 50 mV overpotential than commercial Pt/C and Pt NP/TiC, respectively.

Yoon et al. (2020) presented on the nitridation of 2D Titanium carbide MXene. By varying the amounts of analytically pure $NaNH_2$, either 20 mg, 40 mg, 80 mg or160 mg, were mixed with 200 mg of synthesized Ti_2CT_x in a 10 mL stainless-steel autoclave. Depending on the amounts of $NaNH_2$ used they showed 2 at.% (2N-Ti_2CT_x), 3 at.% (3N-Ti_2CT_x), 5 at.% (5N-Ti_2CT_x) and 11 at.% (11N-Ti_2CT_x) of nitridation degree, respectively.

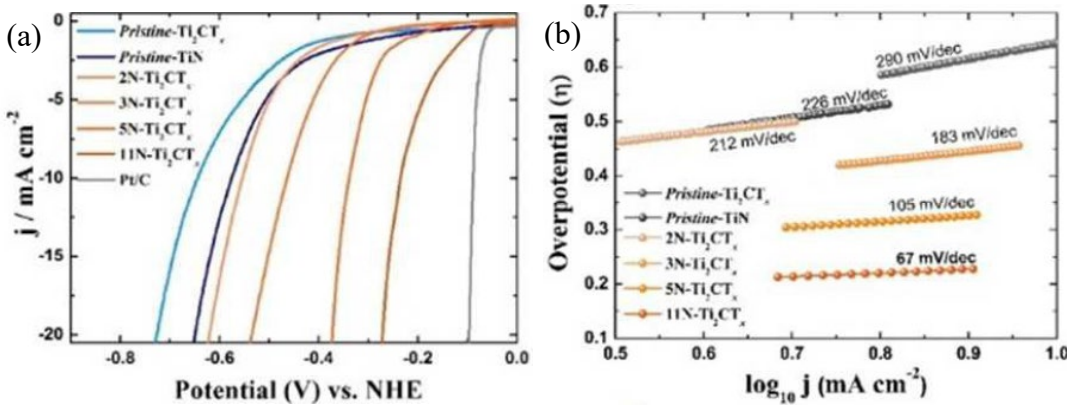

Figure 2.13: (a) Linear sweep voltammetry (LSV curves) without iR correction of electrocatalysts with a scan rate of 10 mV/s; (b) corresponding Tafel slopes. (Yoon et al., 2020)

The Tafel slopes are calculated to be 290 mV/dec (pristine-Ti_2CT_x), 225 mV/dec (cubic TiN), 212 mV/dec (2N-Ti_2CT_x), 183 mV/dec (3N-Ti_2CTx), 105 mV/dec (5N-Ti_2CT_x)

and 67 mV/dec (11NTi$_2$CT$_x$), respectively. The smallest Tafel slope of 11N-Ti$_2$CT$_x$ can be interpreted by the change of rate-determining step (RDS) during the HER processes. It suggests that the RDS for the pristine-Ti$_2$CT$_x$ follows the Volmer step while the 11N-Ti$_2$CT$_x$ may follow the Volmer Heyrovsky step. Although the HER mechanism is still in conflict, a much smaller Tafel slope value indicates better kinetics for the HER processes. Overpotential of 10 mA/cm^2 and the value of Tafel slope as a function of different N content in N-Ti$_2$CT$_x$ (all samples) are summarized in Fig. 2.13.

2.3.3 Molybdenum (Mo)

Developing highly efficient HER electrocatalysts that are low-cost is of utmost importance to realize hydrogen economy. Earth abundant compound such as carbons have attracted tremendous research interest. Among them, molybdenum carbides have exhibit great potential catalytic properties (Miao et al. 2017).

Molybdenum diselenide ($MoSe_2$) has low active sites and poor conductivity that severely restrict its HER performance. Jian et al. (2018) introduce a material of MoO_2 layer on Mo foil, $MoSe_2/MoO_2$ hybrid nanosheets with an abundant edge and high electrical conductivity can be synthesized on the surface of Mo foil to improve HER on the material.

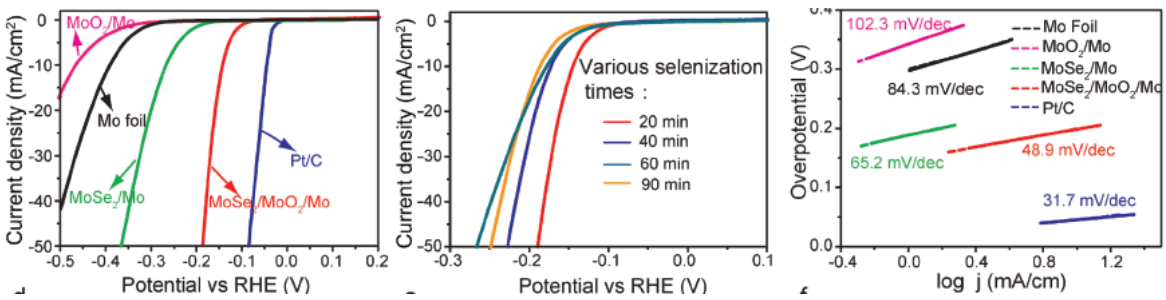

Figure 2.14: a) The polarization curves of $MoSe_2/MoO_2/Mo$, $MoSe_2/Mo$, MoO_2/Mo, Mo foil, and commercial Pt/C. b) The polarization curves of MoO_2/Mo selenized at different times. c) Tafel plots of the catalysts shown in (a). (Jian et al.,2018)

The authors presented their finding (Figure 2.14) on the developed $MoSe_2/MoO_2/Mo$ exhibits highly improved HER performance compared with that of the pure $MoSe_2$ catalyst. $MoSe_2/MoO_2/Mo$ has a small Tafel slope of 48.9 mV dec^{-1}, a low onset potential of 60 mV versus RHE, and a small overpotential of 142 mV versus RHE at a current density of 10 mA cm^{-2}. The high catalytic activities of $MoSe_2/MoO_2/Mo$ are ascribed to the synergistic effects of the abundant active sites at the MoSe2 surface, fast charge transport efficiency between $MoSe_2$ and MoO_2/Mo substrate.

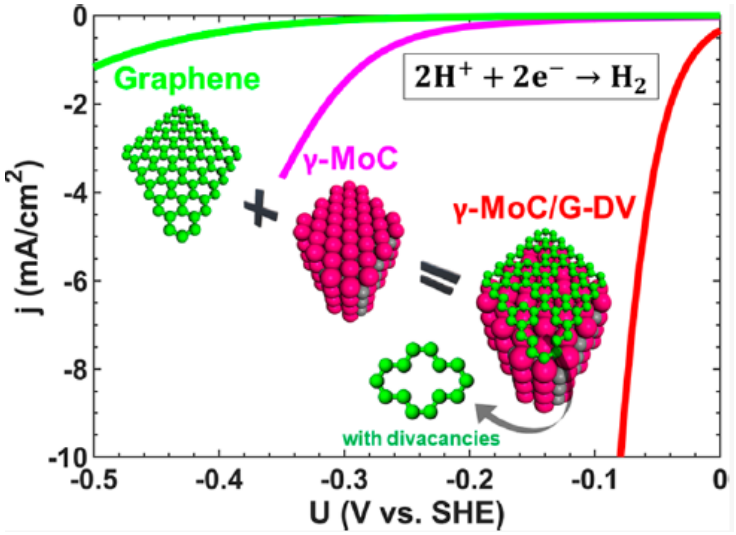

Figure 2.15: Graphene coated molybdenum carbide (MoC/G) (Yang and Saidi.,2020)

An interesting study of graphene coated molybdenum carbide (MoC/G) shown in Figure 2.15 was presented by Yang and Saidi (2020). The HER performance of MoC/G was evaluated at 50 mV/dec, significantly higher compared to MoC only and G only. The authors argue that due to charge transfer effect, extra electrons (holes) on graphene will

occupy graphene's antibonding π* (bonding π) bands. This weakens graphene π bonding and increases hydrogen stabilization as less energy is required to break the graphene π bond.

2.3.4 Tungsten (W)

Ma et al. (2018) report a new type of multi-interfacial nickel/tungsten carbide (Ni/WC) hybrid nanoparticles anchored on N-doped carbon sheets (Ni/WC@NC). This fabricated material (see Figure 2.16) can efficiently and robustly catalyze the hydrogen evolution reaction (HER) with striking kinetic metrics in a wide pH range. Based on Figure 2.17, in 0.5 M H_2SO_4, Ni/WC@NC displays a low overpotential (53 mV at current density of 10 mA cm^{-2}), a small Tafel slope (43.5 mV dec^{-1}), a high exchange current density (0.83 mA cm^{-2}), as well as excellent stability, outperforming most of the current noble-metal-free electrocatalysts.

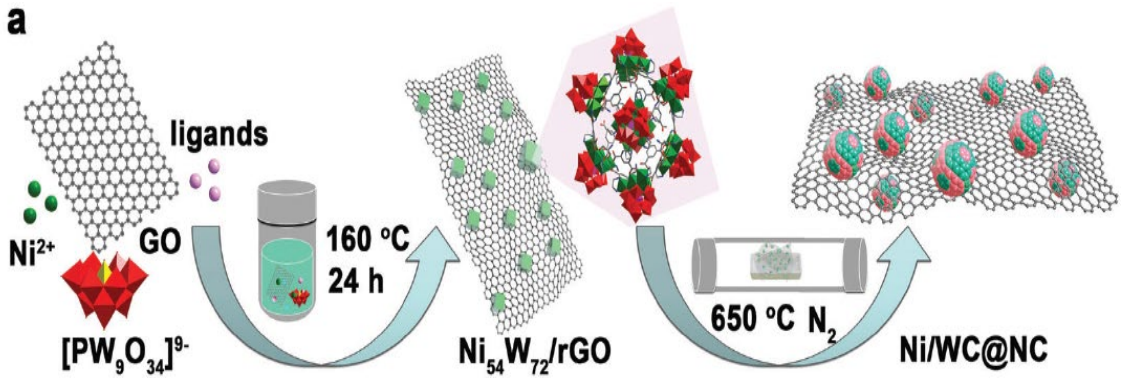

Figure 2.16: Illustration showing the fabrication process of Ni/WC@NC. (Ma et al., 2018)

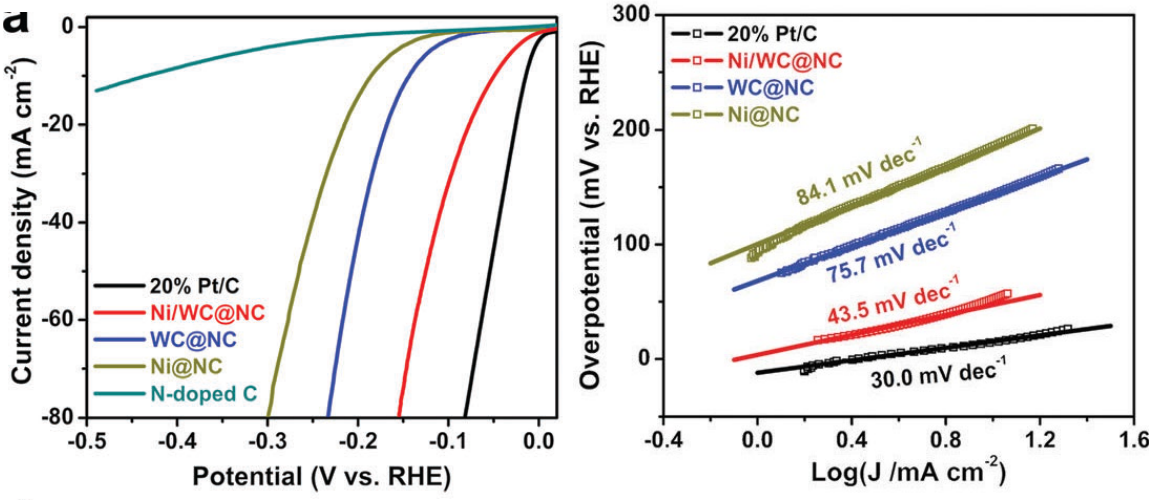

Figure 2.17: (a) Polarization curve of Ni/WC@NC in 0.5 M H_2SO^4 electrolyte at 5 mV s^{-1}, along with those of Ni@NC, WC@NC, N-doped C and Pt/C for comparison. (b) Tafel plots of Pt/C, Ni/WC@NC, Ni@NC and WC@NC. (Ma et al., 2018)

Choosing the right support material is important for improving electrocatalysts in hydrogen production. The tungsten suboxide catalyst that was used to support Pt in our study implies that interactions between the well-matched metal and support can drastically enhance the efficiency of the process.

Bukola et al. (2016) developed a dual performing electrocatalyst for oxygen reduction reaction (ORR) and hydrogen evolution reaction (HER) by co-doped cobalt and nitrogen on tungsten carbide(Co-N/WC) matrix. Its improved ORR and HER activities in 0.1 M KOH were confirmed using a thin-film rotating ring-disk electrode (TF-RRDE) and electrochemical impedance spectroscopy (EIS). The exchange current density and Tafel slope obtained from EIS data for HER are 1.6 x 10^{-2} $mAcm^{-2}$ and 43 mV/dec respectively, suggesting Volmer-Heyrovsky mechanism for HER.

2.3.5 Others (nitrides, oxides, noble metals)

Electronic synergism due to pyridinic and graphitic –nitrogen has been presented by Ning et al. (2019). The authors stated the strong electronic interaction of N-carbon facilitated the electron reduction to produce anion. Isolated pyridinic N and graphitic N can both improve reaction activity. Ma et al. (2019) conducted an experiment to study the efficiency of Nickel cobalt phosphide. The authors presented for HER the Tafel slopes of 37, 57, 63, 66, 78, 119 mV/dec for 3D-NiCoP, NiCoP/2, NiCoP/4, NiP_x, CoP_x and NF, respectively, in 0.5M H_2SO_4 and suggested the Volmer-Heyrovsky mechanism. While suggesting 3D-NiCoP for HER proceeds through the Volmer-Heyrovsky mechanism in 1M KOH exhibits a Tafel slope of 79 mV/dec.

A catalytic effect by sulfate adsorption has been observed for the HER, as it is evident from the higher rate constants obtained for both processes (Volmer and Heyrovsky) in the presence of adsorbing anions. The proposed model for evaluating the rate constants is based on the sites inhibition by anions and cannot explain by itself an increase in the catalytic activity. A quantitative analysis of this effect requires detailed theoretical modeling for the barrier of both steps. A substantial decrease of the transfer coefficient α at higher negative overpotentials has been observed.

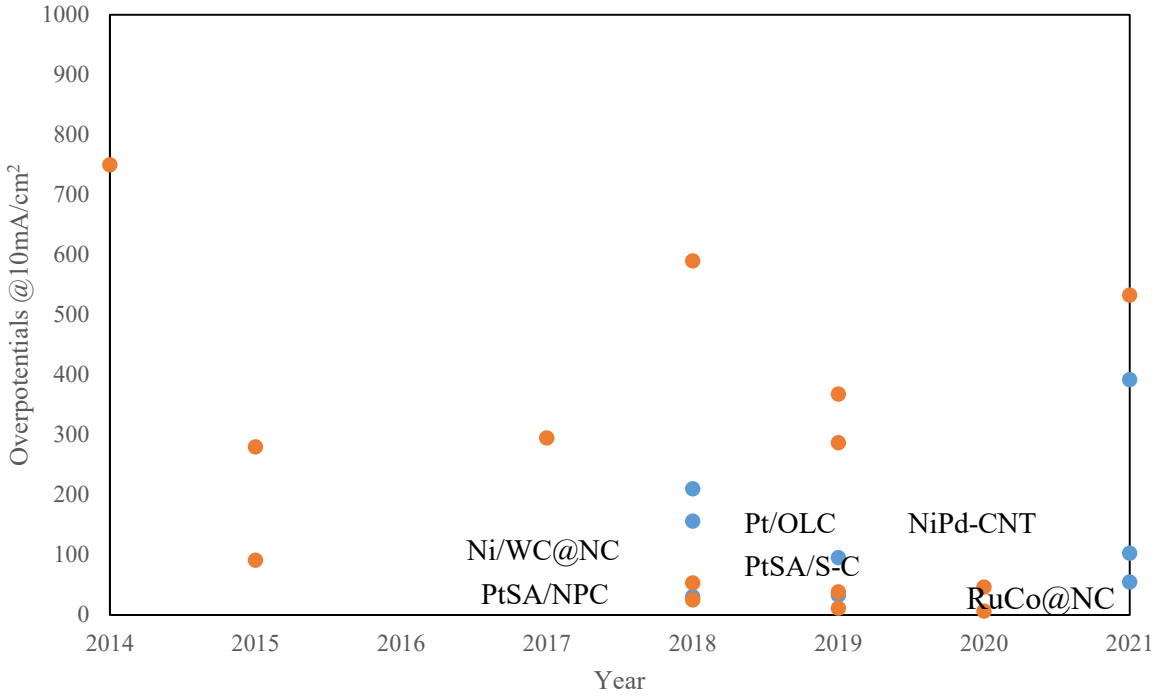

Figure 2.18: Overpotentials @10mA/cm^2 for several studies working with TiC (blue) and doped/undoped graphene or amorphous carbon (orange) electrocatalysts as function of time ranging from 2014-2021.

Based on some of the electrocatalysts listed in table 2.5, it was observed that between (2017-2021) from some of the most notable researchers in the field, Pt like performances were achieved by non Pt doped electrocatalysts working with (1) TiC and (2) graphene or carbon/amorphous carbon group. For example, in 2018 Ma et al. was able to produce a great HER performance of 53 mV@10 mA/cm^2 with TS of 43.5 mV/dec from TM. The electrocatalyst was made by fabricating Nickel and Tungsten carbide nanoparticles on N-doped carbon sheets (Ni/WC@NC). While a few other studies working with Noble metals; for example: Ruthenium-cobalt nanoparticles on Nitrogen doped carbon (RuCo@NC) by Zhang et al. (2020) achieved a staggering 6 mV@10 mA/cm^2 with TS of 26 mV/dec, Nickel oxide and palladium on carbon nanotube (NiPd-CNT) by Bhalotia et al. (2020) presented a 46 mV@10 mA/cm^2 with TS of 38 mV/dec. Figure 2.19 shows the overpotential@10

mA/cm^2 for the works on TiC and doped/undoped carbon by researchers ranging between (2014-2019). The trend clearly shows that some electrocatalyst in recent years were able to achieve Pt like performances.

Table 2.5: Summary of electrocatalysts by category and its performance.

Material	Tafel slope (mV/dec)	Overpotentials, η_{10} (mV)	Ref.
Titanium carbide (TiC)			
Single crystalline {100} TiC nanocubes (TiC{100})	114	-392	Song et al. (2021)
Titanium carbide with carbon films (TiC/C)	182	-451	
Random faceted Titanium carbide (TiC)	386	-815	
Platinum on mesoporous Titanuim carbide and carbon microsphere (Pt@TiC-C)	57	-95.6	Wang et al. (2019)
Titanium carbide with carbon nanorods array (TiC/C)	390		Deng et al. (2018)
2H Molybdenum Selenide on Titanium carbide with carbon nanorods array (2H-MoSe2/TiC-C)	110	-240	
1T Molybdenum Selenide on Titanium carbide with carbon nanorods array (1T-MoSe2/TiC-C)	42	-187	
Nitrogen doped Molybdenum Selenide on Titanium carbide with carbon nanorods array (N-MoSe2/TiC-C)	32	-106	
Platinum on Titanium carbide (Pt/TiC)	44	-156	Sahoo et al. (2018)
Palladium on Titanium carbide (Pd/TiC)	88	-220	
Gold on Titanium carbide (Au/TiC)	76	-230	
Platinum-Titanium nanoparticles on 2D Titanium carbide ($Pt_3Ti@Ti_3C_2T_x$)	32.3	-32.7	Li et al. (2019)
Cobalt modified 2D Titanium Carbide ($Ti_3C_2T_x$:Co)	104.42	-103	Luo et al. (2021)
Nitridation of 2D Titanium Carbide (N-Ti_2CT_x)	67	-210	Yoon et al. (2018)
Single Platinum atoms on 2D Titanium carbide ($Mo_2TiC_2T_x$-Pt)	30	-30	Zhang et al. (2018)
2D Platinum sulfate quantum dots on Titanium carbide (PtS_2/TiC)	60	-55	Jeong et al. (2021)
doped/undoped graphene, carbon, amorphous carbon (G, C, aC)			
Graphite (GC)		-750	Sathe et al. (2014)

Defective graphite (DeG)	99	-520	
Boron sub graphite (B-SuG)	130	-450	
Boron-diamond like carbon (B-DLC)	336-413		Naragino et al. (2013)
Graphite (GC)	142	-533	Liu et al. (2021)
Boron-carbon-nitride (BCN)	42.6	-373	
Boron-carbon-nitrides on graphite (BCN@GCs)	39	-333	
Nitrogen-boron-carbon nanosheet (NBC)	205	-590	Qu et al. (2018)
Nitrogen-sulfur doped graphene (N,S-G)	80.5	-280	Ito et al. (2015)
Nitrogen-Sulfur doped carbon nanosheet (N,S-CN)	76.9	-295	Qu et al. (2017)
Nitrogen-Phosporous doped carbon nanosheet (N,P-CN)	139.3	-550	
Nitrogen doped carbon nanosheet (N-CN)	159.3	-620	
Nitrogen-Boron doped carbon nanosheet (N,B-CN)	198.2	-710	
Ruthenium with defective Nitrogen-phosporus doped carbon nanosheet ($Ru/_{D}$-NPC)	41.7	-68	Li et al. (2022)
Nitrogen doped carbon (NC)	275		Bi et al. (2022)
Nitrogen-Phosporous doped carbon (NPC)	160		
Rhodium in Nitrogen doped carbon (Rh@NC)	101		
P-modified Rhodium in Nitrogen-Phosporous dopen carbon (Rh-P@NPC)	40	-31	
Platinum on carbon (Pt/C)	28	-31	
Amorphous carbon supported Molybdenum Sulphide (MoS2/aC)	40		Zhao et al. (2014)
Cobalt phosphate-Nitrogen doped carbon (CoP-N-C)	42	-91	Zhang et al. (2015)
Platinum on onion like nanosphere carbon (Pt/OLC)	36	-38	Liu et al. (2019)
Amorphous carbon and copper phosphide nanowires (aC/Cu_3P)	72	-287	Manikandan et al. (2019)
Platinum single atom and sulfur doped carbon (PtSA/S-C)	23.51	-11	Yan et al. (2019)
Platinum nano cluster and sulfur doped carbon (PtNC/S-C)	46.92	-53	
Platinum on carbon (Pt/C)	29	-31	
Platinum single atoms on Nitrogen doped Carbon (Pt/NPC)	28	-25	Li et al. (2018)

Platinum on carbon (Pt/C)	31	-33	
Nickel and Tungsten Carbide nanoparticles on N-doped Carbon sheets (Ni/WC@NC)	43.5	-53	Ma et al. (2018)
Nickel oxide and palladium on carbon nanotube (NiPd-CNT)	38	-46	Bhalotia et al. (2020)
Ruthenium Cobalt nanoparticles on Nitrogen doped carbon (RuCo@NC)	26	-6	Zhang et al. (2020)
Carbon nanotubes and graphene like nanosheets with Titanium dioxide doped Cobalt oxide (CoO_x-N-C/TiO_2C)	134	-367.8	He at al. (2019)
Co atoms coordinated with four sulfur atoms supported on N-doped carbon (Co_1-S_4/NC)	60	-114	Tang et al. (2022)
Molybdenum (Mo)			
Molybdenum carbide on graphene (MoC/G)	50		Yang and Saidi (2020)
Cobalt-modified Molybdenum Carbides (Co-MoC)	50.3-77.7	-(15-148)	Bukola et al. (2016)
Molybdenum diselenide and Molybdenum oxide ($MoSe_2$/MoO_2)	48.9	-142	Jian et al. (2018)
Molybdenum sulfate supported Platinum nanoclusters (MoS_2/Pt_{20})	40		Yang and Saidi (2020)
3D Molybdenum sulfate nanosheet on Molybdenum oxide (3D MoS_2/MoO_2)	35.6	-300	Nikam et al. (2015)
Tungsten (W)			
Tungsten sulphide (WS)	129	-604	Yang et al. (2015)
Amorphous nickel and Tungsten sulphide (NiWS)	55	-250	
Amorphous cobalt and Tungsten sulphide (CoWS)	74	-330	
Tungsten Carbide thin film on Tungsten nanoparticles graphite (W_2C@WC)	108	-310	Emin et al. (2018)
Platinum on Tungsten Oxide (Pt/WO_{3-x})		-50	Park et al (2019)
Others (Nitrides, oxides, Noble metals)			

Cobalt nanotubes with Titanium Dioxide Nanodots (TiO_2-NDs/Co NSNTs-CFs)	62	-40	Feng et al. (2017)
Titanium Nitride nanowires (TiN)	54	-92	Han et al. (2016)
Platinum and Ruthenium dimers (Pt-Ru)	28.9	-19.6	Zhang et al. (2019)
Platinum single atom (PtSa)	33.2	-56.9	

2.4 Computational simulation in electrochemistry

There are tremendous opportunities in advancing electrochemical surface science merging computational and experimental methodologies, which leads to many breakthroughs in the research and development of HER electrocatalysts.

In many case studies on computational chemistry, density functional theory (DFT) and ab-initio are among the prominent simulators that are able to quantitatively evaluate the reactivity of an electrode at atomic/molecular level.

On different scenarios finite element method (FEM) and finite different method (FDM) in electrochemistry usually deals with the science between the electrolyte and the surface of the electrode. The application of FEM and FDM can be very vast, for e.g. ranging from the thermodynamics, changes of pH and molecule concentration and flow. FEM in particular is a great software to provide visual in model approximation.

2.4.1 Density functional theory (DFT) and ab-initio

The use of DFT and ab-initio in electrochemistry has shown great progress throughout the year for e.g (Li et al. 2022, Li et al. 2018, Yang and Saidi, 2020). These computational simulators dive in depth on the quantum chemistry studies between the surface and the electronic structure of a solid electrode.

Skulason et al. (2007) present results of density functional theory calculations on a Pt (111) slab with electrochemical double layer. By varying the number of protons/electrons in the double layer they determined the activation energy and predominant reaction mechanism as a function of electrode potential and confirmed by explicit calculations that the variation of

the activation barrier with potential can be viewed as a manifestation of the Brønsted–Evans–Polanyi-type relationship between activation energy and reaction energy found throughout surface chemistry.

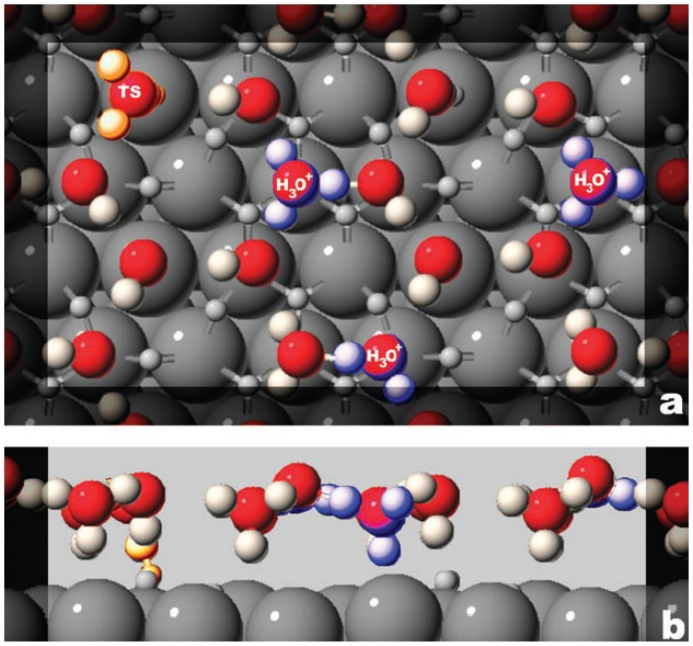

Figure 2.19: An example of top (a) and side (b) view of the model system for the electrochemical double layer above a Pt (111) electrode (Skulason et al., 2007)

In 2019, Li et al. was able to explained the intricate behavior of Pt_3Ti nanoparticles on 2D transition metal carbide. The findings via DFT calculations suggest that the (111) and (100)-terminated Pt_3Ti nanoparticles exhibit *H binding comparable to Pt(111), while the (110) termination has an exergonic *H binding adsorption that poisoned the low overpotential region. This assumption could only be made with the strong supports from the simulation.

Similarly, Lee et al. (2019) presented the electrochemical carbon dioxide reduction to syngas on Pd Bi-metallic hydrides using a combination of in situ characterization and DFT calculations. Figure 2.16 shows an example of results yield from DFT calculation on *H adsorption on various Pd bi-metallic catalysts.

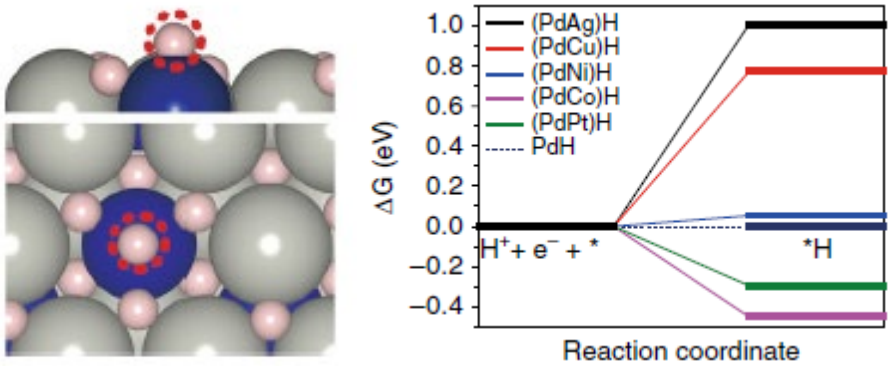

Figure 2.20: An example of DFT results on *H adsorption on Bimetallic catalyst (Lee et al., 2019)

An excellent study of single Pt atoms on MXene by Zhang et al. (2018) using DFT calculations was able to prove that the incorporation of Pt atoms in the MXene lattice resulted in a redistribution of the electronic structure. This finding indicates that the individual single Pt atom can effectively improve the d-electron near the fermi level.

Jin et al. (2020) utilizes DFT calculations to screen for suitable HER catalysts among twenty-four 2-D double transition-metal carbide MXenes. The study helps determine the tthermodynamic stabilities of these materials under HER conditions. There were probably thousand more elaborate findings with strong justifications that were able to be reached using this method and it can only help the advancement of our understanding in electrocatalytic behavior.

2.4.2 Finite difference (FD) and finite element (FE)

The use of finite difference method (FDM) and finite element method (FEM) has dominated the industry in tackling electrochemical problems (Carneiro et al. 2014). Commercial software packages consisting of reaction and transport processes, for example,

offer a multitude of options in modelling both complex and straightforward simulations. Ludwig et al. (2006) state the ability of FEM to generate a mesh with an automatic setting.

Numerous literature presented works utilizing FEM in electrochemistry via COMSOL Multiphysics® as a platform, for e.g., Cutress et al. (2010) and Dickinson et al. (2014) reported a general overview of the software's capacity to perform numerical work in electrochemistry. While a few pieces of literature deal with focus subjects, for e.g., Trinh et al. (2014) used the platform to investigate far-field boundaries using the infinite element method and Lavacchi et al. (2009) reported the simulation of the microelectrodes array on varying *noe* (number of element) using the COMSOL Multiphysics®. Both studies show the accuracies of simulations for different meshing configurations on a 2D axisymmetric model. In 2016, Carneiro et al. investigated the possibility of interfacial pH changes during HER using FEM. Figure 2.22 shows an example of their developed 1D model approach to justify the parallel reactions of metal hydroxide formation in metal electrodeposition. This study shows a good example of a simulation centric investigation.

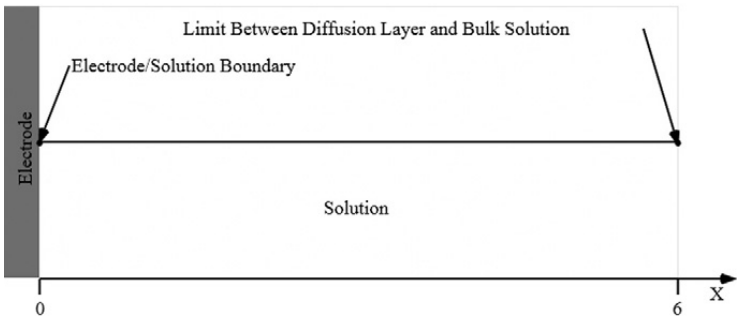

Figure 2.21: An example of 1D model by using FEM to investigate interfacial pH during HER. (Carneiro et al., 2016)

Studies on complex electrocatalyst has been presented by Tu and Wu (2021) on Au@MoS_2 nanoflowers using the combination of both DFT calculations and FEM. COMSOL was used

to model the Au nanoparticles encapsulation by MoS_2 nanoflowers (as shown in Figure 2.23) to verify the significant increase of HER rate.

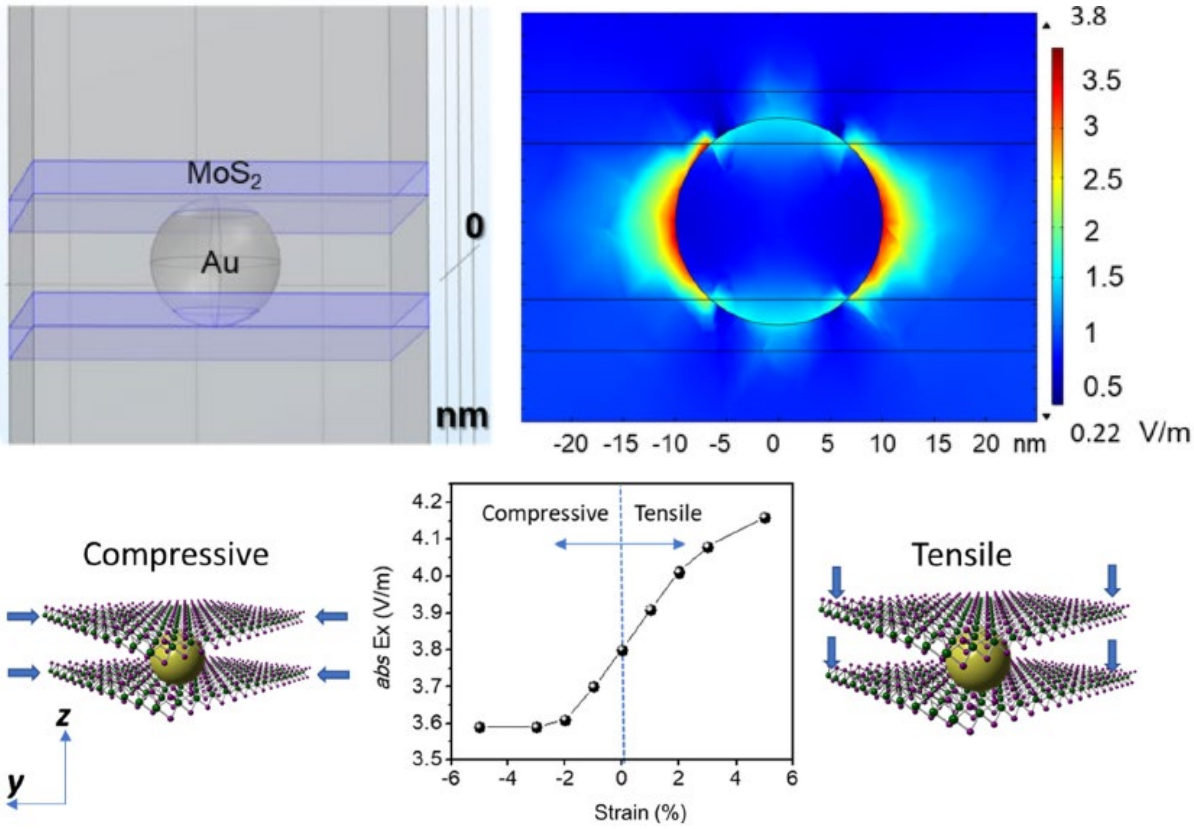

Figure 2.22: Examples of FEM results) on (a) A 3D model of encapsulated Au nanoparticles between two MoS_2 monolayer. (b) Example of simulated electric field of Au@MoS_2. (c) Comparison of the theoretical calculation under the tensile and compressive strain for Au NP sandwiched between two monolayer MoS_2. (Tu and Wu, 2021)

The utilization of adaptive meshing in the FEM was presented by Gavaghan et al. (2006). Several published works described the algorithms behind adaptive meshing to increase accuracy and precision to the developed model (Gavaghan et al. 2006; Harriman et al. 2000) reporting on a pervasive numerical approach on meshing techniques and time stepping limits the error in a model. CFD (one of FEA branches) study by Huang et al. (2020) presents an optimized electrode by manipulating the shape in an electrocatalytic reactor. The

results demonstrated mesh electrode and influential tangential mode in relation to the uniform velocity distribution on electrode surface to promote a uniform solution distribution. Near similar research by Vyroubal and Macak (2019) using ANSYS Fluent software to investigate cyclic voltammetry has proven the ability of ANSYS Fluent as software to model cyclic voltammogram, albeit on simpler macroelectrodes. The difficulties in handling more complex geometries are expressed in their discussion.

More recent numerical research conducted by Uchida et al. (2017a, 2017b) presented extensive works on cyclic voltammetry via FDM simulation using C++ programming. The relation between scan rate speed and the potential waveform was discussed in detail. Linear potential, non-triangular waveform, and semi-circular potential were employed by their dependence on the scan rate in various ways, e.g., to amplify peak current. Another research using computer simulation is conducted by Chirkov et al. (2020) in elucidating the effects of cathode active layer structure on the lithium-oxygen battery overall characteristics during its charging and discharging.

2.5 Chapter Summary

In the beginning of this chapter, an introductory to hydrogen industry was explained. It started from the sources of the hydrogen, the method of processing and estimated efficiency with the commercial readiness of the developed system. Then it began to focus on water splitting techniques in general and on HER specifically. The VHT mechanistic steps in relation to HER was given in details with a number of relevant examples of the mathematical modelling translated from selected experimentation. The main review of electrocatalysts begin after VHT mechanistic steps were elaborated. Breakdown on the vast field of electrocatalysts were provided with focus but not limited to amorphous carbon and

titanium carbide substrates. A few other examples from emerging electrocatalyst were given to share the state and new ideas on the electrocatalytic activity for HER. Finally, a review was given on the implementation of computer simulation in explaining the fascinating phenomena of HER. The utilization of well-known simulation techniques such as FEM and DFT were elaborated by providing figures and quotes from previous notable works. The elaboration includes but not limited to the intrinsic property of a material, the electrocatalytic behavior and possible explanations in HER.

CHAPTER 3

METHODOLOGY

3.1 Design and modeling of redox reaction in electrochemistry using COMSOL Multiphysics

This work demonstrates how to model redox reaction in electrochemistry in different dimensions (1D, 2D axisymmetric and 3D) using COMSOL Multiphysics. In this particular case, the model (Fig 3.1) involves an inert metallic electrode in an electrolyte solution. This study is used in this initial work in building the fundamental in electrochemistry understanding. This basic would serve the large part of this research when the simulation of the Volmer-Heyrovsky-Tafel mechanistic steps is discussed in Chapter 5. When modeling electrochemical reactions, the reaction rates are commonly functions of the concentrations of the reactants in the phase that transports the chemicals close to the electrode. The mass balances of the species must therefore be coupled to the electrode potential that is a time-dependent parameter in the simulation. This is tight together via the Butler-Volmer equations.

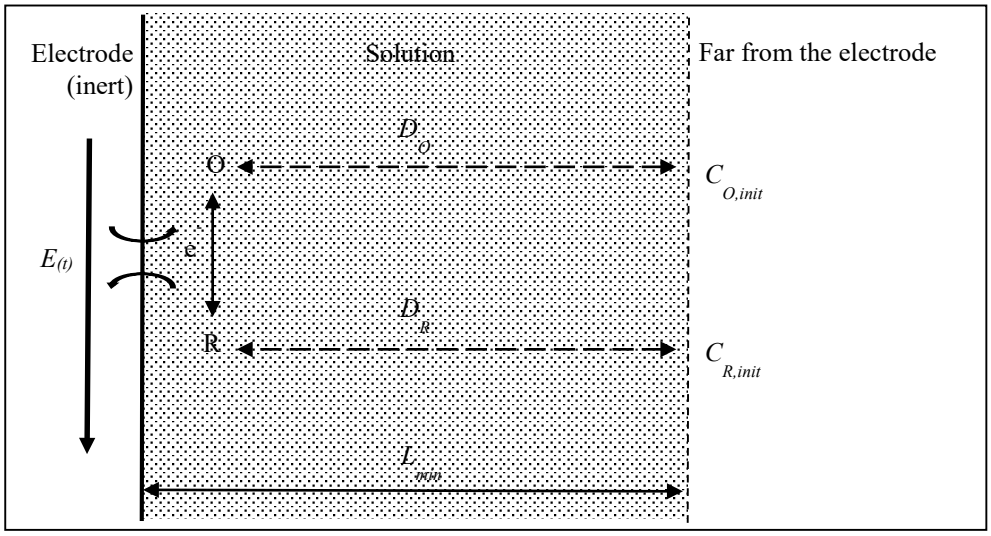

Figure 3.1: Schematic diagram of redox reaction near an electrode

3.1.1 Model definition

The model is translatable to 2D axisymmetric and 1D. But for the purpose of understanding the basic software operations in its modelling and simulation with regards to its precision and accuracy, all geometries of 3D, 2D axisymmetric and 1D are presented in this chapter. Fig 3.2 shows how the 1D model is related to the 2D axisymmetric model domain, and 2D axisymmetric model domain to the 3D geometry.

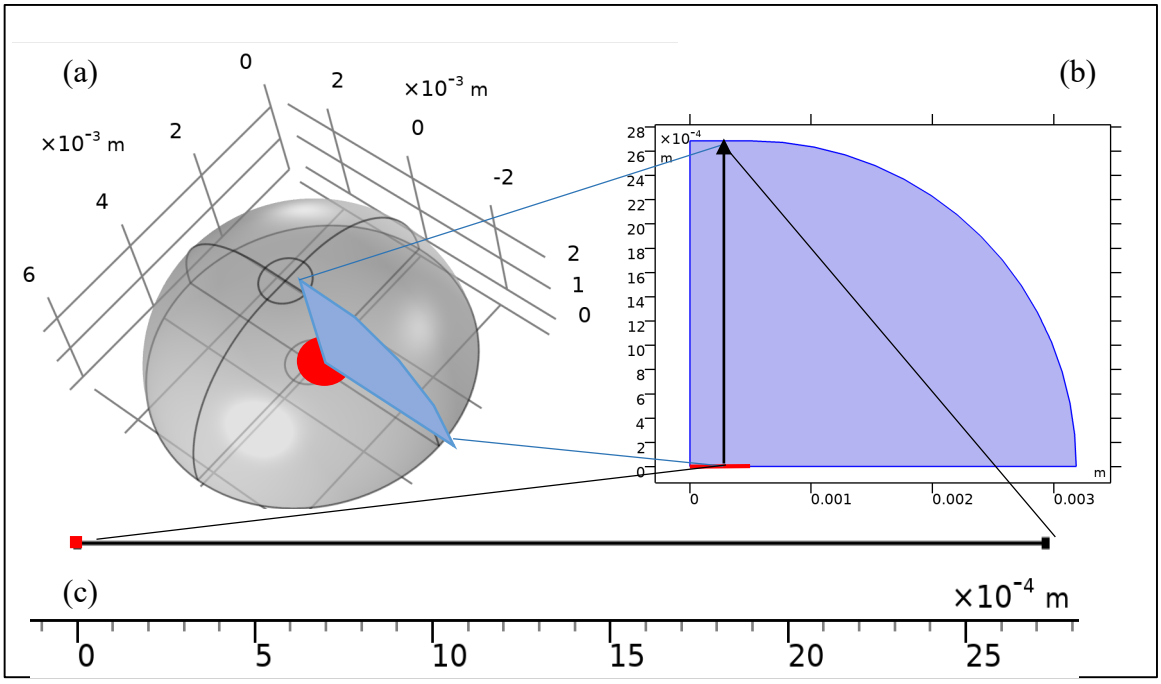

Figure 3.2: (a) 3D geometry showing an exposed electrode as an active surface (red highlighted region) within a near hemispherical domain giving the impression of far from the electrode condition; (b) reduction of 3D to 2D axisymmetric with the blue highlighted region that shows the related domain; (c) 1D model reduced from the 2D axisymmetric domain.

3.1.2 Model equations

An electrochemical reaction requires electrodes and solution as a medium. When a reduction process produces R, the reaction that took place is written as eq (3.1);

$$O + ne^{-} \rightleftarrows R \qquad (3.1)$$

This electrochemical reaction is a reversible process; hence, reversing the reaction will be an oxidation reaction producing O. As represented in Fig 3.1, in the region of interest, the concentration of O, c_O, and R, c_R in mol/m^3 will depend on the diffusivity, D_O (for O) and D_R (for R) in m^2/s. In the present simulation, the diffusivity is assumed to be equal, $D = D_0 = D_R$. The cell potential, $E_{(t)}$ in V, generates the force for the electron, e, to be transferred either in reduction or oxidation.

L_{min} is the minimum length required for a medium considered far from electrode where the initial concentration of O, $c_{O,\,init}$ and R, $c_{R,\,init}$ remain constant. Eq. (3.2) is written to evaluate L_{min}.

$$L_{min} = 6\sqrt{D.t_{end}} \tag{3.2}$$

The introduction of parameter L_{min} was evaluated to avoid any calculation disruption in the domain during calculation. This was implemented by (for eg: Lavachi et al. 2009 and Compton and Banks, 2018). Lavachi et al. (2009) introduced the parameter L_{min} to ensure that the model was numerically stable and accurate. They determined the value of L_{min} by comparing the results of simulations with different values of L_{min} to experimental data. The authors found that a value of L_{min} equal to 5 µm provided good agreement between simulation results and experimental data. While Lee et al. (2001) introduced the parameter L_{min} to avoid numerical instabilities that could occur due to the large gradients in concentration and potential near the electrode surfaces. They determined the value of L_{min} by performing a sensitivity analysis on the model and found that a value of L_{min} equal to 1 µm provided good stability and accuracy in their simulations.

3.1.3 Boundary conditions

In COMSOL, transport of diluted species module was used to represent the species O and R, respectively. The example of the implementation was given in Fig 3.3 while Fig 3.4 shows the option chosen in the selected transport of diluted species (*tds*) module.

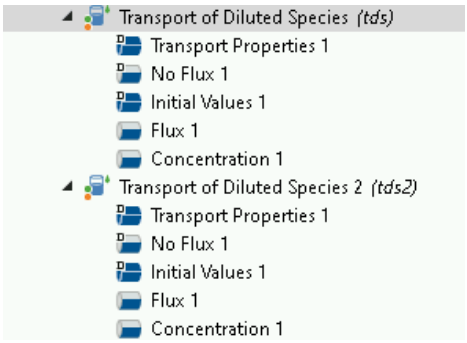

Figure 3.3: Employing transport of diluted species (*tds*) modules to represent species O (*tds*) and species R (*tds2*)

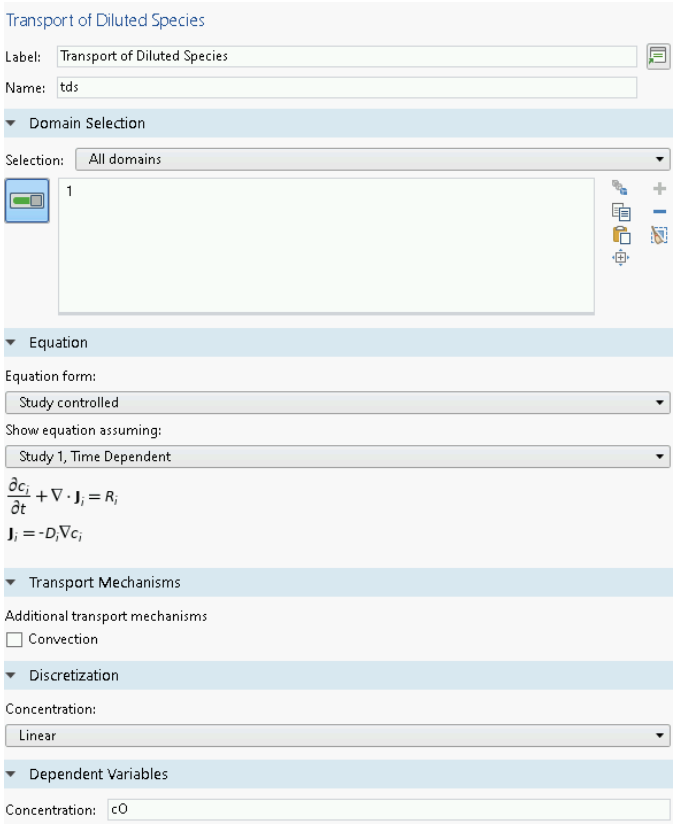

Figure 3.4: The example of selected option in the COMSOL UI.

Considering the kinetics occurring on the electrode. Based on the Nernst equation as shown in eq. (3.3), this equation expresses electrode potential, $E_{(t)}$ at any given time, t of any specified condition.

$$E_{(t)} = E_o + \frac{RT}{nF} \ln Q \tag{3.3}$$

where ln Q is the natural logarithm for the species involved in the reaction, in this case (c_O/c_R), and $(E_{(t)} - E_o)$ is the cell overpotential. Rearranging the equation, the kinetics of the reactions are written as eq. (3.4) for oxidation and eq. (3.5) for reduction. This equation is the equivalent of Butler-Volmer expression on a general one-electron reaction.

$$K_{ox} = k_{\mathrm{ox}} c_{ox} \exp\left(\frac{\alpha n F\left(E_{(t)} - E_{init}\right)}{RT}\right) \tag{3.4}$$

$$K_{red} = k_{\mathrm{red}} c_{red} \exp\left(-\frac{\beta n F\left(E_{(t)} - E_{init}\right)}{RT}\right) \tag{3.5}$$

For the transfer coefficient of O, α and transfer coefficient of R, β is also expressed as $\alpha + \beta = 1$. Considering all the equations described above, the flux on the electrode corresponding to eq (3.1) are given in eq. (3.6-3.7).

$$-J_{Ox} = (K_{ox} - K_{red}) \tag{3.6}$$

$$-J_{Red} = (K_{red} - K_{ox}) \tag{3.7}$$

The flux is an important parameter to be employed in COMSOL as it represents the dynamic of the species involved in the reaction. In Fig 3.5, it shows eq. (3.6) entered in the flux option in the COMSOL user interface (UI) with the selected faces of the active site.

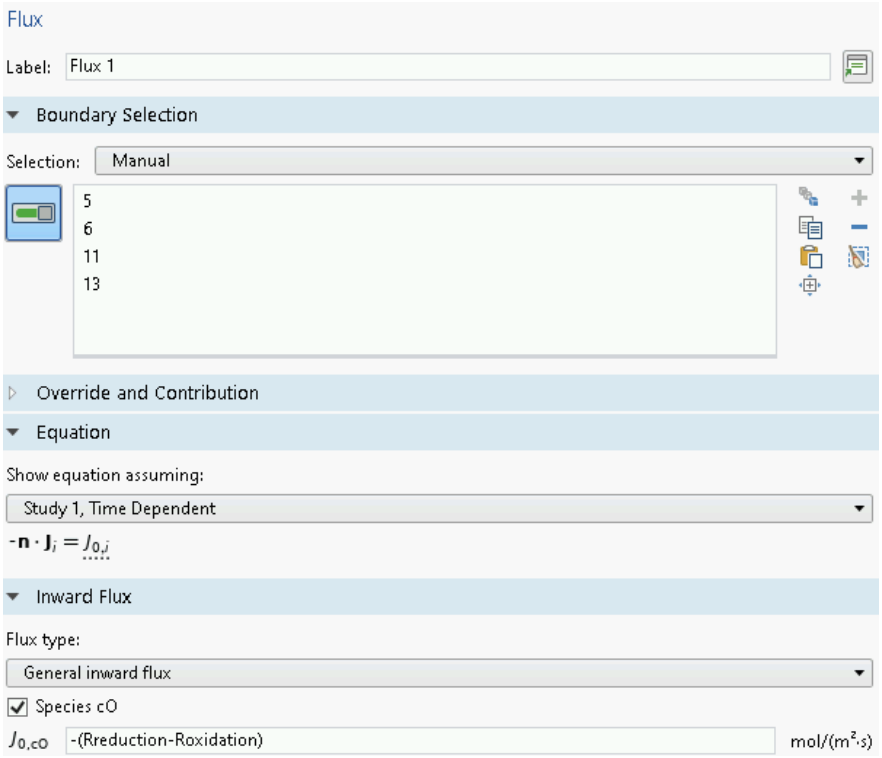

Figure 3.5: Flux window for species O in COMSOL UI.

In linear sweep voltammetry (LSV) function, a linear function describing the potential as a function of time, $E_{(t)}$, is usually used eq (3.8).

$$E_{(t)} = E_{init} - v_b t \tag{3.8}$$

where potential scan rate, v_b is the gradient of the graph in V/s. For this simulation, v_b is kept constant. Eq. (3.9) is employed for cyclic voltammetry with linear ramp overtime (Bard and Faulkner, 2004). This happens when the working potential is ramped in the opposite direction to return to the initial potential.

$$E_{(t)} = |v_b t + E_{rev} - E_{init}| + E_{rev} - E_o \tag{3.9}$$

The plotted graph from this equation (by adopting the parameters in Table 3.1) is illustrated in Fig 3.6.

Table 3.1: Parameters employed for the redox reaction in the COMSOL simulation

Name	Expression	Value	Description
Diff	1e-8[m^2/s]	1×10^{-8} m²/s	Diffusivity (D_0)
kreduction	1[m*s^ - 1]	1 m/s	Reduction kinetics (k_{red})
koxidation	kreduction	1 m/s	Oxidation kinetics (k_{ox})
beta	0.5	0.5	Transfer coefficient for R (β)
alpha	1 - beta	0.5	Transfer coefficient for O (α)
n	1	1	No of electron exchange
R	8.314[J/(mol*K)]	8.314 J/(mol·K)	Universal gas constant
T	298.15[K]	298.15 K	Temperature
E0	0[V]	0 V	standard potential (E_0)
vb	0.1[V/s]	0.1 V/s	Potential scan rate (v_b)
Einit	0.5	0.5	Initial potential (E_{init})
F	96485.3[C/mol]	96485 C/mol	Faradays constant
cOinit	1[mol/m^3]	1 mol/m³	Initial concentration for O ($c_{O,init}$)
cRinit	0[mol/m^3]	0 mol/m³	Initial concentration for R ($c_{R,init}$)
tend	20[s]	20 s	Time stop (t_{end})
tstep	0.1	0.1	Time step (t_{step})
Erev	-0.5[V]	−0.5 V	Reverse potential (E_{rev})
ipc	-0.4463*(((F^3)/(R*T))^(1/2))*(n^(3/2))*(Diff^(1/2))*cOinit*(vb^(1/2))	−8.4956	Peak current (i_{pc})
length	6*((Diff*tend)^0.5)	0.0026833 m	Minimum length (L_{min})
radius	5e-4[m]	5×10^{-4} m	Radius of electrode (r)
area	pi*(radius^2)	7.854×10^{-7} m²	Area of electrode (A)
mesh	2.68e-7[m]	2.68×10^{-7} m	Mesh size
logR	7	7	Log of relative tolerance

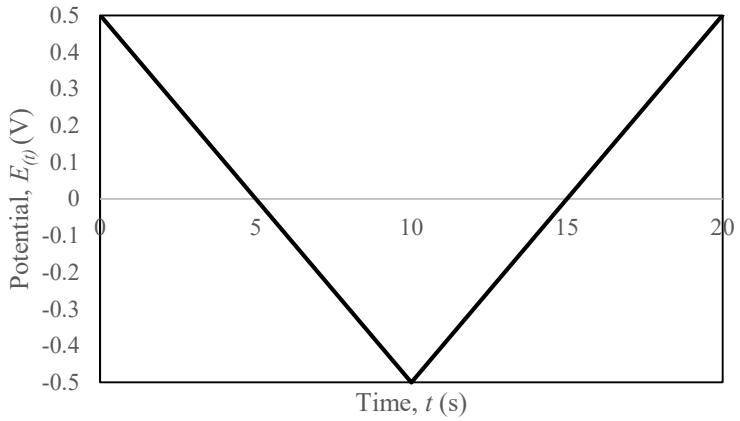

Figure 3.6: Potential, $E_{(t)}$ vs. time, t graph

Fick's first law was adopted in the system. It states that flux is proportional to the concentration gradient with the expression in eq. (3.10).

$$-J_o(x,t) = D_o\left(\frac{\partial C_o(x,t)}{\partial x}\right) \tag{3.10}$$

where $J_o\,(x,t)$ is the diffusive flux as a function of distance, x (m) and time, t (s). D_o represents the diffusion coefficient and $\frac{\partial C_o(x,t)}{\partial x}$ is the concentration gradient on the direction, x in mol/(m^{2}s). For 1D, current, $I_{(t)}$ from the simulation is represented by eq. (3.11) with the area, A, given in eq (3.12).

$$I_{(t)} = -nAF(-J_{ox}) \tag{3.11}$$

$$A = \pi r^2 \tag{3.12}$$

The direction of the diffusion is normal to the selected boundaries. For example, in a 1D model, the flux direction is on the x-axis that is normal to the active site. On the 2D asymmetrical and 3D models, the normal flux is the diffusivity flux on the z-axis. For 3D, the current, $I_{(t),}$ is obtained using eq. (3.13) as integration over the electrode area.

$$I_{(t)} = -nF\int_0^A J \tag{3.13}$$

And the current density, $i_{(t)}$ as $I_{(t)}$ per unit area as given in eq. (3.14)

$$i_{(t)} = \frac{I_{(t)}}{A} \tag{3.14}$$

Table 3.2: Variables employed in the COMSOL simulation

Name	Expression	Unit	Description
Kreduction	kreduction*exp(((-beta*n*F)/(R*T))*(Et - E0))	m/s	Eq. (3.5)
Koxidation	koxidation*exp(((alpha*n*F)/(R*T))*(Et - E0))	m/s	Eq. (3.4)
Rreduction	Kreduction*cO	mol/(m²·s)	Based on Eq. (3.1)
Roxidation	Koxidation*cR	mol/(m²·s)	
Et	abs(vb*t + Erev - Einit) + Erev	V	Eq. (3.9)
Current density	-n*F*(tds.ndflux_cO)	A/m^2	Eq. (3.14) for 1D
	-n*F*intop1(tds.ndflux_cO)/area	A/m^2	Eq. (3.14) for 2D axisymmetric
	-n*F*intop1(tds.ndflux_cO)/area	A/m^2	Eq. (3.14) for 3D

Where "intop1" represents the integration of an area, $\int -J_o$. Figure 3.7 shows the examples in integration menu for 2D axisymmetric and 3D and the selected faces (the area of the electrode or active sites).

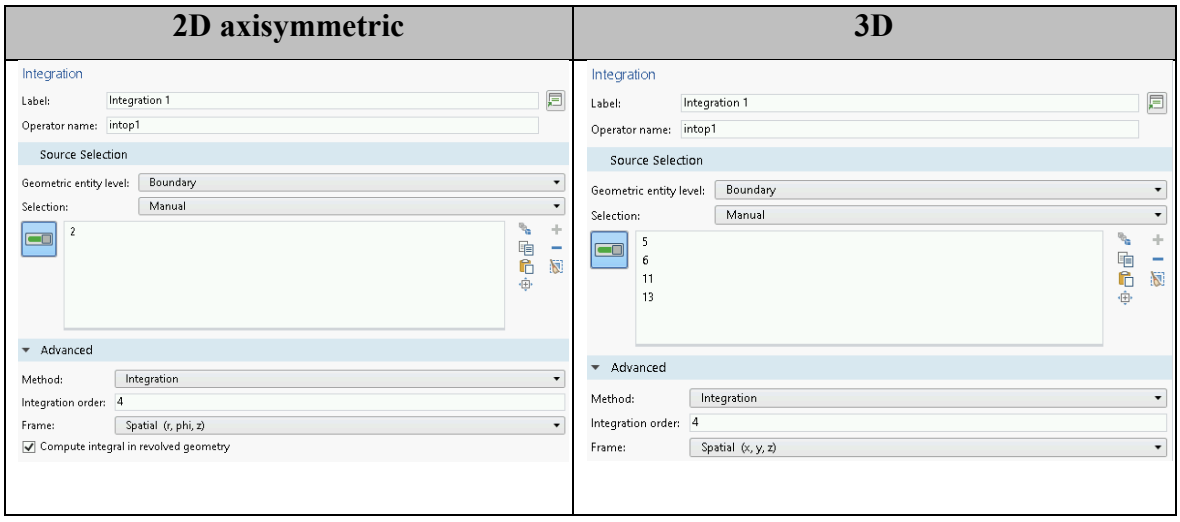

Figure 3.7: Flux window for species O in COMSOL UI.

3.1.4 Geometry and meshing

In this case study, a 1 mm in diameter disk electrode ($r = 5 \times 10^{-4}$ m) was submerged completely in an electrolyte. The complete reduction of the model from 3D to 2D axisymmetric to 1D were shown in Fig. 3.2 (a), (b) and (c) respectively.

Although there are many different options available to develop meshes, the default-free triangular for 1D and 2D axisymmetric (Fig 3.8 and 3.9) and free tetrahedral for 3D (Fig 3.10) meshing are considered reliable because of its capabilities to handle vast variations of element size that are useful in mesh refinement. These mesh types are widely utilized on various designs for quick rendering and adaptability in a specific, sharp-edged geometry (COMSOL Multiphysics® user manual 2014). It is easy to use and reliable when implemented correctly.

Meshing with strategy had proven to yield better results, as presented by Lavachi et al. (2009). The meshing parameters involved are number of elements (*noe)*, boundaries, and edges in the domain. These criteria are essential to reduce the strain on the running application while also saving a tremendous amount of time to generate results.

Figure 3.11 provides examples of the geometry and meshing windows in COMSOL UI by screen capture. The examples show the different options used in constructing the drawing for each of the given geometries.

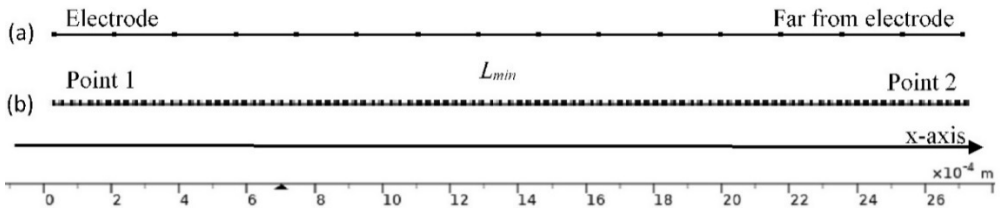

Figure 3.8: Measurement of the 1D model with predefined meshing (a) normal (b) extremely fine setting

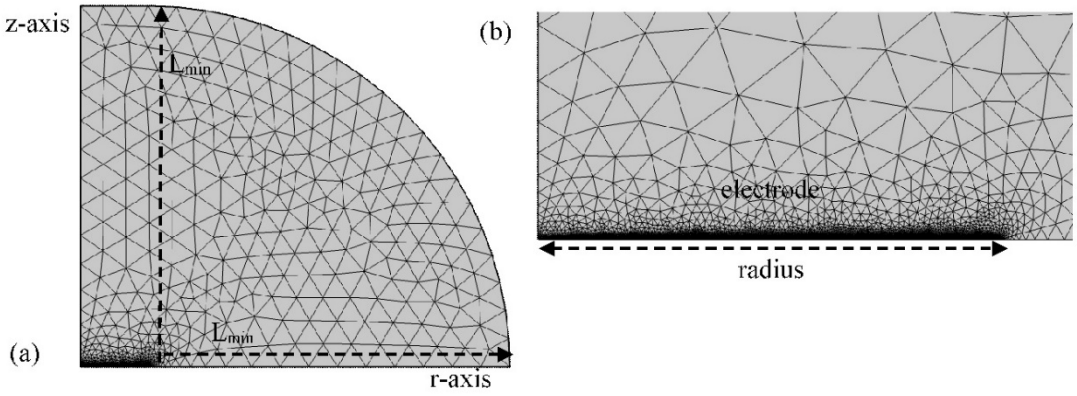

Figure 3.9: (a) Geometry and measurement of the 2D axisymmetric model (b) the measurement of the electrode

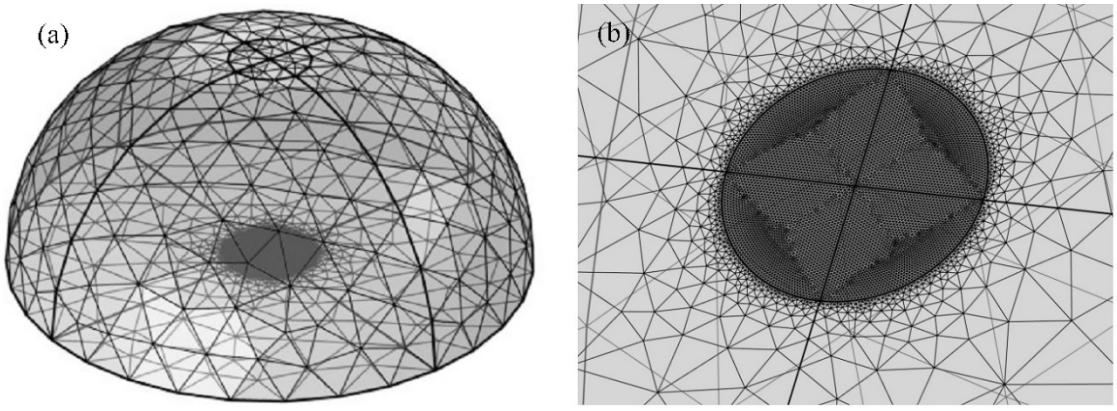

Figure 3.10: (a) Overview of the mesh on 3D simulation (b) concentrated mesh on the electrode

Hence, this study aims to evaluate meshing on different dimensions while having reliable and accurate results under minimal computation time (t_{com}). A more robust meshing on the electrode region is applied to fully cover the propagation of flux in the domain with nodes.

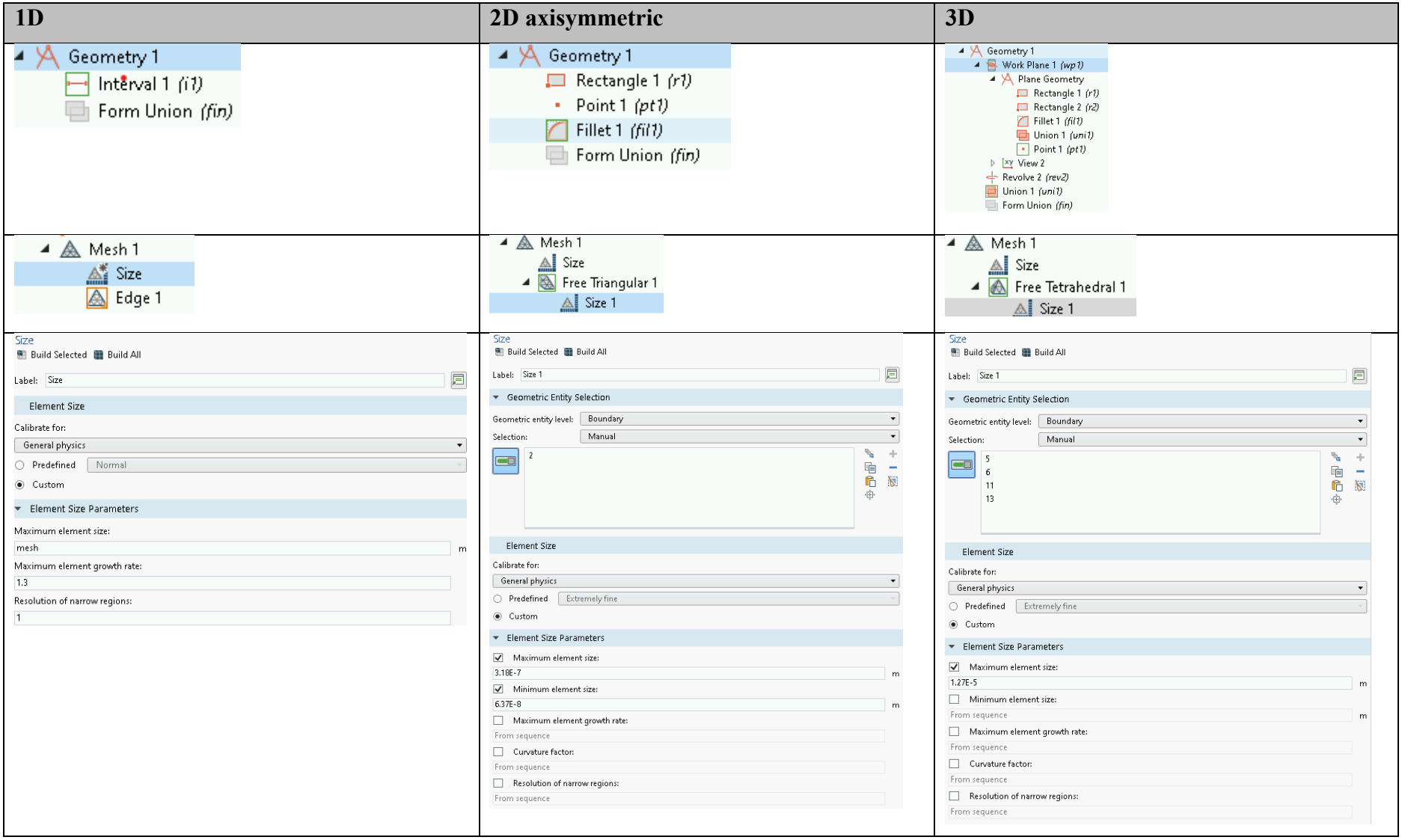

Figure 3.11: Screen capture showing the geometry and meshing windows in COMSOL UI.

3.1.5 Time dependent solver and the relative tolerance (*rtol*)

The study setting in this case study is the time-dependent solver since the overall reaction is time dependent. This takes into account the total duration of the reaction (t_{end}) and the time step (t_{step}) which is the time taken for each of the calculation in between the initial time (start time in this case t = 0 s) until tend. This is written as "range(0,tstep,tend)" in the simulation. Examples of the implementation is shown in Fig. 3.12.

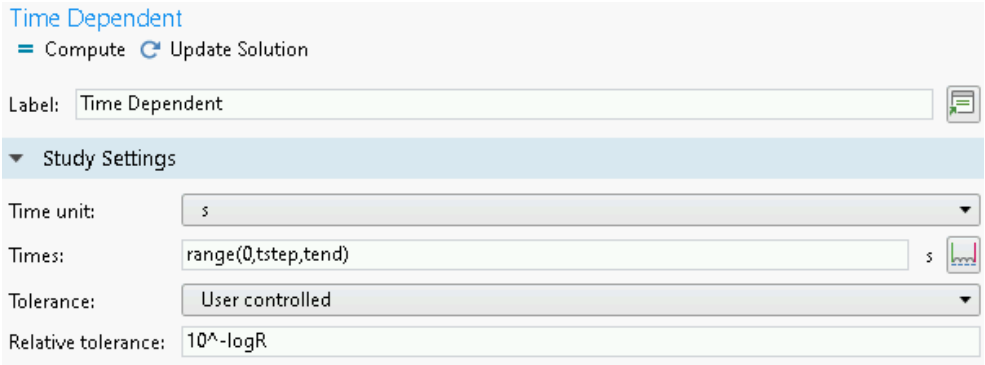

Figure 3.12: The time dependent window under the solver subset that shows the space where time.

Another important parameter that needs to be considered during simulation is the relative tolerance (*rtol*). This is described in the COMSOL Multiphysics® user manual (2014), as the maximum amount of error that a user is willing to allow in the solution. Iterative processes within the solver sequence continue to iterate on the solution attempt until the calculated relative error approximation drops below the pre-specified relative tolerance. This convergence criterion is as described in eq (3.15).

$$\left|\frac{current\ solution - previous\ solution}{current\ solution}\right| < relative\ tolerance \qquad (3.15)$$

The *rtol* values used in a simulation would usually range between $\times 10^{-3}$ and $\times 10^{-10}$ where smaller *rtol* requires longer time to complete the simulation but yields better result precision.

3.2 Design and modeling of Volmer-Heyrovsky-Tafel (VHT) mechanistic steps for hydrogen evolution reaction (HER)

In any conceptual work and computational model, the verification and validation process is vital in providing confidence in the study's results. The verification and validation techniques vary depending on the scenarios and conditions. This was presented by Robinson (2000) on verification and validation life cycle given in Figure 3.13. The diagram shows the process that was adopted in this work to develop a computational model using FEM to calculate the HER performances via the VHT mechanistic steps.

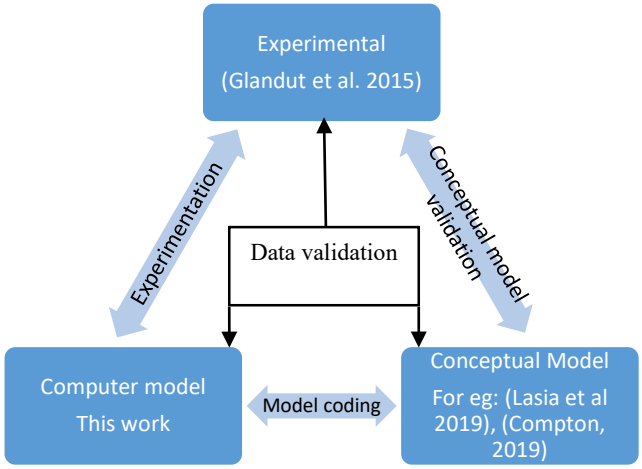

Figure 3.13: Simulation model verification and validation adopted in the modelling process (based on Robinson, 2000).

This work explores modeling hydrogen evolution reaction (HER) phenomena by defining in different dimensions (1D, 2D and 3D in this case study) using COMSOL Multiphysics. In this particular case, the model involves two types of materials and one hybrid arrangement of them;

1. Titanium carbide ($TiC_{0.8}$)
2. Tetrahedral amorphous carbon with 10% doping of platinum (ta-C)
3. Geometrically arrayed of ta-C on $TiC_{0.8}$ substrates (TiC/taC)

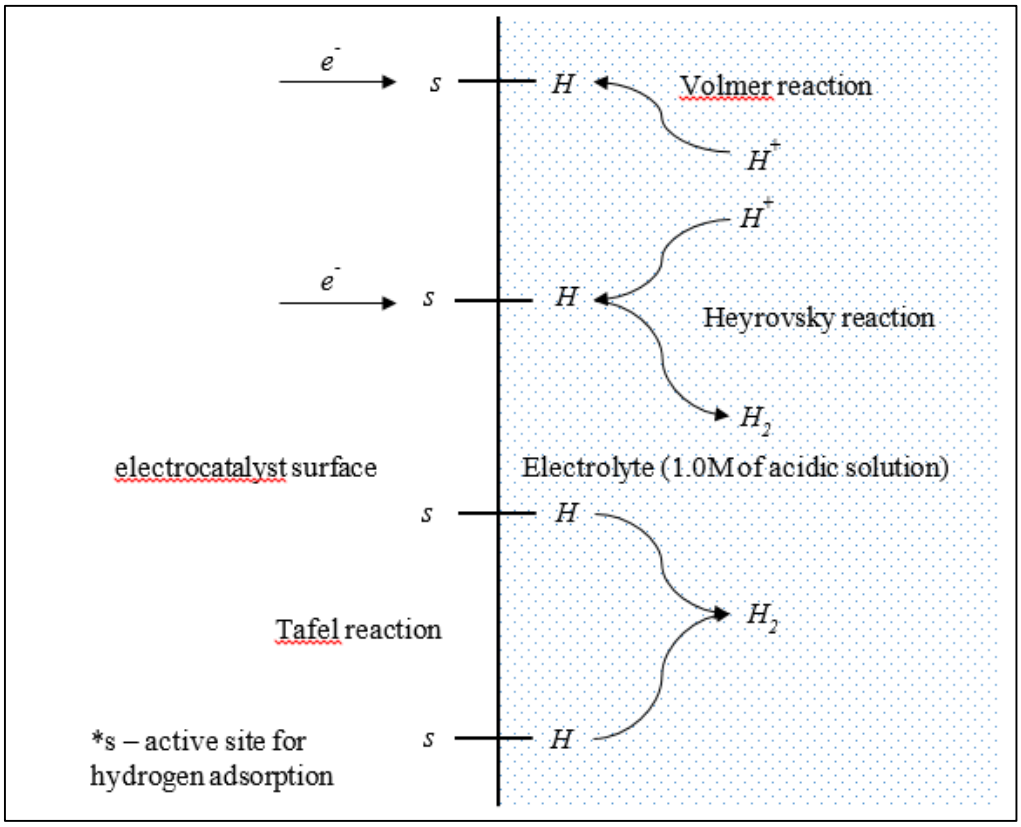

Figure 3.14: Schematic diagram of a VHT reaction on an electrocatalyst surface.

The FEM was modelled based upon the Volmer-Heyrovsky-Tafel (VHT) mechanism for HER (example of the model given in Fig. 3.14) to verify the experimental work on a solitary (1) $TiC_{0.8}$ (where 0.8 signify the carbon vacancy to promote hydrogen adsorption) and (2) ta-C electrocatalyst. Consequently, in order to check the hypothesis that the increased in performance of the (3) hybrid ta-C array on TiC substrate was due to the surface diffusion which leads to H-s (starting from here was called as surface hydride that is also known as adsorbed hydrogen on the catalyst surface) hopping from concentrated region to vacant sites.

The first part of the case study is the verification of the TiC and taC:Pt in acidic solution of 1.0M (1000 mol/m^3). The VHT mechanism is employed using the general PDE of modified mass transport equation on surface, denoted as c_{Hs}, surface concentration

(mol/m^2). Using the verified kinetics parameters from (1) and (2), the values were then adopted on (3) with the implementation of surface diffusion.

3.2.1 Model definition

Firstly, for both (1) and (2) of the 1D model was used. This is deemed sufficient to verify the kinetic parameters of the experimental results, assuming homogeneity on the materials surfaces. Figure 3.15 shows the translation of the works from 3D to 2D and 1D.

Secondly, a 2D model and a 3D model were required in order to verified the findings for (3). For the 2D model the surface diffusion was taken into account, along with the employed kinetics parameters determined from (1) and (2). While for the 3D model, and edge effect was assumed along with surface diffusion and the employed kinetic parameters determined from (1) and (2).

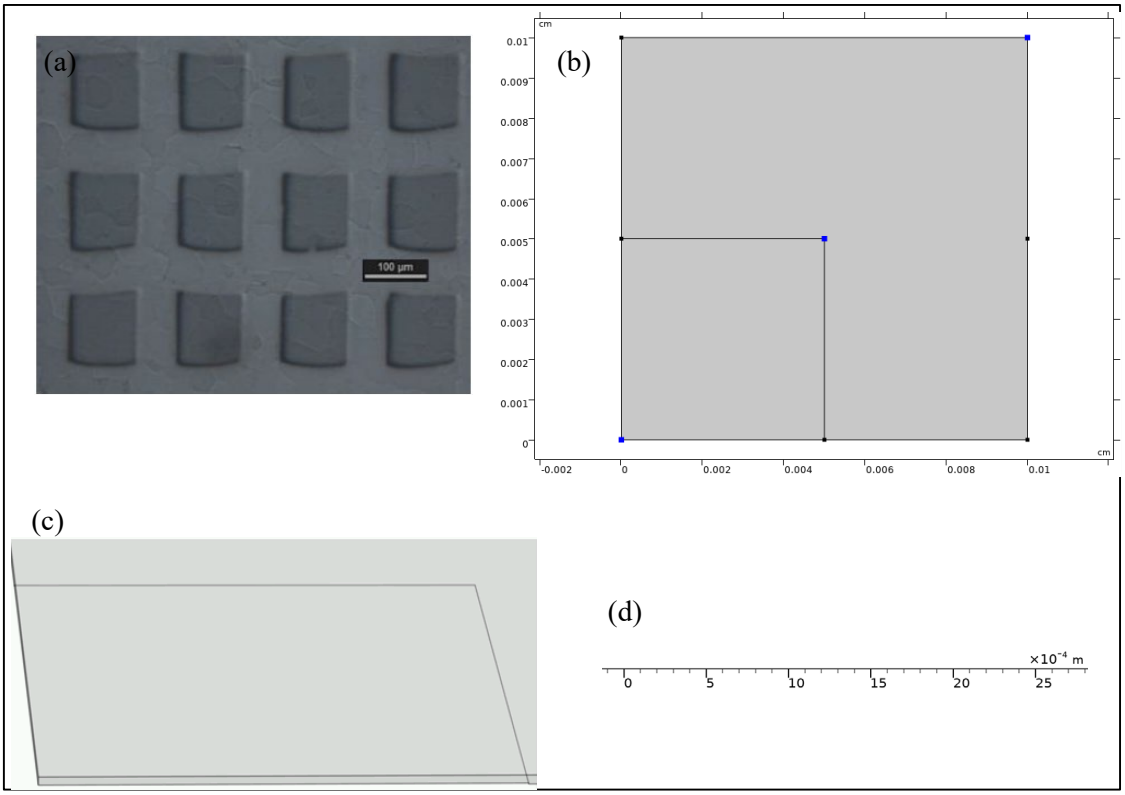

Figure 3.15: (a) Optical micrograph of the TiC/taC:Pt electrode (b) 2D model with smaller square on the bottom left hand-corner is the ta-C (c) 3D model showing the added depth on the ta-C giving the edge effect (d) 1D model.

3.2.2 Model equations

In general, the basic concept of HER is the cathodic side of the electrochemical splitting of water molecules (H_2O) to H_2 (HER) and O_2 (OER). The overall reaction is represented by eq. (3.16), a reaction occurring at the cathode.

$$2H^+ + 2e^- \rightarrow H_2 \qquad (3.16)$$

The elementary steps of HER that occur on the surface of the surface are called the VHT mechanism, where eq. 3.17, 3.18 and 3.19 represent Volmer, Heyrovsky and Tafel steps respectively. These reactions could occur simultaneously in either VH, VT or VHT paths depending on the experimental conditions.

$$H^+ + s + e^- \rightleftarrows Hs \quad (3.17)$$

$$H^+ + Hs + e^- \rightleftarrows H_2 + s \quad (3.18)$$

$$2Hs \rightleftarrows H_2 + 2s \quad (3.19)$$

where H^+ is the hydronium ion in mol/m^3, Hs is the surface hydride in mol/m^2 and s is the the vacant sites on the surface in mol/m^2.

3.2.3 Boundary conditions

Volmer and Heyrovsky are electrochemical reactions, and hence are potential dependent. The rate constants for the forward and the backward reactions are expressed in eqs. (3.20-3.23).

$$K_V = \left(k_V e^{\left(-\frac{\beta_V nF}{RT}\right)\left(E_{(t)} - E_V^o\right)}\right) \quad (3.20)$$

$$K_{-V} = \left(k_{-V} e^{\left(\frac{\alpha_V nF}{RT}\right)\left(E_{(t)} - E_V^o\right)}\right) \quad (3.21)$$

$$K_H = \left(k_H e^{\left(-\frac{\beta_H nF}{RT}\right)\left(E_{(t)} - E_H^o\right)}\right) \quad (3.22)$$

$$K_{-H} = \left(k_{-H} e^{\left(\frac{\alpha_H nF}{RT}\right)\left(E_{(t)} - E_H^o\right)}\right) \quad (3.23)$$

Where k_V and k_{-V} are standard rate constant for forward and backward Volmer step respectively. While K_V and K_{-V} are the rate constants for forward and backward Volmer step respectively. The subscript H would represent the Heyrovsky step. Since Tafel step is a chemical reaction not an electrochemical reaction, hence it is independent of the potential.

The transfer coefficients or symmetry coefficients are represented by β and α in which (α+β = 1). The subscript V and H signify the Volmer and Heyrovsky step respectively. As for the

potential parameters, $E_{(t)}$ is the electrode potential, E^0_V and E^0_H is the standard potential for Volmer and Heyrovsky respectively.

Assuming the Langmuir adsorption isotherm, the reaction rates for the corresponding eq. (3.17-3.19) are presented as eq. (3.24-3.26) respectively.

$$R_{\mathrm{V}} = (K_{\mathrm{V}} c_{\mathrm{H}^+} c_{\mathrm{s}}) - (K_{-\mathrm{V}} c_{\mathrm{Hs}}) \quad (3.24)$$

$$R_{\mathrm{H}} = (K_{\mathrm{H}} c_{\mathrm{H}^+} c_{\mathrm{Hs}}) - \left(K_{-H} c_{H_2} c_s\right) \quad (3.25)$$

$$R_T = (K_T (c_{Hs})^2) - \left(K_{-T} c_{H_2} (c_s)^2\right) \quad (3.26)$$

Several parameters were kept constant throughout the simulations with the following assumptions.

(1) 0.5M of H_2SO_4 of high acidic concentration, hence c_{H^+} = 1000 mol/m^3.

(2) The maximum surface concentration of the material, Γ_{max} = 1 x 10^{-5} mol/m^2 (eg given by Diard et al, 1997 and Bard and Faulkner, 2004).

(3) The hydrogen concentration near the electrode is 0.001M, c_{H2} = 1 mol/m^3.

Pertaining the c_{H2} an elaborate work by Kempainen et al. (2016) had presented the concentration profiles of dissolved H_2 at different current densities as shown in Figure 3.16. The works stated the change of c_{H2} with the change of current density at different distance near the electrode, but a safe assumption of c_{H2} = 1 mol/m^3 can be made to achieve current density of -10 mA/cm^2. To support the assumption made on c_{H2}, Lasia et al. (2019) had cited a work on solubility series in the year 1981 that stated c_{H2} is estimated at 0.0008M or 0.8 mol/m^3.

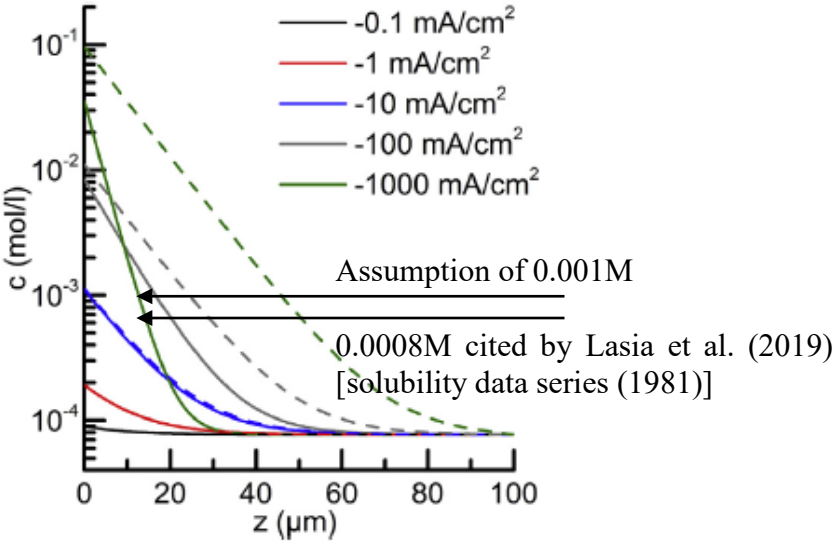

Figure 3.16: Concentration profiles of dissolved H_2 at different current densities with 100 µm diffusion layer thickness (Kempainen et al., 2016)

From the reactions and equations presented in this section, it was observed that there were three important parameters to be noted in this simulation, where;

1. c_{H+} is the concentration of hydronium ion in mol/m^3.
2. c_{Hs} is the concentration of the surface hydride in mol/m^2.
3. c_s is the concentration of the vacant sites on the surface in mol/m^2. Where it can be written as a function of c_{Hs} given the value of Γ_{max}. Therefore, $c_s = (\Gamma_{max} - c_{Hs})$.

Hence given that c_s is a function of c_{Hs}, that leaves c_{H+} and c_{Hs} to be employed in the simulation. The implementation of the parameter c_{H+} can be optional depending on the situation. To emulate the experiment, a high acidic concentration of 1.0M was used and under this condition c_{H+} can be assumed constant.

If c_{H+} is not a constant, then the transport of dilute species module (tds) can be used. Examples can be seen in chapter 3 as this is a similar approach to the ones that has been

described in 3.3. But for this study, the tds option can be applied only on 1D and 3D model where the available domain can be attributed to the acidic medium or electrolyte.

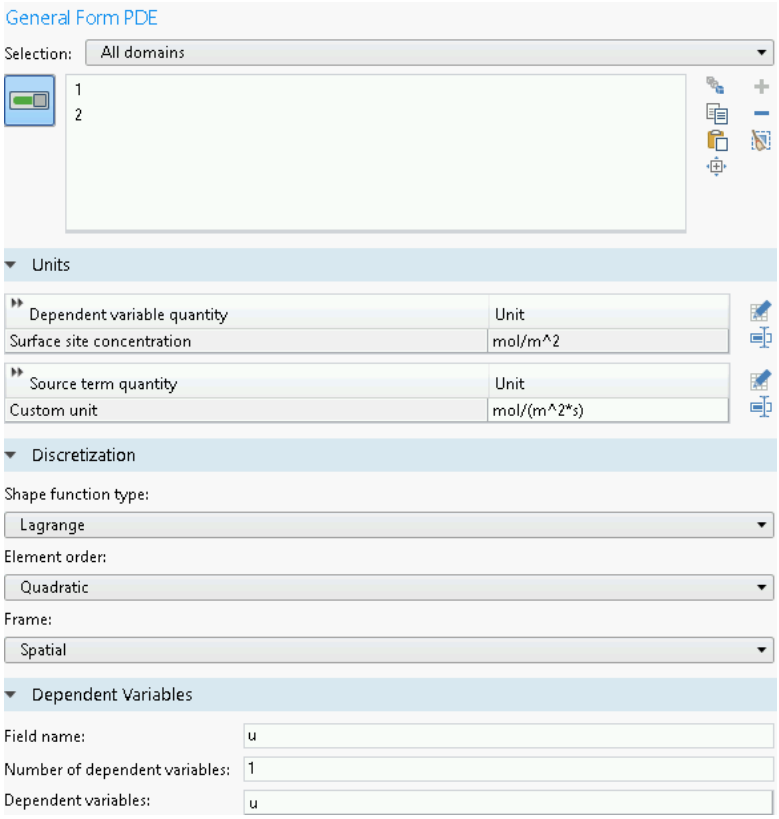

Figure 3.17: The general form PDE window showing the input parameters and selected discretization.

For c_{Hs}, a general form PDE (Fig 3.17 shows the screen capture of the application window) was used. For example, in 1D only one domain is available for selection. For 2D, the geometry of TiC/taC:Pt was designed based on the fabricated electrode from the experiment. Hence, there are two domains available for selection, one of TiC and one of taC. Based on the 2D model, the 3D model includes the height dimension of taC (later to support the assumption of edge effect see Chapter 6.3) was added. Previously in 2D the thickness of taC was assumed negligible. Examples of the applications are given in Figure 3.18 where the subsets represent the created domains that were available for selection.

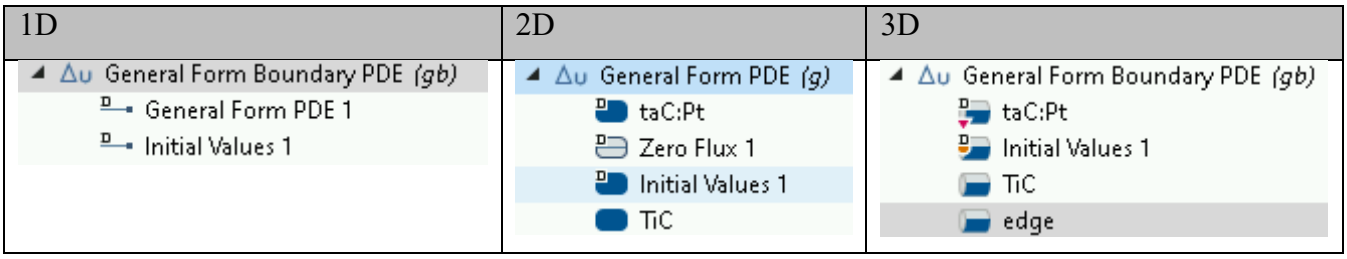

Figure 3.18: The general form PDE window showing the input parameters and selected discretization.

The general PDE equation was employed in COMSOL to facilitate the Fick's 2nd law of diffusion. The general form PDE is written in the form of eq (3.27).

$$e_a \frac{\partial^2 u}{\partial t^2} + d_a \frac{\partial u}{\partial t} + \nabla \cdot \Gamma = f \tag{3.27}$$

Where e_a and d_a are the mass coefficients, Γ is the flux vector and f is the source term. Given that u in this case is c_{Hs} in mol/m^2, the Fick's 2nd law of diffusion is written in eq. 3.28. The mass coefficient, $e_a = 0$ as no second order derivation of time is required. While $d_a = 1$ to facilitate the first order derivation of c_{Hs}. In steady state condition, the Fick's 2nd law of diffusion (1st term) and the total rate reaction (the 2nd term) is equal to zero.

$$\frac{\partial c_{Hs}}{\partial t} + (\nabla c_{Hs})_T = R_v - R_H - 2R_T = 0 \tag{3.28}$$

Where in the 1st term, $\frac{\partial c_{Hs}}{\partial t}$ is the change of Hs concentration overtime in mol/m^2·s and the diffusion term $(\nabla c_{Hs})_T$ is the tangential gradient that consists of the tangential derivatives for each of the spatial directions on the selected boundaries (COMSOL, 2019). The flux vector is written in eq. (3.29) consists of tangent variables specified by the x, y and z-axis depending on the dimensions. D_o is the diffusion coefficients constant of the materials.

$$\nabla \cdot \Gamma = (\nabla c_{Hs})_T = D_o \left[\frac{\partial c_{Hs(tx)}}{\partial x}, \frac{\partial c_{Hs(ty)}}{\partial y}, \frac{\partial c_{Hs(tz)}}{\partial z}\right] \tag{3.29}$$

The 2nd term which is the source term, f is represented by the total rate of VHT steps in mol/m^2·s written based on the reactions in (3.17-3.19). The examples of the employed equations are provided by the screen capture for a 3D model simulation in Fig. 3.19.

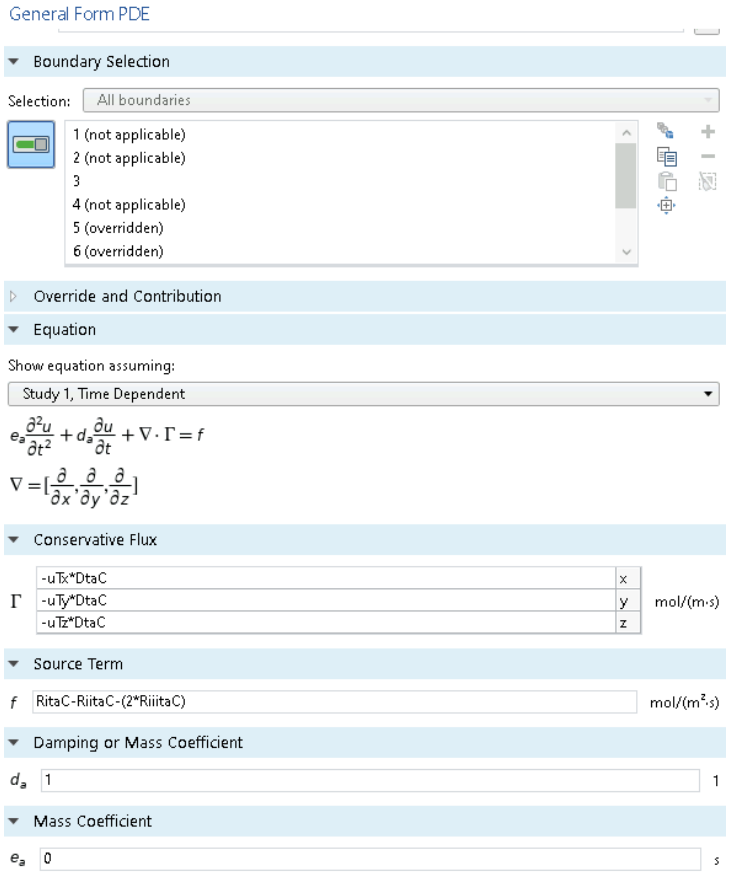

Figure 3.19: Screen capture showing the parameters and the equations employed for taC surface in 3D model.

For the time dependent properties, a similar approach to the example given in Chapter 3 on redox reaction was used. The potential of the system as a function of time, $E_{(t)}$, is written as eq. (3.30);

$$E_{(t)} = |v_b t + E_{rev} - E_{init}| + E_{rev} - E^o \qquad (3.30)$$

By setting the scan rate, v_b at a low value of 1×10^{-6} V/s a slow reaction time like steady state situation was simulated. This was translated into the software transient program of time step,

t_{step} and end time, t_{end}. The equations used for the mentioned parameters are given in eq. (3.31-3.32).

$$t_{end} = \frac{(E_{init} - E_{rev})}{v_b} \times 2 \quad (3.31)$$

$$t_{step} = \frac{t_{end}}{no.\ of\ calculation} \quad (3.32)$$

The standard potential, E^0 is specific to the types electrodes and the mechanistic steps. For example $(E^0_V)_{TiC}$ indicates the standard potential of Volmer step for TiC electrode (shown in Table 3.3). This simulation is modelled to emulate the experimentation of HER where it is known that the cathodic formation of hydrogen occurs at 0 V (examples given by Zubair et al., 2021). Lasia (2019) stated that it is much simpler to refer working potentials to the HER equilibrium that is 0 V. Hence, the E^0 for both TiC and taC electrode under V and H mechanistic steps are assumed as 0 V.

The number of calculations set at 1000 was deemed sufficient in getting reliable results. E_{init} and E_{rev} were varied throughout the simulation depending on the respond of the current output. But in general, E_{init} and E_{rev} was set at +0.2 V and -0.5 V, respectively. Hence, using v_b at 1×10^{-6} V/s will give t_{end} and t_{step} of 1.4×10^{7} s and 1.4×10^{4} s, respectively. For HER simulation, the simulation time could be further reduced by negating the (×2) in eq (3.31). This is because when modelled correctly (for example sufficiently low v_b, and *rtol* values used) simulations would exhibit similar plots of the current, moving from positive potentials to negative potentials, and negative potentials to positive potentials. The multiplication by two is to facilitate the full cycle from E_{init} to E_{rev} and back to E_{init}. Hence, by negating the multiplication by two, the model only simulating the potential E_{init} to E_{rev}.

Based on the work such as (Glandut et al., 2006a and Glandut et al., 2006b) the equation for current density for single electrode system is written in eq. (3.33). The currents are due to

the electrons transfer during the Volmer and Heyrovsky steps occurring on the surface of the electrode. By integrating the Volmer and Heyrovsky rate reactions on the electrode surface and the multiplication with Faraday's constant and number of electron moving the current equation is written as eq. (3.34). Similar formulizations can also been found in Compton and Banks (2018).

$$i = \frac{I_\sigma}{A_\sigma} = (-nF(R_V + R_H)_\sigma) \tag{3.33}$$

$$I_\sigma = -nF \int_0^{\sigma_D} \int (R_V + R_H)_\sigma \, d\sigma \tag{3.34}$$

A more complex approach is needed for the case of 2D and 3D model on the TiC/taC system. Referring to Fig. 3.15(a), there is a noticeable segregation of TiC part and taC:Pt part on the TiC/taC electrode surface. The kinetic parameters of the TiC part and the taC:Pt part was assumed similar to the one of solitary TiC and solitary taC:Pt that should already be determined on a 1D model. This assumption was based on Yang et al. (2020) stating substrate interactions have no effect on the intrinsic HER activity. This statement supports our assumption that taC:Pt properties on TiC substrate remains unchanged. Therefore, supported by this argument, the total current, I_{Tot} should follow eq. (3.35).

$$I_{Tot} = I_{TiC} + I_{taC} \tag{3.35}$$

Dividing the current over the effective surface area, A_{Tot} would then give the current density, i as shown in the eq. (3.36). Consequently, the Tafel plot can be obtained by plotting eq. (3.37) against the potential, $E_{(t)}$.

$$i_{Tot} = \frac{I_{Tot}}{A_{Tot}} \tag{3.36}$$

$$\log_{10}(i_{Tot}) = \log_{10} \frac{(I_{TiC} + I_{taC})}{A_{Tot}} \tag{3.37}$$

Additionally, the analytical equation provided in eq. (3.38) can be used to verify the Tafel plot for an irreversible VH mechanism (Bard and Faulkner, 2004).

$$J = 2F\Gamma_{max}c_{H^+}\frac{(K_V K_H)}{K_V + K_H} \tag{3.38}$$

All of the essential parameters and equations in this simulation are summarized on Table 3.3 (for parameters) and Table 3.4 (for variables).

Table 3.3: Parameters employed for VHT mechanistic steps in the COMSOL simulation

Name	Expression	Value	Description
n	1	1	No of electron
R	8.314[J/(mol*K)]	8.314 J/(mol·K)	Universal gas constant
T	298.15[K]	298.15 K	Temperature
F	96485.3[C/mol]	96485 C/mol	Faradays constant
H2	1[mol/m^3]	1 mol/m³	Hydrogen concentration (c_{H2})
vb	1e-8[V/s]	1×10^{-8} V/s	Potential scan rate (v_b)
Einit	0.5	0.5	Initial potential (E_{init})
cstar	1000[mol/m^3]	1000 mol/m³	Initial concentration for H^+ (c_{H+})
Gmax	1e-5[mol/m^2]	1×10^{-5} mol/m²	Maximum concentration of Hs (Γ_{max})
tend	2e8	2×10^{8}	Time stop (t_{end})
tstep	2e5	2×10^{5}	Time step (t_{step})
Erev	-0.5[V]	−0.5 V	Reverse potential (E_{rev})
side	100e-6[m]	1×10^{-4} m	Width of the electrocatalyst (w)
length	100e-6[m]	1×10^{-4} m	Length of the electrocatalyst (l)
areaTot	length^2	1×10^{-8} m²	Total surface area of the electrocatalyst (A_{Tot})
Parameters for taC:Pt			
kitaC	2.8e-6[s^(-1)/(mol/m^3)]	2.8×10^{-6} m³/(s·mol)	Volmer forward standard rate constant for taC $(k_v)_{taC}$
kiitaC	4.8e-8[s^(-1)/(mol/m^3)]	4.8×10^{-8} m³/(s·mol)	Heyrovsky forward standard rate constant for taC $(k_h)_{taC}$
kmitaC	2.8e-2[s^ - 1]	0.028 1/s	Volmer backward standard rate constant for taC $(k_{-v})_{taC}$
kmiitaC	4.8e-6[m^3/mol*s^ - 1]	4.8×10^{-6} m³/(s·mol)	Heyrovsky backward standard rate constant for taC $(k_{-h})_{taC}$

Name	Expression	Value	Description
kiiitaC	0[(m^2)/(mol*s)]	0 $m^2/(s \cdot mol)$	Tafel forward standard rate constant for taC $(K_t)_{taC}$
kmiiitaC	0[(m^5)/((mol^2)*s)]	0 $m^5/(s \cdot mol^2)$	Tafel backward standard rate constant for taC $(K_{-t})_{taC}$
bitaC	0.25	0.25	Volmer transfer coefficient for taC $(\beta_v)_{taC}$
alitaC	1 - bitaC	0.75	Volmer transfer coefficient for taC $(\alpha_v)_{taC}$
biitaC	0.82	0.82	Heyrovsky transfer coefficient for taC $(\beta_h)_{taC}$
aliitaC	1 - biitaC	0.18	Heyrovsky transfer coefficient for taC $(\alpha_h)_{taC}$
E0itaC	0[V]	0 V	Volmer standard potential for taC $(E_{0v})_{taC}$
E0iitaC	0[V]	0 V	Heyrovsky standard potential for taC $(E_{0h})_{taC}$
DtaC	1e-6[m^2/s]	1.0×10^{-6} m^2/s	Surface diffusion constant for taC
areataC	lengthtaC^2	2.5×10^{-9} m^2	Surface area of taC (A_{taC})
lengthtaC	50e-6[m]	5.0×10^{-6} m	Length of taC (l_{taC})
Parameters for TiC			
kiTiC	1.1e-6[s^(-1)/(mol/m^3)]	1.1×10^{-8} $m^3/(s \cdot mol)$	Volmer forward standard rate constant for TiC $(k_v)_{TiC}$
kiiTiC	1.09e-5[s^(-1)/(mol/m^3)]	1.09×10^{-5} $m^3/(s \cdot mol)$	Heyrovsky forward standard rate constant for TiC $(k_h)_{TiC}$
kmiTiC	1.1e-2[s^ - 1]	0.011 1/s	Volmer backward standard rate constant for TiC $(k_{-v})_{TiC}$
kmiiTiC	1.1e-3[m^3/mol*s^ - 1]	0.0011 $m^3/(s \cdot mol)$	Heyrovsky backward standard rate constant for TiC $(k_{-h})_{TiC}$
kiiiTiC	1e3[(m^2)/(mol*s)]	1000 $m^2/(s \cdot mol)$	Tafel forward standard rate constant for TiC $(k_t)_{TiC}$
kmiiiTiC	6e2[(m^5)/((mol^2)*s)]	600 $m^5/(s \cdot mol^2)$	Tafel backward standard rate constant for TiC $(k_{-t})_{TiC}$
biTiC	0.77	0.77	Volmer transfer coefficient for TiC $(\beta_v)_{TiC}$
aliTiC	1 - biTiC	0.23	Volmer transfer coefficient for TiC $(\alpha_v)_{TiC}$
biiTiC	0.25	0.25	Heyrovsky transfer coefficient for TiC $(\beta_h)_{TiC}$
aliiTiC	1 - biiTiC	0.75	Heyrovsky transfer coefficient for TiC $(\alpha_h)_{TiC}$
E0iTiC	0[V]	0 V	Volmer standard potential for TiC $(E_{0v})_{TiC}$

Name	Expression	Value	Description
E0iiTiC	0[V]	0 V	Heyrovsky standard potential for TiC $(E_{0h})_{TiC}$
DTiC	1e-6[m^2/s]	1×10^{-6} m²/s	Surface diffusion constant for TiC
areaTiC	areaTot - areataC	7.5×10^{-9} m²	Surface area of TiC (A_{TiC})

Table 3.4: Variables employed for VHT mechanistic steps in the COMSOL simulation

Name	Expression	Unit	Description
KitaC	kitaC*exp(((-bitaC*n*F)/(R*T))*(Et - E0itaC))	m³/(s·mol)	Eq. (3.20) for taC
KiitaC	kiitaC*exp(((-biitaC*n*F)/(R*T))*(Et - E0iitaC))	m³/(s·mol)	Eq. (3.21) for taC
KmitaC	kmitaC*exp((((1 - bitaC)*n*F)/(R*T))*(Et - E0itaC))	1/s	Eq. (3.22) for taC
KmiitaC	kmiitaC*exp((((1-biitaC)*n*F)/(R*T))*(Et - E0iitaC))	m³/(s·mol)	Eq. (3.23) for taC
RitaC	KitaC*cstar*(GmaxtaC - u) - (KmitaC*u)	mol/(m²·s)	Eq. (3.24) for taC
RiitaC	KiitaC*cstar*u - (KmiitaC*H2*(Gmax - u))	mol/(m²·s)	Eq. (3.25) for taC
RiiitaC	kiiitaC*(u^2) - kmiiiTiC*H2*(Gmax - u)^2	mol/(m²·s)	Eq. (3.26) for taC
CurrenttaC	-F*intop1(RitaC + RiitaC)	A	Eq. (3.34) for taC
KiTiC	kiTiC*exp(((-biTiC*n*F)/(R*T))*(Et - E0iTiC))	m³/(s·mol)	Eq. (3.20) for TiC
KiiTiC	kiiTiC*exp(((-biiTiC*n*F)/(R*T))*(Et - E0iiTiC))	m³/(s·mol)	Eq. (3.21) for TiC
KmiTiC	kmiTiC*exp((((1-biTiC)*n*F)/(R*T))*(Et - E0iTiC))	1/s	Eq. (3.22) for TiC
KmiiTiC	kmiiTiC*exp((((1-biiTiC)*n*F)/(R*T))*(Et-E0iiTiC))	m³/(s·mol)	Eq. (3.23) for TiC
RiTiC	KiTiC*cstar*(GmaxTiC - u) - (KmiTiC*u)	mol/(m²·s)	Eq. (3.25) for TiC
RiiTiC	KiiTiC*cstar*u - (KmiiTiC*H2*(Gmax - u))	mol/(m²·s)	Eq. (3.26) for TiC
RiiiTiC	kiiiTiC*(u^2) - kmiiiTiC*H2*(Gmax - u)^2	mol/(m²·s)	Eq. (3.27) for TiC
CurrentTiC	-F*intop2(RiTiC + RiiTiC)	A	Eq. (3.34) for TiC
TotalCurrent	CurrenttaC + CurrentTiC	A	Eq. (3.35)
Current density	(CurrenttaC + CurrentTiC)/areaTot	A/m²	Eq. (3.36)
Et	abs(vb*t + Erev - Einit) + Erev	V	Eq. (3.30)
JtaC	-2*F*Gmax*cstar*((KitaC*KiitaC)/(KitaC + KiitaC))	A/m²	Eq. (3.38) for taC
JTiC	-2*F*Gmax*cstar*((KiTiC*KiiTiC)/(KiTiC + KiiTiC))	A/m²	Eq. (3.38) for TiC

3.2.4 Geometry and meshing

The 1D model for case studies (1) and (2) were very straightforward considering the homogenous surface. The model was setup to be robust with the inclusion of electrolyte (acid concentration) manipulation for further parametric study. The length of the domain follows the L_{min} described in section 3.3.1 for the condition of far from the electrode.

For 2D and 3D models, the geometry follows the fabricated electrode as shown in Fig. 3.15 (a). The smaller square with dimension of 2.5×10^{-6} m $\times$ 2.5×10^{-6} m (on the bottom left corner in Fig 3.15 (b) is taC that was deposited on TiC as substrate (the exposed ¾ part of the total square). In 3D model, a thickness of 100 nm was considered for taC:Pt on the TiC substrate. This area was dub as the edge effect (see assumption later in section Chapter 6.3). Fig. 3.20 shows the illustration of the domain for the 3D model. To emulate the experiment of using high acid concentration, the acid concentration can be assumed as a constant. This assumption has rendered the height of the domain moot. Hence the height of the domain can be set as any value larger than the thickness. To shorten the simulation time, smaller dimensions are suggested. In this simulation, the height of the domain was set as 50 μm.

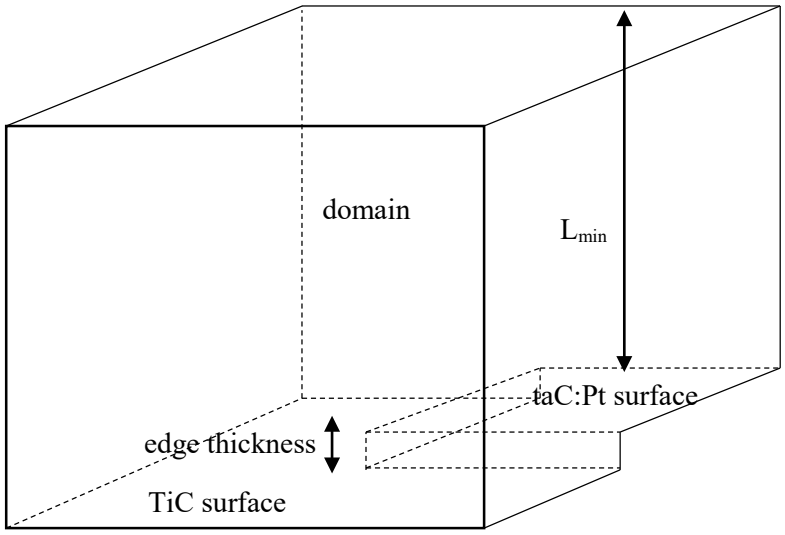

Figure 3.20: Sketching of the 3D TiC/taC domain.

Results accuracy and precision was assured by strategic meshing of all the models by following the guidelines provided from chapter 3 and 4. Figure 3.21 shows the model with meshing for 2D and 3D model. Further information on the geometry and meshing are provided in Table 3.5 with all the provided numbers are dimensionless values. Based on the study in chapter 3 and 4, *rtol* adopted in this study is 1×10^{-6}.

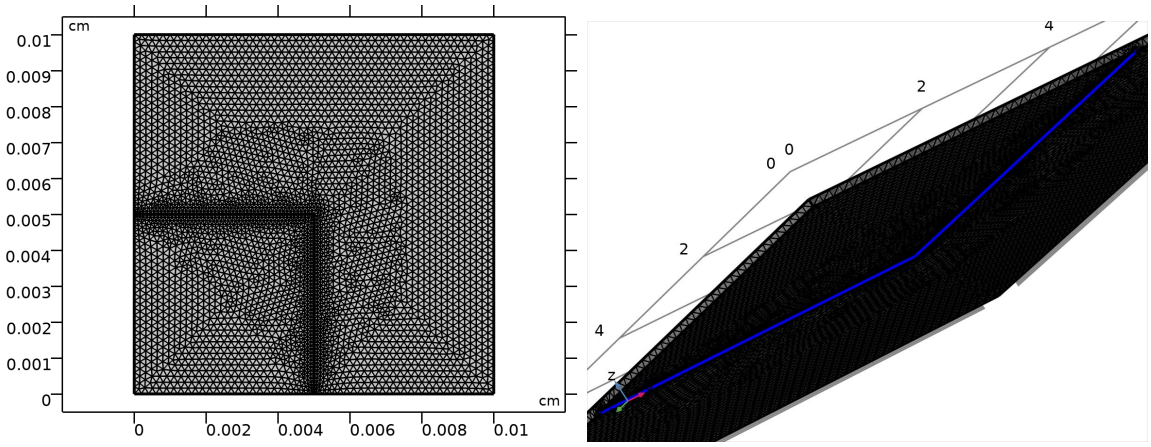

Figure 3.21: Geometry and meshing of 2D and 3D models.

Table 3.5: Geometry and information of the 1D, 2D and 3D model.

Description	**1D**	**2D**	**3D**
Geometry			
Number of domains	1	2	1
Number of boundaries	2	9	9
Number of edges			21
Number of vertices		8	14
Mesh statistic			
Minimum element quality	1.0	0.7634	0.187
Average element quality	1.0	0.9807	0.6472
Tetrahedron			36779
Triangle		8056	22826

Description	1D	2D	3D
Geometry			
Edge element	50	308	1038
Vertex element	2	8	14

3.3 Chapter Summary

This first part of this chapter in chapter (3.1) introduces the condition of the simulated redox reaction. The model purpose is to compare the reliability of COMSOL to provide accurate data across different geometries (1D, 2D axisymmetric and 3D). The employed equations were described in subchapter (3.1.1-3.1.3) which includes the assumptions and values of the parameters used in the simulation. Examples of the adopted models and user interfaces were provided in abundance to guide the reader throughout the simulation process. In subchapter 3.1.4, the meshing techniques and processes were described in details by providing the illustration of the meshed models. Finally, a brief explanation on *rtol* setup was given in subchapter 3.1.5. The implementation of time dependent solver and the adopted *rtol* value were controlled by user to ensure a reliable result can be obtained in appropriate amount of time.

This second part of this chapter in sub-chapter (3.2) introduces the condition of the VHT mechanistic steps in HER. The model purpose is to verify the experimental work on a solitary (1) $TiC_{0.8}$ and (2) ta-C electrocatalyst. Consequently, in order to check the hypothesis that the increased in performance of the (3) hybrid ta-C array on TiC substrate was due to the surface diffusion which leads to H-s hopping from concentrated region to vacant sites.

The employed equations were described in sub-chapter (3.2.1-3.2.3) which includes the assumptions and values of the parameters used in the simulation. Examples of the adopted

models and user interfaces were provided in abundance to guide the reader throughout the simulation process. In sub-chapter 3.2.4, the meshing techniques and processes were described in details by providing the illustration of the meshed models.

CHAPTER 4

DATA ACCURACY AND PRECISION OF COMSOL MULTIPHYSICS SIMULATIONS FOR THE REDOX REACTION

4.1 Introduction

This study thoroughly focuses on the COMSOL ability to produce reliable results on different dimensions by manipulating the meshing and the relative tolerance. Consequently, this study also explores the best way to obtain reliable results in a short amount of time. Reliability in this context is the ability to produce accurate and precise results. Where accuracy by definition is the measure of closeness to true value while precise is a measure of reproducibility (Stallings and Wilmore, 1971).

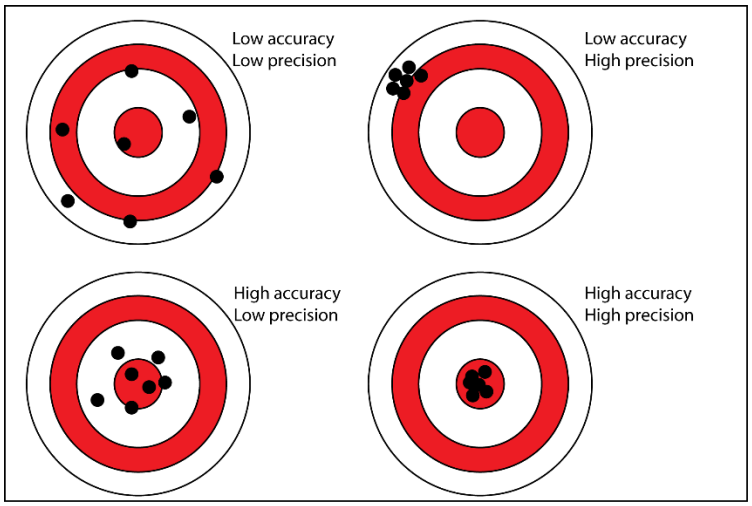

Figure 4.1: Schematic diagram differentiating accuracy and precision (Stallings and Wilmore, 1971)

The parameters that are involved in the meshing are the maximum element size and the consequent number of element, *noe*. These parameters come as both predefined or customizable values. The resulting peak current, I_p (mA), and the time taken for the

simulation to complete, t_{com} (s) are recorded for all the different meshing applications. A summary of the overall result from the simulation is shown in Table 4.1. The numerical relative tolerance value used in this study was kept at 1×10^{-8} (except in the sub chapter 4.5 on relative tolerance, *rtol*) to ensure high precision of results obtained.

Table 4.1: Summary of meshes on I_p and t_{com} for 1D, 2D axisymmetric, and 3D simulation.

Mesh		**Max element size (m)**	***noe***	**I_p (µA)**	**Percentage error, %**	**t_{com} (s)**
1-dimension						
Predefined	Normal (Fig 3.8a)	1.80×10^{-4}	15	-7.041	5.508	120
	Fine	1.42×10^{-4}	19	-6.837	2.465	123
	Finer	9.93×10^{-5}	27	-6.692	0.292	145
	Extra Fine	5.37×10^{-5}	50	-6.668	-0.073	167
	Extremely Fine (Fig 3.8b)	2.68×10^{-5}	100	-6.669	-0.060	173
User defined	Custom 1	2.68×10^{-6}	1002	-6.673	-0.037	338
	Custom 2	2.68×10^{-7}	10013	-6.673	-0.037	1050
Initial mesh	Normal (Fig 4.8)	1.80×10^{-4}	adaptive	-6.667	-0.082	301
2-dimension asymmetric						
Predefined	Normal	2.13×10^{-4}	466	-10.817	37.272	141
	Fine	1.69×10^{-4}	460	-9.909	25.749	139
	Finer	1.18×10^{-4}	494	-9.208	16.853	177
	Extra fine	6.37×10^{-5}	544	-8.576	8.832	207
	Extremely fine	3.18×10^{-5}	785	-8.173	3.718	267
User-defined	Custom 1 (Fig 3.9)	3.18×10^{-6}	2635	-7.924	0.558	633
	Custom 2	3.18×10^{-7}	23638	-7.895	0.190	2248
Initial mesh	Normal (Fig 4.9a,b)	2.13×10^{-4}	adaptive	-8.311	5.470	1155
	Custom 2 (Fig 4.9c,d)	3.18×10^{-4}	adaptive	-7.871	-0.114	6563
3-dimension						
Predefined	Normal	6.37×10^{-4}	4488	-12.78	62.195	3952
	Finer	3.50×10^{-4}	4737	-11.03	40.038	4135
	Extremely Fine	1.27×10^{-4}	5736	-9.641	21.129	5454
User defined	Custom (Fig 3.10)	1.27×10^{-5}	97474	-8.081	2.538	225906
Initial mesh	Normal	6.37×10^{-4}	adaptive	-8.742	10.914	15390
	Extremely Fine (Fig 4.10)	1.27×10^{-4}	adaptive	-8.532	8.249	20156

4.2 Effect of meshing on the 1D simulation

Fig 4.2 is plotted to visualize the effect of mesh density on the current vs. potential graph during redox reaction. Slight changes are observed on the chart throughout the different meshing used. Decreasing the element size consequently gives finer mesh as the *noe* in the domain is increased. The analytical expression and the percentage error expression are

shown in eq. (4.1-4.2) (Bard and Faulkner 2001). The percentage error was calculated by comparing the simulated I_p with the theoretical $I_{p,linear}$ value.

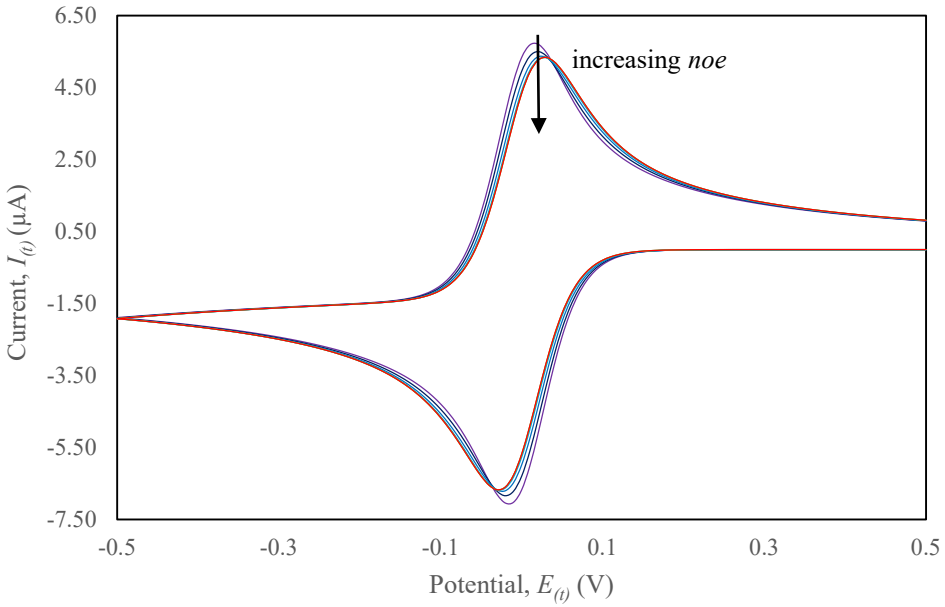

Figure 4.2: Current, $I_{(t)}$ (A) vs. Potential, $E_{(t)}$ (V) of different meshing on 1D

$$I_{p,linear} = -0.4463\left(\frac{F^3}{RT}\right)^{\frac{1}{2}} n^{\frac{3}{2}} D_o{}^{\frac{1}{2}} c_{init} v_b{}^{\frac{1}{2}} A = -8.4956\ \mu A \quad (4.1)$$

$$\%_{er} = \frac{I_p - I_{p,linear}}{I_{p,linear}} \times 100\% \quad (4.2)$$

The default “normal” predefined meshing has an acceptable 5.5% error. While the predefined “extremely fine” mesh has a -0.60% error, the negative value shows smaller I_p values than the theoretical one. Refining the meshes further to smaller element size with Custom 1 and Custom 2 indicates no significant I_p changes at -6.6725 µA with an error of only -0.037%. Hence, this findings proves that the study gives very accurate and reliable data on 1D.

4.3 Effect of meshing on the 2D asymmetric and 3D simulation

Two sets of meshing were designed to observe their effect on the simulation results' accuracy and precision. The element sizes were manipulated on two regions; (1) far from the electrode and (2) close to the electrode. The current, $I_{(t)}$ on 2D axisymmetric geometries is evaluated using eq. (4.3) (Compton and Banks, 2018). A simplified schematic diagram as illustrated in Fig 4.3 demonstrates the cylindrical integration on the 2D axisymmetric model.

$$I_{(t)} = -2\pi nDF \int_0^r r \frac{\partial c_O}{\partial z} dr \tag{4.3}$$

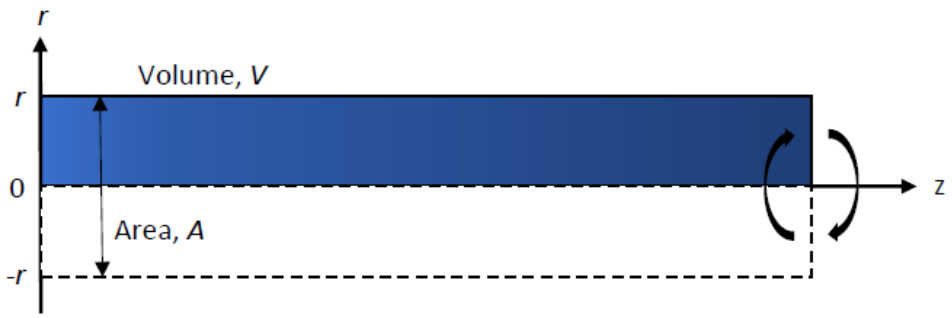

Figure 4.3: Diagram of the cylindrical integration along the z-axis in a 2D axisymmetric model

Fig 4.4 displays the concentration profile at 20 s with potential of 0 V for the 2D axisymmetric and 3D simulated model. The arrows show the flux propagation of O in the domain. Which reveals the diffusion happens in a non-linear manner and is projected near hemispherical contour due to of the edge effect near the electrode. This is due to the low scan rate, v_b. Theoretical expression of I_p on 2D axisymmetric and 3D models are evaluated using eq. (4.4 and 4.5) as described by Compton and Banks (2018). The percentage error was calculated by substituting $I_{p,linear}$ with $I_{p,non-linear}$ using eq (4.4-4.5). Evaluating this expression gives an $I_{p,\ non\text{-}linear}$ value of -7.88 μA.

$$I_{p,non-linear} = -4Frc_{o_{init}}D_o\left(0.34e^{-0.66\sqrt{\sigma}} + 0.66 - 0.13e^{\frac{-11}{\sqrt{\sigma}}} + 0.351\sqrt{\sigma}\right) \quad (4.4)$$

$$\sigma = -\frac{Frv_b}{RTD_o} \quad (4.5)$$

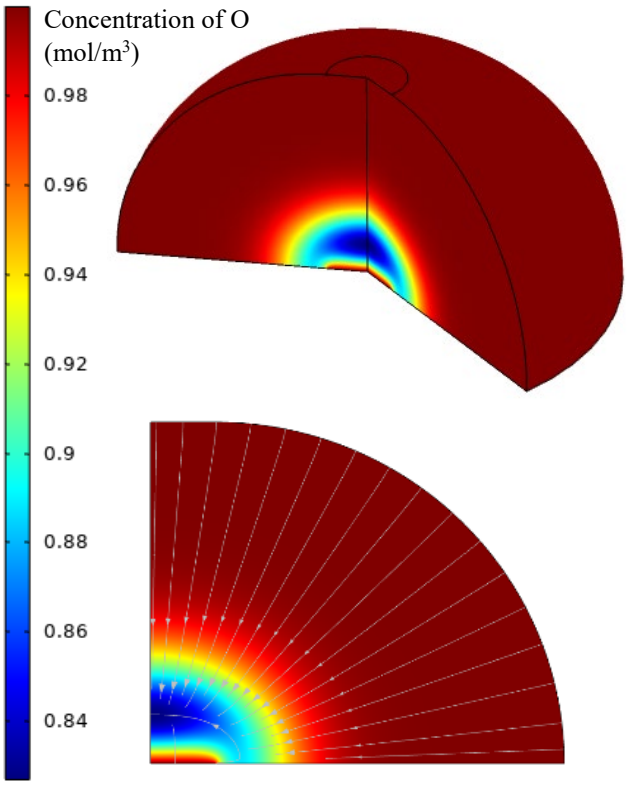

Figure 4.4: Concentration profile at t = 20 s, E^0 = 0 V on 2D axisymmetric and 3D simulations

Table 4.2 summarizes the *noe* for the mesh using only the predefined "extremely fine" setting on the electrode boundary. There is no noticeable difference in the data gathered for these different settings as shown in Figure 4.5. On "normal" predefined mesh, the I_p is identical to the ones with "finer" meshing. Therefore, it is safe to assume that the density of mesh outside of the focus region (electrode) does not affect the results obtained from the simulation and is considered a case of poor meshing with no significant meaning (Lavachi et al. 2009). This assumption is also extended to the 3D model.

Table 4.2: Meshing on the non-localized region (region far from the electrode) on I_p accuracies and time taken for 2D axisymmetric simulation

Predefined Mesh	Max element size (m)	*noe*	I_p (µA)	Percentage error, %	t_{com} (s)
Normal	2.13×10^{-4}	785	-8.173	3.723	267
Fine	1.69×10^{-4}	1012	-8.176	3.706	277
Finer	1.18×10^{-4}	1711	-8.175	3.744	309
Extra fine	6.37×10^{-5}	4984	-8.172	3.756	387
Extremely fine	3.18×10^{-5}	19167	-8.134	3.718	703

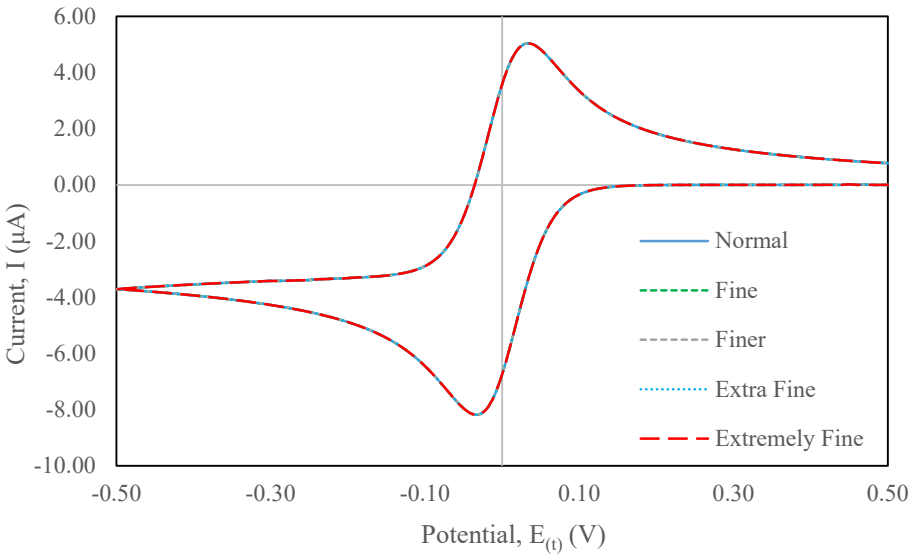

Figure 4.5: Current, $I_{(t)}$ (A) vs. Potential, $E_{(t)}$ (V) of different meshing on 2D axisymmetric

Significant changes were observed throughout the tested meshing when meshes were more concentrated on the electrode (see Figures 3.9 and 3.10). By referring to Fig 4.6, using the "normal" predefined mesh with 466 *noe*, I_p is recorded at -10.817 µA showing more than 37% error. When the *noe* was increased to 785, the I_p reading was -8.173 µA with a 3.72% error. Then, the *noe* was drastically increased from 2635 to 23638 while only slight changes on I_p were observed from -7.924 µA to -7.895 µA and took around 633 s (10.55 min) and 2248 s (37.47 min) to complete, respectively. Approximately 25 min longer t_{com} on the final

mesh shows pointless time spent on higher *noe*, as less than 1% error could be achieved in approximately 10 min.

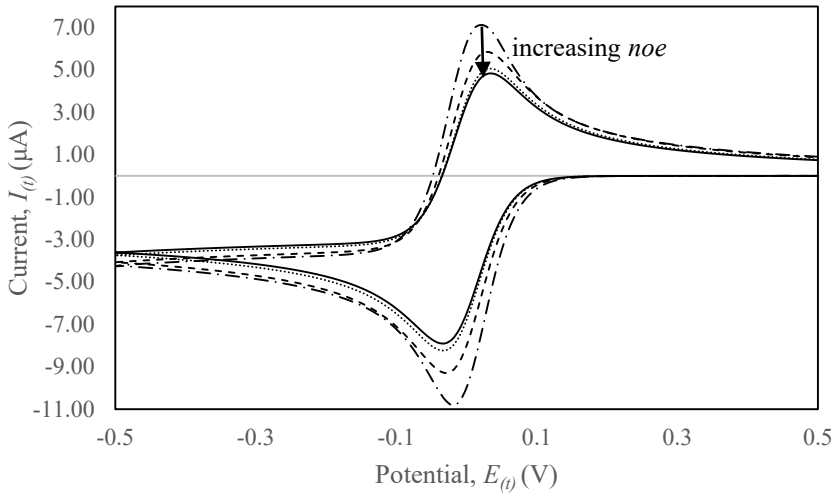

Figure 4.6: Current, $I_{(t)}$ (µA) vs. Potential, $E_{(t)}$ (V) of different meshing on 2D axisymmetric

From the 3D model, I_p for user defined "Custom" mesh containing 97479 *noe* peaked at -8.08 µA with a -2.5% error. The t_{com} took more than 225000 s (2.5 days) to complete. This is the most refined mesh that the CPU could process before running out of memory (CPU specifications in Table 4.3). By using the predefined setting, normal and finer meshing with *noe* of 4488 and 4737 respectively, shows results of -12.78 µA (62.20% error) and -11.03 mA (40.04% error) respectively. Compared to extremely fine meshing using a predefined setting with 5736 *noe*, the I_p reading is at -9.641 µA with 21.13% error, taking 5454 s to complete, that is still not good enough to be an acceptable result. Therefore, custom meshing was adopted to further refined *noe* and to increase the accuracy of the result.

Table 4.3: CPU specifications for this study

Operating system	Windows 10 Professional 64 bits (10.0, version 14393)

Processor	Intel® Xeon® CPU E5-2630v4 @2.20GHz (40 CPUs) ~ 2.2GHz
Memory	131072 MB RAM

This study proved that an error of 2.5% was obtained on very concentrated meshing on the 3D model. The drawback is that it takes 40 times longer to complete than using the available predefined meshing, which gives around 21% error which is not acceptable in many cases. The longer t_{com} is also noted to be partly due to the low *rtol* of $1x10^{-8}$. Therefore, in our opinion, this is considered a necessary drawback in working with a 3D model.

4.4 Adaptive meshing

One of the easiest ways to do mesh refinement on a model is utilizing the adaptive meshing option. This is a simple method to test the sensitivity of the results produced from the model. In COMSOL, the adaptive meshing option can be found under the solver sub menu as shown in Figure 4.7 screen capture.

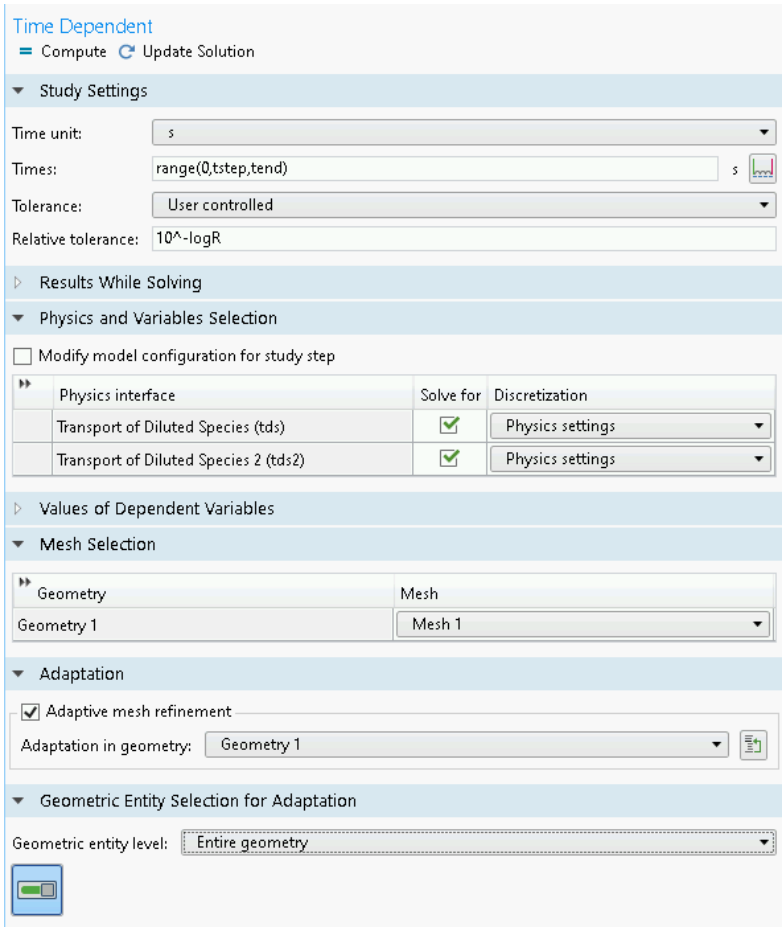

Figure 4.7: The extension of the time dependent window giving the option for adaptive meshing and its entity selection.

In this study, adaptive meshing was tested on varying initial meshes for all three dimensions. Since these are transient models, the evolution of meshing from the initial meshing at t = 0 s to the final meshing at t = 20 s are visualized. It can be observed that the mesh is seen to adapt with the propagating flux inside the domain (in Figure 4.8-4.10). On the 1D in Fig 4.8, an initial mesh of 15 *noe* gives an error of around 0.08% and took 301 s to complete. On the 2D axisymmetric (Fig 4.9), initially coarser mesh achieved an error of approximately 5.47% at -8.31 µA and took 1115 s execution time. A very stark contrast was observed from meshing with the same *noe* but without the adaptive meshing. Additionally, when adaptive meshing was applied on higher *noe*, the I_p peaked at -7.871 µA that is -0.114% different

from the calculated value. A slight improvement was accomplished in the results from non-adaptive meshing by less than 0.2% error.

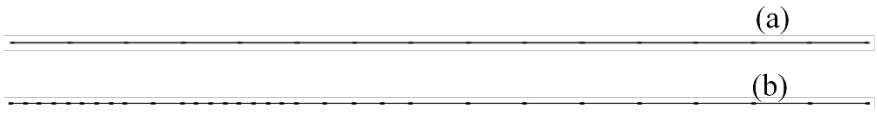

Figure 4.8: Adaptive meshing on 1D simulation (a) Initial mesh of 15 *noe* (b) Final mesh of 30 *noe*.

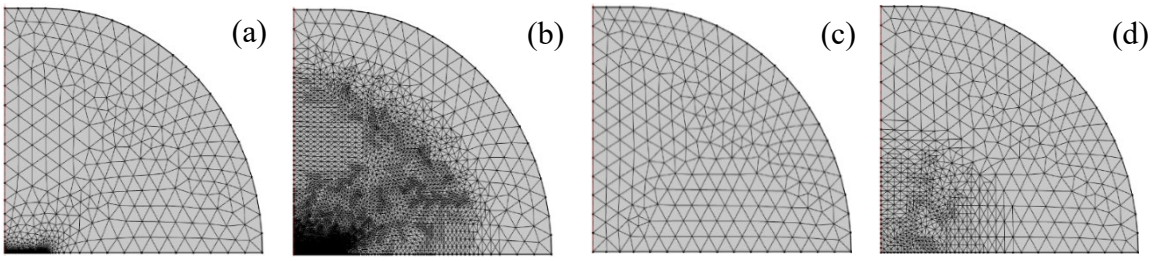

Figure 4.9: Adaptive meshing on 2D axisymmetric simulation (a) Initial mesh of 23638 *noe* (b) Final mesh of 40450 *noe* (c) Initial mesh of 466 *noe* (d) Final mesh of 1424 *noe*.

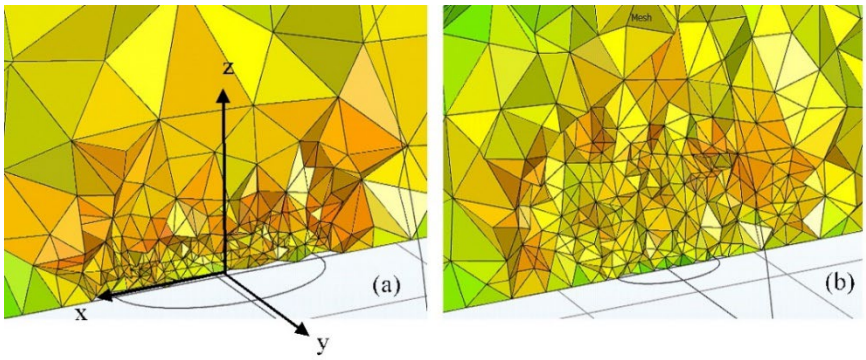

Figure 4.10: Adaptive meshing on 3D simulation (a) Initial mesh of 5736 *noe* (b) Final mesh of 18908 *noe*.

For 3D simulation with adaptive meshing, two initial meshing were tested using two predefined settings; (1) normal and (2) extremely fine (Fig 4.10). Both predefined settings

give results of less than 11% error and it takes more than 15000 s to complete each simulation. The outcome reveals an improvement of 2.4% error, which is considered significant in getting the percentage error to 8.25%. Compared to non-adaptive meshing on a predefined setting, the percentage error was reduced to nearly 3 times smaller while taking more than four times longer to complete.

4.5 Relative tolerance

Relative tolerance, *rtol* is described in the COMSOL Multiphysics® user manual (2014), as the maximum amount of error that a user is willing to allow in the solution. Iteration of solution are calculated until the relative error approximation drops below the pre-specified relative tolerance. This was described in eq (3.15) in subchapter 3.3.3.

A test was conducted in this study to see the sensitivity of the *rtol* value on the (1) accuracy of peak current at -0.02V, $I_{p\ -0.02}$ (μA), and the (2) time taken to complete the computation, t_{com} (s). In this simulation, the meshing across all of the three geometries are kept at "extremely fine" settings (refer to Table 4.1 for the resulting I_p) for a viable comparison.

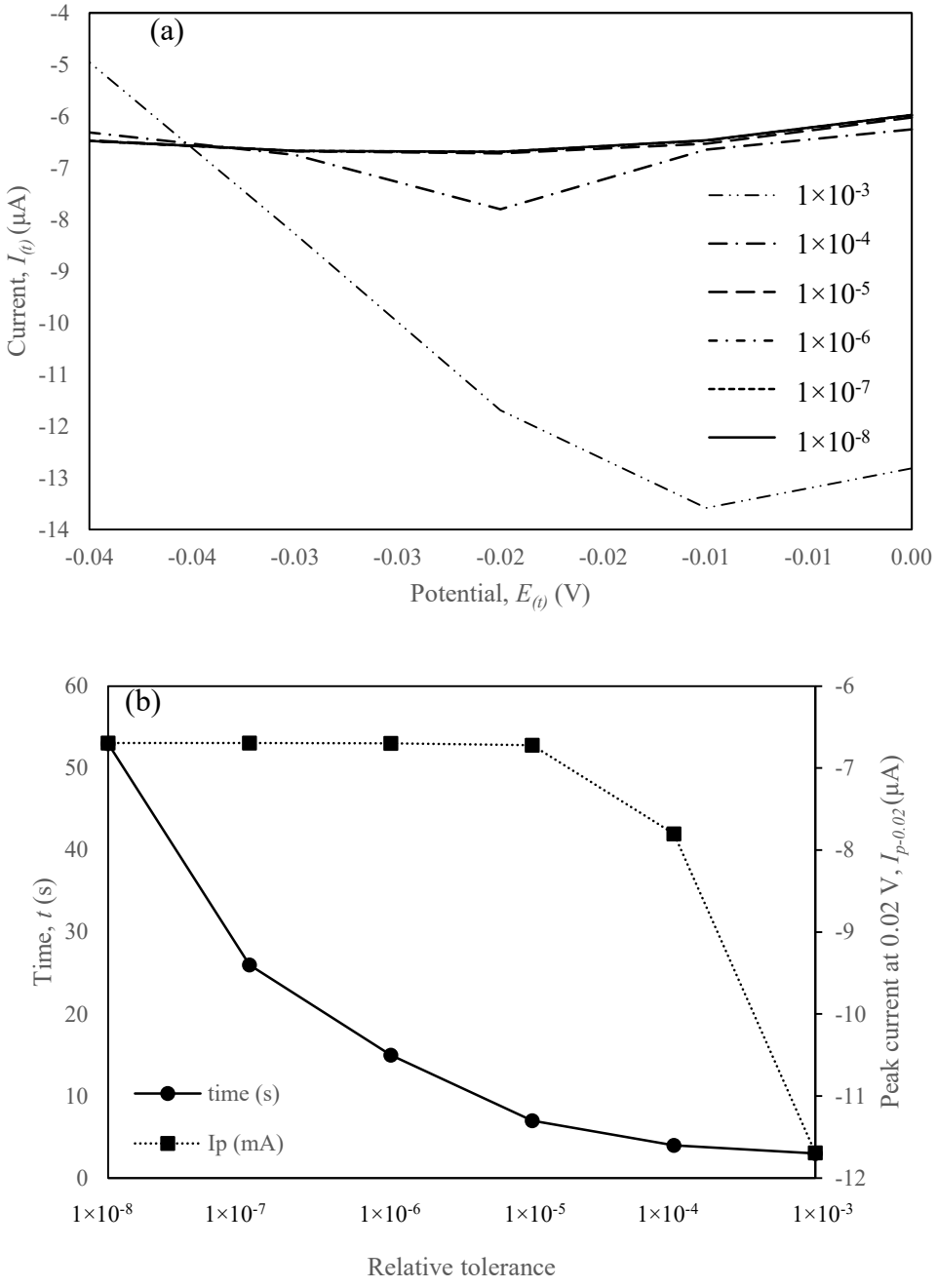

Figure 4.11: (a) Plot of relative tolerance (*rtol*) for current, $I_{(t)}$ vs potential, $E_{(t)}$ and (b) Computation time, *t* in s, and peak current value at -0.02 V, $I_{p\ -0.02}$ in µA vs relative tolerance (*rtol*) for 1-D model

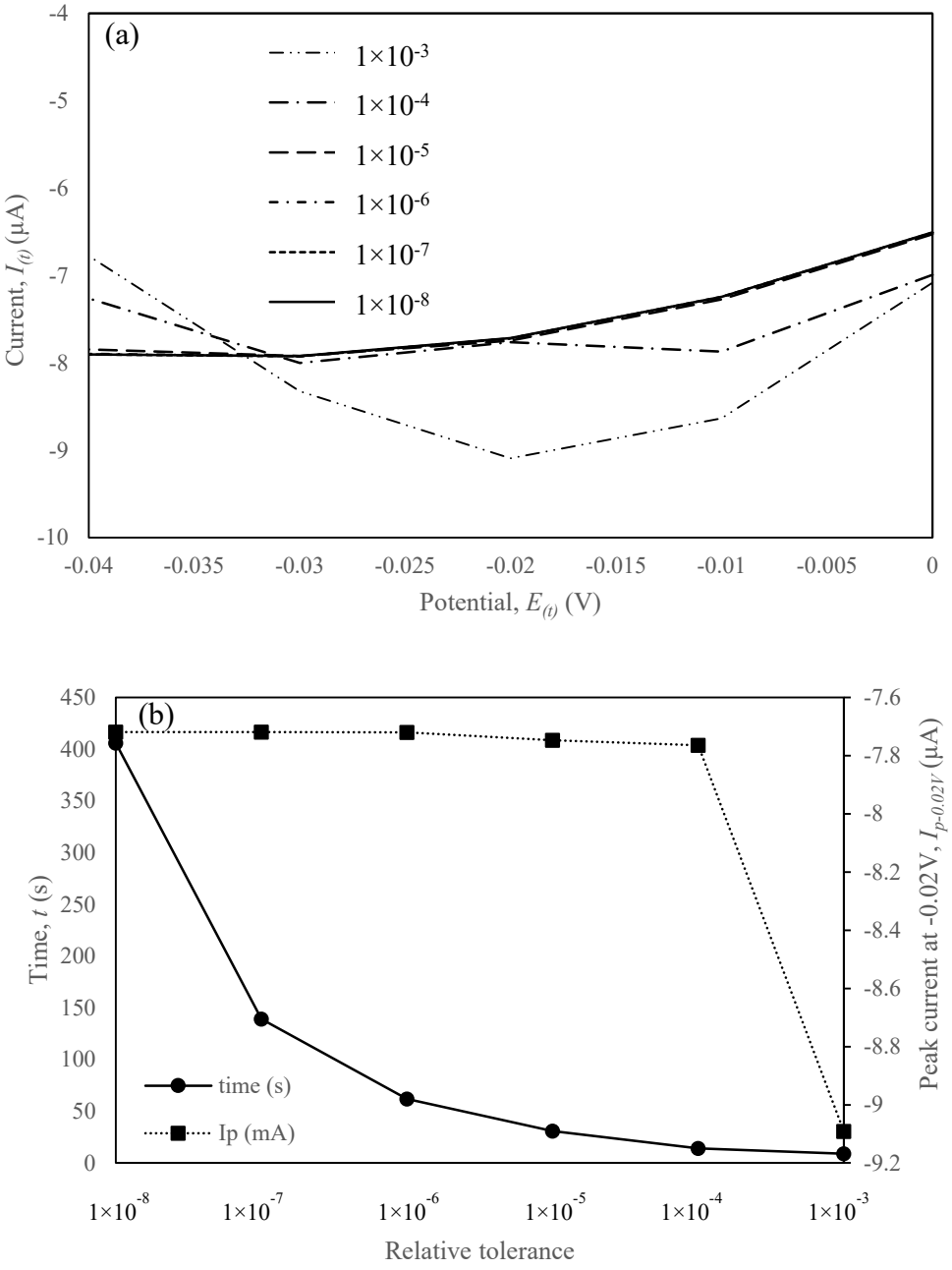

Figure 4.12: (a) Plot of relative tolerance (*rtol*) for current, $I_{(t)}$ against potential, $E_{(t)}$ and (b) Computation time, t in s, and peak current value at -0.02 V, $I_{p\,-0.02}$ in µA against relative tolerance (*rtol*) for 2D axisymmetric.

Based on the plotted graphs in Figures 4.11 and 4.12 the *rtol* values of 1×10^{-5} and 1×10^{-4} are sufficient in the simulation for both of the 1D and 2D axisymmetric to obtain accurate results. The t_{com} rises exponentially at smaller *rtol* for the 1D, and 2D axisymmetric and is

almost linear on the 3D. For *rtol* value less than 1×10^{-5}, the $I_{p\ -0.02}$ shows no change, proving the selected *rtol* is accurate for the given simulation.

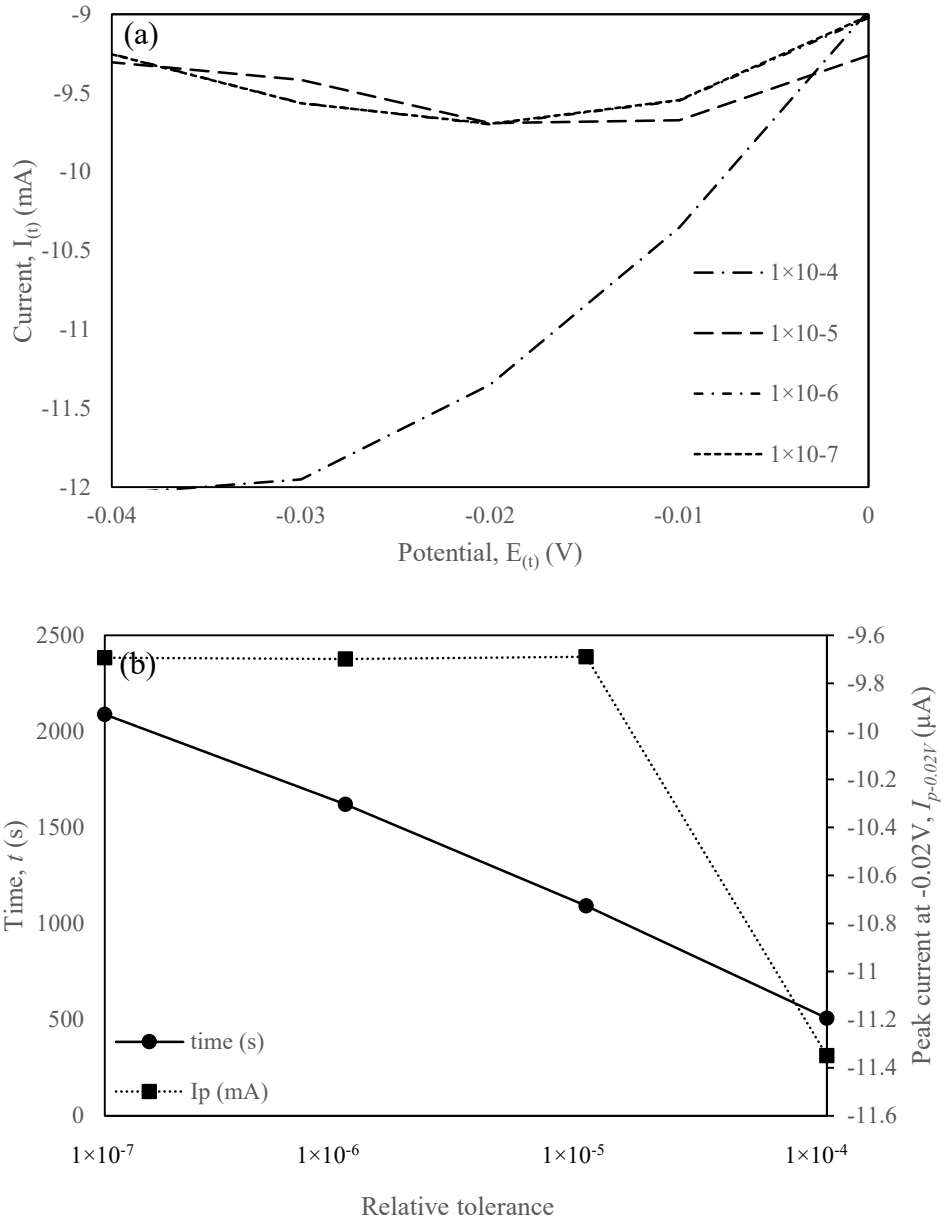

Figure 4.13: (a) Plot of relative tolerance (*rtol*) for current, $I_{(t)}$ against potential, $E_{(t)}$. (b) Computation time, *t* in s, and peak current value at -0.02 V, $I_{p\ -0.02}$ in µA against relative tolerance (*rtol*) for 3D.

For 3D, Fig 4.13 shows that the $I_{p-0.02V}$ is peaked at around -9.7 µA when *rtol* is 1×10^{-5} taking around 1200 s (20 mins) to complete calculation. That shows good argument with the given

I_p for 3D predefined “extremely fine” meshing with 21% error (as shown in Table 4.1). By using large *rtol* value for e.g. 1×10^{-4}, it takes nearly half the time to complete (around 500 s) compared to when *rtol* is 1×10^{-5}. But the recorded $I_{p\text{-}0.02V}$ was around 11.35 mA that was very far from the theoretical value. This proves that the *rto*l value is essential only in attaining precise results but not the accuracy and it has a significant role in the t_{com}. This shows that good meshing is required and it needs to be paired with optimal *rtol* value to yield quick and accurate results.

4.6 Discussion

A simple correlation on meshing, accuracy, and computation time are presented in this work. It aims to function as a guide on more advanced electrochemistry works using this platform. The study shows a non-linear diffusion on the 2D axisymmetric and 3D models. These viewpoints are not available in the 1D model where the diffusion is always assumed to be linear in its propagation. However, it works differently on model with more dimensions. Therefore, some unportrayable flux can now be visualized by the mesh. Fig 4.14 compares the $I_{(t)}$ produced by the linear and non-linear diffusion simulated in this study. The 2D axisymmetric and 3D models show great coherency in the result. A similar trend on $I_{(t)}$ vs $E_{(t)}$ plot justifies our argument on the semi-spherical diffusion occurring in the domain.

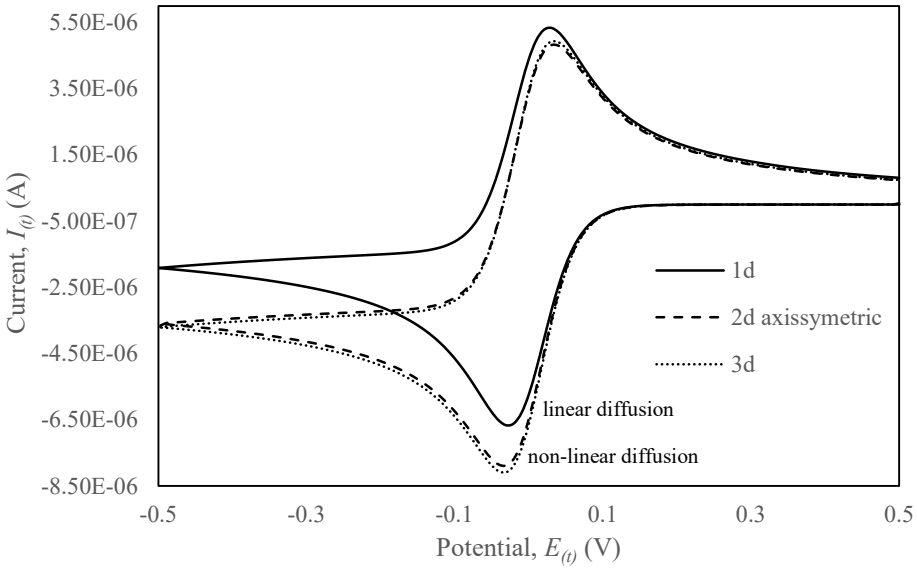

Figure 4.14: Comparison of current, $I_{(t)}$ vs. potential $E_{(t)}$ of the 1D, 2D axisymmetric, and 3D model on recommended meshing.

Further comparison on I_p was plotted against the maximum element size across the different dimensions in Figure 4.15. Figures 4.16 and 4.17 were plotted in segregation to visualize the I_p and the percentage error against max element size for 1D and 2D axisymmetric and 3D models, respectively. Theoretical values of the I_p on linear diffusion and non-linear diffusion are indicated in the graph. The 1D model shows quick convergence on peaked value as the trend flattens early. With the inclusion of semi-spherical diffusion on 2D axisymmetric and 3D models, a somewhat linear correlation is observed on the element size and I_p before the peaked converged on element sizes of less than 10^{-5} m. A slight discrepancy between the 2D axisymmetric and 3D results was calculated to be less than 3%, showing excellent simulation consistency across all models. These findings further support claims by Cutress et al. (2010) on the software abilities (as stated in sub-chapter 1.4.2 on simulation pertaining 3D geometries).

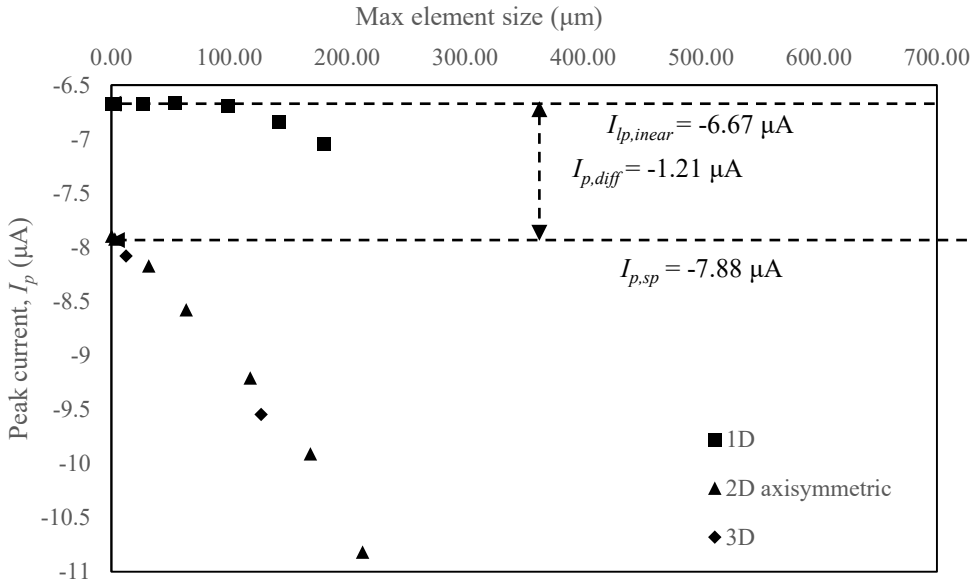

Figure 4.15: Plot of I_p against max element size for 1D, 2D axisymmetric, and 3D model.

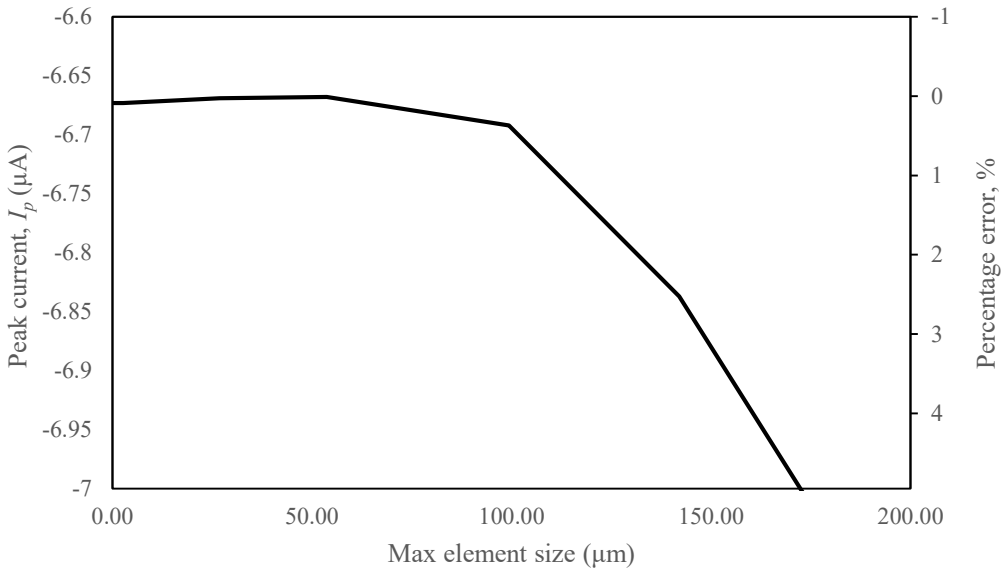

Figure 4.16: Plot of I_p and percentage error, % against max element size for 1D model.

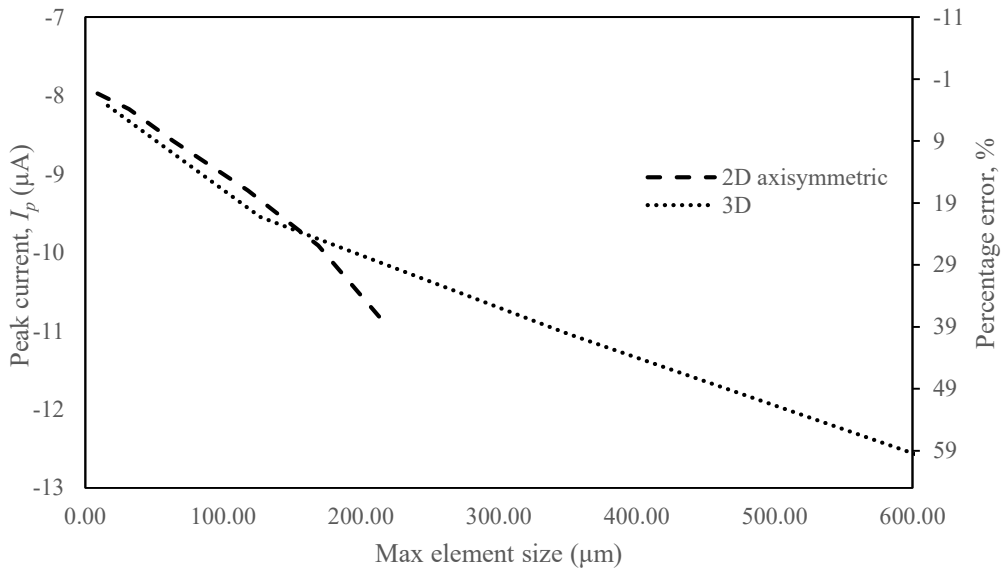

Figure 4.17: Plot of I_p and percentage error, % against max element size for 2D axisymmetric and 3D model.

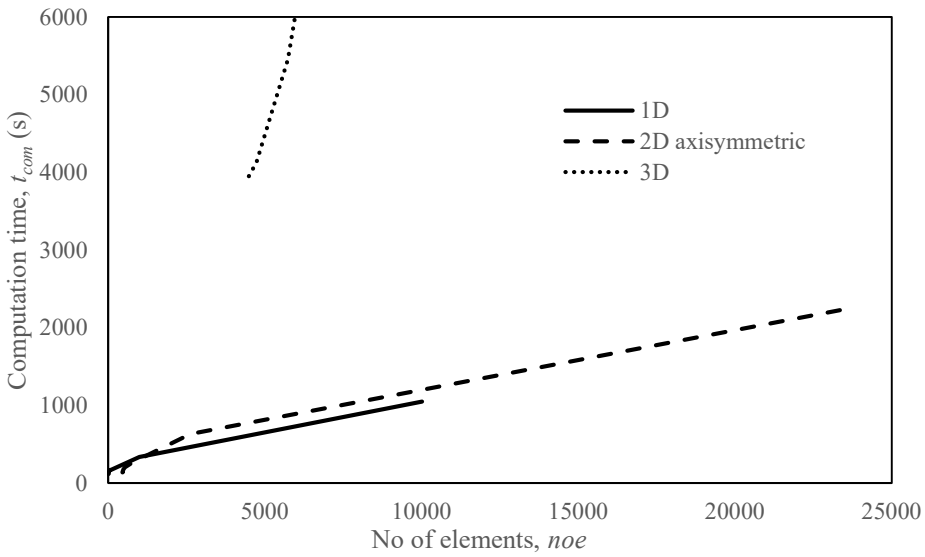

Figure 4.18: t_{com} against *noe* on 1D, 2D axisymmetric, and 3D model

A plot recording the *noe* effects on t_{com} is given in Fig 4.18. It showed 3D simulations having longer t_{com} even on lower *noe* than the other models by quite a significant amount. Some might argue that the 3D model is knowingly going to take longer to simulate. This statement was supported by Cutress et al. (2010) in their overview on COMSOL

Multiphysics®' ability with 3D model. The reasoning behind this comparison is to enlighten the readers on the direct effect of different meshing approach and the *rtol* values on the t_{com} in dealing with 1D, 2D axisymmetric and 3D geometries. These models offer great precision on both complex and straightforward geometries through these findings.

4.7 Chapter Summary

A FEM study on transient redox reaction of a single electrode disk was successfully simulated using the commercial software COMSOL Multiphysics®. This study proved the software's consistency across all dimensions to produce results less than 2.5% error. Using a *rtol* value of 1×10^{-8} the 1D simulation took around 2 minutes to complete, while the 2D axisymmetric simulation completed about 10 minutes. The 3D simulation took a significantly longer time of approximately five days to complete. An error of 2.5% was obtained using a custom mesh giving more than 90000 *noe* on a 3D model. The drawback is that it takes 40 times longer to complete than the available predefined meshing, which offers around 21% error. Therefore, this is considered a necessary drawback in working with a 3D model.

A slight discrepancy between 2D axisymmetric and 3D results on finest meshing was recorded to have less than 3% difference due to the CPU capacity limitation. Adaptive meshing works well on 1D. When standard predefined meshing was used, an error of 5.5% was obtained, and the error was reduced to 0.082% on adaptive meshing with the same setting while the t_{com} was doubled. On 2D axisymmetric, “normal” predefined mesh yields around 37.3% error, and the error can be reduced to 5.5% with adaptive meshing with t_{com} taking nearly ten times longer. For 3D simulation with adaptive meshing, using “normal”

and “extremely fine” predefined initial mesh gives an error of 10.9% and 8.2%, respectively. It takes more than 15000 s to complete each calculation. Compared to those without adaptive meshing, the percentage error was reduced to 4 times smaller while taking more than four times longer to complete the simulation. Adaptive meshingare recommended for beginner users. However, it will prolong the simulation time and is even more time-consuming on complex geometries. It is suggested to manually mesh as it can give better results in a much shorter time. Relative tolerance (*rtol*) study shows that the value of 1×10^{-4} is adequate for 2D axisymmetric and 1×10^{-5} for both 1D and 3D for optimal t_{com}. The use of lower *rtol* values would only increase t_{com} as further iterations shows no significant changes. Further study on complex reactions using this platform is justified and highly recommended.

CHAPTER 5

PARAMETRIC STUDY AND ANALYSIS OF VOLMER-HEYROVSKY-TAFEL (VHT) STEPS FOR THE HYDROGEN EVOLUTION REACTION (HER)

5.1 Introduction

A typical cyclic voltammogram (CV) can be categorized into four regions as shown in Figure 5.1. Platinum, Pt is used as an example because of its excellent catalytic properties was widely used a reference for emerging electrocatalyst. Starting with the high potential regions of around (>0.65 V vs RHE) where RHE is the reversible hydrogen electrode, the Pt surface undergoes oxidation and reduction. Between the potentials of (0.35 V – 0.65 V vs RHE) it was called a double layer region where no Faradaic reactions occur. The third region being referred to as the hydrogen underpotential deposition (H_{UPD}) region where the protons are discharged on the Pt surface which happens in the potential regions of 0.05 V – 0.35 V vs RHE. Finally, the HER region where H_2 is produced that occurs at negative potentials. This work present in this chapter is devoted in elaborating the details pertaining to the HER region.

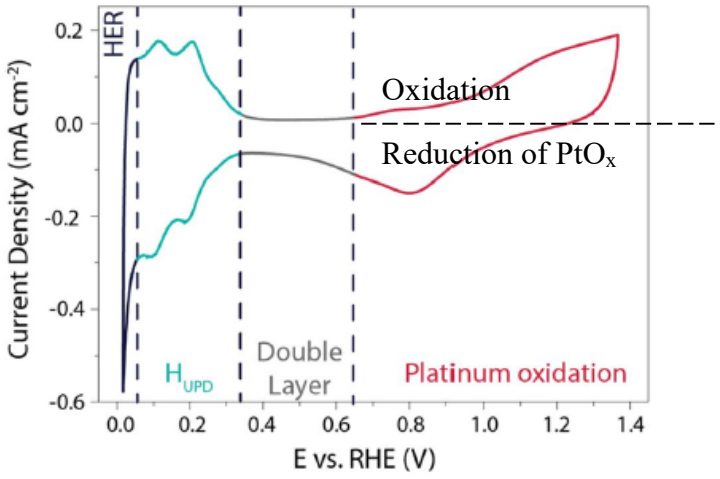

Figure 5.1: Cyclic voltammogram recorded on a polycrystalline Pt electrode at 50 mVs^{-1} in a 0.5 M H_2SO_4 solution degassed with argon (Dubouis and Grimaud, 2019)

In this study, an investigation on the kinetics parameters for HER is conducted via FEM to study the effect of Volmer-Heyrovsky-Tafel (VHT) reactions under acidic solution (H^+). A transient simulation program (with steady-state parameters) is run to see the effect of several kinetic parameters that were manipulated, namely;

a) Standard rate constants, k_v, k_{-v}, k_h, k_{-h}, k_t and k_{-t}.

b) Charge transfer coefficients, β_v, and β_h.

The results are observed to see the effects on (1) concentration of hydride surface, c_{Hs} in mol/m^2 (2) current density, j in mA/cm^2 and (3) Tafel plots which is the $\log_{10} j$ (in mA/cm^2). Based on the Volmer, Heyrovsky and Tafel reactions, Table 5.1 summarized the sign convention indicating the increment or decrement of the involved components in the simulation.

Table 5.1: Summary showing the effect of VHT forward and backward reactions on components involved for each steps.

Reactions		**H^+**	**s**	**Hs**	**H_2**
Volmer	Forward	Constant	$-(\Gamma_s - c_{Hs})$	$+c_{Hs}$	0
	Backward	Constant	$+(\Gamma_s - c_{Hs})$	$-c_{Hs}$	0
Heyrovsky	Forward	Constant	$+(\Gamma_s - c_{Hs})$	$-c_{Hs}$	$+c_{H2}$
	Backward	Constant	$-(\Gamma_s - c_{Hs})$	$+c_{Hs}$	$-c_{H2}$
Tafel	Forward	Constant	$+(\Gamma_s - c_{Hs})^2$	$-(c_{Hs})^2$	$+c_{H2}$
	Backward	Constant	$-(\Gamma_s - c_{Hs})^2$	$+(c_{Hs})^2$	$-c_{H2}$

+ produced, - consumed

This chapter will include the elaboration on the formulation of reversibility in VHT reactions. Comparison will be made on the difference of HER responses assuming irreversible and reversible reactions. Finally, the idea of kinetic parameters permutation and its effect on the performance of HER will be discussed at the end of this chapter.

5.2 Volmer-Heyrovsky (VH) irreversible reactions

The standard rate constant for Volmer forward reaction (eq. 5.1), k_v with the charge transfer coefficient for Volmer, β_v were observed to see their effect on the HER performance namely the surface concentration of Hs (mol/m^2) and current density, j (mA/cm^2). The Butler-Volmer expression on a general one-electrode reaction written as eq. (5.2) was used to solve the rate constant for Volmer, K_v in m^3/mol.s, Consequently, the rate of Volmer forward reaction, R_v in mol/m^{2}s was then written as eq. (5.3) in terms of the concentration of H^+, c_{H^+} in mol/m^3 and the concentration of the vacant sites, c_s in mol/m^2.

$$H^+ + s + e^- \xrightarrow{k_v} Hs \tag{5.1}$$

$$K_v = \left(k_v e^{\left(-\frac{\beta_v nF}{RT}\right)(E_{(t)}-E_o)}\right) \tag{5.2}$$

$$R_v = K_v c_{H^+} c_s \tag{5.3}$$

Similarly, the Heyrovsky forward reaction was written as (eq. 6.4) with the standard rate constant, k_h, and the charge transfer coefficient for Heyrovsky, β_h. Using the Butler-Volmer expression, eq. (5.5) give the Heyrovsky rate constant, K_h. Rate of Heyrovsky forward reaction, R_h in mol/m^{2}s was then written as eq. (5.6) in terms of the surface concentration of H^+, c_{H^+} in mol/m^3 and the surface concentration of Hs, c_{Hs} in mol/m^2.

$$H^+ + Hs + e^- \xrightarrow{k_h} H_2 + s \tag{5.4}$$

$$K_h = \left(k_h e^{\left(-\frac{\beta_h nF}{RT}\right)(E_{(t)}-E_o)}\right) \tag{5.5}$$

$$R_h = K_h c_{H^+} c_{Hs} \tag{5.6}$$

Generally, this parametric study adopts the values of Table 5.2 to evaluate the HER performances via the plotted diagram of adsorbed hydrogen concentration, c_{Hs} on the

electrocatalyst, the consequent current density and its corresponding Tafel plots. Therefore, in the following subchapters, the values of the parameters will be retained unless mentioned or varied.

Table 5.2: General values of the parameters adopted in the parametric study

Name	Expression	Value	Description
ki	1e-4[s^(-1)/(mol/m^3)]	1×10^{-4} m³/(s·mol)	Volmer forward standard rate constant *(k_v)*
kii	1e-6[s^(-1)/(mol/m^3)]	1×10^{-6} m³/(s·mol)	Heyrovsky forward standard rate constant *(k_h)*
kiii	1e3[(m^2)/(mol*s)]	1000 m²/(s·mol)	Tafel forward standard rate constant*(k_t)*
bi	0.5	0.5	Volmer transfer coefficient *(β_v)*
ali	1 - bitaC	0.5	Volmer transfer coefficient *(α_v)*
bii	0.5	0.5	Heyrovsky transfer coefficient *(β_h)*
alii	1 - biitaC	0.5	Heyrovsky transfer coefficient *α_h)*
E0i	0[V]	0 V	Volmer standard potential *(E_{0v})*
E0ii	0[V]	0 V	Heyrovsky standard potential *(E_{0h})*
vb	1e-6[V/s]	1×10^{-6} V/s	Potential scan rate (v_b)
Einit	0.6[V]	0.6 V	Initial potential (E_{init})
Erev	-0.6[V]	−0.6 V	Reverse potential (E_{rev})
tend	1.2e6	1.2×10^{6} s	Time stop (t_{end})
tstep	1.2e3	1.2×10^{3} s	Time step (t_{step})
cstar	1000[mol/m^3]	1000 mol/m³	Initial concentration for H^+ (c_{H+})
Gmax	1e-5[mol/m^2]	1×10^{-5} mol/m²	Maximum concentration of Hs (Γ_{max})

Another important note is the initial potential, E_{init} used was 0.6 V where the time started from 0 s with the reverse potential, E_{rev} at -0.6 V. This potential range was applied to implement the practice of measuring overpotentials at 10 mA/cm^2 or usually written as η_{10}. It is a popular method to measure the water–splitting reactions for HER and OER by measuring the overpotential required to reach the current density of 10 mA/cm^2 (Wei and Xu, 2018). Considering the study is an irreversible reaction, the graphs were plotted only in the HER region which in this case is between -0.6 V < η < 0 V. A very slow scan rate is

usually use during experiment. Similarly, in the simulation a slow potential scan rate of 1×10^{-6} Vs^{-1} was used, this is to depict the steady state nature of the experiment.

5.2.1 Effect of Volmer: standard rate constant, k_v and charge transfer coefficient, β_v.

When the k_v increases in a VH irreversible reaction, the c_{Hs} increases. This was demonstrated in Figure 5.2(a), where on slow kinetics of $k_v = 1\times10^{-6}$ m^3/mol.s the c_{Hs} on the catalyst were estimated to be only 50% fill. The was due to Heyrovsky reaction that consumed the c_{Hs} on the surface. When k_v was increased to 1×10^{-4} m^3/mol.s the c_{Hs} on the catalyst surface were nearly 100% indicating that $R_v>R_h$ where Hs produced is more than it is consumed. This is further proven when k_v was increased to 1×10^{-2} m^3/mol.s but no further changes were observed showing that Heyrovsky reaction is the rate determining step (RDS) with the provided standard rate constant of k_v and k_h in the simulation. The corresponding j vs η in Figure 5.2 (b) shows that at η_{10} for $k_v = 1\times10^{-6}$ m^3/mol.s is approximately -0.6 V while $k_v > 1\times10^{-4}$ m^3/mol.s is capped at approximately -0.56 V. The tafel plots (Figure 5.2 (c)) provide a slope of 118.8 mV/dec on all three k_v variations and the exchange current densities, j_o of 9.6×10^{-8} A/cm^2 and around 1.9×10^{-7} A/cm^2 respectively.

In addition, a parametric swept on the charge transfer coefficient of the Volmer reaction, β_v shows its effect (β_v = 0.25, 0.5 and 0.75). When β_v = 0.25 the c_{Hs} shows a decrease unlike when β_v = 0.5 and 0.75. A small β_v coefficient indicates a slower electron transfer during Volmer reaction, hence the following Heyrovsky steps consumed the built up Hs on the catalyst surface.

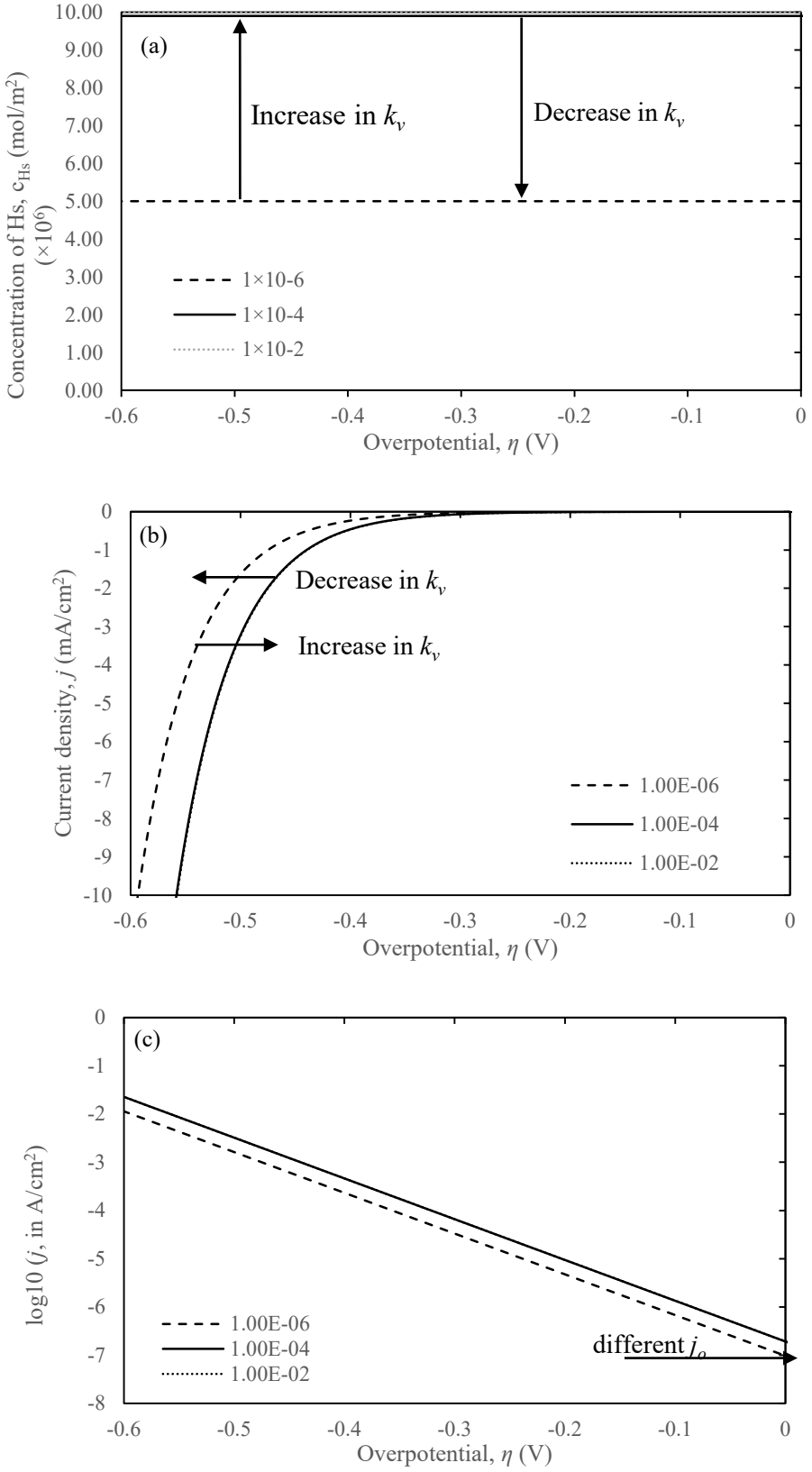

Figure 5.2: Comparison on the Volmer standard rate constant, k_v = (1×10^{-6}, 1×10^{-4},1×10^{-2}) m^3/mol.s against overpotential, η, on the (a) concentration profile of Hs, c_{Hs} (mol/m^2) (b) current density, j (mA/cm^2) and (c) the corresponding Tafel plots in A/cm^2.

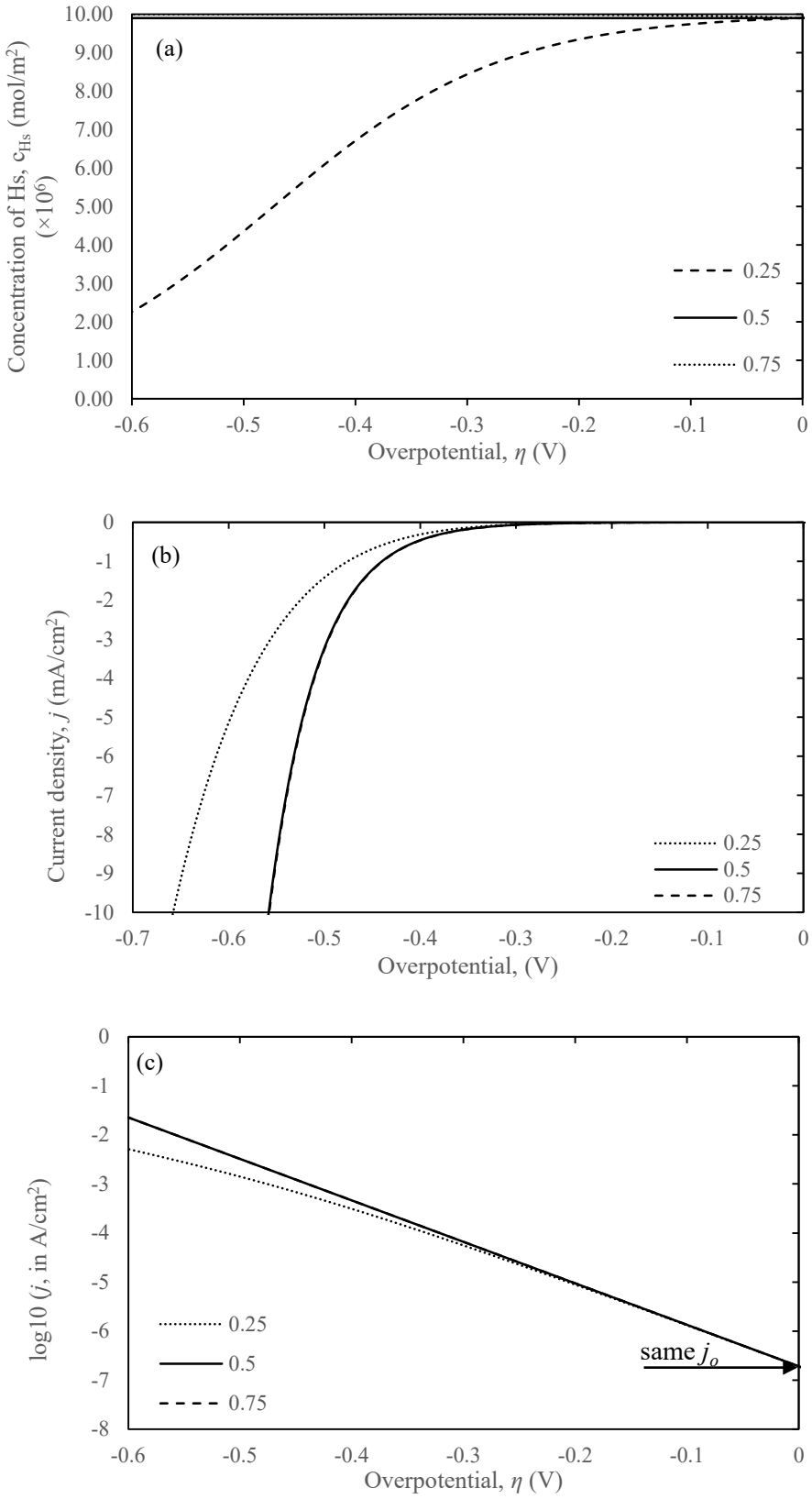

Figure 5.3: Comparison on the Volmer charge transfer coefficient, β_v = (0.25, 0.5, 0.75) against overpotential, η, on the (a) concentration profile of Hs, c_{Hs} (mol/m^2) (b) current density, j (mA/cm^2) and (c) the corresponding Tafel plots in A/cm^2.

In figure 5.3(b), when $\beta_v = 0.25$, due to less c_{Hs}, η_{10} were observed at estimated -0.67 V. The corresponding Tafel plots shows a slope of 160 mV/dec between ($-0.6<\eta<-0.4$) V while a slope of 118.8 mV/dec was retained at lower overpotential of $\eta>-0.3$ V. When $\beta_v = 0.75$, the slope was not discernable from when $\beta_v = 0.5$. This shows the HER performance could not improve further even at higher charge transfer coefficient for Volmer, due to the c_{Hs} reaching maximum capacity on the catalyst surface. Only with faster Heyrovsky could improve the HER performance. Noticeably, the exchange current density, j_o does not change with the change of β_v.

5.2.2 Effect of Heyrovsky: k_h and β_h.

When the k_h is increased in a VH irreversible reactions, the c_{Hs} decreases. This is demonstrated in Figure 5.4(a), when ($k_h = 1\times10^{-4}$ m^3/mol.s) the c_{Hs} on the catalyst surface were estimated to be only 50% fill. This is due to Heyrovsky reaction that consumes c_{Hs} on the surface. When k_h decreases to 1×10^{-6} m^3/mol.s the c_{Hs} on the catalyst surface were nearly 100% indicating that $R_h<R_v$ where Hs produced is more than it was consumed. This is further proven when k_h was decreased to 1×10^{-8} m^3/mol.s. There are no further changes observed showing that Heyrovsky reaction is the rate determining step (RDS) with the provided standard rate constant of k_v and k_h in the simulation. On the contrary, when the corresponding j vs η was plotted in Figure 5.4(b) it shows that at η_{10} for $k_h = 1\times10^{-8}$ m^3/mol.s was at estimated -0.8 V. This is considered significantly lower in comparison to $k_h = 1\times10^{-6}$ m^3/mol.s (with approximately similar plot of c_{Hs} vs η diagram) that recorded η_{10} of -0.57 V. When the k_h was increased to 1×10^{-4} m^3/mol.s the η_{10} obtained was approximately -0.37 V. While in Figure 5.4(c) the Tafel plot provide a slope of 118.8 mV/dec on all three k_h variations and the exchange current densities, j_o of 1.9×10^{-9} A/cm^2, 1.9×10^{-7} A/cm^2 and

around 9.6×10^{-6} A/cm^2 respectively. The lower j at lower k_h can be attributed to the slower kinetics of Heyrovsky reaction which means slower H_2 production. At this point, regardless of the of rapidity of Volmer reaction (high k_v), it was limited by the Heyrovsky reaction. Hence the high c_{Hs} recorded in c_{Hs} vs η diagram for low k_h value of 1×10^{-8} m^3/mol.s and 1×10^{-6} m^3/mol.s.

A parametric sweep on the charge transfer coefficient of the Heyrovsky reaction, β_h shows the effect of this parameter (β_h = 0.25, 0.5 and 0.75). It shows that when β_h = 0.75, c_{Hs} shows a decrement unlike when β_h = 0.25 and 0.5. A direct opposite to the ones of Volmer reaction, β_v. A small β_h coefficient indicates a slower electron transfer during Heyrovsky reaction. In figure 5.5(b), when β_h = 0.75, due to higher β_h, the η_{10} were observed at estimated -0.39 V. While lower β_h of 0.25 and 0.5 recorded η_{10} of approximately -1.1 V and -0.57 V respectively. The corresponding Tafel plots shown in Figure 5.5(c) for β_h = 0.25, 0.5, and 0.75 shows a slope of 236.4, 118.8, and 79.2 mV/dec respectively between ($-0.4<\eta<0$) V. The given figures clearly show that when β_h is high the electron transfer is rapid consequently increasing the H_2 formation. At this point, it shows the HER performance was determined by the rate of Heyrovsky reaction. Only with faster Heyrovsky could improve the HER performance. Similar to the charge transfer coefficient for Volmer reaction, the charge transfer coefficient for Heyrovsky reaction, β_h does not change the exchange current density, j_o.

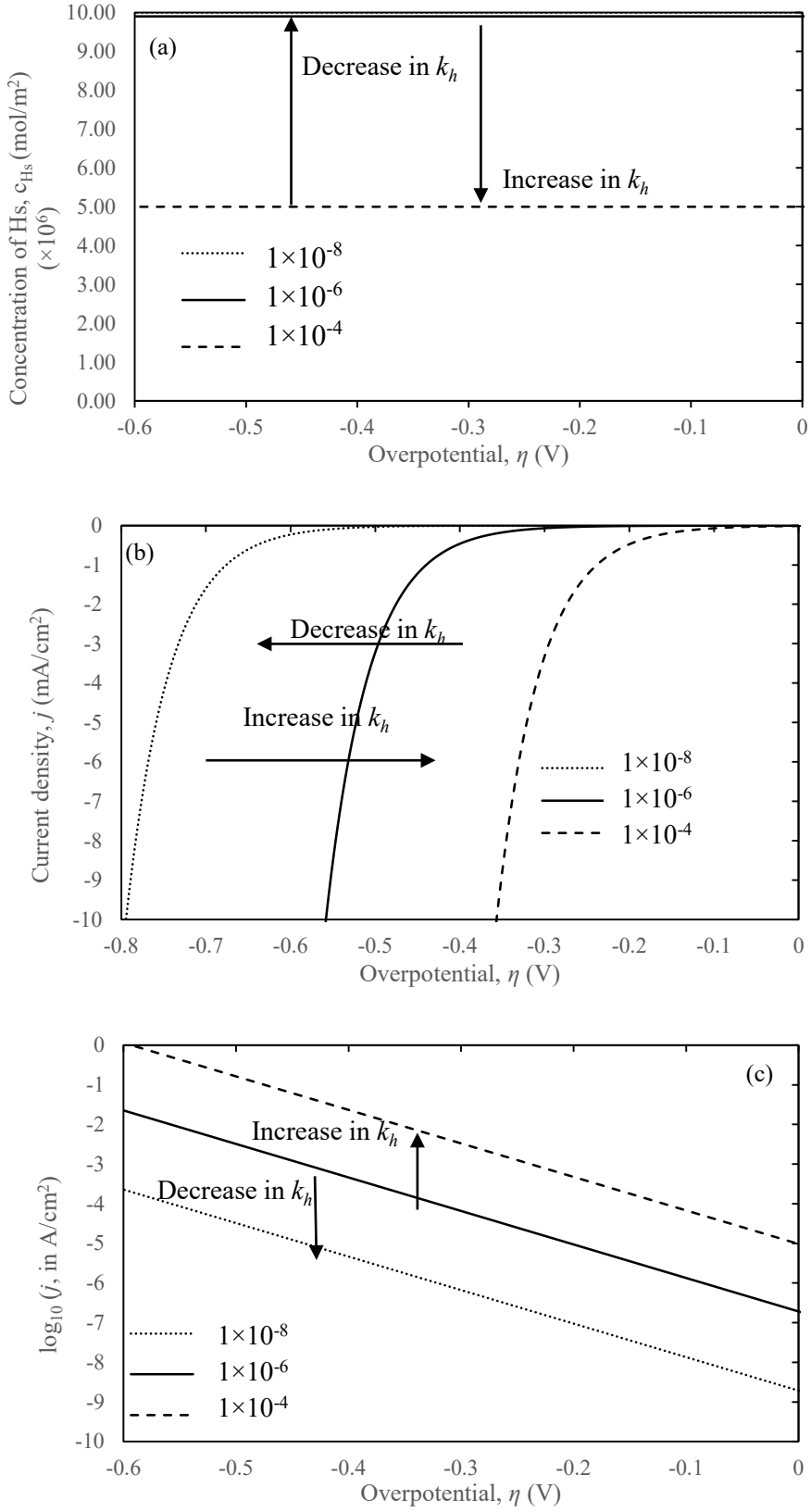

Figure 5.4: Comparison on the Heyrovsky standard rate constant, k_h = (1×10^{-8}, 1×10^{-6},1×10^{-4}) m^3/mol.s against overpotential, η, on the (a) concentration profile of Hs, c_{Hs} (mol/m^2) (b) current density, j (mA/cm^2) and (c) the corresponding Tafel plots in A/cm^2.

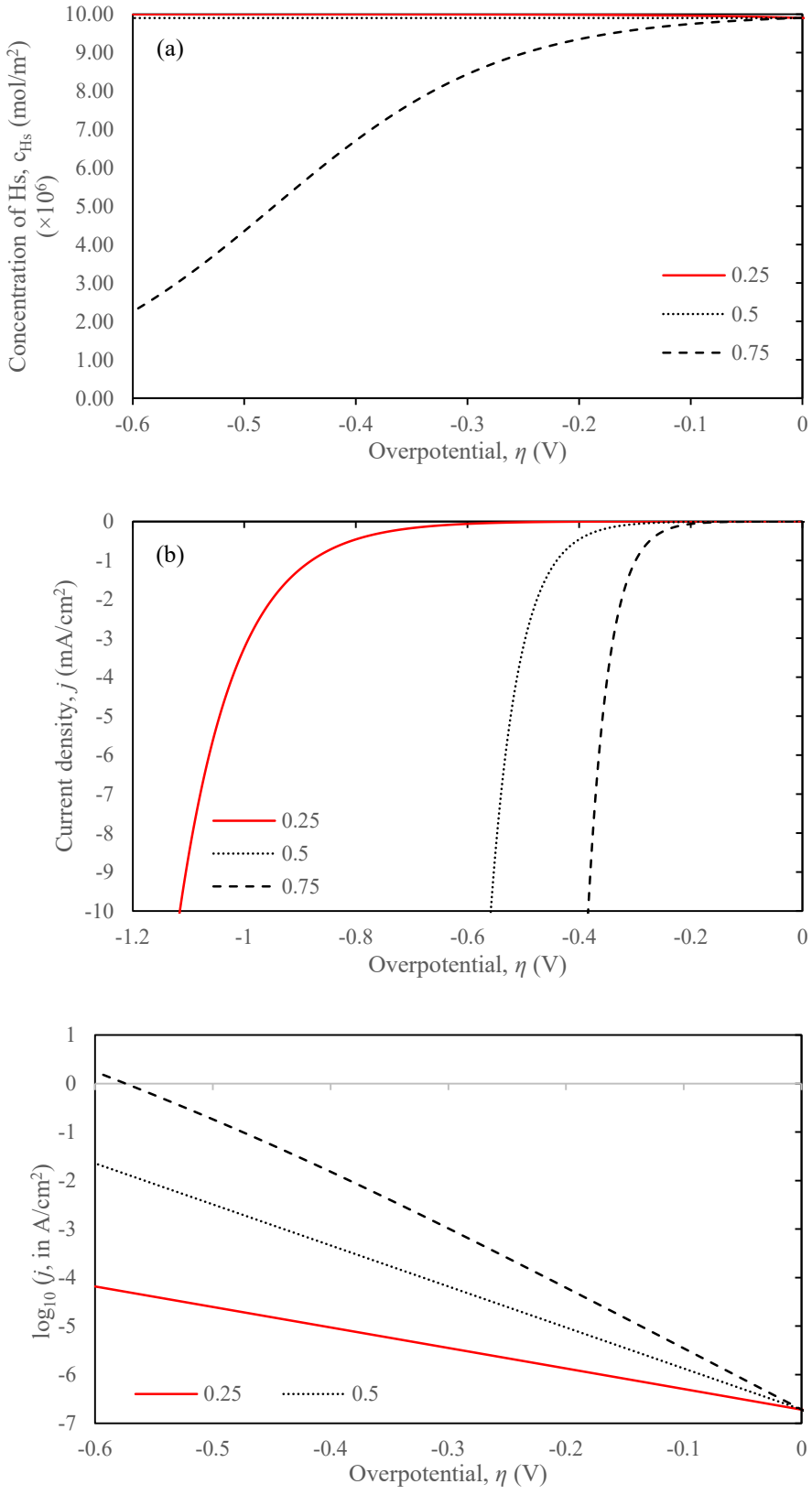

Figure 5.5: Comparison on the Heyrovsky charge transfer coefficient, β_h = (0.25, 0.5, 0.75) against overpotential, η, on the (a) concentration profile of Hs, c_{Hs} (mol/m^2) (b) current density, j (mA/cm^2) and (c) the corresponding Tafel plots in A/cm^2.

5.3 Volmer-Tafel (VT Irreversible)

The Tafel step is a non-electrochemical reaction that can be preceded by the Volmer step. Some materials exhibit HER that were dominated by VT reaction. For example, Skúlason et al. (2010) presented a Pt (111) study with VT reaction on HER. The Tafel forward reaction is written as eq. (5.7).

$$2\mathrm{Hs} \xrightarrow{K_t} \mathrm{H_2} + 2\mathrm{s} \tag{5.7}$$

$$R_t = K_t {c_{Hs}}^2 \tag{5.8}$$

The reaction rate, R_t (mol/m^2.s), written in terms of c_{Hs} is given in eq. (5.8). The effect of Tafel was visualized in figure 5.6. This simulation was modelled between ($-0.8<\eta<0.2$) V to provide a wider potential range on the HER performances in order to give better observation of the model. Hence, the consequent values of t_{end} and t_{step} used for this simulation based on the potential ranges are 1×10^6 s and 1×10^3 s respectively. Figure 5.6(a) shows the concentration profile of Hs on the electrocatalyst surface where by increasing K_t, c_{Hs} reached Γ_{max} at much lower overpotential. This indicates that more Hs was consumed during Tafel reaction to form H_2. When the K_t was decreased Hs increased at much quicker pace.

The increased formation of H_2 by the increasing of K_t is proven in higher current density showed in Figure 5.6(b) plot of j (mA/cm^2) vs overpotential, η. The corresponding tafel plots (Figure 5.6(c)) indicates that when VT reactions occur, a flat plateau (due to Tafel reaction) is observed after slope. Based on the plot provided by the simulation, the difference of the current output is approximately the same as the difference in the K_t values. For example, the K_t values projected in the figure has a difference of 1×10^3. Hence the three times higher magnitude of current output was projected when K_t is 1×10^6 compared to 1×10^3.

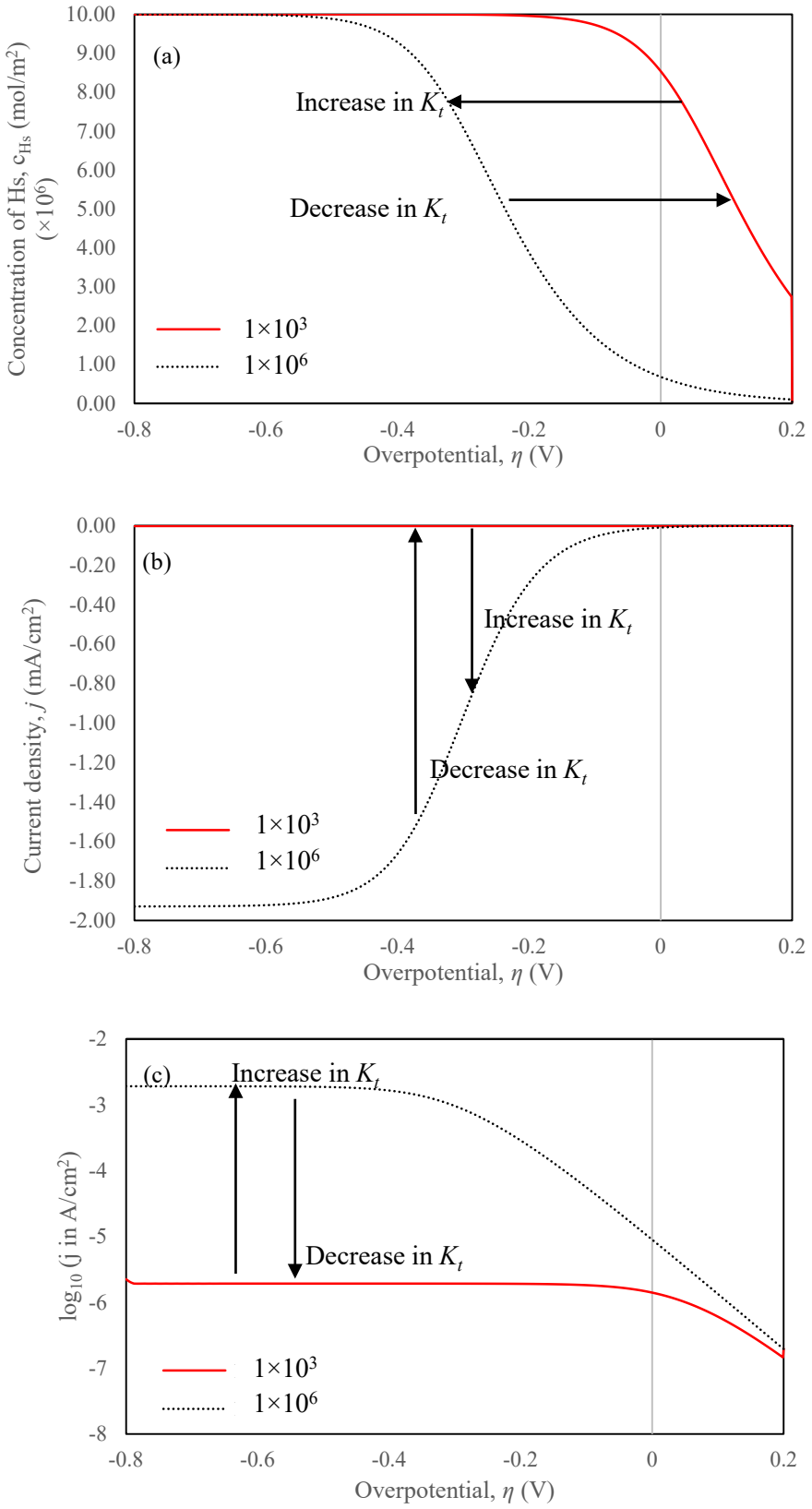

Figure 5.6: Comparison on the Tafel standard rate constant, $K_t = (1\times10^3, 1\times10^6)$ m^3/mol.s against overpotential, η, on the (a) concentration profile of Hs, c_{Hs} (mol/m^2) (b) current density, j (mA/cm^2) and (c) the corresponding Tafel slope in A/cm^2.

5.4 The VHT mechanism with reversible reaction

This part is an extension of the work presented on the irreversible VH and VT reactions, by considering their reverse reaction. The reverse reactions were written in eq. (5.9), (5.10) and (5.11) for Volmer, Heyrovsky and Tafel respectively.

$$Hs \xrightarrow{k_{-v}} H^+ + s + e^- \tag{5.9}$$

$$H_2 + s \xrightarrow{k_{-h}} H^+ + Hs + e^- \tag{5.10}$$

$$H_2 + 2s \xrightarrow{K_{-t}} 2Hs \tag{5.11}$$

Given the fact that Volmer and Heyrovsky are electrochemical and potential dependent, and the rate constants for steps and these backward reactions can be expressed as eq. (5.12) and (5.13), respectively:

$$K_{-v} = \left(k_{-v} e^{\left(-\frac{(1-\beta_v)nF}{RT}\right)(E_{(t)}-E_o)}\right) \tag{5.12}$$

$$K_{-h} = \left(k_{-h} e^{\left(-\frac{(1-\beta_v)nF}{RT}\right)(E_{(t)}-E_o)}\right) \tag{5.13}$$

Assuming the Langmuir adsorption isotherm, the reaction rates for the corresponding eq. (5.9 – 5.11) combined with eq. (5.1), (5.4) and (5.7) are presented in eq. (5.14 – 5.16):

$$R_v = (K_v c_{H^+} c_s) - (K_{-v} c_{Hs}) \tag{5.14}$$

$$R_h = (K_h c_{H^+} c_{Hs}) - \left(K_{-h} c_{H_2} c_s\right) \tag{5.15}$$

$$R_t = (K_t (c_{Hs})^2) - \left(K_{-t} c_{H_2} (c_s)^2\right) \tag{5.16}$$

In experimental electrochemistry, hydrogen electrodes are used as reference electrodes. This reference is called standard hydrogen electrode (SHE) and ideal condition where redox half reactions occurs at overpotential, $\eta = 0$. Extensive to the SHE, more robust method of

referencing called reversible hydrogen electrode (RHE) is widely used because it is pH independence (Gross, 2022).

Examples of the HER formulations with the consideration of reversible reactions were made examples by Bhardwaj et al. (2014) and Lasia (2019) for Volmer, Heyrovsky and Tafel (VHT) mechanisms written in eq. (5.17). At this point the reaction rates, $R_v = R_h = R_t = 0$. The first term is for VH mechanisms, the second term is for VT mechanisms, and the third term is for HT mechanisms.

$$\frac{K_v K_h}{K_{-v} K_{-h}} = \frac{{K_v}^2 K_t}{{K_{-v}}^2 K_{-t}} = \frac{{K_h}^2 K_t}{{K_{-h}}^2 K_{-t}} = 1 \tag{5.17}$$

In extension, by rearranging eq. (5.14 – 5.16) the kinetic ratio parameters are introduced to determine the kinetic value for the reverse step. The ratio of Volmer kinetics, κ_V, the ratio of Heyrovsky kinetics, κ_H and the ratio of Tafel kinetics, κ_T are expressed as eq. (5.18 – 5.20) respectively. In these expressions, the parameter c_{Hs0} represents the concentration of Hs when η_{RHE} = 0V.

Since $\eta_{RHE} = (E_{(t)} - E_0) = 0$, hence $k_v = K_v$, $k_{-v} = K_{-v}$, $k_h = K_h$, $k_{-h} = K_{-h}$.

$$\kappa_V = \frac{K_v}{K_{-v}} = \frac{c_{Hs_0}}{c_{H^+}(G_{max} - c_{Hs_0})} \tag{5.18}$$

$$\kappa_H = \frac{K_h}{K_{-h}} = \frac{c_{H_2}(G_{max} - c_{Hs_0})}{c_{H^+} c_{Hs_0}} \tag{5.19}$$

$$\kappa_T = \frac{K_t}{K_{-t}} = \frac{c_{H_2}(G_{max} - c_{Hs_0})^2}{{c_{Hs_0}}^2} \tag{5.20}$$

By using eq. 5.18, Figure 5.7 was plotted showing the trend of the surface concentration, c_{Hs0} when η_{RHE} = 0 V. Based on the figure it shows that $c_{Hs0} = \Gamma_{max}$ if the $\kappa_V \geq 1$ or when $k_v > k_{-v}$ (Volmer forward step dominates). And if $\kappa_V \leq 1$ or $k_v < k_{-v}$ than $c_{Hs0} < \Gamma_{max}$ (Volmer reverse

step dominates). This tell the condition of the electrode surface in between the half reaction of oxidation and reduction.

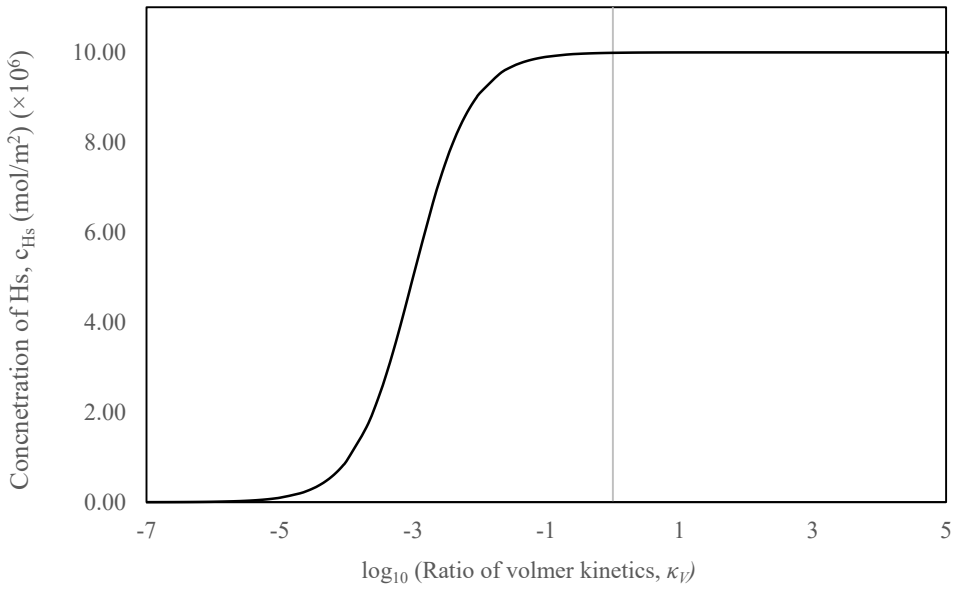

Figure 5.7: Concentration of Hs at η = 0 V, c_{Hs0} (mol/m^2) against the ratio of Volmer kinetics, κ_V.

Consequently, when standard rate constant of forward Volmer, k_v, Heyrovsky, k_h and Tafel, k_t reactions were pre-determined, and either one of the standard rate constant of the reverse reaction is given value, for example k_{-v}, then the other two parameters (k_{-h} and k_{-t}) can be calculated by solving c_{Hs0} using eq. (5.21). The written expressions for the reverse reactions standard rate constant are given as eq. (5.22 and 5.23) for Heyrovsky and Tafel step respectively.

$$c_{Hs_0} = \frac{\kappa_V c_{H^+} \Gamma_{max}}{1 + k_V c_{H^+}} \tag{5.21}$$

$$k_{-h} = K_{-h} = \frac{K_h c_{H^+} c_{Hs_0}}{c_{H_2}(G_{max} - c_{Hs_0})} \tag{5.22}$$

$$K_{-t} = \frac{K_t {c_{Hs_0}}^2}{c_{H_2}(G_{max} - c_{Hs_0})^2} \tag{5.23}$$

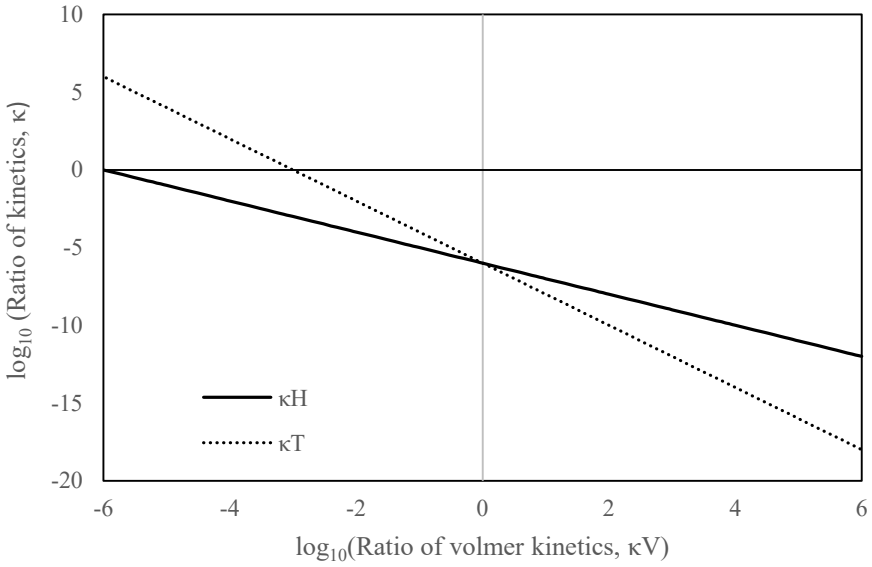

Figure 5.8: Concentration of Hs at η = 0 V, c_{Hs0} (mol/m^2) against the ratio of Volmer kinetics, κ_V.

Figure 5.8 is the plot for the corresponding kinetic ratios of Heyrovsky, κ_H and Tafel, κ_T against the kinetic ratio of Volmer, κ_V. The figure was plotted based on the calculation involving eq. (5.21 – 5.23) to obtained the rate constant values for the reverse reaction for each of the mechanistic steps involved *(*K_{-h}, and K_{-t}). For example, when κ_V = 1, then the consequence Heyrovsky kinetics ratio should be $\kappa_H = 1\times10^{-3}$ and Tafel kinetics ratio is $\kappa_T = 1\times10^{-3}$. Thus solving K_{-h}, and K_{-t}. Although, these ratios are only applicable for reversible reaction with η_{RHE} = 0 V and given that the c_{H+} = 1000 mol/m^3.

By using the formulation given above, plots of VH steps with reversible reaction for (1) surface concentration, c_{Hs} in mol/m^2 in Figure 5.8(a-b) (2) current density, j in mA/cm^2 in Figure 5.9(a-b) and (3) tafel plots a $\log_{10} j$ (in mA/cm^2) in Figure 5.11 for different k_{-v} were presented. The datasets for each of varied k_{-v} were tabulated in Table 5.3. The reversibility of VHT reactions were tested based upon the set k_{-v} values of (1×10^{-6}, 1×10^{-4}, 1×10^{-2}, 1, 1×10^{2}, 1×10^{4}) s^{-1} and κ_V of (1×10^{2}, 1, 1×10^{-2}, 1×10^{-4}, 1×10^{-6}, 1×10^{-8}) respectively.

Table 5.3: Complete dataset for varied k_{-v} used in the simulation.

Name	Dataset 1	Dataset 2	Dataset 3	Dataset 4	Dataset 5	Dataset 6
k_v ($m^3/(s \cdot mol)$)	1×10^{-4}	1×10^{-4}	1×10^{-4}	1×10^{-4}	1×10^{-4}	1×10^{-4}
k_{-v} (1/s)	1×10^{-6}	1×10^{-4}	1×10^{-2}	1×10^{0}	1×10^{2}	1×10^{4}
$\kappa_V = (k_v/k_{-v})$	1×10^{2}	1×10^{0}	1×10^{-2}	1×10^{-4}	1×10^{-6}	1×10^{-8}
k_h ($m^3/(s \cdot mol)$)	1×10^{-6}	1×10^{-6}	1×10^{-6}	1×10^{-6}	1×10^{-6}	1×10^{-6}
k_{-h} ($m^3/(s \cdot mol)$)	1×10^{2}	1×10^{-0}	1×10^{-2}	1×10^{-4}	1×10^{-6}	1×10^{-8}
$\kappa_H = (k_h/k_{-h})$	1×10^{-8}	1×10^{-6}	1×10^{-4}	1×10^{-2}	1×10^{0}	1×10^{2}
β_v	0.5	0.5	0.5	0.5	0.5	0.5
α_v	0.5	0.5	0.5	0.5	0.5	0.5
β_h	0.5	0.5	0.5	0.5	0.5	0.5
α_h	0.5	0.5	0.5	0.5	0.5	0.5

The c_{Hs} profiles visualize in Figure 5.9 shows different trends for different k_{-v} values. The concentration of Hs, c_{Hs} start with Γ_{max} when k_{-v} <1 at positive overpotentials and decreased to 9.9×10^{-6} mol/m^2 while the c_{Hs} start at 0 on k_{-v} >1. This indicates that when the reverse reaction is fast, low Hs are observed when the electrode began the reduction process. While low k_{-v} indicates more Hs are on the electrocatalyst that were not oxidized. This finding is similar and thus supports to the plot of Figure 5.7.

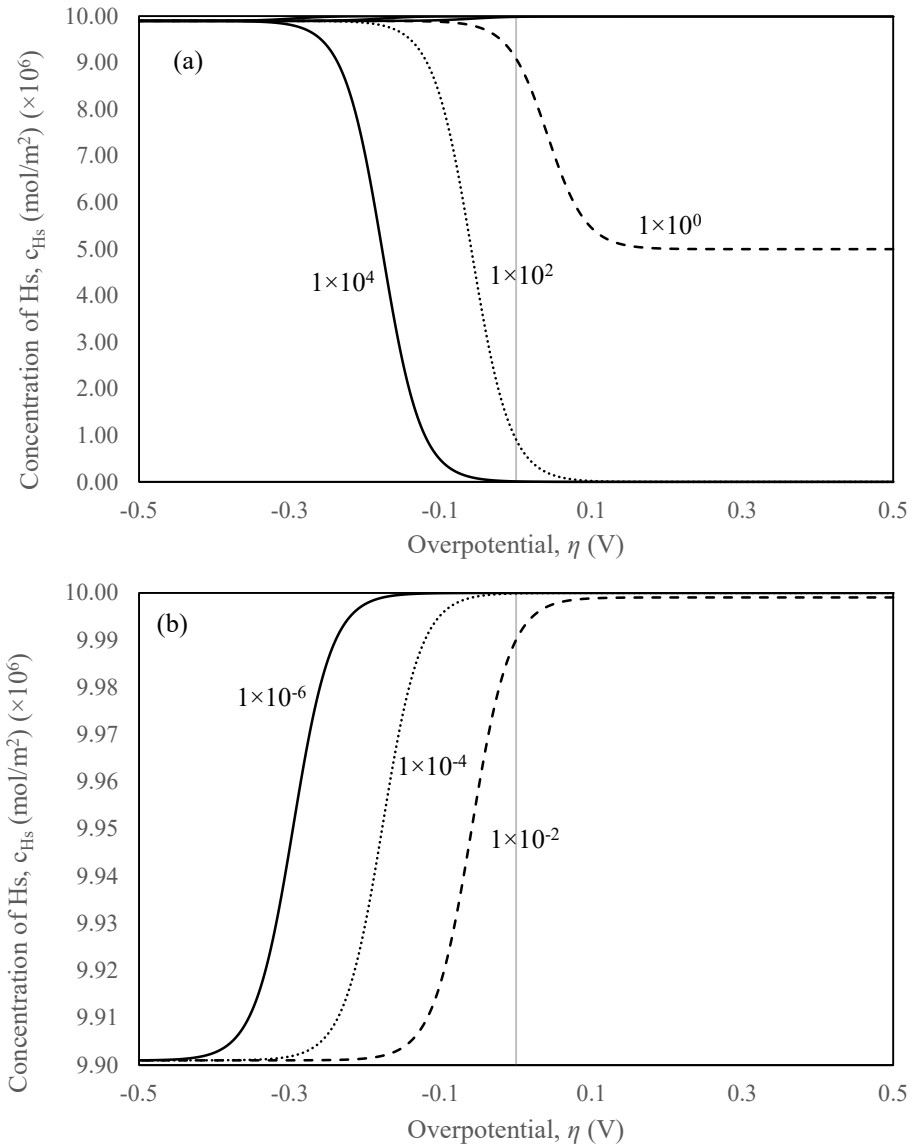

Figure 5.9: Plot of different k_{-v} ranging from (a) 1×10^0 s^{-1} to 1×10^4 s^{-1} and (b) the close-up plot ranging from (1×10^{-6} to 1×10^{-2}) s^{-1} for concentration of Hs, c_{Hs} (mol/m^2) against the overpotential, η (V).

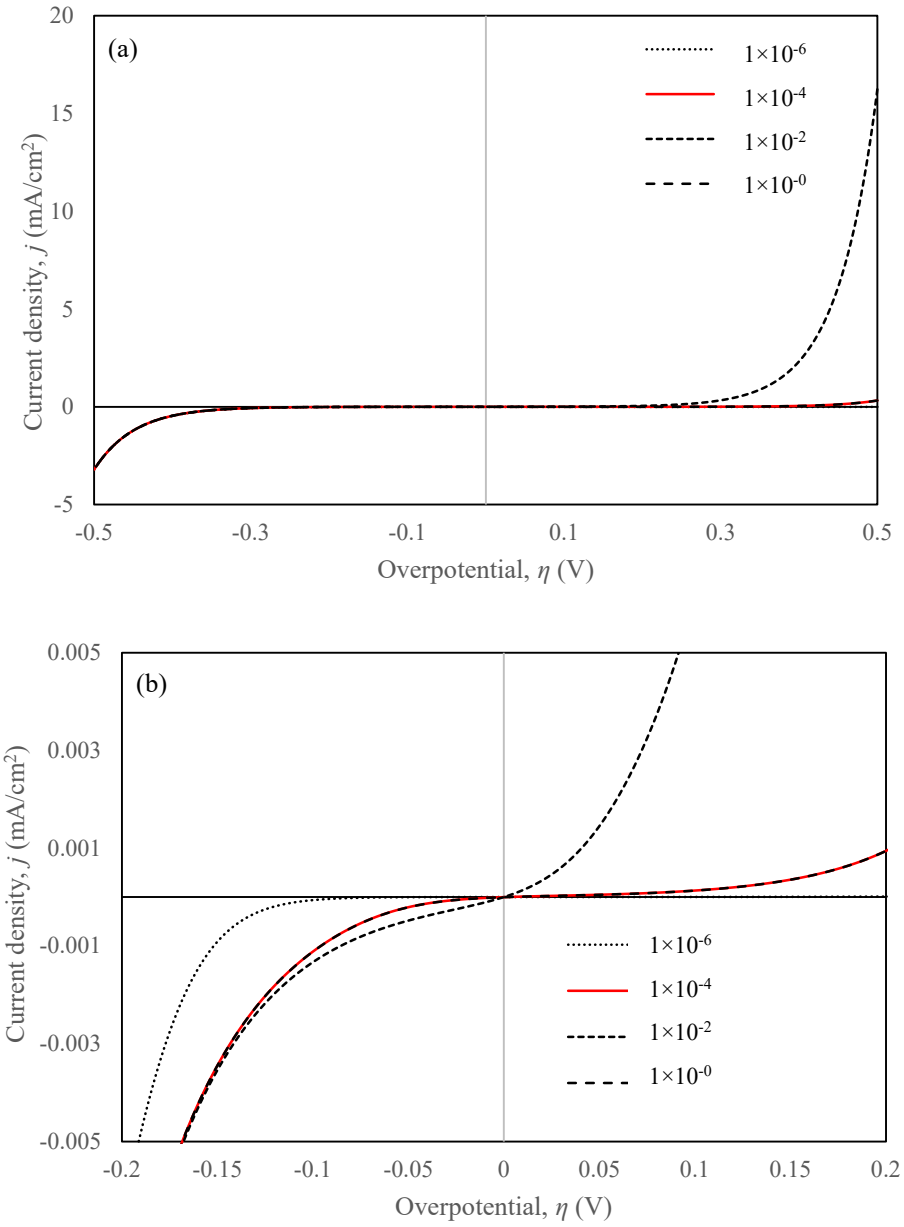

Figure 5.10: The corresponding current density, j (mA/cm^2) of Figure 6.9 for (a) k_{-v} ranging from (1×10^{-6} to 1) s^{-1} and (b) the close-up plot at lower overpotentials, η (V).

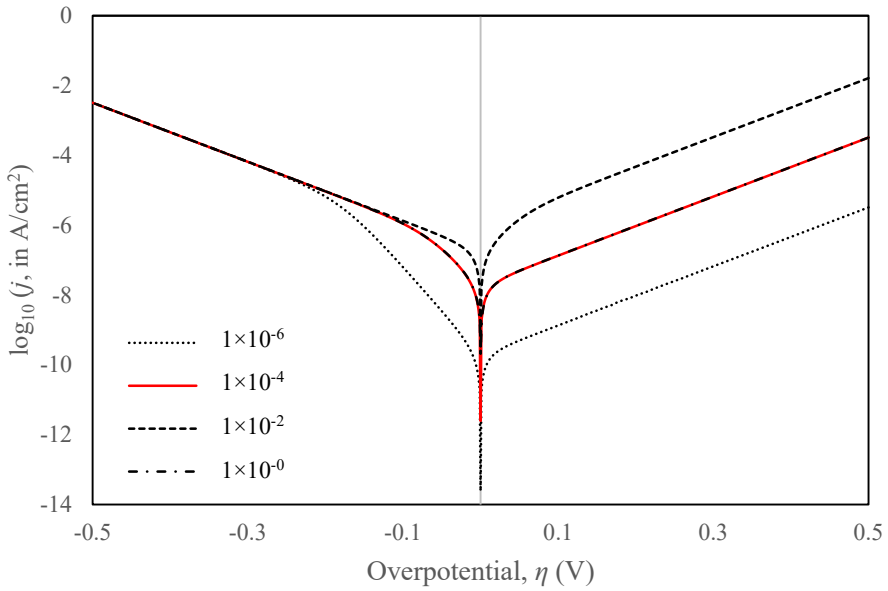

Figure 5.11: The corresponding Tafel plots in A/cm^2 for Figure 6.10.

When projected to j (mA/cm^2) vs overpotential, η (Figure 5.10) and its corresponding Tafel plots (Figure 5.11) interesting trends were observed. A couple of k_{-v} values exhibit similar current output hence similar tafel plots. For example, when $k_{-v} = 1\times10^{-4}$ s^{-1} and $k_{-v} = 1$ s^{-1}, the current output overlays each other indicating similar behavior albeit different c_{Hs} profiles. This numerical ambiguity is very similar to permutations of kinetic parameters (discussed in next subchapter 5.5). The exhibit of permutation trends was observed between dataset 1 and 6, dataset 2 and 5, and dataset 3 and 4. The difference is only by the value of k_{-v} and consequently k_{-h}. It was observed that the overlays are only true to symmetrical cases where charge transfer coefficient is 0.5. It is not applicable for materials with charge transfer coefficient of $\alpha \neq 0.5$, $\beta \neq 0.5$.

Observation on the effect of k_{-v} on the current output shows that for Dataset 1, steeper slope is exhibits at low overpotential compared to dataset 2 and dataset 3 before the same trends are observed for dataset 4, 5 and 6. Steeper slopes can be obtained by employing $k_{-v} < 1\times10^{-6}$ s^{-1} or $k_{-v} > 1\times10^{4}$ s^{-1}. This will directly affect the plot on the HOR region. When steeper

slope is obtained on the HER region, then lower current output is observed in the HOR region. HOR are not elaborated in this discussion and could be taken into consideration in future work.

5.4.1 Comparison between reversible and irreversible reactions on HER performances

Comparisons were made on the effect of reversibility and irreversibility in VH steps as example. Based upon the results presented in the previous sections, specifically in subchapter 5.2 and 5.4, the reversible reaction proved to have varying effect in the lower overpotential region of HER region. Figure 5.12 was plotted using the parameters provided in Table 5.4.

Table 5.4: VH dataset for Figure 5.11.

Name	Reversible	Irreversible
k_v ($m^3/(s \cdot mol)$)	1×10^{-4}	1×10^{-4}
k_{-v} (1/s)	1×10^{-1}	0
$\kappa_V = (k_v/k_{-v})$	1×10^{-3}	0
k_h ($m^3/(s \cdot mol)$)	1×10^{-6}	1×10^{-6}
k_{-h} ($m^3/(s \cdot mol)$)	1×10^{-3}	0
$\kappa_H = (k_h/k_{-h})$	1×10^{-3}	0
K_t ($m^2/(s \cdot mol)$	0	0
K_{-t} ($m^5/(mol^2 \cdot s)$)	0	0
β_v	0.5	0.5
α_v	$1-\beta_v$	0.5
β_h	0.5	0.5
α_h	$1-\beta_h$	0.5

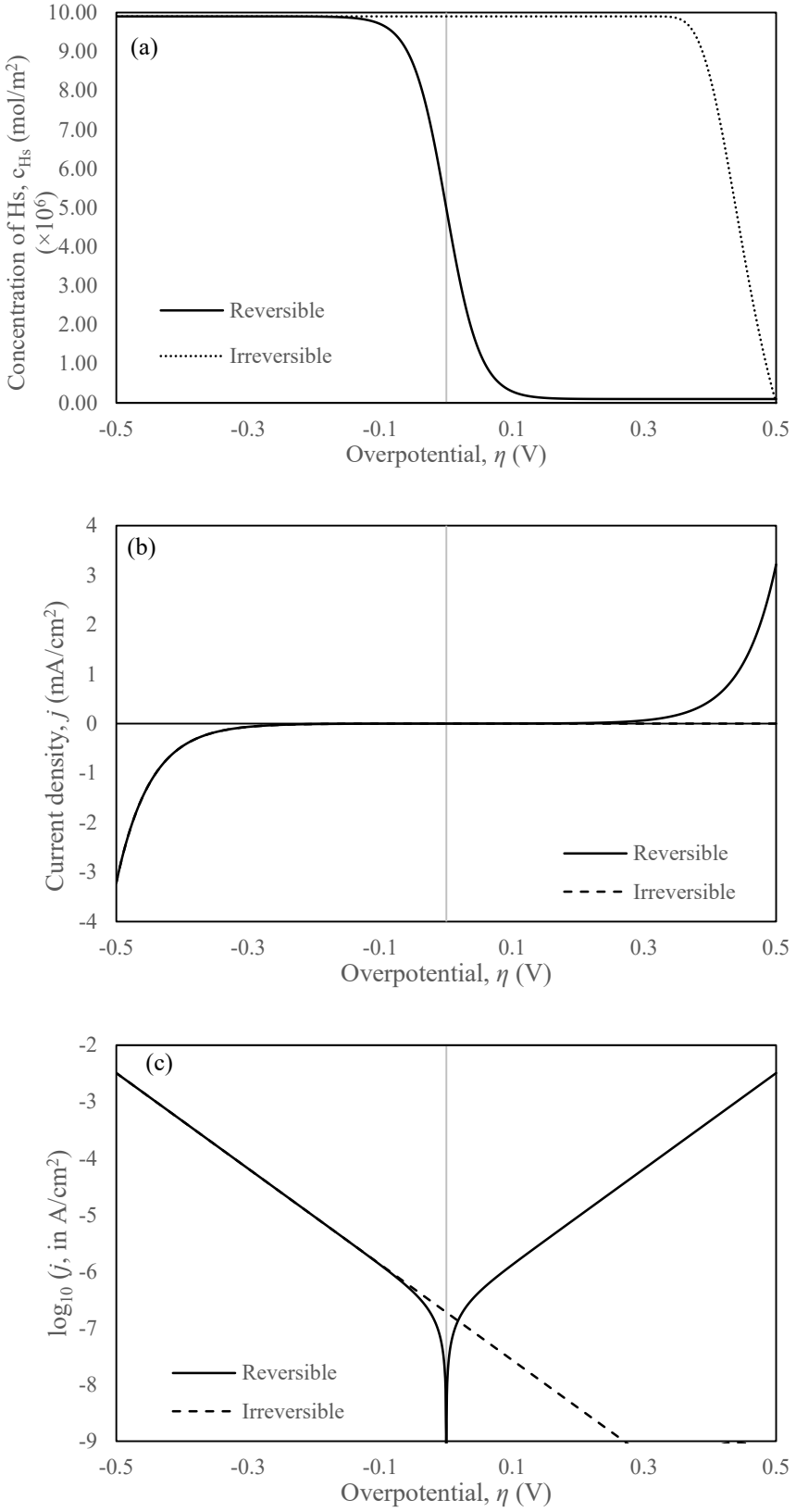

Figure 5.12: Comparison on the VHT reversible and irreversible reactions on the (a) concentration profile of Hs, c_{Hs} (mol/m^2) (b) current density, j (mA/cm^2) and (c) the corresponding Tafel plots in A/cm^2 against overpotential, η (V).

Figure 5.12 (a) provide the information on the c_{Hs} profiles for both considered reactions of reversible and irreversible. The formation of Hs occurred at much later due to the reverse reactions. While for irreversible reactions the formation of Hs due to the Volmer reaction happens almost instantaneously. Projected onto the current density plot in Figure 5.12(b), 0 mA/cm^2 was generated when $\eta > 0$ V while retaining similar plot of current output when $\eta < 0$ V. The slopes near the $\eta = 0$ V on both HER side and HOR side due to the effect of the reverse reactions was clearly visualized by the Tafel plots in figure 5.12(c) implying the significant effect of reverse reactions near lower overpotential.

5.5 Kinetic parameters permutation

Permutation happens when two sets of solutions exist in determining the kinetic parameters. The parameters can be inversed as written in eq. (5.24).

$$k_v \leftrightarrow k_h, k_{-v} \leftrightarrow k_{-h}, k_t \leftrightarrow k_{-t}, \beta_v \leftrightarrow \beta_h \tag{5.24}$$

Table 5.5: VH permutated dataset for Figure 5.12.

Name	Dataset 1	Dataset 2
k_v (m³/(s·mol))	1×10^{-4}	1×10^{-6}
k_{-v} (1/s)	1×10^{-1}	1×10^{-3}
$\kappa_V = (k_v/k_{-v})$	1×10^{-3}	1×10^{-3}
k_h (m³/(s·mol))	1×10^{-6}	1×10^{-4}
k_{-h} (m³/(s·mol))	1×10^{-3}	1×10^{-1}
$\kappa_H = (k_h/k_{-h})$	1×10^{-3}	1×10^{-3}
K_t (m²/(s·mol)	0	0
K_{-t} (m⁵/(mol²·s))	0	0
β_v	0.5	0.5
α_v	1-β_v	0.5
β_h	0.5	0.5

α_h	1-β_h	0.5

Figure 5.13 shows the plots for two datasets where Dataset 2 is the permutation of Dataset 1 (values in Table 5.5). The example given is a symmetrical charge transfer coefficient of $\beta_v = \beta_h = 0.5$ for VH reversible reactions. Figure 5.13(b) and figure 5.13(c) that show the plots for the current density, j (mA/cm^2) and the corresponding Tafel plot respectively proved the similar HER performances with equal current output in A for both dataset 1 and dataset 2.

Where else for the concentration of Hs, c_{HS} (mol/m^2) depicted in figure 5.12(a) shows that the permutation of kinetic parameters has reverse profiles to each other. These permutated sets produce similar number in terms of current. The only difference being is the change of the hydrogen surface coverage, θ_H to (1-θ_H). This ambiguity arises from solving the numerical expressions and is not able to be distinguish experimentally. Though Lasia (2019) had mentioned that it is generally accepted that the c_{Hs} would increase with the increase of negative potential. But this has never been proven.

In conclusion, Table 5.6 shows the summary of VHT kinetic parameters effects on the concentration of Hs, c_{Hs}, overpotential, η, and Tafel plots. Based on the parametric study conducted in this chapter increasing the standard rate constant of either V, H and T would consequently increase the overpotential and the current density, j. While the charge transfer coefficient have no effects on the exchange current density, j_0. But the current density, j increase with the increase of the charge transfer coefficient.

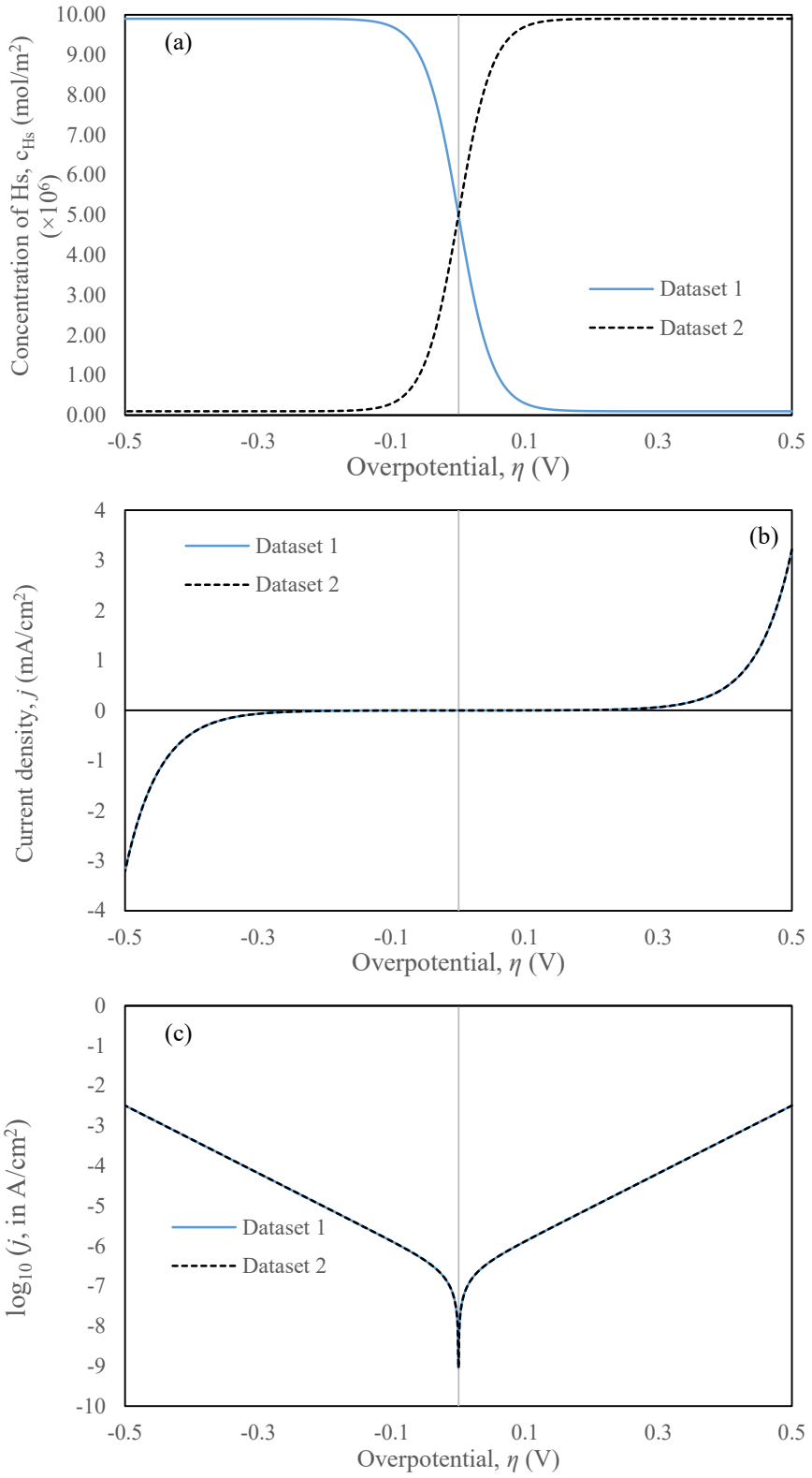

Figure 5.13: Comparison on the permutated datasets on the (a)concentration profile of Hs, c_{Hs} (mol/m^2), (b) current density, j (mA/cm^2) and the corresponding (c) Tafel plots in A/cm^2.

Table 5.6: Summary on the effect of VHT kinetic parameters on the concentration of Hs, c_{Hs}, overpotential, η and Tafel plots.

Kinetic parameters		Concentration of Hs, c_{Hs} (mol/m^2)	Overpotential @10mA/cm^2 (η_{10})	Tafel plots	
				$\log_{10}$ (current density, j in mA/cm^2)	Exchange current density, j_0)
Volmer (v)					
Standard rate constant, k_v	Increase k_v	Increase	Increase	Increase	Increase
	Decrease k_v	Decrease	Decrease	Decrease	Decrease
Charge transfer coefficient, β_v	Increase β_v	Increase	Increase	Increase	No change
	Decrease β_v	Decrease	Decrease	Decrease	
Heyrovsky (h)					
Standard rate constant, k_h	Increase k_h	Decrease	Increase	Increase	Increase
	Decrease k_h	Increase	Decrease	Decrease	Decrease
Charge transfer coefficient, β_h	Increase β_h	Decrease	Increase	Increase	No change
	Decrease β_h	Increase	Decrease	Decrease	
Tafel (t)					
Standard rate constant, K_t	Increase k_t	Increase	Increase	Increase	Increase
	Decrease k_t	Decrease	Decrease	Decrease	Decrease

5.6 Chapter Summary

This chapter described in detail the effect of Volmer step, Heyrovsky step and Tafel step via the implementation of standard rate constant k_v, k_h and k_t respectively. In addition, the effect of charge transfer coefficient for Volmer step and Heyrovsky step value were also presented. The increase and decrease of these parameters were explained in terms of the surface concentration, c_{Hs} (mol/m^2), current density, j and Tafel plots. This parametric study would provide readers with sufficient information to determine the kinetic parameters involved in any experimental HER results.

The formulation of VHT with reversible reaction was discussed by varying the Volmer reverse step as an example. This model is very helpful in estimating the reverse reaction kinetics if the data on HOR region is not available. Comparison between HER plots of irreversible and reversible steps are given to show readers the distinctive difference between these two assumptions.

Some experimental data could only be fitted by taking reversibility into consideration. This happens in our study on TiC/taC:Pt (discussed in Chapter 6), where the experimental data was only limited to HER region, hence the reverse kinetic could not be identified. Furthermore, the slope is much too steep at low overpotential that it was impossible to fit the data without reversible reaction. With the help of the reversible reaction formulation, the reverse kinetic could be estimated and the steep slope could be fit perfectly.

The idea of permutation was discussed with few examples given. Permutation occurs when two sets of parameters were directly inverse with each other, thus exhibiting the same current output but inverse surface concentration.

CHAPTER 6

HYDROGEN EVOLUTION REACTION ANALYSIS OF ARRAYED PLATINUM-DOPED TETRAHEDRAL AMORPHOUS CARBON ON TITANIUM CARBIDE

6.1 Introduction

An FEM model based on the VHT mechanistic steps was simulated. The kinetic parameters for TiC and taC:Pt were obtained via the 1D model simulation to justify the results recorded in experimentation by Glandut et. al (2015). This was done by comparing the experimental Tafel plots for solitary TiC and taC:Pt with the Tafel plots obtained from the simulation as shown Figure 6.1.

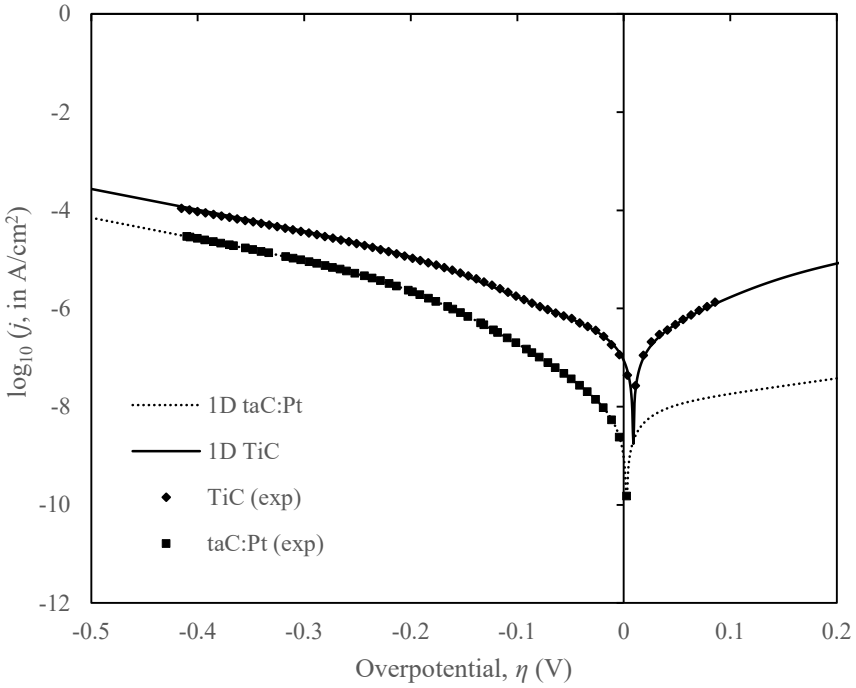

Figure 6.1: Tafel plots plot of fitted line from simulation and the experimental curve for $\log_{10}$ of current density, (j in A/cm^2) against the cell overpotential, η in V.

The model adopted the formulation that was described in Chapter 3.2 assuming reversible reactions. 1D model is deemed sufficient to model a solitary electrode as homogeneity was

assumed across the surface. The values of the kinetic parameters were listed in Table 6.1. The reverse standard rate constant for Volmer, Heyrovsky and Tafel (k_{-v}, k_{-h} and k_{-t}) were extrapolated from the limited experimental plots. Based on the works conducted in Chapter 5, the range of overpotential used in this section is ($-0.5 < \eta/V < 0.2$).

Table 6.1: Kinetics parameters of TiC electrode and taC electrode

Electrode	**TiC**	**taC:Pt**
k_v ($m^3/(mol \cdot s)$)	6.1×10^{-7}	4.8×10^{-8}
k_{-v} (1/s)	8×10^{-3}	4.8×10^{-5}
k_h (($m^3/(mol \cdot s)$)	1.09×10^{-5}	2.8×10^{-6}
k_{-h} (($m^3/(mol \cdot s)$)	1.09×10^{-3}	2.8×10^{-3}
k_t ($m^2/(mol \cdot s)$)	1×10^{2}	0
k_{-t} ($m^5/(mol^2 \cdot s)$)	1×10^{3}	0
β_v	0.77	0.82
β_h	0.25	0.25
Area (m^2)	7.5×10^{-9}	2.5×10^{-9}

It was noticed that on experimental TiC Tafel plots a small hump occurred at $\eta < 0.05$ V. This is due to Tafel contribution. To fit the experimental TiC Tafel plots, Tafel reactions was added in the formulation to model the slight hump. Since η_{RHE} deviates slightly from 0 V, the kinetic parameters obtained using the reversible reactions formulation in Chapter 5.4 could not perfectly fit the experimental plot. Hence minor changes were applied on the reverse kinetics parameters to have a better fit of the plot. Comparison between the kinetic parameters value were tabulated in Table 6.2 assuming for Set 1: VH reversible reactions using eq. (5.18 – 5.22) and Set 2: VHT reversible reactions.

Table 6.2: Different sets of kinetic parameters for TiC

Parameters	Set 1	Set 2
k_v (m³/(mol·s))	6.1×10^{-7}	6.1×10^{-7}
k_{-v} (1/s)	6.1×10^{-3}	8×10^{-3}
k_h ((m³/(mol·s))	1.09×10^{-5}	1.09×10^{-5}
k_{-h} ((m³/(mol·s))	1.09×10^{-3}	1.09×10^{-3}
k_t (m²/(mol·s))	0	1×10^{2}
k_{-t} (m⁵/(mol²·s))	0	1×10^{3}
β_v	0.77	0.77
β_h	0.25	0.25

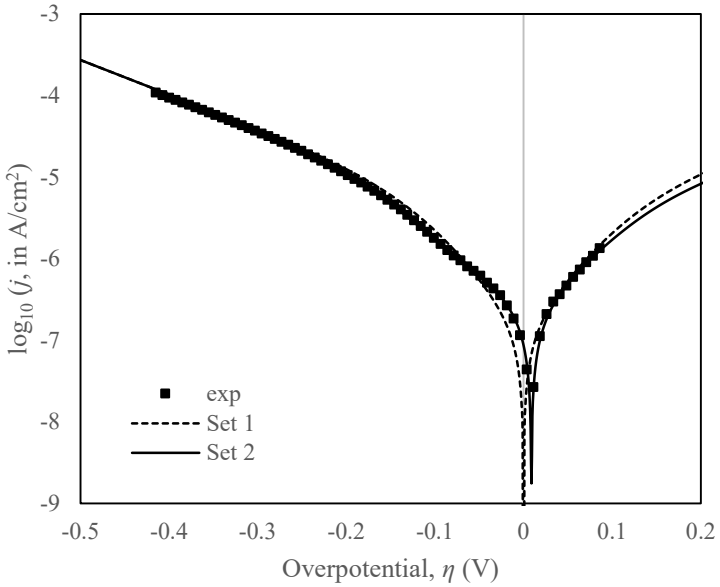

Figure 6.2: Comparison between simulated TS for TiC assuming VH and VHT reversible reactions.

Figure 6.2 shows the plotted Tafel plots drawing the comparison from Set 1 and Set 2 of Table 6.2. The perfect fitting on Set 2 when VHT was applied shows that Tafel reactions occurred on the surface of TiC electrode during HER. Based on the obtained kinetic parameters for TiC and taC:Pt in Table 6.1, the c_{Hs} (mol/m^2) vs η (V) and the j (mA/cm^2) vs η (V) were plotted in Figure 6.3 (a) and (b). These provides new information in understanding the behavior and the properties of the studied electrocatalyst.

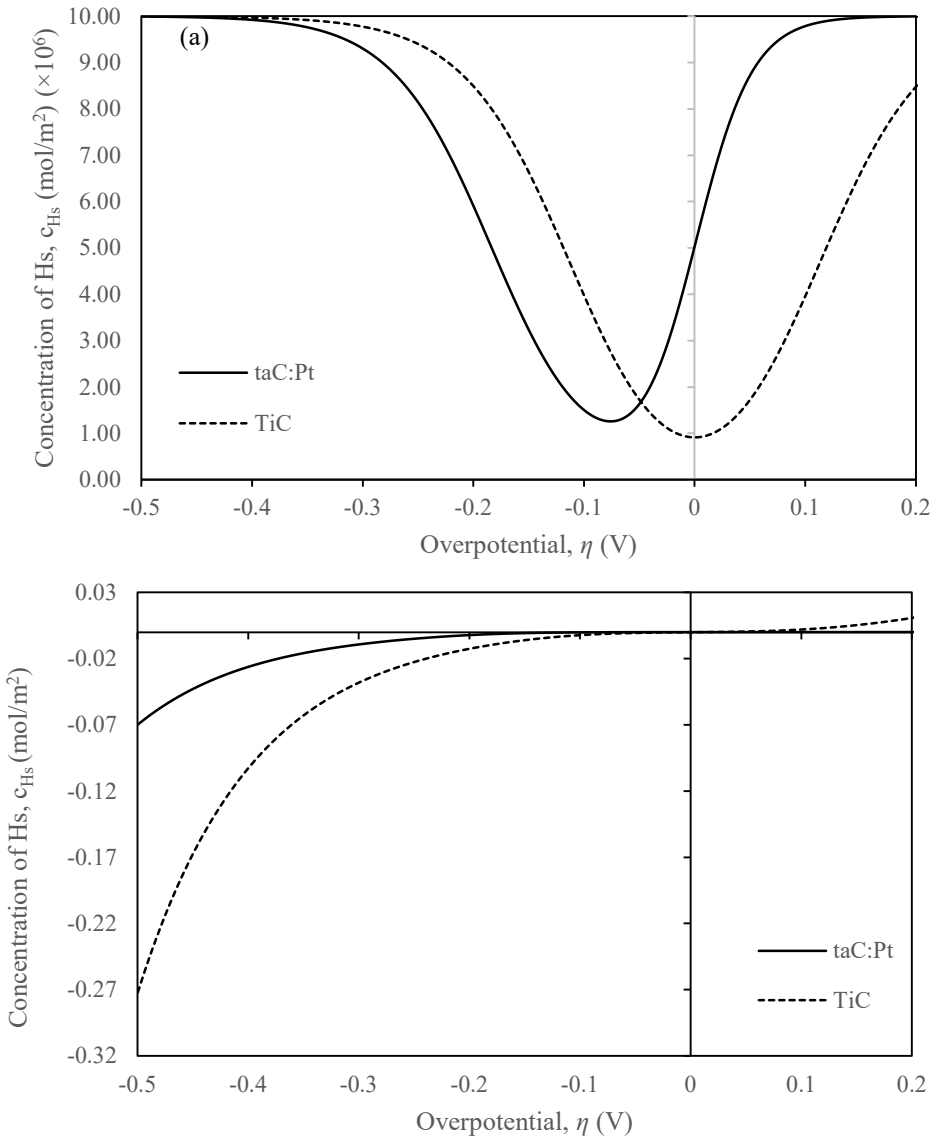

Figure 6.3: Corresponding (a) c_{Hs} (mol/m^2) vs η (V) and (b) the j (mA/cm^2) vs η (V) for TiC and taC:Pt from tafel plots Figure 6.2.

The c_{Hs} plots clearly shows that on TiC surface, the Hs was consumed quicker compared to taC:Pt surface. Due to the faster rate, the output currents are slightly higher indicating that TiC shows better catalytic properties than taC:Pt. The current density, j recorded are about -0.07 mA/cm^2 at -0.5 V for taC:Pt and -0.27 mA/cm^2 for TiC at the similar potential. Based on the 1D simulation results given for both TiC and taC:Pt, the author was utterly convinced

of the adopted VHT formulation in the simulation. The model that was developed here could provide better insight on the electrocatalyst properties and their catalytic behavior.

6.2 The effect of surface diffusion

One of the main reason for using FEM in this work is to study the effect of surface diffusion on the catalyst performances. Figure 6.4 shows the illustration of the VH mechanistic steps with the effect of surface diffusion. In recent years, multiple studies often presented a better performing catalyst of hybrid or composites materials. A lot of work has provided significant information on the catalytic activity by pointing out the change of electronic structure and increase of active sites via microscopic view for eg: Protopopova et al., (2015), Qu et al., (2017) and Liu et al., (2021). Many attributed the enhanced catalytic activity to the formation of bonding between the substrate and the doped compounds onto the electrodes.

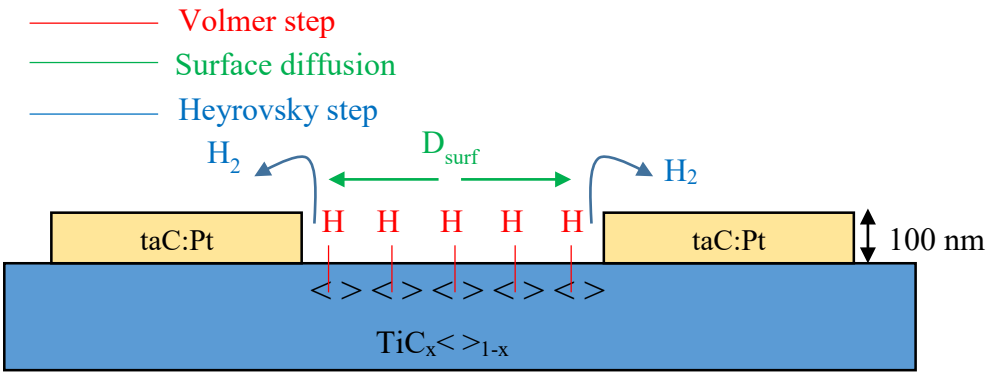

Figure 6.4: Illustration of VH steps with surface diffusion

Only selective cases can be model using FEM. Additionally, given the arrayed structure and the clear separation surface profiles (border) between TiC and taC:Pt catalyst, it provides a huge opportunity to geometrically modelled the electrocatalyst. The macroscopic view of the catalyst was visualized by studying the effect of diffusivity on the c_{Hs} on the surface.

Based on the work done using 1D model in the previous section to verify the kinetics parameters of TiC and taC:Pt, an extensive 2D model was developed to observed the effect of surface diffusion on the novel TiC/taC:Pt catalyst. In this study, taC:Pt have a thickness of approximately 100 nm that was deposited onto the TiC surfaces (as shown in Figure 6.5).

Initially the assumption made was the characteristics of the deposited taC:Pt on TiC support remains the same which mean the kinetics parameters in Table 6.1 were unchanged. This assumption was made based on a study by Yang et al. (2020) which states that the substrate interactions have no effect on the intrinsic HER activity, which is different from the behaviors reported for single- or few-atom catalysts. Yang further added that any metal nano-carbons with at least two layers of thickness would be exempted from the impact of substrates.

The effect of surface diffusion, D_{surf} in m^2/s on the surface of the TiC and taC:Pt, was discussed in this section. The kinetic parameters employed in this 2D simulations are based upon the results obtained in 1D simulation for solitary TiC and taC:Pt catalyst while taking permutation (discussed in Chapter 5.4) into considerations. The dataset for the kinetic permutations were tabulated in Table 6.2. The surface diffusion of TiC and taC:Pt used in this simulation are both 1×10^{-8} m^2/s. Eq. (3.35 – 3.37) were used to calculate the current density, j (mA/cm^2) in this section.

Table 6.3: Kinetic parameters for different datasets with permutation combinations.

Electrode	Dataset 1		Dataset 2		Dataset 3		Dataset 4	
	TiC	taC:Pt	TiC	taC:Pt	TiC	taC:Pt	TiC	taC:Pt
k_v ($m^3/(mol \cdot s)$)	1.1×10^{-6}	4.8×10^{-8}	1.1×10^{-6}	2.8×10^{-6}	1.1×10^{-5}	4.8×10^{-8}	1.1×10^{-5}	2.8×10^{-6}
k_{-v} (1/s)	1.1×10^{-2}	4.8×10^{-5}	1.1×10^{-2}	2.8×10^{-3}	1.1×10^{-3}	4.8×10^{-5}	1.1×10^{-3}	2.8×10^{-3}
k_h ($(m^3/(mol \cdot s))$	1.1×10^{-5}	2.8×10^{-6}	1.1×10^{-5}	4.8×10^{-8}	1.1×10^{-6}	2.8×10^{-6}	1.1×10^{-6}	4.8×10^{-8}
k_{-h} ($(m^3/(mol \cdot s))$	1.1×10^{-3}	2.8×10^{-3}	1.1×10^{-3}	4.8×10^{-5}	1.1×10^{-2}	2.8×10^{-3}	1.1×10^{-2}	4.8×10^{-5}
k_t ($m^2/(mol \cdot s)$)	1.0×10^{-4}	0	1.0×10^{-4}	0	1.0×10^{-4}	0	1.0×10^{-4}	0
k_{-t} ($m^5/(mol^2 \cdot s)$)	1.0×10^{-2}	0	1.0×10^{-2}	0	1.0×10^{-2}	0	1.0×10^{-2}	0
β_v	0.77	0.82	0.77	0.25	0.25	0.82	0.25	0.25
β_h	0.25	0.25	0.25	0.82	0.77	0.25	0.77	0.82

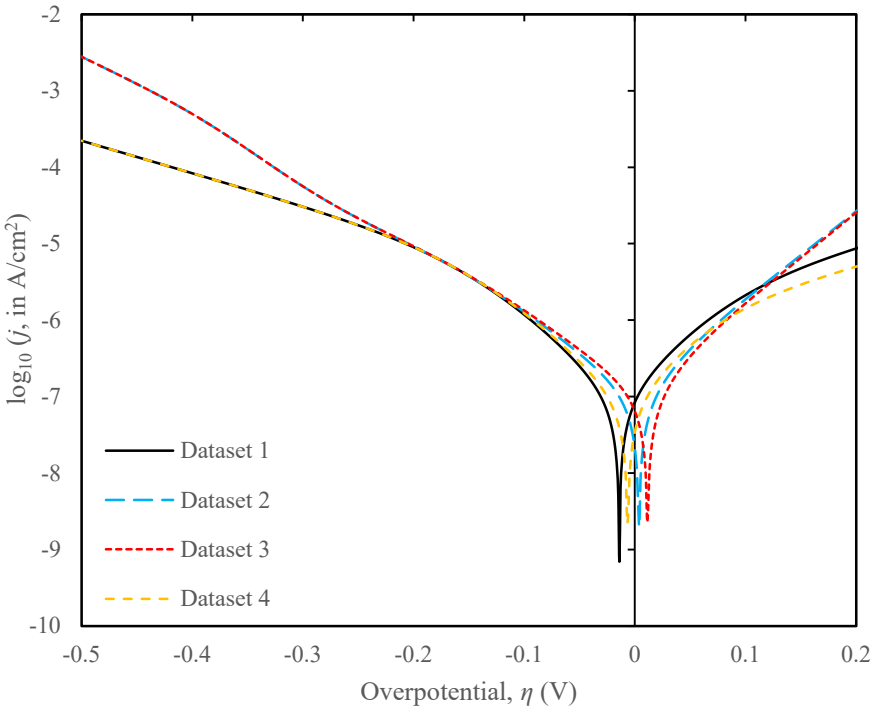

Figure 6.5: Tafel plots for Datasets (Table 6.3) with different permutations kinetic parameters.

Figure 6.5 shows the Tafel plots for each of the given dataset where Dataset 1 was a combination of the initial values determined from the 1D simulation for both TiC and taC:Pt. The summary of the additional three datasets are listed as follows.

1. Dataset 2: (initial values for TiC and permutated values for taC:Pt)
2. Dataset 3: (permutated values for TiC and initial values for taC:Pt)

3. Dataset 4: (permutated values for TiC and permutated values for taC:Pt)

Based on the graph, the use of initial kinetic parameters on both surface TiC and taC:Pt on 2D does not offer any significant changes on the Tafel plots. Given the reversible reactions, changes are observed on the $\eta_{RHE} \neq 0$ V that was due to numerical ambiguity of the solution. Otherwise dataset 1 and 4 shows similar slopes where no possible changes on the current are observed. While dataset 2 and 3 show increased in current output from $\eta < -0.3$V with similar trends.

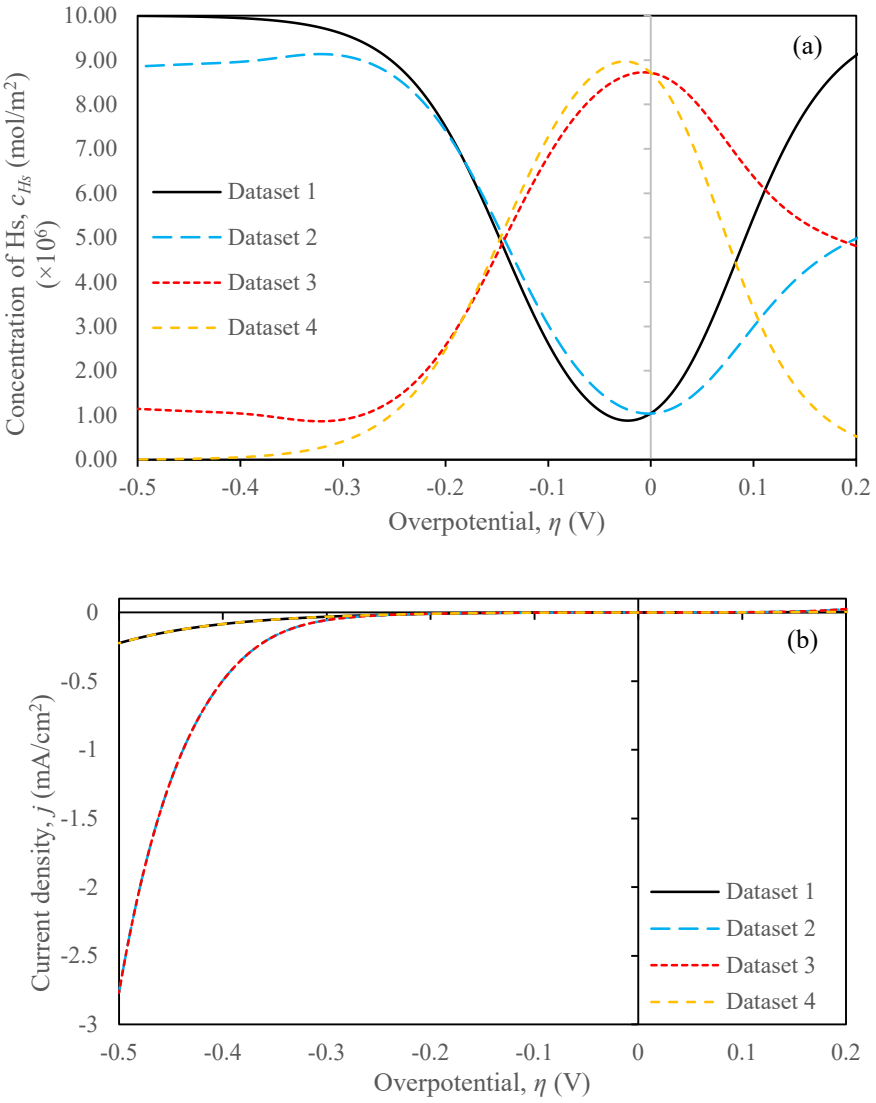

Figure 6.6: Corresponding (a) c_{Hs} (mol/m^2) vs η (V) and (b) the j (mA/cm^2) vs η (V) for TiC and taC:Pt from Tafel plots Figure 6.5.

The corresponding plots for the concentration of Hs against the potential, c_{Hs} (mol/m^2) vs η (V) was provided in Figure 6.6(a) and the current density, j (mA/cm^2) vs η (V) in Figure 6.5(b). The concentration profiles were recorded at the center (point between taC:Pt and TiC) of the modelled electrode as shown in Figure 3.15(b). The plotted c_{Hs} and j clearly shows that dataset 4 is a permutation of dataset 1 and dataset 3 is the permutation of dataset 2. This is because the curves are symmetrical between the permutated sets, respectively. More interestingly, datasets 2 and 3 seem to show clear increased in current output albeit changes only occurred at η < -0.3 V.

Table 6.4: Set of surface diffusion values adopted in the simulation for surface TiC and taC:Pt

Set	Variation 1	Variation 2	
	D_{TiC} (m^2/s) = D_{taC} (m^2/s)	D_{TiC} (m^2/s)	D_{taC} (m^2/s)
Set 1	1×10^{-14}	1×10^{-12}	1×10^{-12}
Set 2	1×10^{-12}	1×10^{-12}	1×10^{-6}
Set 3	1×10^{-10}	1×10^{-6}	1×10^{-12}
Set 4	1×10^{-8}	1×10^{-6}	1×10^{-6}
Set 5	1×10^{-6}	-	-
Set 6	1×10^{-4}	-	-

Consequently, elaboration on the effect of surface diffusion will be given herewith for dataset 1 and 2. There were two variations of test performed on the surface diffusivity. The first is to analyse the effect of surface diffusivity when $D_{TiC} = D_{taC}$ for 1×10^{-14}, 1×10^{-12}, 1×10^{-10}, 1×10^{-8}, 1×10^{-6}, and 1×10^{-4} m^2/s. Figure 7.7 shows the Tafel plots for (a) Dataset 1 and (b) Dataset 2 employing variation 1 on D_{surf}. Based on the plots in Figure 6.7(a), there were no visible changes on the current output for every tested D_{surf} of set (1 – 6). However, changes were observed when dataset 2 were tested with different sets of D_{surf}. By increasing the D_{surf} from 1×10^{-14} m^2/s to 1×10^{-4} m^2/s, there were noticeable increase of current density branching from η < -0.25 V. For example, when the overpotential @-500 mV the current densities

recorded are -0.3, 0.5, -14.7, and -18.5 mA/cm^2 respectively. Significant increase of current output was attributed to the fast surface diffusion, aiding the Hs to be adsorb and desorb rapidly. But as pointed out in Figure 6.7(b) any further decrease beyond 1×10^{-14} m^2/s would not yield any changes, similarly any further increase beyond 1×10^{-14} m^2/s would not have increase the current output.

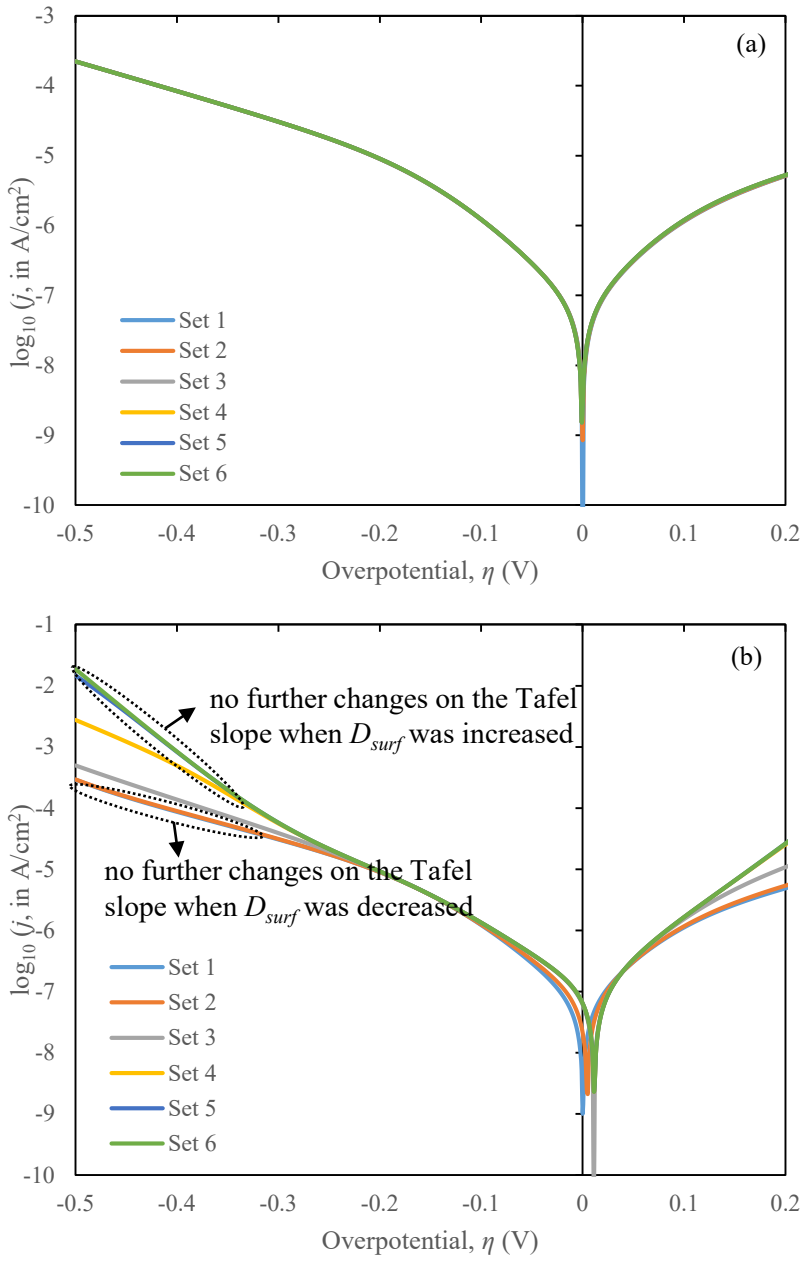

Figure 6.7: Tafel plots for (a) Dataset 1 and (b) Dataset 2 while employing variation 1 on surface diffusion, D_{surf} values

With this new information, the surface diffusion was tested using the value given in variation 2 (Table 6.4). Based on variation 1, knowing that no significant changes occurred when $D_{surf} \leq 1\times10^{-12}$ m^2/s and $D_{surf} \geq 1\times10^{-6}$ m^2/s, these values were selected for testing in variation 2. This test is to verify the effect of non-homogenous D_{surf} on the electrode behaviour. Figure 6.8 shows the plot for Dataset 1 on (a) the Tafel plots (b) j (mA/cm^2) vs η and (c) c_{Hs} vs η. No glaring changes took place at different sets of surface diffusion values tested. Similar patterns were observed on Set (1 – 4).

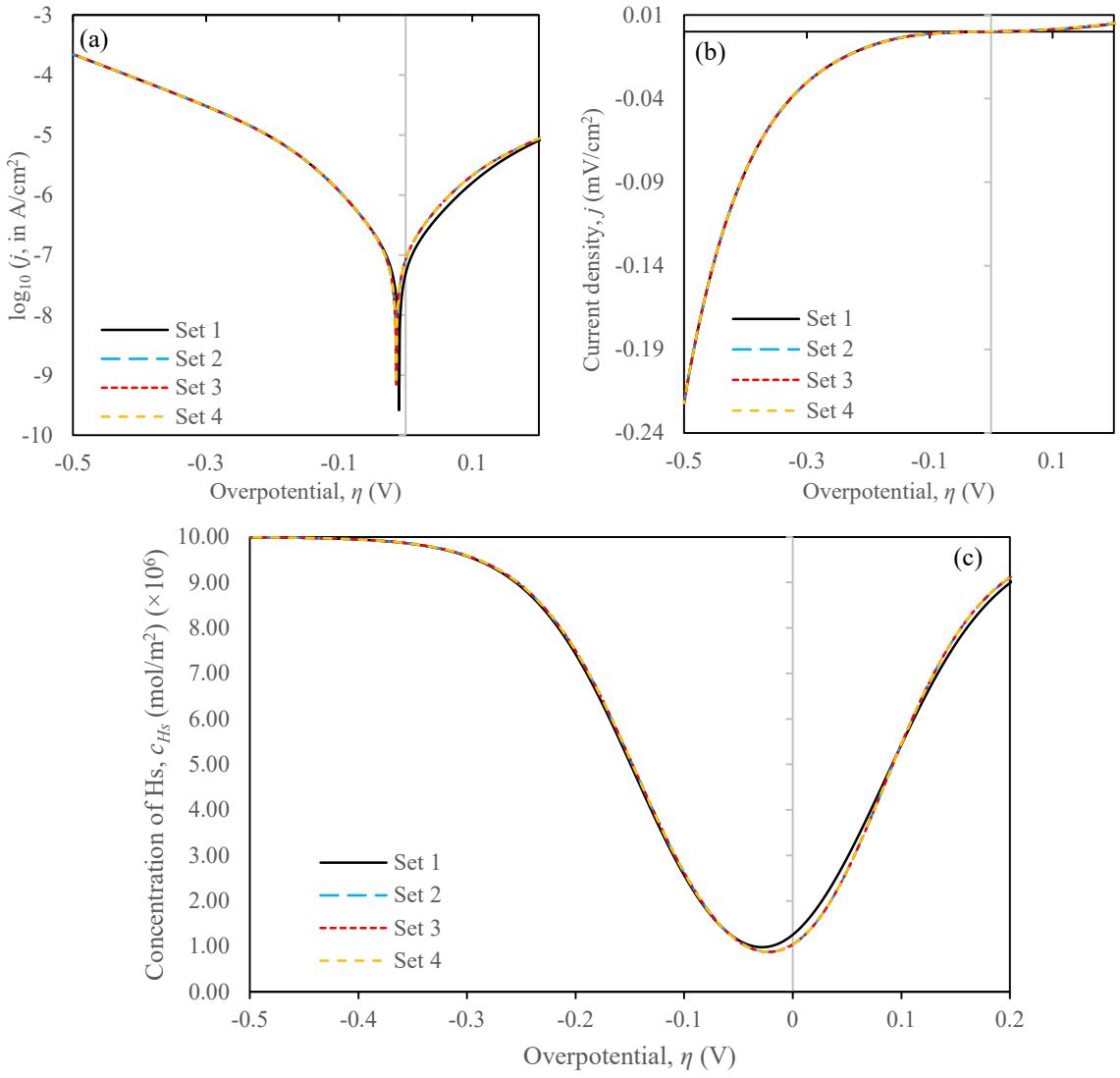

Figure 6.8: Plots of (a) the Tafel plots (b) j (mA/cm^2) vs η and (c) c_{Hs} vs η for dataset 1 with variation 2

When dataset 2 were tested with the different surface diffusion values, the increased current output was shown by set 3 and set 4 (similar to set 6 in variation 1) only. Plots with variation 2 for dataset 2 were given in Figure 6.9.

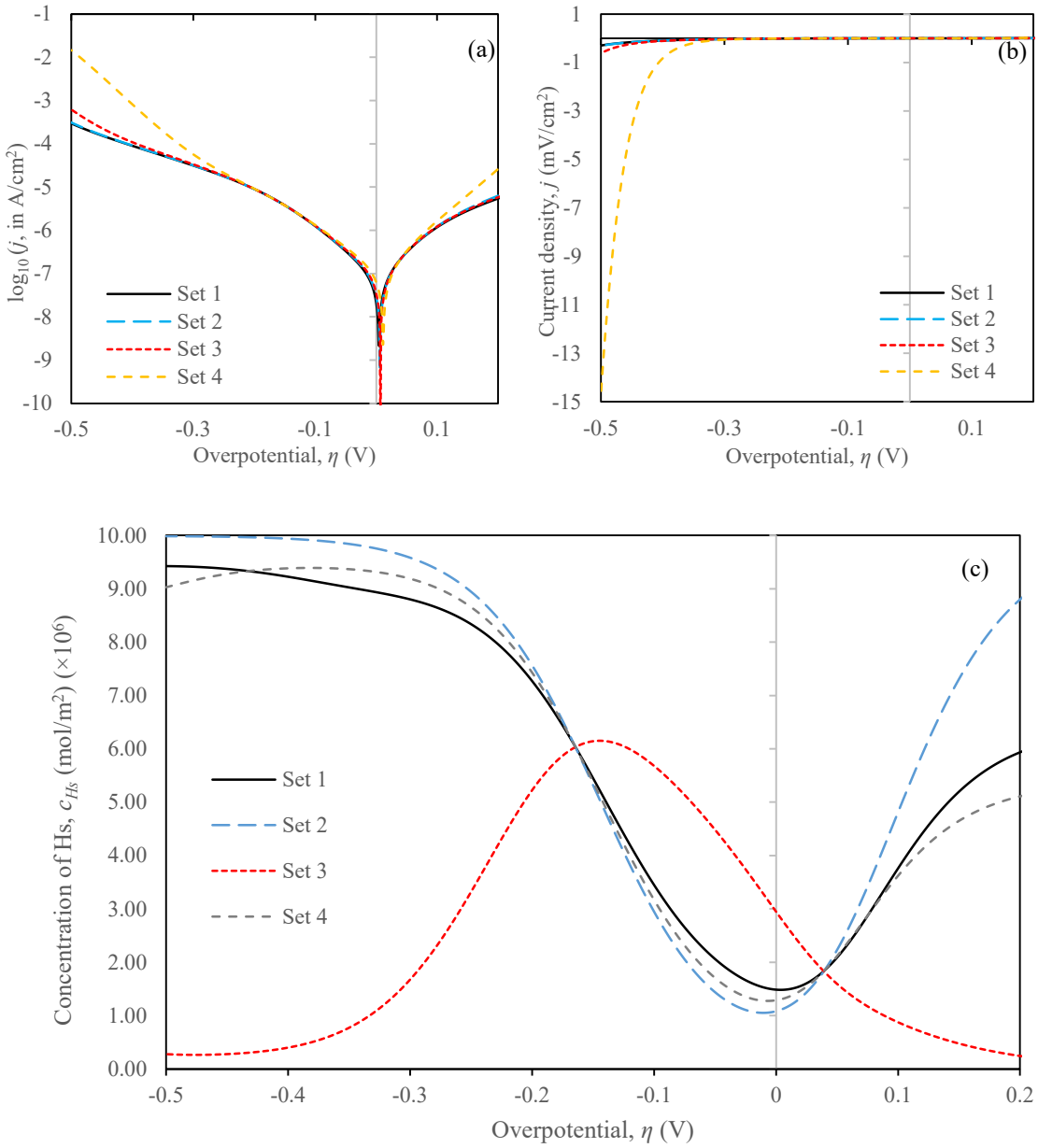

Figure 6.9: Plots of (a) the Tafel plots (b) j (mA/cm^2) vs η and (c) c_{Hs} vs η for dataset 2 with variation 2

While set 1 and set 2 shows similar plots despite set 2 having $D_{taC} > D_{TiC}$. On the contrary when $D_{TiC} > D_{taC}$ as shown by Set 3, slight increment was visible at η < -300 mV albeit not as much as when both the surfaces were highly diffusive, $D_{taC} = D_{TiC} = 1\times10^{-6}$ m^2/s (Set 4). By referring to Figure 6.9(c) the c_{Hs} for Set 3 gives the opposite trends in comparison to Set 1, 2 and 4. The c_{Hs} began to increase between -0.15 < η/V < +0.2 V until it reached approximately 6×10^{-6} mol/m^2. Then the c_{Hs} dropped to an estimate of 2×10^{-7} mol/m^2. This was unlike Set 1, 2 and 4 that facilitate higher c_{Hs} and began to show concentration decrement in between 0.0 < η/V < 0.2 V. While c_{Hs} increased from 0 V until c_{Hs} reached nearly 90 % filled. This shows that at higher surface diffusion, the Hs are quicker to be absorbed and desorbed by the surface of the electrocatalyst. Hence higher current output portrayed in Figure 6.9(a) and (b). Slightly lower c_{Hs} was observed at Dataset 2 compared to Dataset 1 when η > 0 V (HOR region). Therefore, surface diffusion set 4 was used in the simulation to get the best possible outcome of higher current output.

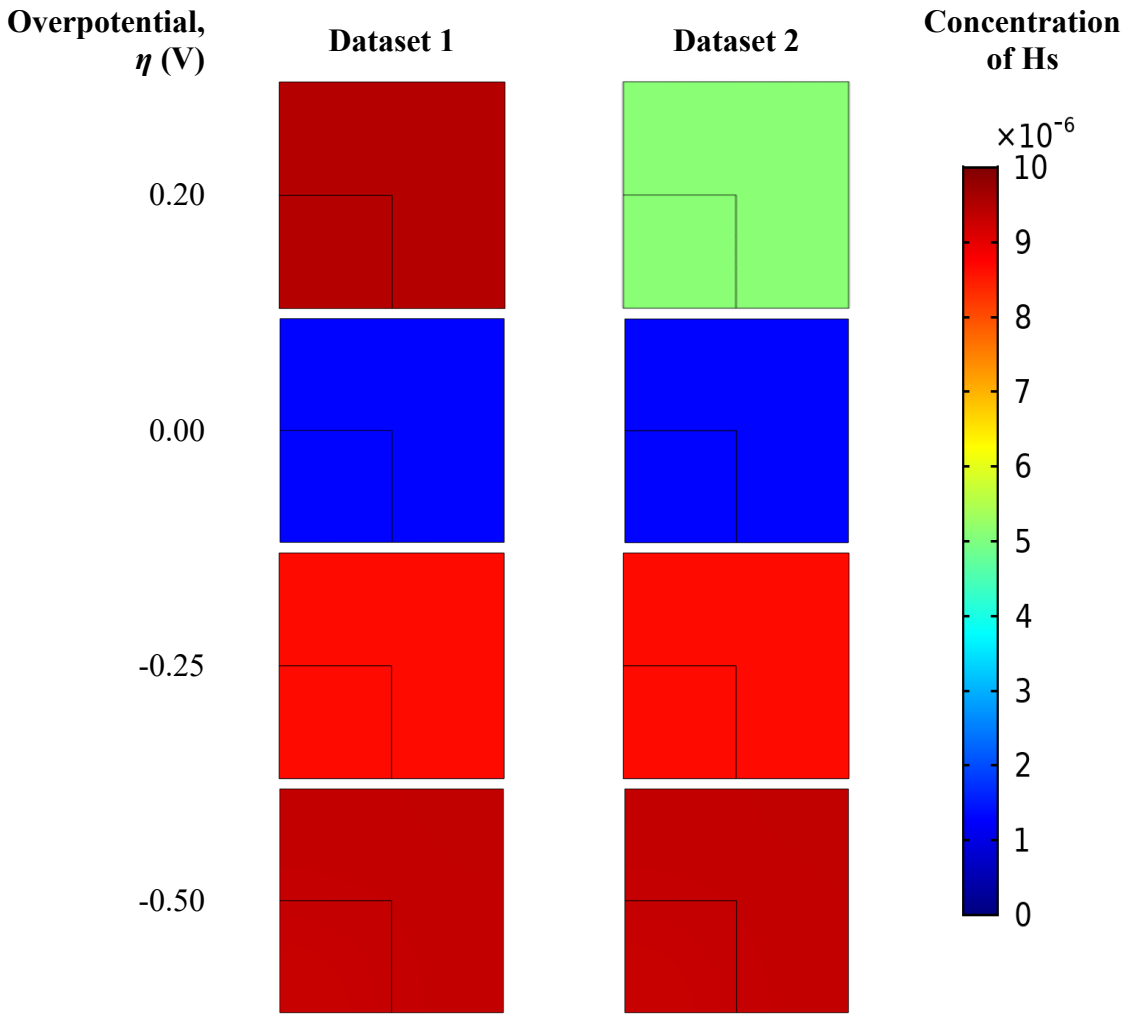

Figure 6.10: Concentration profile of Hs, c_{Hs} on the TiC/taC:Pt surface for Dataset 1 and 2 when $D_{taC} = D_{TiC} = 1\times10^{-6}$ m^2/s.

Figure 6.10 shows the 2D concentration profiles for the TiC and taC:Pt composite electrode for both dataset 1 and 2. The profiles were barely noticeable from taC surface to TiC surface giving the impression near homogeneity between surfaces TiC and taC:Pt. This was due to the high value of D_{TiC} and D_{taC}. The concentration profiles due to diffusion approaching η = -0.5 V were shown in this comparison. Initially, high c_{Hs} were recorded which started to decrease approaching 0 V. This was due to the reverse reaction of Volmer in HOR region. But different on concentration can be seen with dataset 2 having lower concentration of around 4.7×10^{-6} mol/m^2 at $\eta = 0.2$ V compared to dataset 1 estimated around 8.8×10^{-6} mol/m^2 at similar potential. At 0 V, both datasets show very low c_{Hs}. At this point, similar trends

were observed on both datasets for c_{Hs}. When potential was reduced further to -0.25 V, Hs concentration began to increased due to Volmer reaction. The Hs across the catalyst's surfaces were near equal albeit slight different in concentration when it reaches -0.5 V, a point where Volmer reaction dominates thus Hs achieved near Γ_{max}.

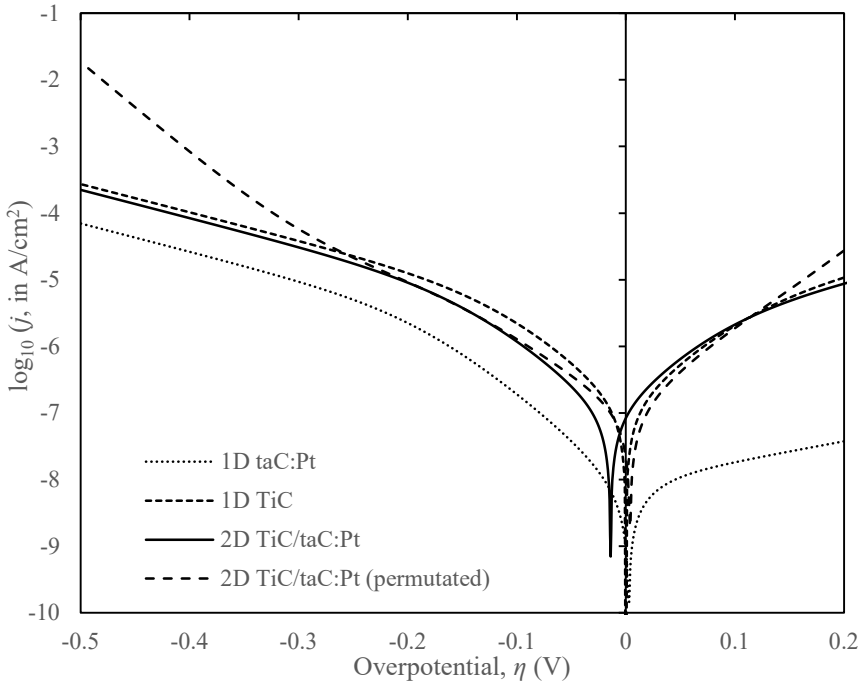

Figure 6.11: $\log_{10}$ (j in A/cm^2) vs potential of TiCtaC electrode with surface diffusion.

Here forth summarized the results for the conducted study on the effect of surface diffusion. In Figure 6.11, the current density of solitary taC:Pt and TiC was plotted along with the simulation from the 2D model results for TiC/taC:Pt electrode. The two plotted Tafel plots from the 2D simulations are of dataset 1 and dataset 2 having $D_{surf} = D_{TiC} = D_{taC} = 1\times10^{-6}$ m^2/s. This is to show that by using the initial values for the kinetic parameters (Dataset 1) would not have yield any significant increase in the current output albeit at high D_{surf} value. That was changed when taC:Pt kinetic parameters were permutated to facilitate more adsorption and desorption of Hs activity occurring on the electrode surface. The current

output was significantly higher with the application of high D_{surf} values. The surface diffusion effect was estimated to cap between $1\times10^{-14} \leq D_{surf} \leq 1\times10^{-6}$ m^2/s. No further changes on the current output was observed out of this deployed range. Permutation of TiC kinetic parameters only leads to more symmetrical curve cases of Dataset 1 and 2 as shown in Figure 6.6(a).

Conclusively, the surface diffusion theory is not sufficient in proving the higher magnitude in HER performance obtained from the TiC/taC:Pt. The increased of current are only noticeable at higher overpotential showing different plot to the one of the experiment. While it may not justify the experimental curved, but it was able to show that surface diffusion theoretically does have an effect on the current density of our electrode.

Due to the outcome, an analytical approach was made to verify the limitations of the equations employed in the simulation. Based on literature study for HER, most electrocatalysts exhibit Volmer-Heyrovsky (VH) mechanism. Thus, using the data obtained from the experimental results, the $(R_v+R_h)_{exp}$ in mol/m^2.s was calculated by fitting the experimental curve using the simulation that was developed for 1D model. Since most of the parameters were already predetermined in the experiment, the only parameter left that could affect the current response is c_{Hs}. Hence, a rearranged rate reaction equation was used to evaluate the c_{Hs} against the overpotential. The derivation uses a 1D rate reaction equation by assuming homogenous surface with VH mechanisms. This was written in terms of c_{Hs} and c_s as given in Eq. 6.1. Provided that c_s is given as eq. 6.2, hence eq. 6.3 was obtained to solve c_{Hs}.

$$(R_v + R_h)_{exp} = c_{Hs}(K_h c_{H^+} - K_{-v}) + c_s\left(K_v c_{H^+} - K_{-h} c_{H_2}\right) \quad (6.1)$$

$$\text{Since, } c_s = (\Gamma_{max} - c_{Hs}) \quad (6.2)$$

$$c_{Hs} = \frac{(R_v+R_h)_{exp}+\Gamma_{max}(K_v c_{H^+}-K_{-h}c_{H_2})}{K_h c_{H^+}-K_{-v}-K_v c_{H^+}-K_{-h}c_{H_2}} \quad (6.3)$$

Figure 6.12 shows the plot of possible c_{Hs} concentrations against the tested overpotential, η to achieve $(R_v+R_h)_{exp}$. Two solutions were obtained from the calculation and both were not acceptable as a possible solution. Given the assumption of max active sites used is Γ_{max}= 1×10^{-5} mol/m^2 the $c_{Hs}>\Gamma_{max}$ is not a possible outcome from the calculation.

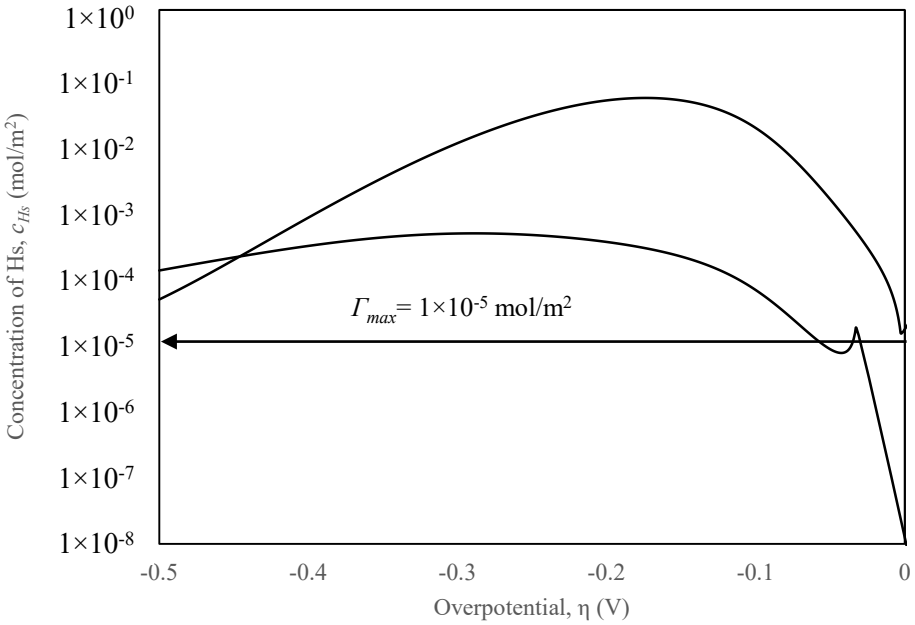

Figure 6.12: Concentration of Hs, c_{Hs} (mol/m^2) against overpotential, η plotted from $(R_v+R_h)_{exp}$.

In extension, further verification on the highest possible current output were evaluated using VH rate reaction. Considering the only forward reactions, the current density, j is written in eq. (6.4)

$$j = -nF\int[c_{Hs}(K_h c_{H^+}) + c_s(K_v c_{H^+})]_{TiC} + \int[c_{Hs}(K_h c_{H^+}) + c_s(K_v c_{H^+})]_{taC} \quad (6.4)$$

The kinetics parameters for both TiC electrode and taC:Pt catalyst in Table 6.1 were used to evaluate $\log_{10}(j)$ at η = -0.2 V with concentration of Hs, c_{Hs} ranging from 0 to $\Gamma_{max} = 1\times10^{-5}$ mol/m^2.

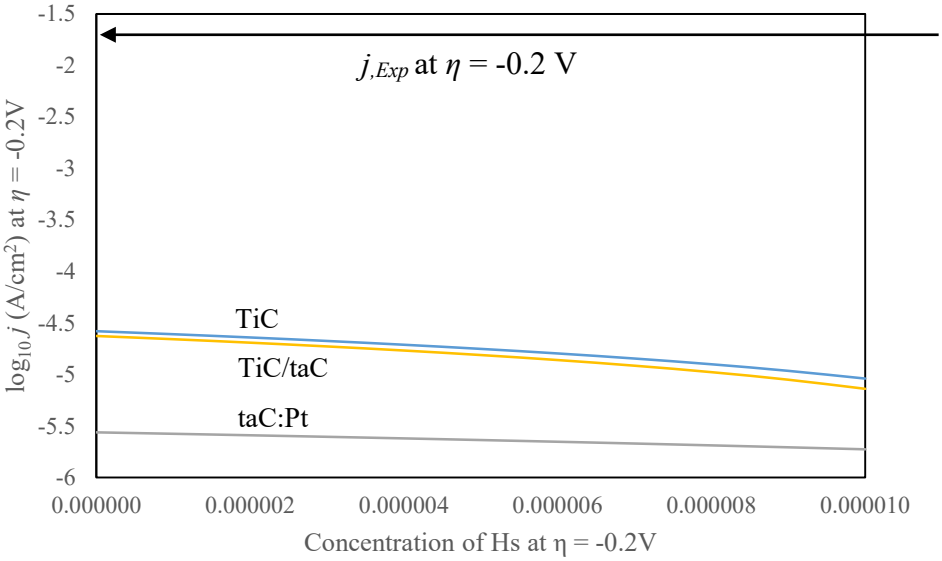

Figure 6.13: $\log_{10}$ of current density vs Hs concentration at η = -0.2 V

Figure 6.13 shows that eq. (6.4) is not adequate to achieve the current output of TiC/taC:Pt via experiment. The maximum attainable current for $j_{TiC/taC}$ is only a fraction higher than j_{TiC} which is far from the projected current output from experimental result. Thus proving that the current equations employed is insufficient in justifying the enhanced electrocatalytic activity. Therefore, in the following section the addition of edge effect is proposed to show the good fitting on the experimental data via simulation and analytical equations.

6.3 The edge effect between TiC substrate and taC:Pt

The use of FEM analysis to explain the higher kinetic activity of TiC/taC:Pt due to surface diffusion is not enough to justify the experimental findings. The addition of edge effect was

deemed necessary to explain the higher magnitude of current from TiC/taC:Pt electrode. Hence improved kinetics are assumed on the edges that was supported by Jian et al. (2018) and Yang et al. (2020) indicating higher kinetics at the edge between the two materials.

A new dimension was given in the model to take the edge into consideration. Hence, the thickness of an estimated 100 nm was added to the taC:Pt half. With the added kinetic properties on the edge of taC:Pt catalyst, eq. (6.5) was used to evaluate the current density produced.

$$j = -nF\left([(R_v+R_h)A]_{TiC} + [(R_v+R_h)A]_{taC} + [(R_v+R_h)A]_{edge}\right) \quad (6.5)$$

A 3D model was designed in order to simulate the HER performance with the consideration of surface diffusion and edge effect. Further information on the model was thoroughly discussed in section 3.2.5. The 3D simulation was developed to study the effect of edge effect and surface diffusion. While retaining the kinetic parameters obtained for both TiC and taC:Pt from previous section, the kinetic parameters for the edge was determined and tabulated in Table 6.5 (using eq. 6.5). Concurrently, the effect of surface diffusion was conducted by employing the $D_{surf} = D_{TiC} = D_{taC}$ values of 1×10^{-12}, 1×10^{-9} and 1×10^{-6} m^2/s. This values were selected based upon the surface diffusion study presented on the 2D model. Having known that no further changes could occur beyond $1\times10^{-12} < D_{surf,}$ $m^2/s < 1\times10^{-6}$ and $D_{TiC} \neq D_{taC}$ does not improve the current any better than $D_{TiC} = D_{taC}$ with higher diffusivity values.

Figure 6.14 shows the Tafel plots for the 3D model study with the effect of edge effect and surface diffusion. Based on the plots, significant increase was observed by the addition of edge effect. This implies that there is very rapid VH mechanisms occurring at the edge between TiC and taC:Pt. The effect of surface diffusion shows no changes on the current

output for all tested D_{surf}. This result was very similar to the results obtained from our simulation on the effect of surface diffusion using 2D model for Dataset 1 where no permutation was applied. One possible explanation for this is because the electrode surface was homogenous in concentration. Hence, the diffusion of Hs from surface taC to TiC or TiC to taC does not incurred any significant outcome.

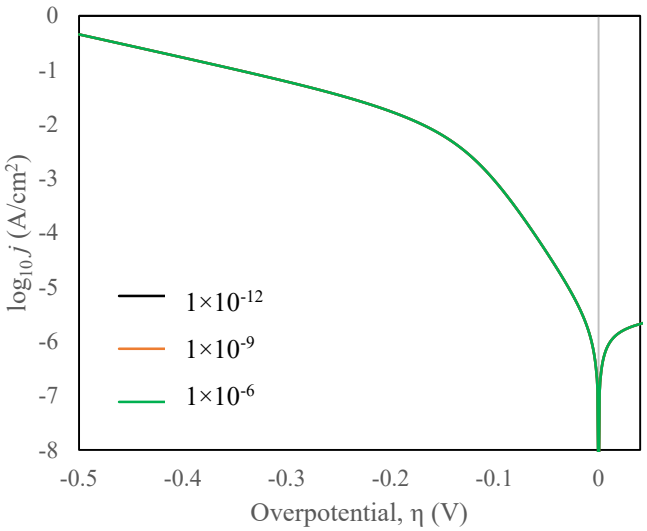

Figure 6.14: Tafel plots for 3D simulation (no kinetic parameters permutation) with edge effect and surface diffusion, $D_{surf} = 1\times10^{-12}$, 1×10^{-9}, 1×10^{-6} m^2/s.

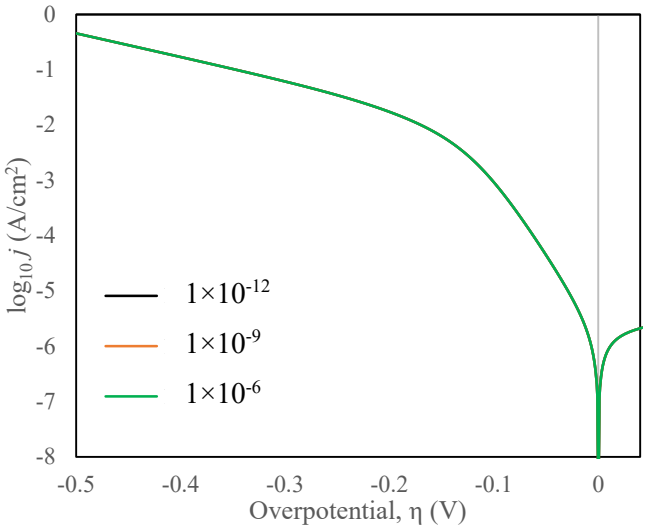

Figure 6.15: Tafel plots for 3D simulation (taC:Pt kinetic parameters permutation) with edge effect and surface diffusion, $D_{surf} = 1\times10^{-12}$, 1×10^{-9}, 1×10^{-6} m^2/s.

Similar test on the effect of surface diffusion was carried out for taC:Pt having permutated kinetic parameters (similar to dataset 2 in chapter 6.1). Figure 6.15 shows that similar to the results exhibit by the non-permutated taC:Pt from previous paragraph, no changes can be observed on all tested D_{surf}. This would imply that the kinetic properties on the edge was extremely quick in comparison to the TiC and taC:Pt surfaces (by approximately a factor of 10^4) that it overshadows the contribution from TiC and taC:Pt surfaces. The current output was dominated by the response of the reaction on the edge between TiC and taC:Pt.

Table 6.5: Kinetics parameters of TiC electrode and taC:Pt electrode

Electrode	**TiC**	**taC:Pt**	**edge**	**Pt/C**
k_v ($m^3/(mol \cdot s)$)	6.1×10^{-6}	4.8×10^{-8}	9×10^{1}	3
k_{-v} (1/s)	8.0×10^{-2}	4.8×10^{-5}	9×10^{1}	3×10^{7}
k_h ($m^3/(mol \cdot s)$)	1.09×10^{-5}	2.8×10^{-6}	4	3×10^{1}
k_{-h} ($m^3/(mol \cdot s)$)	1.09×10^{-3}	2.8×10^{-3}	4×10^{6}	3
k_t ($m^2/(mol \cdot s)$)	1×10^{2}	0	0	0
k_{-t} ($m^5/(mol^2 \cdot s)$)	1×10^{3}	0	0	0
β_v	0.77	0.82	0.9	0.5
β_h	0.25	0.25	0.25	0.5
Area (m^2)	7.5×10^{-9}	2.5×10^{-9}	1×10^{-11}	

Finally, to show the performances of each of the studied electrocatalysts, comparison was made on TiC, taC:Pt, and TiC/taC:Pt A good fit of the experimental curve was obtained using the VHT kinetic parameters all electrocatalysts (listed in Table 6.5). Kinetic parameters for the best performing electrocatalyst that is platinum (Pt) electrode was also made available for reference. The data can be extracted from well documented articles (for eg: Campos-Roldan et al., (2018) and Yan et al., (2019)).

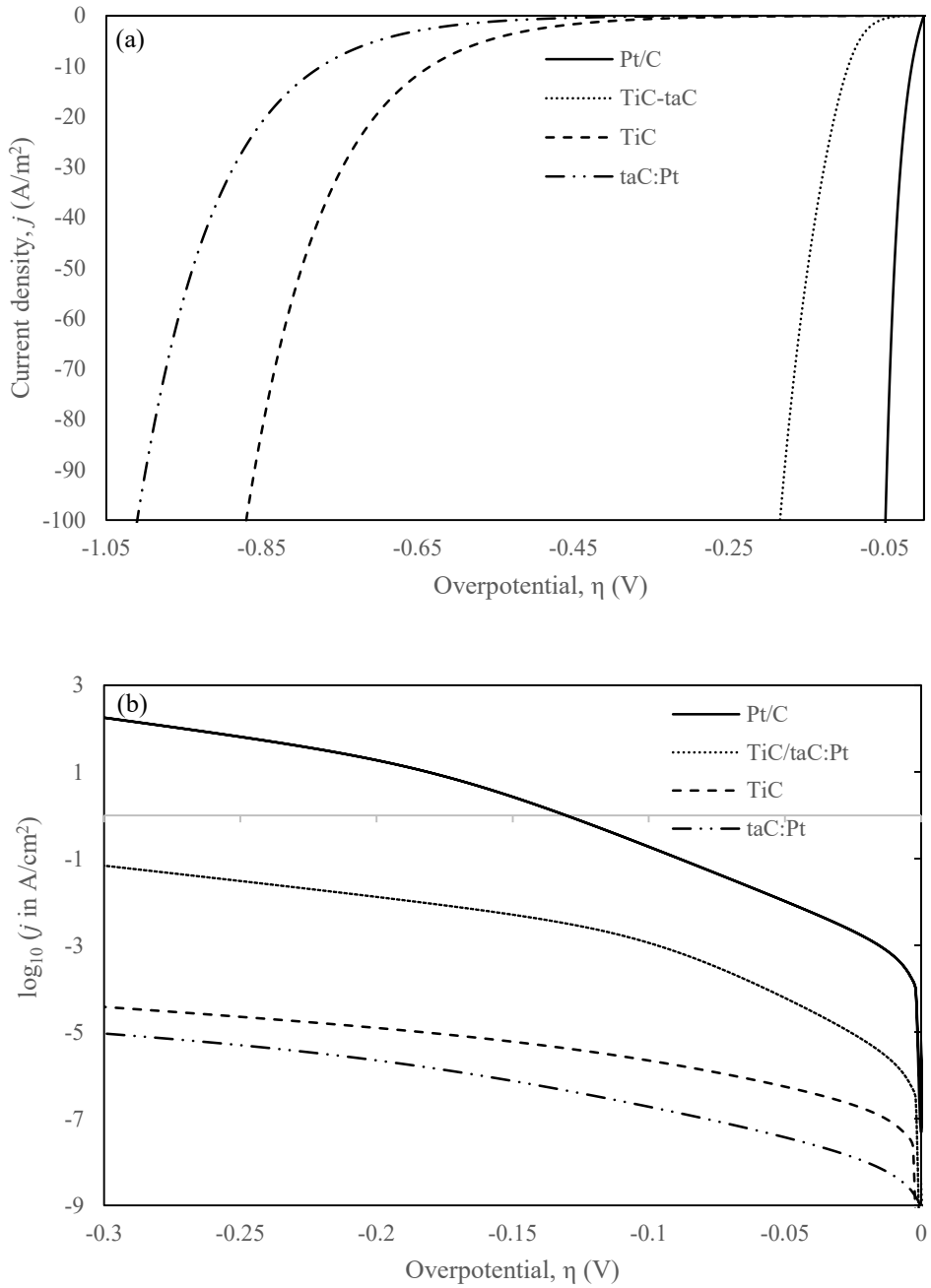

Figure 6.16: (a) HER polarisation curves and (b) Tafel plots of TiC, taC:Pt, TiC/taC:Pt and Pt/C.

The current density, *j,* against overpotential, *η,* obtained via simulation was plotted along with Pt comparison in Figure 6.16 (a). The y-axis was capped at 100 A/m^2 or 10 mA/cm^2 to provide a better view to obtained η_{10} *or* η@10 mA/cm^2. The corresponding Tafel plots were

plotted in Figure 6.16 (b). It was clear that Pt is a much superior electrocatalyst in comparison to the tested materials.

The HER performances were recorded in terms of (1) Tafel plot, (2) overpotentials, η@10 mA/cm^2 and (3) the exchange current density, j_0 of the tested catalysts were recorded in Table 6.6. TiC/taC:Pt and Pt shows a Volmer dominated reaction with a low Tafel plots of less than 40 mV/dec at a low η = (10~100 mV) and η_{10} of 185 and 50 mV respectively. Comparatively, solitary TiC and taC:Pt recorded significant higher Tafel plots are between (60~110) mV/dec at low η = (10~200 mV) and η_{10} of 871 and 1009 mV, respectively.

Table 6.6: Summary of the HER performances of the electrocatalyst

Materials	Tafel slope (mV/dec)	Overpotentials at 10 mA/cm^2, η_{10} (mV)	Exchange current density, j_o (mA/cm^2)
taC:Pt	60~104 @ -10~-200 mV	-1009	1.26×10^{-8}
TiC	54~114 @ -10~-200 mV	-871	2.00×10^{-7}
TiC/taC:Pt	20~40 @ -10~-100 mV	-185	1.00×10^{-6}
Pt/C	15~40 @ -10~-100 mV	-50	2.00×10^{-3}

Through the implementation of edge effect and surface diffusion, the experimental curve of TiC/taC:Pt was able to be justified. The developed FEM model had successfully estimated the behavior of the novel TiC/taC:Pt catalyst. The model was able to predict the c_{Hs} on the catalyst surface given in Figure 6.17 for a 1D model of taC:Pt, TiC and Pt.

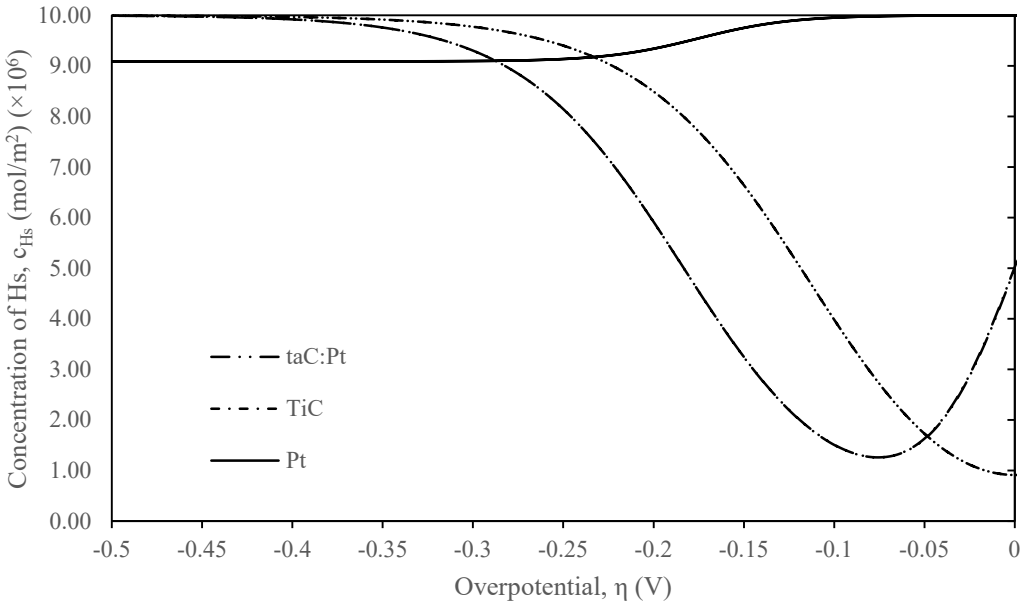

Figure 6.17: Concentration of adsorbed hydrogen on the electrocatalyst surface.

The concentration profile of Hs was illustrated in Figure 6.18 for 3D simulation assuming edge effect and Figure 6.19 for 2D simulation assuming only surface diffusion. Based on figures the higher catalytic activity was due to the higher concentration of Hs at the edge. The decrease of c_{Hs} on TiC and taC:Pt are visible in this region while the c_{HS} at the edge remained at near maximum capacity at $\Gamma_{max} = 1\times10^{-5}$ mol/m^2. Point 1, Point 5 and point 8 for Figure 6.19 represents the taC:Pt (bottom left corner), the edge (the centre point of the square) and TiC (upper right corner) respectively.

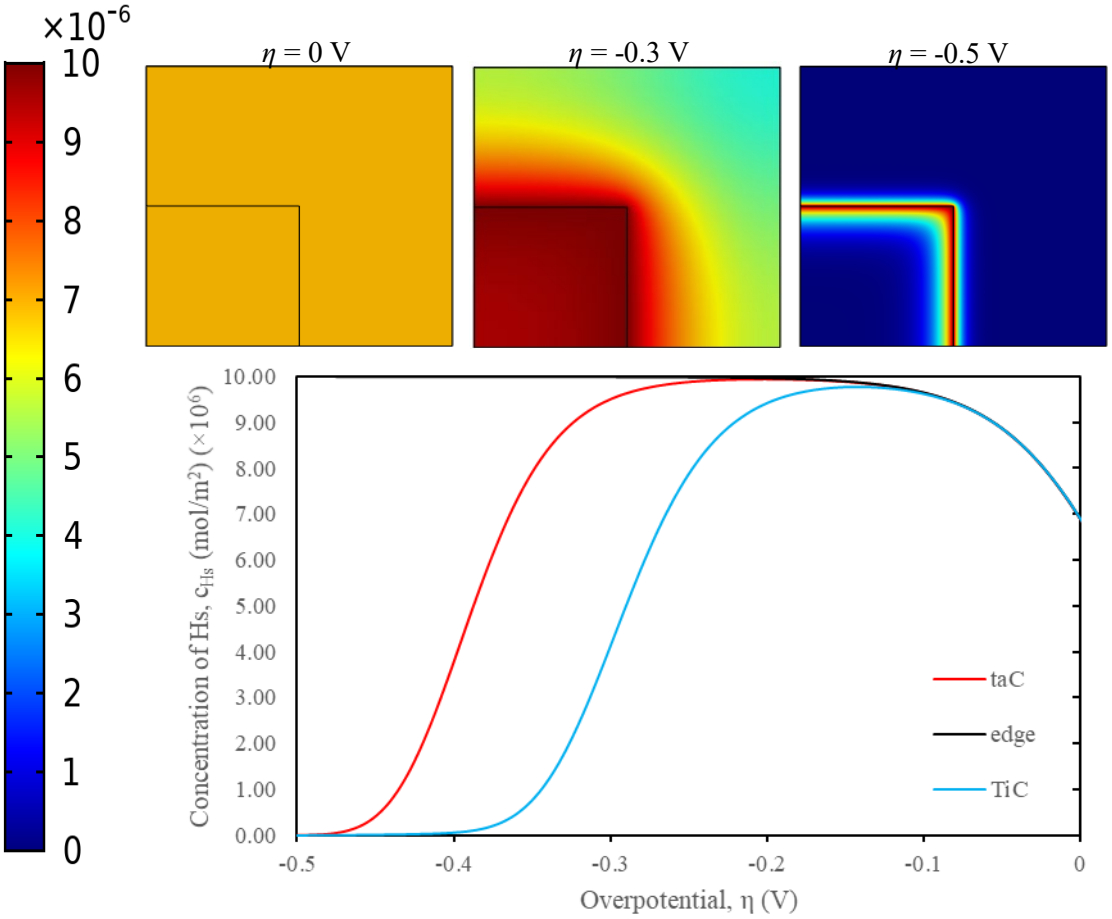

Figure 6.18: Topview of 3D simulation with surface diffusion and edge effect: The concentration profiles for Hs at η = (0, -0.3, -0.5) V and the extracted c_{Hs} curves at different point of the electrocatalyst surface.

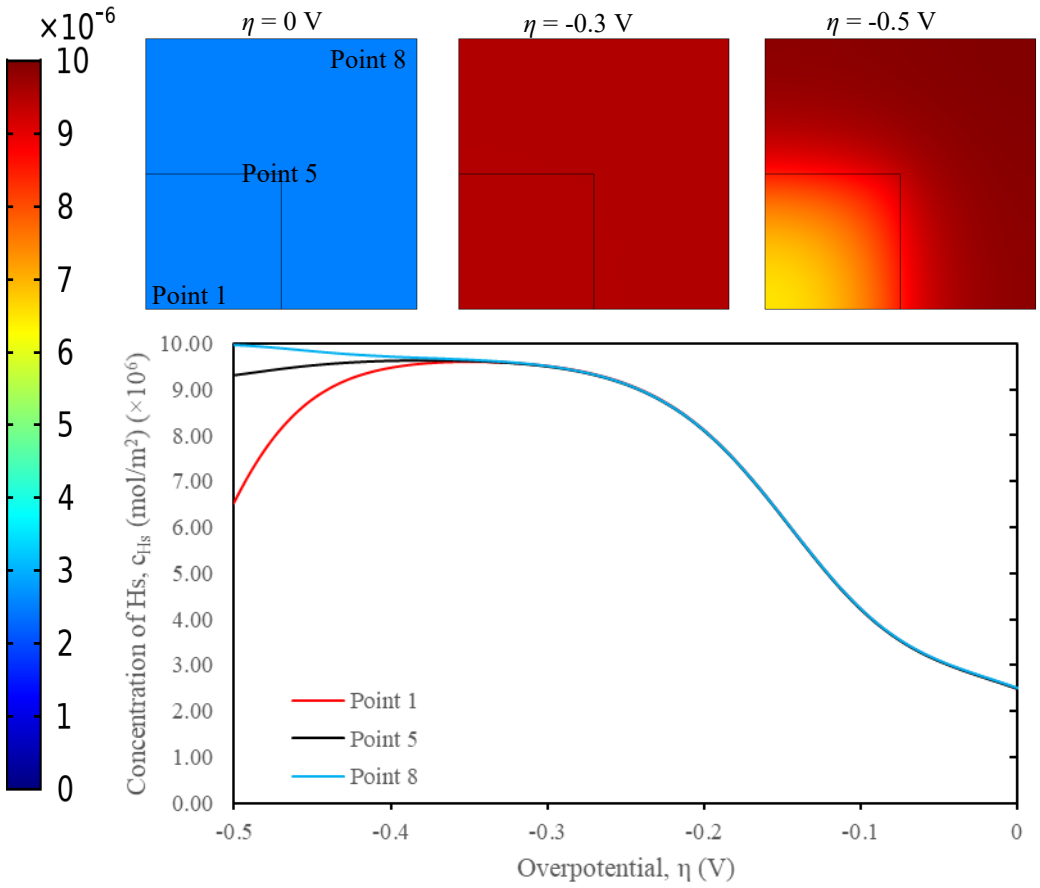

Figure 6.19: The concentration profiles for Hs at η = (0, -0.3, -0.5) V and the extracted c_{Hs} curves at different point of the catalyst surface.

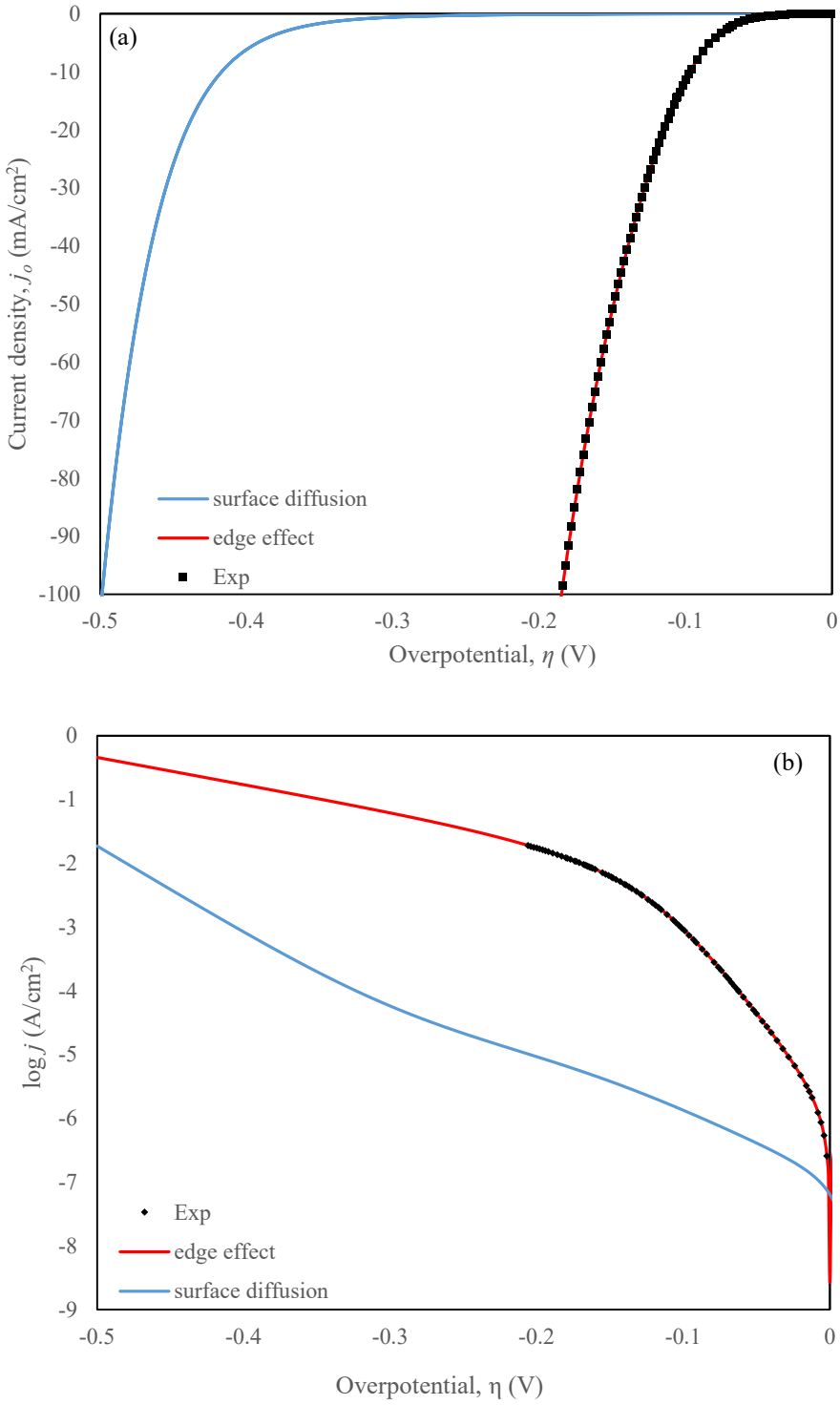

Figure 6.20: Comparison with the experimental plot on the HER polarization curves using eq. (7.4) for surface diffusion and eq. (6.5) for edge effect. (a) current density, j (mA/cm^2) vs overpotential, η and (b) Tafel plots.

Results from the simulation in terms of current density, j_0 are plotted in Figure 6.20 in comparison with the experimental curve by using the parameters obtained from simulation provided in Table 6.5. Based on the graph, the simulation plot of the model with edge effect shows great coherency with the experimental plot. The edge effect was defined with the consideration of the thickness (approximately 100 nm) of the deposited taC:Pt catalyst on TiC support. This edge does not behave similarly to either TiC or taC:Pt. The only possible explanation for this occurrence is because the edge exhibits enhanced kinetic properties due to the formation of bonding between the catalyst (Zhao et al., (2014), Jiao et al. (2018) and Manikandan et al. (2019)). The possibility of alloy effect occurring was described by Zhang et al. (2020) between the metals presence in the catalyst. In our case, Ti and Pt could interacts thus changing the electronic structure and improved the charge transfer efficiency.

6.4 Chapter Summary

This chapter was divided into three main parts discussing the results pertaining the simulation work that was based on the experimental work by Glandut et. al (2015) on taC:Pt, TiC and TiC/taC electrocatalysts for HER.

In sub-chapter 6.1, by implementing the VHT mechanistic steps equation for HER, the developed 1D model was able to determine the kinetics parameters for both TiC and taC:Pt where TiC exhibits VHT steps and taC exhibits VH steps. The simulation results show great coherency with the experimental results.

The simulation result for the hybrid electrocatalyst of TiC/taC were discussed in sub-chapter 6.2 and 6.3. Where in sub-chapter 6.2 the effect of surface diffusion was taken into consideration. The effect of kinetic parameters permutation with surface diffusivity shows

some increased in current output but was unable to achieve the current output obtained from the experiment.

Which then leads to the assumption of edge effect in sub-chapter 6.3. An edge effect was created from the thickness of taC:Pt on the TiC support. The edge exhibits kinetic properties unlike both TiC or taC:Pt. The kinetic parameters were determined using the simulation and a dataset was found to show great coherency with the experimental result. Surface diffusion was rendered negligible because of the high kinetic parameters on the edge in comparison to the TiC and taC:Pt surface.

CHAPTER 7

CONCLUSION AND FUTURE OUTLOOKS

7.1 Conclusion

In this chapter, this work would like to conclusively summarize the objectives that were outlined at the beginning of the thesis.

1. A robust redox reaction model with similar operating conditions was successfully developed on 1D, 2D axisymmetric and 3D geometries (discussed in Chapter 3.1). The simulation results show that the software was able to produce results with less than 3% error when compared to the analytical method across all geometries (presented in Chapter 4).
2. A 1D HER simulation was modelled by employing the VHT mechanistic step based on the experimental conditions by Glandut et al. (2015) to determine the kinetic parameters for TiC and taC:Pt. By using the pre-determined kinetic parameters obtained in 1D simulation, 2D and 3D geometries were developed using similar models in 1D with the inclusion of surface diffusion and edge effect for TiC/taC catalyst (discussed in Chapter 3.2).
3. A parametric work was presented in terms of the kinetic parameters of VHT rates and the charge transfer coefficient to observe their effect on the concentration of hydride surface, c_{Hs} and current density, j. Table 5.6 in chapter 5 shows the summary of VHT kinetic parameters effects on the concentration of Hs, c_{Hs}, overpotential, η, and Tafel plots. It was presented that increasing the standard rate constant of either V, H and T would consequently increase the overpotential and the current density, j. While the charge transfer coefficient have no effects on the exchange current density,

j_0. But the current density, j increase with the increase of the charge transfer coefficient. In addition, discussion on VHT reversible reactions was given as consideration for better fitting of some experimental results. This parametric study provides sufficient information for the determination of the kinetic parameters involved in any experimental HER results.

4. The developed 1D model was able to determine the kinetics parameters for both TiC and taC:Pt where TiC exhibits VHT steps and taC exhibits VH steps. The simulation results show great coherency with the experimental results. For TiC/taC, the effect of kinetic parameters permutation with surface diffusivity shows some increased in current output but was unable to achieve the current output obtained in the experiment. The addition of edge effect was deemed necessary to explain the higher magnitude of current from TiC/taC:Pt electrode. The edge exhibits kinetic properties unlike both TiC or taC:Pt. The kinetic parameters were determined using the simulation and a dataset was found to show great coherency with the experimental result. Surface diffusion was rendered negligible because of the high kinetic parameters on the edge in comparison to the TiC and taC:Pt surface (discussed in Chapter 6).

7.2 Future outlooks

Based on the study presented in this thesis, the use of COMSOL to model and verify the experimental work was proven reliable and feasible. The successfulness of the developed HER model to simulate the VHT mechanistic steps create a huge opportunity for further study. Here are several recommendations for future works;

1. **Surface diffusion and edge effect:** Since this work prove the edge effects contributes to the improved HER, hence different configurations of TiC/taC formations are suggested to be studied. For eg: Circular taC on TiC support, triangular TiC on taC support and etc. While surface diffusion might not have supported our findings but our simulation has shown that HER were positively affected by this factor. (recommended for experimentation and simulation)
2. **Effect of taC thickness:** Varying the thickness of taC ie: 10 nm, 100 nm and etc while observing their effects on HER specifically the Tafel plots.
3. **Decreasing the platinum concetration on taC surface:** Varying the platinum load and on taC hence determining the optimum Pt load that could increase the HER.
4. **Varying the composition of carbide:** Find the effect of TiC carbon vacancy ie: TiC-0.8, 0.6, 0.4 and etc to determine the optimum level of carbon vacancy that would provide the best HER.
5. **Exploring other transition metal:** Substituting titanium with other transition metal for eg; Molybdenum carbide (MoC). Doping Nickel in taC rather than Pt as some studies for eg: Wang et al., 2015 and Xue et al., 2020 suggest Ni function better as doped material compared to Pt.
6. **Density functional theory calculations:** The use of DFT calculation to evaluate the energy required for the binding of H by the materials in the catalysts. The DFT results can supplement the assumption made on the edge effect and provide strong justification on the FEM findings.
7. **Effect of other operating parameters:** The effect of pH's for eg: conducting the HER in alkaline medium, temperatures and pressures were suggested on TiC, taC

and TiC/taC to observe the response on the concentration of Hs and current output (recommended for experimentation and simulation).

8. **Kinetic parameters data library of materials:** This work has proven that the adopted model provides reliable results and are easy to use. The determined kinetic parameters are independent from any other parameters such as the concentration of H^+ or H_2, temperatures and pressures. If the kinetic parameters for different types of materials were determined using the same evaluation, this can be very useful as a handbook for electrochemist (recommended for simulation).

REFERENCES

Airbus (obtained online on 2022, April 25). Towards the world's first zero-emission commercial aircraft. (https://www.airbus.com/en/innovation/zero-emission/hydrogen/zeroe

Almazán-Ruiz, F. J., Caballero, F. V., Cruz-Díaz, M. R., Rivero, E. P., & González, I. (2012). Scale-up of rotating cylinder electrode electrochemical reactor for Cu (II) recovery: Experimental and simulation study in turbulence regimen. *Electrochimica acta*, 77, 262-271.

Antonini, C., Treyer, K., Streb, A., van der Spek, M., Bauer, C., & Mazzotti, M. (2020). Hydrogen production from natural gas and biomethane with carbon capture and storage–A techno-environmental analysis. *Sustainable Energy & Fuels*, *4*(6), 2967-2986.

Azara, A., Benyoussef, E. H., Mohellebi, F., Chamoumi, M., Gitzhofer, F., & Abatzoglou, N. (2019). Catalytic Dry Reforming and Cracking of Ethylene for Carbon Nanofilaments and Hydrogen Production Using a Catalyst Derived from a Mining Residue. *Catalysts*, *9*(12), 1069.

Azizi, O., Jafarian, M., Gobal, F., Heli, H., & Mahjani, M. G. (2007). The investigation of the kinetics and mechanism of hydrogen evolution reaction on tin. *International Journal of Hydrogen Energy*, *32*(12), 1755-1761.

Azizian, S., & Eris, S. (2021). Adsorption isotherms and kinetics. In *Interface Science and Technology* (Vol. 33, pp. 445-509). Elsevier.

Bahtic F. (2021, July 26). World's 1st hydrogen–powered ferry delivered. Offshore Energy. https://www.offshore-energy.biz/worlds-1st-hydrogen-powered-ferry-delivered/

Bard, A. J., Faulkner, L. R., & White, H. S. (2004). *Electrochemical methods: fundamentals and applications*. John Wiley & Sons.

Bernama (2020, November 24) Sarawak aspires to become major hydrogen exporter. Bernama. https://themalaysianreserve.com/2020/11/24/sarawak-aspires-to-become-major-hydrogen-exporter/

Bernama (2021, July 12). Petronas-UKM hydrogen research yielding positive results. Bernama. https://www.theedgemarkets.com/article/petronasukm-hydrogen-research-yielding-positive-results

Bernama, (2021, July 27). Hydrogen economy can help Malaysia reduce greenhouse gases — Minister. The Sun Daily.https://www.thesundaily.my/local/hydrogen-economy-can-help-malaysia-reduce-greenhouse-gases-minister-AI8129075

Bernama (2021, July 17). Sarawak Energy, Pestech sign agreement to explore alternative renewable energy. The Edge Market. https://www.theedgemarkets.com/article/sarawak-energy-pestech-sign-agreement-explore-alternative-renewable-energy

Bhalothia, D., Shuan, L., Wu, Y. J., Yan, C., Wang, K. W., & Chen, T. Y. (2020). A highly mismatched NiO 2-to-Pd hetero-structure as an efficient nanocatalyst for the hydrogen evolution reaction. *Sustainable Energy & Fuels*, 4(5), 2541-2550.

Bi, J., Zhai, X., Liu, G., Chi, J. Q., Wang, X., Chen, S., ... & Wang, L. (2022). Low loading of P modified Rh nanoparticles encapsulated in N, P-doped carbon for boosted and pH-universal hydrogen evolution reaction. *International Journal of Hydrogen Energy*, *47*(6), 3791-3800

Bicelli, L. P. (1986). Hydrogen: a clean energy source. *International journal of hydrogen energy*, 11(9), 555-562.

Bukola, S., Merzougui, B., Creager, S. E., Qamar, M., Pederson, L. R., & Noui-Mehidi, M. N. (2016). Nanostructured cobalt-modified molybdenum carbides electrocatalysts for

hydrogen evolution reaction. *International Journal of Hydrogen Energy*, 41(48), 22899-22912.

Campos-Roldán, C. A., González-Huerta, R. G., & Alonso-Vante, N. (2018). The oxophilic and electronic effects on anchored platinum nanoparticles on sp2 carbon sites: the hydrogen evolution and oxidation reactions in alkaline medium. *Electrochimica Acta*, 283, 1829-1834.

Carneiro-Neto, E. B., Lopes, M. C., & Pereira, E. C. (2016). Simulation of interfacial pH changes during hydrogen evolution reaction. *Journal of Electroanalytical Chemistry*, *765*, 92-99.

Chialvo, M. G., & Chialvo, A. C. (1994). Hydrogen evolution reaction: Analysis of the Volmer-Heyrovsky-Tafel mechanism with a generalized adsorption model. *Journal of Electroanalytical Chemistry*, *372*(1-2), 209-223.

Chirkov, Y. G., Rostokin, V. I., Andreev, V. N., & Bogdanovskaya, V. A. (2020). Computer Simulation of the Structure and Operation Mechanisms for the Active Layer of Lithium–Oxygen Battery Cathode. *Russian Journal of Electrochemistry*, 56, 230-238.

Chen, P., Ye, J., Wang, H., Ouyang, L., & Zhu, M. (2021). Recent Progress of Transition Metal Carbides/Nitrides for Electrocatalytic Water Splitting. *Journal of Alloys and Compounds*, 160833.

Compton, R. G., & Banks, C. E. (2018). *Understanding voltammetry*. World Scientific.

Cuevas, F., Zhang, J., & Latroche, M. (2021). The vision of France, Germany, and the European Union on future hydrogen energy research and innovation. *Engineering*.

Cutress, I. J., Dickinson, E. J., & Compton, R. G. (2010). Analysis of commercial general engineering finite element software in electrochemical simulations. *Journal of Electroanalytical Chemistry,* 638(1), 76-83.

Debe, M. K. (2012). Electrocatalyst approaches and challenges for automotive fuel cells. *Nature*, 486(7401), 43-51.

Deng, S., Yang, F., Zhang, Q., Zhong, Y., Zeng, Y., Lin, S., ... & Tu, J. (2018). Phase modulation of (1T-2H)-$MoSe_2$/TiC-C shell/core arrays via nitrogen doping for highly efficient hydrogen evolution reaction. *Advanced Materials*, 30(34), 1802223.

Diard, J. P., Le Gorrec, B., & Montella, C. (1997). Non-linear impedance for a two-step electrode reaction with an intermediate adsorbed species. *Electrochimica acta*, *42*(7), 1053-1072.

Dickinson, E. J., Ekström, H., & Fontes, E. (2014). COMSOL Multiphysics®: Finite element software for electrochemical analysis. A mini-review. *Electrochemistry Communications*, 40, 71-74.

Dubouis, N., & Grimaud, A. (2019). The hydrogen evolution reaction: from material to interfacial descriptors. *Chemical Science*, *10*(40), 9165-9181.

Durst, J., Simon, C., Hasché, F., & Gasteiger, H. A. (2014). Hydrogen oxidation and evolution reaction kinetics on carbon supported Pt, Ir, Rh, and Pd electrocatalysts in acidic media. *Journal of The Electrochemical Society*, *162*(1), F190.

Emin, S., Altinkaya, C. E. S. U. R., Semerci, A., Okuyucu, H. A. S. A. N., Yildiz, A., & Stefanov, P. (2018). Tungsten carbide electrocatalysts prepared from metallic tungsten nanoparticles for efficient hydrogen evolution. *Applied Catalysis B: Environmental*, 236, 147-153.

Etula, J., Wester, N., Liljestrom, T., Sainio, S., Palomaki, T., Arstila, K., ... & Laurila, T. (2021). What Determines the Electrochemical Properties of Nitrogenated Amorphous Carbon Thin Films?. *Chemistry of Materials*, *33*(17), 6813-6824.

Feng, J. X., Xu, H., Dong, Y. T., Lu, X. F., Tong, Y. X., & Li, G. R. (2017). Efficient hydrogen evolution electrocatalysis using cobalt nanotubes decorated with titanium dioxide nanodots. Angewandte Chemie International Edition, 56(11), 2960-2964.

Ferri, T., Gozzi, D., & Latini, A. (2007). Hydrogen evolution reaction (HER) at thin film and bulk TiC electrodes. *International journal of hydrogen energy*, 32(18), 4692-4701.

Furukawa S., Nomura M., Haji T., Nishihara M., Mendoza O., Sonede Y., Matsumoto H., Preparation of hydrophobic electrocatalyst layer and inorganic porous electrolyte layer for water absorbing porous electrolyte electrolysis cell, *Int. J. of Hydrogen Energy*, 2018, 43(27), 11903-11912.

Gavaghan, D. J., Gillow, K., & Süli, E. (2006). Adaptive finite element methods in electrochemistry. *Langmuir*, 22(25), 10666-10682.

Glandut, N., Malec, A. D., Mirkin, M. V., & Majda, M. (2006). Electrochemical studies of the lateral diffusion of TEMPO in the aqueous liquid/vapor interfacial region. *The Journal of Physical Chemistry B*, *110*(12), 6101-6109.

Glandut, N., Monson, C. F., & Majda, M. (2006). Electrochemistry of TEMPO in the aqueous liquid/vapor interfacial region: Measurements of the lateral mobility and kinetics of surface partitioning. *Langmuir*, *22*(25), 10697-10704.

Glandut, N., Orlianges, J.C., and Bidron, G., (2015) Hydrogen evolution reaction at titanium carbide-supported, platinum-doped tetrahedral amorphous carbon array electrodes. EMN Ceramics Meeting 2015.

Gottlieb, E., Kopeć, M., Banerjee, M., Mohin, J., Yaron, D., Matyjaszewski, K., & Kowalewski, T. (2016). In-situ platinum deposition on nitrogen-doped carbon films as a

source of catalytic activity in a hydrogen evolution reaction. *ACS applied materials & interfaces*, 8(33), 21531-21538.

Gross, A. (2022). Reversible vs. standard hydrogen electrode scale in interfacial electrochemistry from a theoretician's atomistic point of view.

Han, Y., Yue, X., Jin, Y., Huang, X., & Shen, P. K. (2016). Hydrogen evolution reaction in acidic media on single-crystalline titanium nitride nanowires as an efficient non-noble metal electrocatalyst. *Journal of Materials Chemistry A*, 4(10), 3673-3677.

Hao, Y. M., Nakajima, H., Inada, A., Sasaki, K., & Ito, K. (2019). Overpotentials and reaction mechanism in electrochemical hydrogen pumps. *Electrochimica Acta*, *301*, 274-283.

Harding. R. (2021, July 12). High costs dog Tokyo's hydrogen buses. Financial Times. https://www.ft.com/content/2b9dd655-6b64-416c-a83f-1fe1002da7d5

Harriman, K., Gavaghan, D. J., Houston, P., & Süli, E. (2000). Adaptive finite element simulation of currents at microelectrodes to a guaranteed accuracy. Theory. *Electrochemistry Communications*, 2(3), 157-162.

He, L., Liu, J., Hu, B., Liu, Y., Cui, B., Peng, D., ... & Liu, B. (2019). Cobalt oxide doped with titanium dioxide and embedded with carbon nanotubes and graphene-like nanosheets for efficient trifunctional electrocatalyst of hydrogen evolution, oxygen reduction, and oxygen evolution reaction. *Journal of Power Sources*, 414, 333-344.

Huang, L., Dai, C., Liu, J., & Feng, Y., (2020). Optimization of electrode shape and influent mode of electrocatalytic reactor based on CFD simulation. *Chinese Journal of Environmental Engineering*, 14(10), 2742-2750.

Ito, Y., Cong, W., Fujita, T., Tang, Z., & Chen, M. (2015). High catalytic activity of nitrogen and sulfur co-doped nanoporous graphene in the hydrogen evolution reaction. *Angewandte Chemie*, *127*(7), 2159-2164.

Jeong, S., Mai, H. D., Nguyen, T. K., Youn, J. S., Nam, K. H., Park, C. M., & Jeon, K. J. (2021). Atomic interactions of two-dimensional PtS2 quantum dots/TiC heterostructures for hydrogen evolution reaction. *Applied Catalysis B: Environmental*, 293, 120227.

Jian, C., Cai, Q., Hong, W., Li, J., & Liu, W. (2018). Edge-Riched $MoSe_2/MoO_2$ Hybrid Electrocatalyst for Efficient Hydrogen Evolution Reaction. *Small*, 14(13), 1703798.

Jin, D., Johnson, L. R., Raman, A. S., Ming, X., Gao, Y., Du, F., ... & Meng, X. (2020). Computational screening of 2D ordered double transition-metal carbides (MXenes) as electrocatalysts for hydrogen evolution reaction. *The Journal of Physical Chemistry C*, 124(19), 10584-10592.

Kahyarian, A., Brown, B., & Nesic, S. (2017). Mechanism of the hydrogen evolution reaction in mildly acidic environments on gold. *Journal of The Electrochemical Society*, *164*(6), H365.

Kelly N.A., Hydrogen production via water electrolysis, Adv. in Hydrogen Production, Storage and Distribution, 2014, 159-185.

Kichigin, V. I., & Shein, A. B. (2015). Kinetics and mechanism of hydrogen evolution reaction on cobalt silicides in alkaline solutions. *Electrochimica Acta*, *164*, 260-266.

Kichigin, V. I., & Shein, A. B. (2020). The kinetics of hydrogen evolution reaction accompanied by hydrogen absorption reaction with consideration of subsurface hydrogen as an adsorbed species: Polarization curve. *Journal of Electroanalytical Chemistry*, *873*, 114427.

Koster, D., Zeradjanin, A. R., Battistel, A., & La Mantia, F. (2019). Extracting the kinetic parameters of the hydrogen evolution reaction at Pt in acidic media by means of dynamic multi-frequency analysis. *Electrochimica Acta*, *308*, 328-336.

Lakshmi, R. B., Harikrishnan, N. P., & Juliet, A. V. (2017). Comparative analysis of 2D and 3D models of a PEMFC in COMSOL. *Applied Surface Science*, 418, 99-102.

Lasia, A. (1974). Electrochemical reduction mechanism of phthalimide in DMF. *Journal of Electroanalytical Chemistry and Interfacial Electrochemistry*, *52*(2), 229-236.

Lasia, A. (2010). Hydrogen evolution reaction. *Handbook of fuel cells*, *815*.

Lasia, A. (2019). Mechanism and kinetics of the hydrogen evolution reaction. *international journal of hydrogen energy*, *44*(36), 19484-19518.

Laurila, T., & Caro, M. A. (2018). Special features of the electrochemistry of undoped tetrahedral amorphous carbon (ta-C) thin films. In *Encyclopedia of Interfacial Chemistry: Surface Science and Electrochemistry* (pp. 856-862). Elsevier.

Lavacchi, A., Bardi, U., Borri, C., Caporali, S., Fossati, A., & Perissi, I. (2009). Cyclic voltammetry simulation at microelectrode arrays with COMSOL Multiphysics®. *Journal of Applied Electrochemistry*, 39(11), 2159.

Lee, C., Wei, X., Kysar, J. W., & Hone, J. (2008). Measurement of the elastic properties and intrinsic strength of monolayer graphene. *science*, *321*(5887), 385-388.

Lee, J. H., Kattel, S., Jiang, Z., Xie, Z., Yao, S., Tackett, B. M., ... & Chen, J. G. (2019). Tuning the activity and selectivity of electroreduction of CO_2 to synthesis gas using bimetallic catalysts. *Nature communications*, *10*(1), 1-8.

Li, M. S., Filice, F. P., & Ding, Z. (2016). Determining live-cell topography by scanning electrochemical microscopy. *Journal of Electroanalytical Chemistry*, 779, 176-186.

Li, T., Liu, J., Song, Y., & Wang, F. (2018). Photochemical solid-phase synthesis of platinum single atoms on nitrogen-doped carbon with high loading as bifunctional catalysts for hydrogen evolution and oxygen reduction reactions. *ACS catalysis*, *8*(9), 8450-8458.

Li, W., Zhang, H., Zhang, K., Hu, W., Cheng, Z., Chen, H., ... & Kou, Z. (2022). Monodispersed Ruthenium Nanoparticles Interfacially Bonded with Defective Nitrogen-and-Phosphorus-Doped Carbon Nanosheets Enable pH-universal Hydrogen Evolution Reaction. *Applied Catalysis B: Environmental*, 121095.

Li, Z., Qi, Z., Wang, S., Ma, T., Zhou, L., Wu, Z., ... & Wu, Y. (2019). In situ formed Pt3Ti nanoparticles on a two-dimensional transition metal carbide (MXene) used as efficient catalysts for hydrogen evolution reactions. *Nano letters*, 19(8), 5102-5108

Lim. H. P. (2021, July 22). Sarawak launches its Post Covid-19 Development Strategy 2030. Borneo Post Online. https://www.theborneopost.com/2021/07/22/sarawak-launches-its-post-covid-19-development-strategy-2030/

Lin, D., & Lasia, A. (2017). Electrochemical impedance study of the kinetics of hydrogen evolution at a rough palladium electrode in acidic solution. *Journal of Electroanalytical Chemistry*, *785*, 190-195.

Liu, D., Li, X., Chen, S., Yan, H., Wang, C., Wu, C., ... & Song, L. (2019). Atomically dispersed platinum supported on curved carbon supports for efficient electrocatalytic hydrogen evolution. *Nature Energy*, *4*(6), 512-518.

Liu, Y., Ali, R., Ma, J., Jiao, W., Yin, L., Mu, C., & Jian, X. (2021). Graphene-Decorated Boron–Carbon–Nitride-Based Metal-Free Catalysts for an Enhanced Hydrogen Evolution Reaction. *ACS Applied Energy Materials*, *4*(4), 3861-3868.

Ludwig, K., & Speiser, B. (2006). EChem++–An object-oriented problem-solving environment for electrochemistry: Part 4. Adaptive multilevel finite elements applied to electrochemical models algorithm and benchmark calculations. *Journal of Electroanalytical Chemistry*, 588(1), 74-87.

Luo, R., Li, R., Jiang, C., Qi, R., Liu, M., Luo, C., ... & Peng, H. (2021). Facile synthesis of cobalt modified 2D titanium carbide with enhanced hydrogen evolution performance in alkaline media. *International Journal of Hydrogen Energy*, *46*(64), 32536-32545.

Ma, Y. Y., Lang, Z. L., Yan, L. K., Wang, Y. H., Tan, H. Q., Feng, K., ... & Li, Y. G. (2018). Highly efficient hydrogen evolution triggered by a multi-interfacial Ni/WC hybrid electrocatalyst. *Energy & Environmental Science*, 11(8), 2114-2123.

Malek Msheik, Sylvain Rodat, Stéphane Abanades. Methane Cracking for Hydrogen Production: A Review of Catalytic and Molten Media Pyrolysis. *Energies*, MDPI, 2021, 14, 10.3390/en14113107.

Manual, C. M. U. (2014). COMSOL Multiphysics.

Manikandan, A., Sriram, P., Hsu, K. C., Wang, Y. C., Chen, C. W., Shih, Y. C., ... & Chueh, Y. L. (2019). Electrochemically active novel amorphous carbon (aC)/Cu_3P peapod nanowires by low-temperature chemical vapor phosphorization reaction as high efficient electrocatalysts for hydrogen evolution reaction. *Electrochimica Acta*, 318, 374-383.

Mazloomi, K., & Gomes, C. (2012). Hydrogen as an energy carrier: Prospects and challenges. *Renewable and Sustainable Energy Reviews*, 16(5), 3024-3033.

Midilli, A., Kucuk, H., Topal, M. E., Akbulut, U., & Dincer, I. (2021). A comprehensive review on hydrogen production from coal gasification: Challenges and Opportunities. *International Journal of Hydrogen Energy*, *46*(50), 25385-25412.

Nady, H., El-Rabiei, M. M., Abd El-Hafez, G. M., & Fekry, A. M. (2021). Electrochemical determination of niobium cathode as an efficient electrocatalyst for hydrogen generation in acidic media. *International Journal of Hydrogen Energy*, *46*(42), 21785-21795.

Naragino, H., Yoshinaga, K., Nakahara, A., Tanaka, S., & Honda, K. (2013, June). Enhancement of electrical conductivity and electrochemical activity of hydrogenated amorphous carbon by incorporating boron atoms. In *Journal of Physics: Conference Series* (Vol. 441, No. 1, p. 012042). IOP Publishing.

Naterer, G. F., Dincer, I., & Zamfirescu, C. (2013). Nuclear Energy and Its Role in Hydrogen Production. In *Hydrogen Production from Nuclear Energy* (pp. 21-64). Springer, London.

Ngoh, S. K., & Njomo, D. (2012). An overview of hydrogen gas production from solar energy. *Renewable and Sustainable Energy Reviews*, *16*(9), 6782-6792.

Nichols, F., Liu, Q., Sandhu, J., Azhar, Z., Cazares, R., Mercado, R., ... & Chen, S. (2022). Platinum-complexed phosphorous-doped carbon nitride for electrocatalytic hydrogen evolution. *Journal of Materials Chemistry A*.

Nikam, R. D., Lu, A. Y., Sonawane, P. A., Kumar, U. R., Yadav, K., Li, L. J., & Chen, Y. T. (2015). Three-dimensional heterostructures of MoS_2 nanosheets on conducting MoO_2 as an efficient electrocatalyst to enhance hydrogen evolution reaction. *ACS applied materials & interfaces*, 7(41), 23328-23335.

Ning, X., Li, Y., Ming, J., Wang, Q., Wang, H., Cao, Y., ... & Yu, H. (2019). Electronic synergism of pyridinic-and graphitic-nitrogen on N-doped carbons for the oxygen reduction reaction. *Chemical science*, *10*(6), 1589-1596.

Park, J., Lee, S., Kim, H. E., Cho, A., Kim, S., Ye, Y., ... & Lee, J. (2019). Investigation of the support effect in atomically dispersed Pt on WO3− x for utilization of Pt in the hydrogen evolution reaction. *Angewandte Chemie International Edition*, 58(45), 16038-16042.

Pattni V. (2021, October 11). Toyota Mirai drives 845 miles on a tank of hydrogen, sets world record. Top Gear. https://www.topgear.com/car-news/electric/toyota-mirai-drives-845-miles-tank-hydrogen-sets-world-record

Pistorius M. (2021, October 5). France hopes to become world leader in green hydrogen. Euractiv. https://www.euractiv.com/section/politics/short_news/france-hopes-to-become-world-leader-in-green-hydrogen/

Program review report 2019 [Internet]. Brussels: European Commission; 2019 Available from: https://www.fch.europa.eu/publications/program-review-report-2019

Protopopova, V., Iyer, A., Wester, N., Kondrateva, A., Sainio, S., Palomäki, T., ... & Koskinen, J. (2015). Ultrathin undoped tetrahedral amorphous carbon films: The role of the underlying titanium layer on the electronic structure. *Diamond and Related Materials*, 57, 43-52.

Qu, L., Zhang, Z., Zhang, H., Zhang, H., & Dong, S. (2018). Transformation from graphitic C3N4 to nitrogen-boron-carbon ternary nanosheets as efficient metal-free bifunctional electrocatalyst for oxygen reduction reaction and hydrogen evolution reaction. *Applied Surface Science*, *448*, 618-627.

Qu, K., Zheng, Y., Zhang, X., Davey, K., Dai, S., & Qiao, S. Z. (2017). Promotion of electrocatalytic hydrogen evolution reaction on nitrogen-doped carbon nanosheets with secondary heteroatoms. *ACS nano*, *11*(7), 7293-7300.

Robinson, S. (1997, December). Simulation model verification and validation: increasing the users' confidence. In Proceedings of the 29th conference on Winter simulation (pp. 53-59).

Ruderman, A., Juarez, M. F., Soldano, G., Avalle, L. B., Beltramo, G., Giesen, M., & Santos, E. (2013). Current transients for the hydrogen evolution reaction at high overpotentials on silver electrodes in acid solutions: Experiments and modelling. *Electrochimica Acta*, *109*, 403-410.

Sathe, B. R., Zou, X., & Asefa, T. (2014). Metal-free B-doped graphene with efficient electrocatalytic activity for hydrogen evolution reaction. *Catalysis science & technology*, *4*(7), 2023-2030

Sahoo, S. K., Ye, Y., Lee, S., Park, J., Lee, H., Lee, J., & Han, J. W. (2018). Rational design of TiC-supported single-atom electrocatalysts for hydrogen evolution and selective oxygen reduction reactions. *ACS Energy Letters*, 4(1), 126-132.

Somasundaram, K., Birgersson, E., & Mujumdar, A. S. (2011). Analysis of a model for an electrochemical capacitor. *Journal of The Electrochemical Society*, 158(11), A1220.

Shervedani, R. K., & Amini, A. (2015). Sulfur-doped graphene as a catalyst support: influences of carbon black and ruthenium nanoparticles on the hydrogen evolution reaction performance. *Carbon*, *93*, 762-773

Skúlason, E., Tripkovic, V., Björketun, M. E., Gudmundsdóttir, S., Karlberg, G., Rossmeisl, J., ... & Nørskov, J. K. (2010). Modeling the electrochemical hydrogen oxidation and

evolution reactions on the basis of density functional theory calculations. *The Journal of Physical Chemistry C*, 114(42), 18182-18197.

Stallings, W. M., & Gillmore, G. M. (1971). A note on “accuracy” and “precision”. *Journal of Educational Measurement*, *8*(2), 127-129.

Song, M., Chen, D., Yang, Y., Xiang, M., Zhu, Q., Zhao, H., ... & Chen, X. B. (2021). Crystal Facet Engineering of Single-Crystalline TiC Nanocubes for Improved Hydrogen Evolution Reaction. *Advanced Functional Materials*, 31(6), 2008028.

Tang, H., Gu, H., Li, Z., Chai, J., Qin, F., Lu, C., ... & Chen, W. (2022). Engineering the Coordination Interface of Isolated Co Atomic Sites Anchored on N-Doped Carbon for Effective Hydrogen Evolution Reaction. *ACS Applied Materials & Interfaces*.

Trinh, D., & Touzain, S. (2014). Numerical simulation of the far-field boundaries onto a microdisk electrode using the infinite element. *Journal of Electroanalytical Chemistry*, 729, 1-8.

Tu, C. Y., & Wu, J. M. (2021). Localized surface plasmon resonance coupling with piezophototronic effect for enhancing hydrogen evolution reaction with Au@MoS_2 nanoflowers. *Nano Energy*, *87*, 106131.

Uchida, Y., Kätelhön, E., & Compton, R. G. (2017). Cyclic voltammetry with non-triangular waveforms: Electrochemically reversible systems. *Journal of Electroanalytical Chemistry*, 801, 381-387.

Uchida, Y., Kätelhön, E., & Compton, R. G. (2017). Cyclic voltammetry with non-triangular waveforms: Electrochemically reversible systems. *Journal of Electroanalytical Chemistry*, 801, 381-387.

Vilekar, S. A., Fishtik, I., & Datta, R. (2010). Kinetics of the hydrogen electrode reaction. *Journal of the electrochemical society*, *157*(7), B1040.

Vogel, Y. B., Darwish, N., Kashi, M. B., Gooding, J. J., & Ciampi, S. (2017). Hydrogen evolution during the electrodeposition of gold nanoparticles at Si (100) photoelectrodes impairs the analysis of current-time transients. *Electrochimica Acta*, *247*, 200-206.

Vyroubal, P., & Mačák, M. (2019). Investigation of Cyclic Voltammetry in Ansys Fluent. *ECS Transactions*, 95(1), 467.

Washburn, E. W., & Urey, H. C. (1932). Concentration of the H_2 isotope of hydrogen by the fractional electrolysis of water. *Proceedings of the National Academy of Sciences of the United States of America*, 18(7), 496.

Watzele, S., Fichtner, J., Garlyyev, B., Schwämmlein, J. N., & Bandarenka, A. S. (2018). On the dominating mechanism of the hydrogen evolution reaction at polycrystalline Pt electrodes in acidic media. *ACS Catalysis*, *8*(10), 9456-9462.

Wang, L., Lin, C., Huang, D., Chen, J., Jiang, L., Wang, M., ... & Jin, J. (2015). Optimizing the volmer step by single-layer nickel hydroxide nanosheets in hydrogen evolution reaction of platinum. *ACS Catalysis*, *5*(6), 3801-3806.

Wang, J. X., Springer, T. E., & Adzic, R. R. (2006). Dual-pathway kinetic equation for the hydrogen oxidation reaction on Pt electrodes. *Journal of the Electrochemical Society*, 153(9), A1732.

Wang, Y., Deng, H., Ye, C., Hu, K., & Yan, K. (2019). Facile synthesis of mesoporous TiC-C nanocomposite microsphere efficient for hydrogen evolution. *Journal of Alloys and Compounds*, 775, 348-352.

Wei, C., & Xu, Z. J. (2018). The comprehensive understanding of as an evaluation parameter for electrochemical water splitting. *Small Methods*, 2(11), 1800168.

Wong. J., (2020, November 16). Sarawak Energy, Petronas plan green hydrogen venture. The Star. https://www.thestar.com.my/business/business-news/2020/11/16/seb-ties-up-with-petronas

Xue, S., Haid, R. W., Kluge, R. M., Ding, X., Garlyyev, B., Fichtner, J., ... & Bandarenka, A. S. (2020). Enhancing the hydrogen evolution reaction activity of platinum electrodes in alkaline media using nickel–iron clusters. *Angewandte Chemie International Edition*, *59*(27), 10934-10938.

Yan, Q. Q., Wu, D. X., Chu, S. Q., Chen, Z. Q., Lin, Y., Chen, M. X., ... & Liang, H. W. (2019). Reversing the charge transfer between platinum and sulfur-doped carbon support for electrocatalytic hydrogen evolution. *Nature communications*, *10*(1), 1-9.

Yang, L., Wu, X., Zhu, X., He, C., Meng, M., Gan, Z., & Chu, P. K. (2015). Amorphous nickel/cobalt tungsten sulfide electrocatalysts for high-efficiency hydrogen evolution reaction. *Applied Surface Science*, 341, 149-156.

Yang, T. T., & Saidi, W. A. (2020). Graphene Activation Explains the Enhanced Hydrogen Evolution on Graphene-Coated Molybdenum Carbide Electrocatalysts. *The journal of physical chemistry letters*, 11(7), 2759-2764.

Yang, T. T., Tan, T. L., & Saidi, W. A. (2020). High Activity toward the Hydrogen Evolution Reaction on the Edges of MoS2-Supported Platinum Nanoclusters Using Cluster Expansion and Electrochemical Modeling. *Chemistry of Materials*, 32(3), 1315-1321.

Yoon, Y., Tiwari, A. P., Lee, M., Choi, M., Song, W., Im, J., ... & An, K. S. (2018). Enhanced electrocatalytic activity by chemical nitridation of two-dimensional titanium carbide MXene for hydrogen evolution. *Journal of Materials Chemistry A*, 6(42), 20869-20877.

Yunus. A., (2021, July 12). Assess value chain holistically to drive green economy agenda, says PM. News Straits Times. https://www.nst.com.my/news/nation/2021/07/710717/assess-value-chain-holistically-drive-green-economy-agenda-says-pm

Zhang, F., Zhu, Y., Chen, Y., Lu, Y., Lin, Q., Zhang, L., ... & Wang, H. (2020). RuCo alloy bimodal nanoparticles embedded in N-doped carbon: a superior pH-universal electrocatalyst outperforms benchmark Pt for the hydrogen evolution reaction. *Journal of Materials Chemistry A*, 8(25), 12810-12820.

Zhang, L., Si, R., Liu, H., Chen, N., Wang, Q., Adair, K., ... & Sun, X. (2019). Atomic layer deposited Pt-Ru dual-metal dimers and identifying their active sites for hydrogen evolution reaction. *Nature communications*, 10(1), 1-11.

Zhang, J., Zhao, Y., Guo, X., Chen, C., Dong, C. L., Liu, R. S., ... & Wang, G. (2018). Single platinum atoms immobilized on an MXene as an efficient catalyst for the hydrogen evolution reaction. *Nature Catalysis*, 1(12), 985-992.

Zhang, Z., Hao, J., Yang, W., & Tang, J. (2015). Defect-Rich CoP/Nitrogen-Doped Carbon Composites Derived from a Metal–Organic Framework: High-Performance Electrocatalysts for the Hydrogen Evolution Reaction. *ChemCatChem*, *7*(13), 1920-1925.

Zhao, X., Zhu, H., & Yang, X. (2014). Amorphous carbon supported MoS 2 nanosheets as effective catalysts for electrocatalytic hydrogen evolution. *Nanoscale*, *6*(18), 10680-10685.

Zhu, J., Hu, L., Zhao, P., Lee, L. Y. S., & Wong, K. Y. (2019). Recent advances in electrocatalytic hydrogen evolution using nanoparticles. *Chemical reviews*, 120(2), 851-918.

Zubair, M., Hassan, M. M. U., Mehran, M. T., Baig, M. M., Hussain, S., & Shahzad, F. (2021). 2D MXenes and their heterostructures for HER, OER and overall water splitting: a review. *International Journal of Hydrogen Energy*.

APPENDICES

Publications

1. Ramji, H. R., Glandut, N., Absi, J., Lim, S. F., & Khan, A. A. (2022, August). Comparative study of a transient redox reaction on a single electrode microdisk using finite element analysis. In *AIP Conference Proceedings* (Vol. 2610, No. 1, p. 030001). AIP Publishing LLC.
2. Ramji, H. R., Glandut, N., Absi, J., Lim, S. F., & Khan, A. A. (2023, February). Parametric study and analysis of Volmer-Heyrovsky-Tafel (VHT) steps for Hydrogen evolution reaction (HER). (to be Submitted)
3. Ramji, H. R., Glandut, N., Absi, J., Lim, S. F., & Khan, A. A. (2023, February). Hydrogen evolution reaction analysis of arrayed Platinum-doped tetrahedral amorphous carbon on Titanium carbide. (to be Submitted)

VHT 3D TICTAC

Report date	Dec 14, 2022 8:45:28 AM

CHAPTER 8 CONTENTS

1 Global Definitions

Date	Jun 11, 2022 12:49:03 PM

GLOBAL SETTINGS

Name	VHT 3D TiCtaC.mph
Path	D:\ramjip01\Desktop\Volmer Heyrovsky\VHT 3D TiCtaC.mph
Version	COMSOL Multiphysics 5.5 (Build: 359)
Unit system	SI

USED PRODUCTS

COMSOL Multiphysics
CAD Import Module

1.1 PARAMETERS

PARAMETERS 1

Name	Expression	Value	Description
n	1	1	
R	8.314[J/(mol*K)]	8.314 J/(mol·K)	
T	298.15[K]	298.15 K	
F	96485.3[C/mol]	96485 C/mol	

Name	Expression	Value	Description
kitaC	2.8e-6[s^(-1)/(mol/m^3)]	2.8E−6 m³/(s·mol)	
kiitaC	4.8e-8[s^(-1)/(mol/m^3)]	4.8E−8 m³/(s·mol)	
bitaC	0.25	0.25	
alitaC	1 - bitaC	0.75	
biitaC	0.82	0.82	
aliitaC	1 - biitaC	0.18	
E0itaC	0[V]	0 V	standard potential
E0iitaC	0[V]	0 V	
vb	1e-6[V/s]	1E−6 V/s	
Einit	0.5	0.5	
cstar	1000[mol/m^3]	1000 mol/m³	
Gmax	1e-5[mol/m^2]	1E−5 mol/m²	
tend	1e6	1E6	

Name	Expression	Value	Description
tstep	1e3	1000	
Erev	-0.5[V]	−0.5 V	
kiTiC	6.1e-7[s^(-1)/(mol/m^3)]	6.1E−7 $m^3/(s \cdot mol)$	
kiiTiC	1.09e-5[s^(-1)/(mol/m^3)]	1.09E−5 $m^3/(s \cdot mol)$	
biTiC	0.77	0.77	
aliTiC	1 - biTiC	0.23	
biiTiC	0.25	0.25	
aliiTiC	1 - biiTiC	0.75	
E0iTiC	0[V]	0 V	
E0iiTiC	0[V]	0 V	
DtaC	1e-8[m^2/s]	1E−8 m^2/s	
DTiC	1e-8[m^2/s]	1E−8 m^2/s	
side	100e-6[m]	1E−4 m	

Name	Expression	Value	Description
GmaxtaC	Gmax	1E−5 mol/m²	
GmaxTiC	Gmax	1E−5 mol/m²	
length	100e-6[m]	1E−4 m	
areaTot	length^2	1E−8 m²	
areataC	lengthtaC^2	2.5E−9 m²	
lengthtaC	50e-6[m]	5E−5 m	
areaTiC	areaTot - areataC	7.5E−9 m²	
lengthTiCtaC	100e-6[m]	1E−4 m	
areaTiCtaC	lengthTiCtaC*thickness	1E−11 m²	
kiTiCtaC	0.4[s^(-1)/(mol/m^3)]	0.4 m³/(s·mol)	
kiiTiCtaC	9[s^(-1)/(mol/m^3)]	9 m³/(s·mol)	
biTiCtaC	0.77	0.77	

Name	Expression	Value	Description
aliTiCtaC	1 - bitaC	0.75	
biiTiCtaC	0.25	0.25	
aliiTiCtaC	1 - biitaC	0.18	
E0iTiCtaC	0[V]	0 V	standard potential
E0iiTiCtaC	0[V]	0 V	
DTiCtaC	1e-8[m^2/s]	1E−8 m²/s	
kmiTiC	0[s^ - 1]	0 1/s	
kmiiTiC	0[m^3/mol*s^ - 1]	0 m³/(s·mol)	
H2	1[mol/m^3]	1 mol/m³	
kmitaC	0[s^ - 1]	0 1/s	
kmiitaC	0[m^3/mol*s^ - 1]	0 m³/(s·mol)	
kmiTiCtaC	4e-1[s^ - 1]	0.4 1/s	
kmiiTiCtaC	9e6[m^3/mol*s^ - 1]	9E6 m³/(s·mol)	
thickness	100e-9[m]	1E−7 m	

Name	Expression	Value	Description
kiiitaC	0[(m^2)/(mol*s)]	0 m²/(s·mol)	
kmiiitaC	0[(m^5)/((mol^2)*s)]	0 m⁵/(s·mol²)	
kiiiTiC	0[(m^2)/(mol*s)]	0 m²/(s·mol)	
kmiiiTiC	0[(m^5)/((mol^2)*s)]	0 m⁵/(s·mol²)	
kiiiTiCtaC	0[(m^2)/(mol*s)]	0 m²/(s·mol)	
kmiiiTiCtaC	0[(m^5)/((mol^2)*s)]	0 m⁵/(s·mol²)	

2 Component 1

Date	May 24, 2021 2:35:24 PM

SETTINGS

Description	Value
Unit system	Same as global system
Geometry shape order	Automatic

SPATIAL FRAME COORDINATES

First	Second	Third
x	y	z

MATERIAL FRAME COORDINATES

First	Second	Third
X	Y	Z

GEOMETRY FRAME COORDINATES

First	Second	Third
Xg	Yg	Zg

MESH FRAME COORDINATES

First	Second	Third
Xm	Ym	Zm

2.1 DEFINITIONS

2.1.1 Variables

8.1.1 Variables 1

SELECTION

Geometric entity level	Entire model

Name	Expression	Unit	Description
KitaC	kitaC*exp(((-bitaC*n*F)/(R*T))*(Et - E0itaC))	m³/(s·mol)	
KiitaC	kiitaC*exp(((-biitaC*n*F)/(R*T))*(Et - E0iitaC))	m³/(s·mol)	
RitaC	KitaC*cstar*(Gmax - u) - (KmitaC*u)	mol/(m²·s)	
RiitaC	KiitaC*cstar*u - (KmiitaC*H2*(Gmax - u))	mol/(m²·s)	
Et	abs(vb*t + Erev - Einit) + Erev	V	
CurrenttaC	-F*intop1(RitaC + RiitaC)	A	
KiTiC	kiTiC*exp(((-biTiC*n*F)/(R*T))*(Et - E0iTiC))	m³/(s·mol)	
KiiTiC	kiiTiC*exp(((-biiTiC*n*F)/(R*T))*(Et - E0iiTiC))	m³/(s·mol)	
RiTiC	KiTiC*cstar*(Gmax - u) - (KmiTiC*u)	mol/(m²·s)	

Name	Expression	Unit	Description
RiiTiC	(KiiTiC*cstar*u) - (KmiiTiC*H2*(Gmax - u))	mol/(m²·s)	
CurrentTiC	-F*intop2(RiTiC + RiiTiC)	A	
TotalCurrent	CurrenttaC + CurrentTiC + CurrentTiCtaC	A	
JtaC	-2*F*Gmax*cstar*((KitaC*KiitaC)/(KitaC + KiitaC))	A/m²	
JTiC	-2*F*Gmax*cstar*((KiTiC*KiiTiC)/(KiTiC + KiiTiC))	A/m²	
KiTiCtaC	kiTiCtaC*exp(((-biTiCtaC*n*F)/(R*T))*(Et - E0iTiCtaC))	m³/(s·mol)	
KiiTiCtaC	kiiTiCtaC*exp(((-biiTiCtaC*n*F)/(R*T))*(Et - E0iiTiCtaC))	m³/(s·mol)	
RiTiCtaC	KiTiCtaC*cstar*(Gmax - u) - (KmiTiCtaC*u)	mol/(m²·s)	
RiiTiCtaC	KiiTiCtaC*cstar*u - (KmiiTiCtaC*H2*(Gmax - u))	mol/(m²·s)	

Name	Expression	Unit	Description
CurrentTiCtaC	-F*intop3(RiTiCtaC + RiiTiCtaC)	A	
KmiTiC	kmiTiC*exp((((1 - biTiC)*n*F)/(R*T))*(Et - E0iTiC))	1/s	
KmiiTiC	kmiiTiC*exp((((1 - biiTiC)*n*F)/(R*T))*(Et - E0iiTiC))	m³/(s·mol)	
KmitaC	kmitaC*exp((((1 - bitaC)*n*F)/(R*T))*(Et - E0itaC))	1/s	
KmiitaC	kmiitaC*exp((((1 - biitaC)*n*F)/(R*T))*(Et - E0iitaC))	m³/(s·mol)	
KmiTiCtaC	kmiTiCtaC*exp((((1 - biTiCtaC)*n*F)/(R*T))*(Et - E0iTiCtaC))	1/s	
KmiiTiCtaC	kmiiTiCtaC*exp((((1 - biiTiCtaC)*n*F)/(R*T))*(Et - E0iiTiCtaC))	m³/(s·mol)	
RiiitaC	kiiitaC*(u^2) - kmiiitaC*H2*(Gmax - u)^2	mol/(m²·s)	
RiiiTiC	kiiiTiC*(u^2) - kmiiiTiC*H2*(Gmax - u)^2	mol/(m²·s)	

Name	Expression	Unit	Description
RiiiTiCtaC	kiiiTiC*(u^2) - kmiiiTiC*H2*(Gmax - u)^2	mol/(m²·s)	

2.1.2 Nonlocal Couplings

8.1.2 Integration 1

Coupling type	Integration
Operator name	intop1

SELECTION

Geometric entity level	Boundary
Selection	Geometry geom1: Dimension 2: Boundary 3

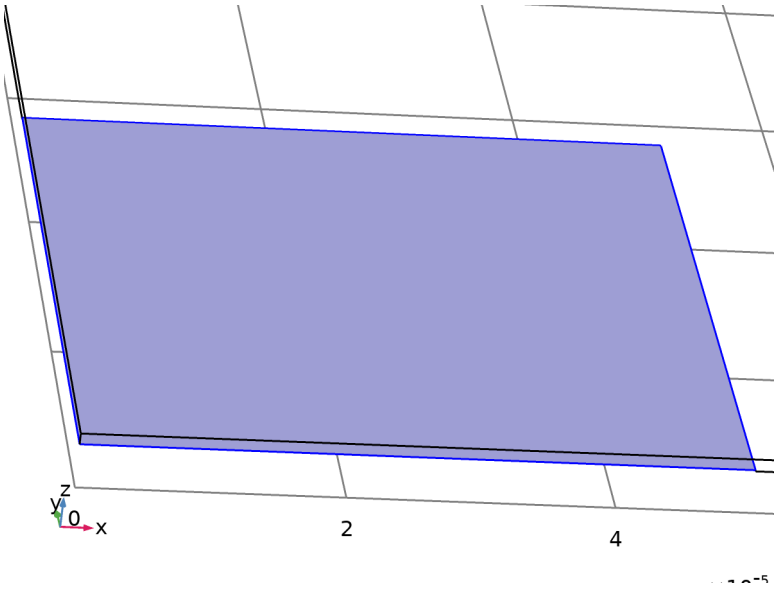

Selection

8.1.3 Integration 2

Coupling type	Integration
Operator name	intop2

SELECTION

Geometric entity level	Boundary
Selection	Geometry geom1: Dimension 2: Boundary 6

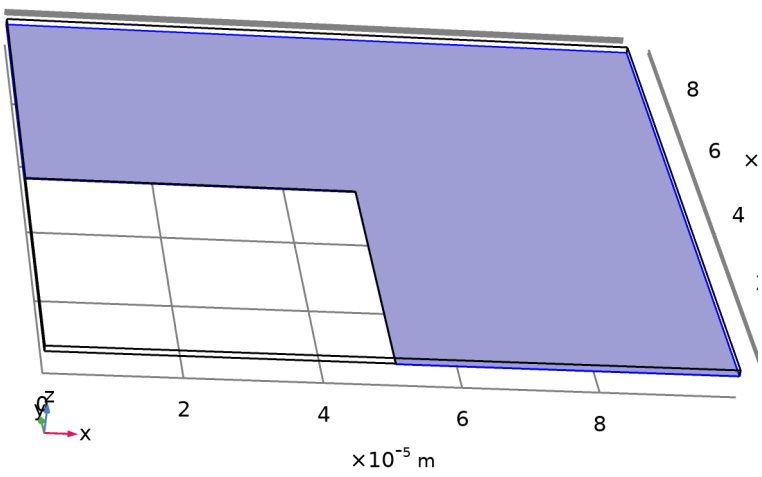

Selection

8.1.4 Integration 3

Coupling type	Integration
Operator name	intop3

SELECTION

Geometric entity level	Boundary

Selection	Geometry geom1: Dimension 2: Boundaries 5, 8

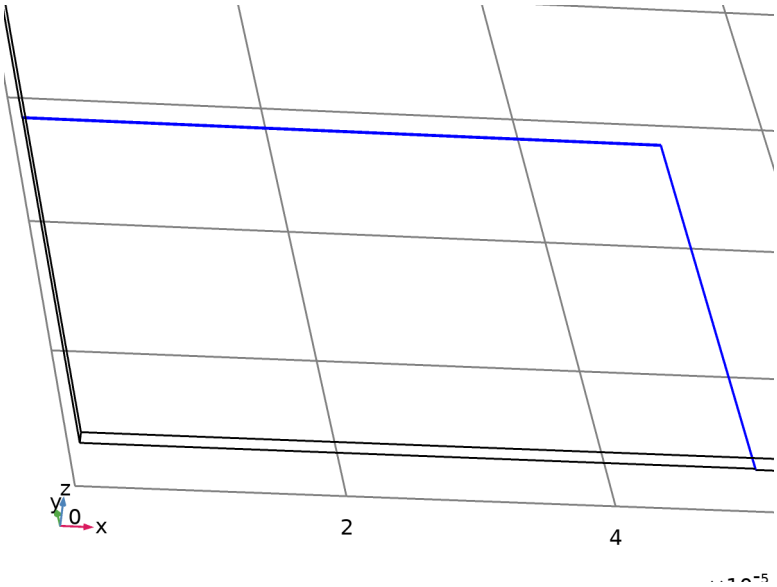

Selection

2.1.3 Coordinate Systems

8.1.5 Boundary System 1

Coordinate system type	Boundary system
Tag	sys1

COORDINATE NAMES

First	Second	Third
t1	t2	n

2.2 GEOMETRY 1

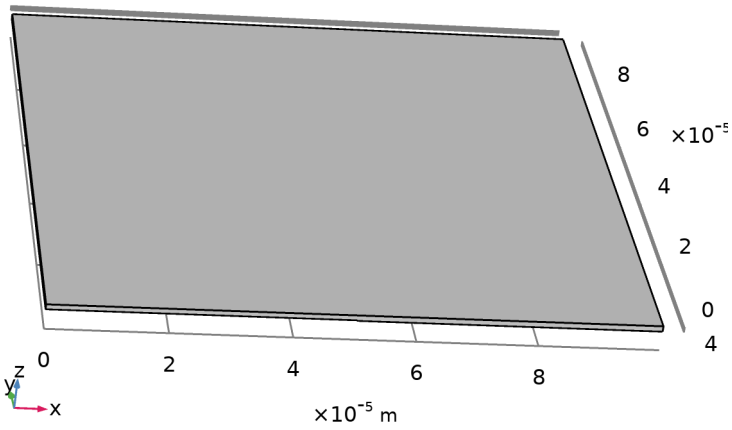

Geometry 1

UNITS

Length unit	m
Angular unit	deg

GEOMETRY STATISTICS

Description	Value
Space dimension	3
Number of domains	1
Number of boundaries	9
Number of edges	21
Number of vertices	14

2.2.1 Block 1 (blk1)

POSITION

Description	Value
Position	{0, 0, 0}

AXIS

Description	Value
Axis type	z - axis

SIZE AND SHAPE

Description	Value
Width	100e-6
Depth	100e-6
Height	1e-6

2.2.2 Block 2 (blk2)

POSITION

Description	Value
Position	{0, 0, 0}

AXIS

Description	Value
Axis type	z - axis

SIZE AND SHAPE

Description	Value
Width	50e-6

Description	Value
Depth	50e-6
Height	thickness

2.2.3 Difference 1 (dif1)

COMPOSE

Description	Value
Keep interior boundaries	Off

2.3 TRANSPORT OF DILUTED SPECIES

USED PRODUCTS

COMSOL Multiphysics

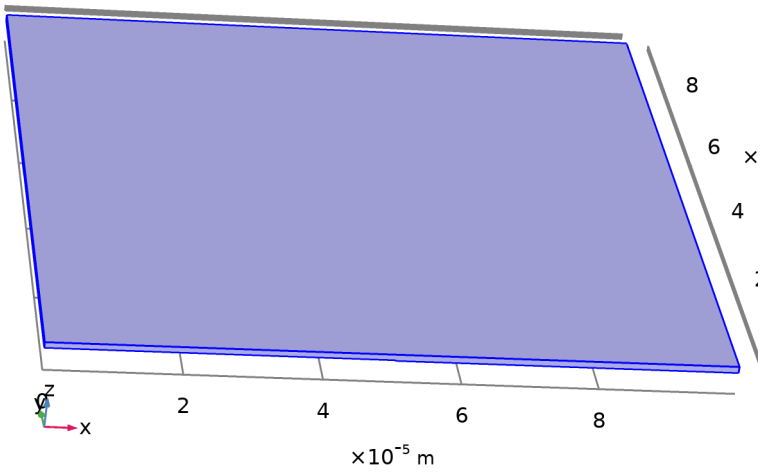

Transport of Diluted Species

SELECTION

Geometric entity level	Domain
Selection	Geometry geom1: Dimension 3: All domains

EQUATIONS

$$\frac{\partial c_i}{\partial t} + \nabla \cdot \mathbf{J}_i = R_i$$
$$\mathbf{J}_i = -D_i \nabla c_i$$

2.3.1 Interface settings

8.1.6 Discretization

SETTINGS

Description	Value
Concentration	Linear

8.1.7 Transport mechanisms

SETTINGS

Description	Value
Convection	Off

2.3.2 Variables

Name	Expression	Unit	Description	Selection	Details
tds.R_c	0	mol/(m³·s)	Total rate expression	Domain 1	+ operation
tds.cP_c	0	mol/kg	Concentration species absorbed to the solid	Domain 1	+ operation

Name	Expression	Unit	Description	Selection	Details
tds.cP_c	0	mol/kg	Concentration species absorbed to the solid	Boundaries 1–9	+ operation
tds.KP_c	0	m^3/kg	Adsorption isotherm, first concentration derivative	Domain 1	+ operation
tds.KP_c	0	m^3/kg	Adsorption isotherm, first concentration derivative	Boundaries 1–9	+ operation
tds.epsilon_p	1	1	Porosity	Domain 1	
tds.theta	tds.epsilon_p	1	Liquid volume fraction	Domain 1	
tds.av	0	1	Gas volume fraction	Domain 1	
tds.nx	dnx	1	Normal vector, x component	Boundaries 1–9	

Name	Expression	Unit	Description	Selection	Details
tds.ny	dny	1	Normal vector, y component	Boundaries 1–9	
tds.nz	dnz	1	Normal vector, z component	Boundaries 1–9	
tds.nxmesh	dnxmesh	1	Normal vector (mesh), x component	Boundaries 1–9	
tds.nymesh	dnymesh	1	Normal vector (mesh), y component	Boundaries 1–9	
tds.nzmesh	dnzmesh	1	Normal vector (mesh), z component	Boundaries 1–9	
tds.nxc	root.nxc/tds.ncLen	1	Normal vector, x component	Boundaries 1–9	
tds.nyc	root.nyc/tds.ncLen	1	Normal vector, y component	Boundaries 1–9	
tds.nzc	root.nzc/tds.ncLen	1	Normal vector, z component	Boundaries 1–9	

Name	Expression	Unit	Description	Selection	Details
tds.ncLen	sqrt(root.nxc^2+ root.nyc^2+root. nzc^2+eps)	1	Help variable	Boundaries 1–9	

2.3.3 Transport Properties 1

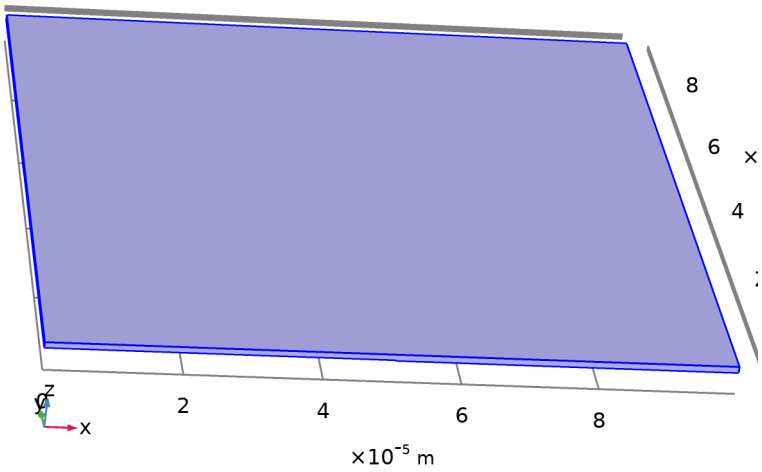

Transport Properties 1

SELECTION

Geometric entity level	Domain
Selection	Geometry geom1: Dimension 3: All domains

EQUATIONS

$$\frac{\partial c_i}{\partial t} + \nabla \cdot \mathbf{J}_i = R_i$$

$$\mathbf{J}_i = -D_i \nabla c_i$$

8.1.8 Diffusion

SETTINGS

Description	Value
Material	None
Diffusion coefficient	User defined
Diffusion coefficient	{{1e-8[m^2/s], 0, 0}, {0, 1e-8[m^2/s], 0}, {0, 0, 1e-8[m^2/s]}}

8.1.9 Coordinate system selection

SETTINGS

Description	Value
Coordinate system	Global coordinate system

8.1.10 Model input

SETTINGS

Description	Value
Temperature	Common model input

8.1.11 Variables

Name	Expression	Unit	Description	Selection	Details
domflux.cx	tds.dflux_cx	mol/(m²·s)	Domain flux, x component	Domain 1	
domflux.cy	tds.dflux_cy	mol/(m²·s)	Domain flux, y component	Domain 1	

Name	Expression	Unit	Description	Selection	Details
domflux.cz	tds.dflux_cz	mol/(m²·s)	Domain flux, z component	Domain 1	
tds.ndflux_c	tds.bndFlux_c	mol/(m²·s)	Normal diffusive flux	Boundaries 1–9	
tds.ntflux_c	tds.bndFlux_c	mol/(m²·s)	Normal total flux	Boundaries 1–9	
tds.bndFlux_c	-dflux_spatial(c)	mol/(m²·s)	Boundary flux	Boundaries 1–9	
tds.D_cxx	1.0E-8[m^2/s]	m²/s	Diffusion coefficient, xx component	Domain 1	+ operation
tds.D_cyx	0	m²/s	Diffusion coefficient, yx component	Domain 1	+ operation
tds.D_czx	0	m²/s	Diffusion coefficient, zx component	Domain 1	+ operation
tds.D_cxy	0	m²/s	Diffusion coefficient, xy component	Domain 1	+ operation

Name	Expression	Unit	Description	Selection	Details
tds.D_cyy	1.0E-8[m^2/s]	m²/s	Diffusion coefficient, yy component	Domain 1	+ operation
tds.D_czy	0	m²/s	Diffusion coefficient, zy component	Domain 1	+ operation
tds.D_cxz	0	m²/s	Diffusion coefficient, xz component	Domain 1	+ operation
tds.D_cyz	0	m²/s	Diffusion coefficient, yz component	Domain 1	+ operation
tds.D_czz	1.0E-8[m^2/s]	m²/s	Diffusion coefficient, zz component	Domain 1	+ operation
tds.Dav_c	(tds.D_cxx+tds.D_cyy+tds.D_czz)/3	m²/s	Average diffusion coefficient	Domain 1	
tds.tflux_cx	tds.dflux_cx	mol/(m²·s)	Total flux, x component	Domain 1	+ operation

Name	Expression	Unit	Description	Selection	Details
tds.tflux_cy	tds.dflux_cy	mol/(m²·s)	Total flux, y component	Domain 1	+ operation
tds.tflux_cz	tds.dflux_cz	mol/(m²·s)	Total flux, z component	Domain 1	+ operation
tds.dfluxMag_c	sqrt(tds.dflux_cx^2+tds.dflux_cy^2+tds.dflux_cz^2)	mol/(m²·s)	Diffusive flux magnitude	Domain 1	
tds.tfluxMag_c	sqrt(tds.tflux_cx^2+tds.tflux_cy^2+tds.tflux_cz^2)	mol/(m²·s)	Total flux magnitude	Domain 1	
tds.dflux_cx	-tds.D_cxx*cx-tds.D_cxy*cy-tds.D_cxz*cz	mol/(m²·s)	Diffusive flux, x component	Domain 1	
tds.dflux_cy	-tds.D_cyx*cx-tds.D_cyy*cy-tds.D_cyz*cz	mol/(m²·s)	Diffusive flux, y component	Domain 1	
tds.dflux_cz	-tds.D_czx*cx-tds.D_czy*cy-tds.D_czz*cz	mol/(m²·s)	Diffusive flux, z component	Domain 1	

Name	Expression	Unit	Description	Selection	Details
tds.grad_cx	cx	mol/m⁴	Concentration gradient, x component	Domain 1	
tds.grad_cy	cy	mol/m⁴	Concentration gradient, y component	Domain 1	
tds.grad_cz	cz	mol/m⁴	Concentration gradient, z component	Domain 1	
tds.Res_c	d(c,t)-tds.R_c	mol/(m³·s)	Equation residual	Domain 1	

8.1.12 Shape functions

Name	Shape function	Unit	Description	Shape frame	Selection
c	Lagrange (Linear)	mol/m³	Concentration	Spatial	Domain 1

8.1.13 Weak expressions

Weak expression	Integration order	Integration frame	Selection
-ct*test(c)+tds.dflux_cx*test(cx)	2	Spatial	Domain 1

Weak expression	Integration order	Integration frame	Selection
+tds.dflux_cy*test(cy)+tds.dflux_cz*test(cz)			
tds.streamline*(isScalingSystemDomain==0)	2	Spatial	Domain 1
tds.crosswind*(isScalingSystemDomain==0)	4	Spatial	Domain 1

2.3.4 No Flux 1

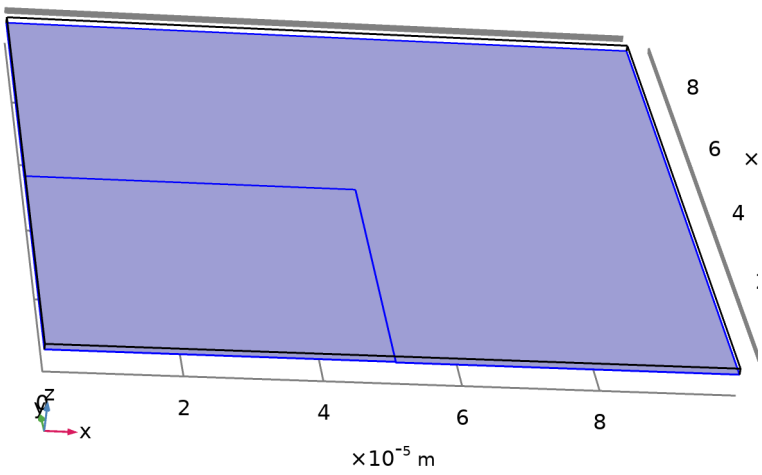

No Flux 1

SELECTION

Geometric entity level	Boundary
Selection	Geometry geom1: Dimension 2: All boundaries

EQUATIONS

$$-\mathbf{n} \cdot \mathbf{J}_i = 0$$

2.3.5 Initial Values 1

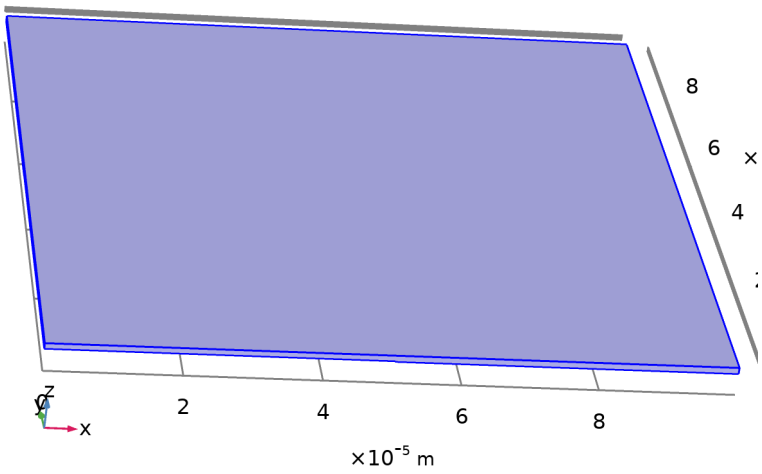

Initial Values 1

SELECTION

Geometric entity level	Domain
Selection	Geometry geom1: Dimension 3: All domains

8.1.14 Initial values

SETTINGS

Description	Value
Concentration	cstar

2.3.6 Symmetry 1

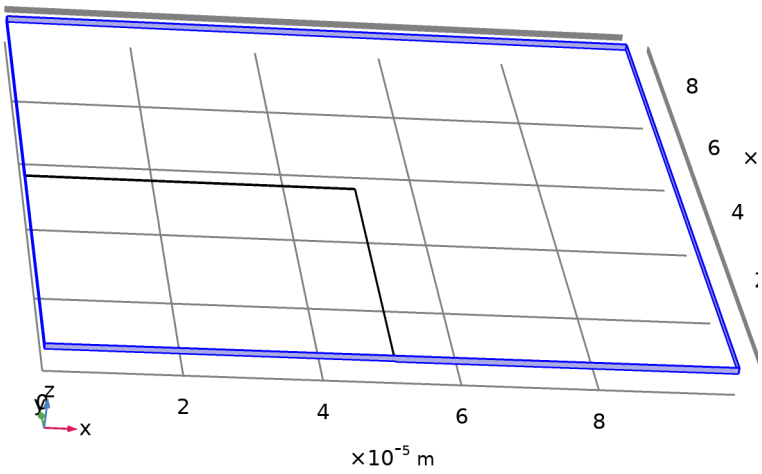

Symmetry 1

SELECTION

Geometric entity level	Boundary
Selection	Geometry geom1: Dimension 2: Boundaries 1–2, 7, 9

EQUATIONS

$-\mathbf{n} \cdot \mathbf{J}_i = 0$

2.3.7 Concentration 1

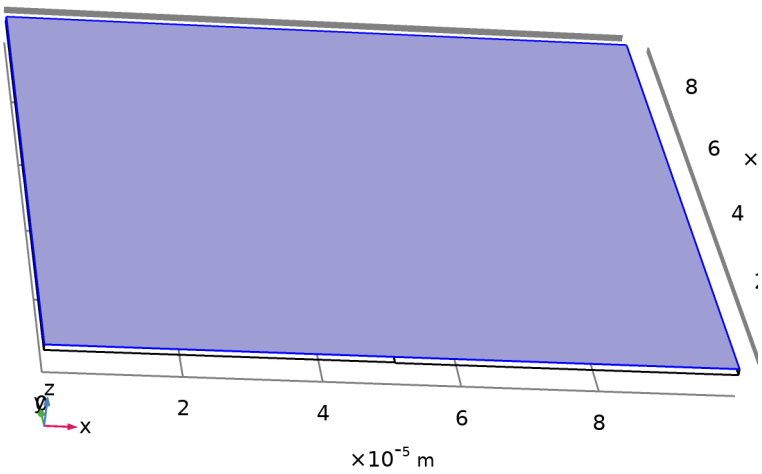

Concentration 1

SELECTION

Geometric entity level	Boundary
Selection	Geometry geom1: Dimension 2: Boundary 4

EQUATIONS

$c_i = c_{0,i}$

8.1.15 Concentration

SETTINGS

Description	Value
Species c	On
Concentration	cstar

8.1.16 Variables

Name	Expression	Unit	Description	Selection
tds.c0_c	cstar	mol/m³	Concentration	Boundary 4

8.1.17 Constraints

Constraint	Constraint force	Shape function	Selection	Details
-c+tds.c0_c	test(-c+tds.c0_c)	Lagrange (Linear)	Boundary 4	Elemental

2.4 GENERAL FORM BOUNDARY PDE

USED PRODUCTS

COMSOL Multiphysics

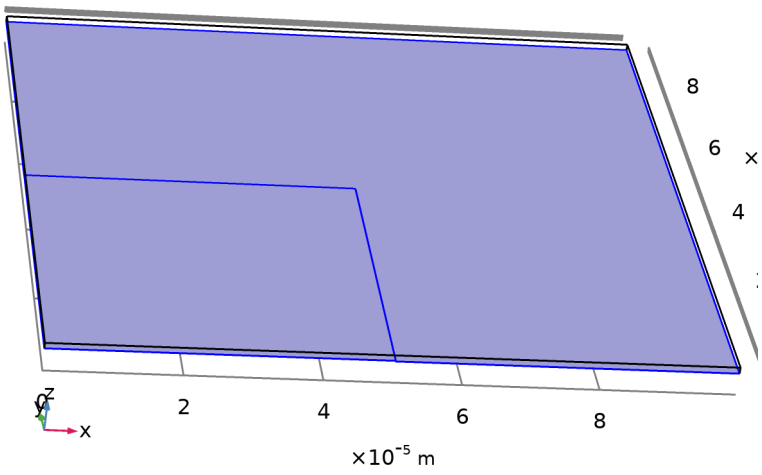

General Form Boundary PDE

SELECTION

Geometric entity level	Boundary

Selection	Geometry geom1: Dimension 2: Boundaries 3, 5–6, 8

2.4.1 Interface settings

8.1.18 Discretization

SETTINGS

Description	Value
Shape function type	Lagrange
Element order	Quadratic
Frame	Spatial

8.1.19 Units

Dependent variable quantity	Unit
Custom unit	mol/(m^2)

Source term quantity	Unit
Custom unit	mol/((m^2)*s)

2.4.2 taC:Pt

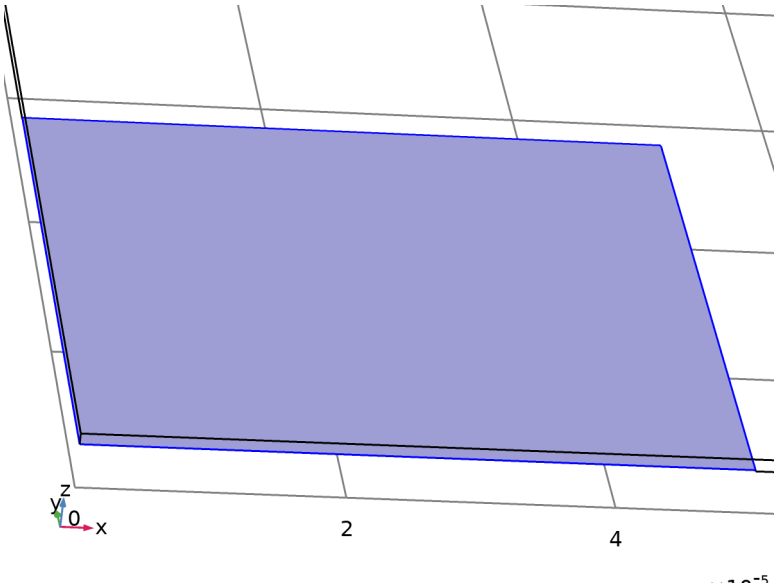

taC:Pt

SELECTION

Geometric entity level	Boundary
Selection	Geometry geom1: Dimension 2: All boundaries

EQUATIONS

$$e_a\frac{\partial^2 u}{\partial t^2}+d_a\frac{\partial u}{\partial t}+\nabla\cdot\Gamma=f$$

$$\nabla=[\frac{\partial}{\partial x},\frac{\partial}{\partial y},\frac{\partial}{\partial z}]$$

SETTINGS

Description	**Value**
Source term	RitaC - RiitaC - (2*RiiitaC)
Conservative flux	{-uTx*DtaC, -uTy*DtaC, -uTz*DtaC}
Mass coefficient	0
Damping or mass coefficient	1

8.1.20 Variables

Name	Expression	Unit	Description	Selection
domflux.ux	-uTx*DtaC	mol/(m·s)	Domain flux, x component	Boundary 3
domflux.uy	-uTy*DtaC	mol/(m·s)	Domain flux, y component	Boundary 3
domflux.uz	-uTz*DtaC	mol/(m·s)	Domain flux, z component	Boundary 3

8.1.21 Shape functions

Name	Shape function	Unit	Description	Shape frame	Selection
u	Lagrange (Quadratic)	mol/m²	Dependent variable u	Spatial	Boundary 3

2.4.3 Initial Values 1

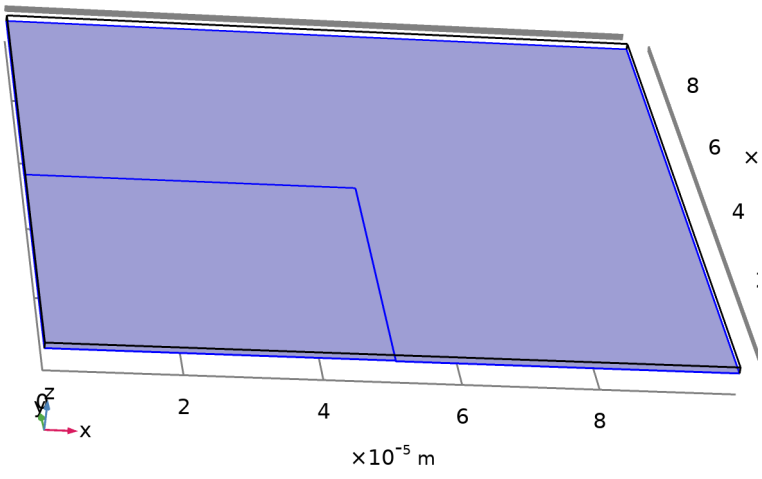

Initial Values 1

SELECTION

Geometric entity level	Boundary
Selection	Geometry geom1: Dimension 2: All boundaries

SETTINGS

Description	Value
Initial value for u	0
Initial time derivative of u	0

2.4.4 TiC

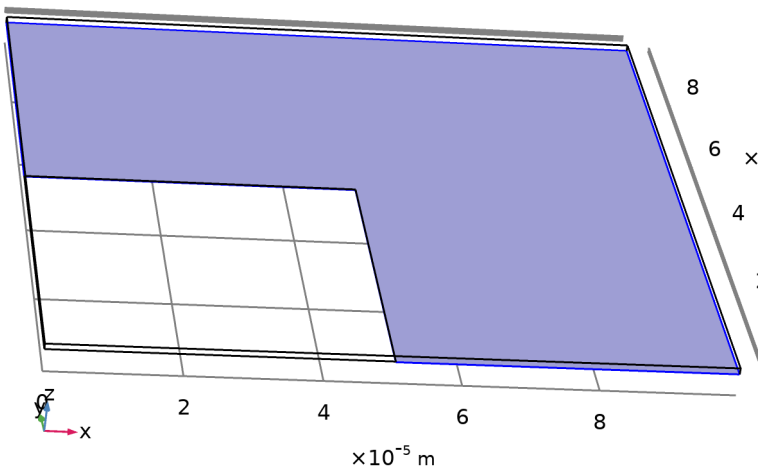

TiC

SELECTION

Geometric entity level	Boundary
Selection	Geometry geom1: Dimension 2: Boundary 6

EQUATIONS

$$e_a\frac{\partial^2 u}{\partial t^2}+d_a\frac{\partial u}{\partial t}+\nabla\cdot\Gamma=f$$

$$\nabla=[\frac{\partial}{\partial x},\frac{\partial}{\partial y},\frac{\partial}{\partial z}]$$

SETTINGS

Description	Value
Source term	RiTiC - RiiTiC - (2*RiiiTiC)
Conservative flux	{-uTx*DTiC, -uTy*DTiC, -uTz*DTiC}
Mass coefficient	0
Damping or mass coefficient	1

8.1.22 Variables

Name	Expression	Unit	Description	Selection
domflux.ux	-uTx*DTiC	mol/(m·s)	Domain flux, x component	Boundary 6
domflux.uy	-uTy*DTiC	mol/(m·s)	Domain flux, y component	Boundary 6
domflux.uz	-uTz*DTiC	mol/(m·s)	Domain flux, z component	Boundary 6

8.1.23 Shape functions

Name	Shape function	Unit	Description	Shape frame	Selection
u	Lagrange (Quadratic)	mol/m²	Dependent variable u	Spatial	Boundary 6

2.4.5 edge

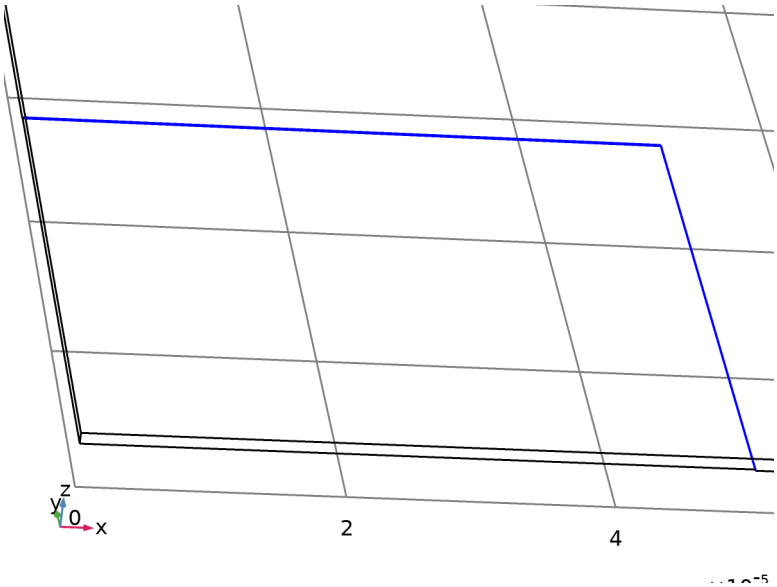

edge

SELECTION

Geometric entity level	Boundary
Selection	Geometry geom1: Dimension 2: Boundaries 5, 8

EQUATIONS

$$e_a\frac{\partial^2 u}{\partial t^2}+d_a\frac{\partial u}{\partial t}+\nabla\cdot\Gamma=f$$

$$\nabla=[\frac{\partial}{\partial x},\frac{\partial}{\partial y},\frac{\partial}{\partial z}]$$

SETTINGS

Description	**Value**
Source term	RiTiCtaC - RiiTiCtaC - (2*RiiiTiC)
Conservative flux	{-uTx*DTiCtaC, -uTy*DTiCtaC, -uTz*DTiCtaC}
Mass coefficient	0
Damping or mass coefficient	1

8.1.24 Variables

Name	Expression	Unit	Description	Selection
domflux.ux	-uTx*DTiCtaC	mol/(m·s)	Domain flux, x component	Boundaries 5, 8
domflux.uy	-uTy*DTiCtaC	mol/(m·s)	Domain flux, y component	Boundaries 5, 8
domflux.uz	-uTz*DTiCtaC	mol/(m·s)	Domain flux, z component	Boundaries 5, 8

8.1.25 Shape functions

Name	Shape function	Unit	Description	Shape frame	Selection
u	Lagrange (Quadratic)	mol/m²	Dependent variable u	Spatial	Boundaries 5, 8

2.5 MESH 1

MESH STATISTICS

Description	Value
Minimum element quality	0.187

Description	Value
Average element quality	0.6472
Tetrahedron	36779
Triangle	22826
Edge element	1038
Vertex element	14

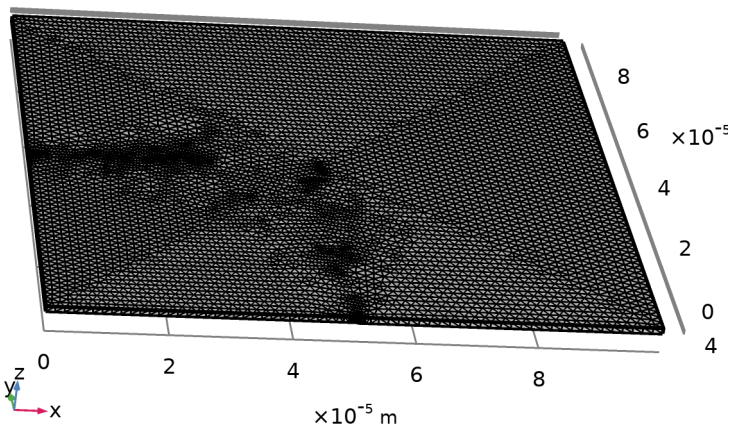

Mesh 1

2.5.1 Size (size)

SETTINGS

Description	Value
Maximum element size	8.0E-6
Minimum element size	1.0E-6
Curvature factor	0.5

Description	Value
Resolution of narrow regions	0.6
Maximum element growth rate	1.45
Predefined size	Fine

2.5.2 Free Tetrahedral 1 (ftet1)

SELECTION

Geometric entity level	Domain
Selection	Remaining

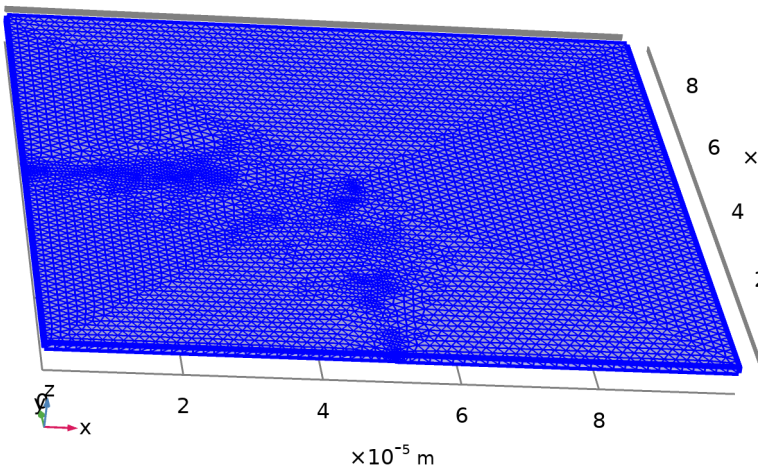

Free Tetrahedral 1

8.1.26 Size 1 (size1)

SELECTION

Geometric entity level	Boundary
Selection	Geometry geom1: Dimension 2: Boundaries 5, 8

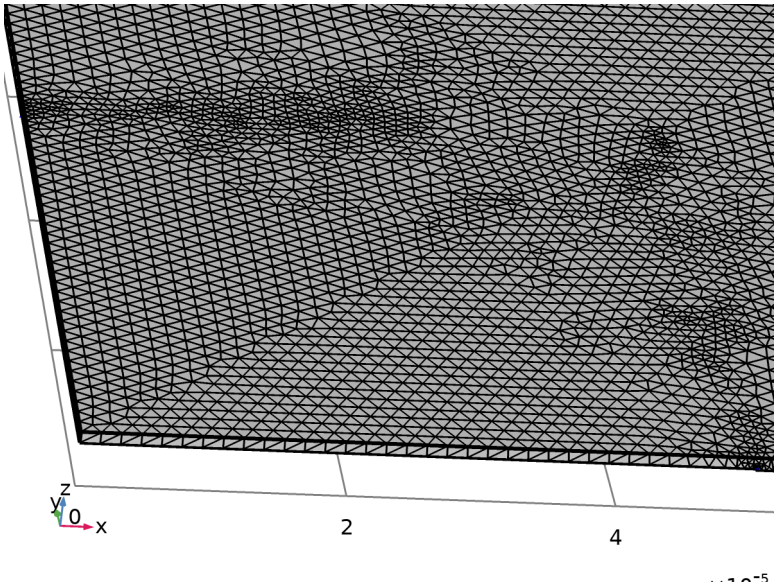

Size 1

SETTINGS

Description	**Value**
Maximum element size	5.5E-6
Minimum element size	4.0E-7
Curvature factor	0.4
Resolution of narrow regions	0.7
Maximum element growth rate	1.4
Predefined size	Finer

3 Study 1

COMPUTATION INFORMATION

Computation time	44 min 48 s
CPU	Intel64 Family 6 Model 79 Stepping 1, 20 cores
Operating system	Windows 10

3.1 PARAMETRIC SWEEP

Parameter name	Parameter value list	Parameter unit
DTiC	1e-12,1e-8,1e-6	m^2/s
DtaC	1e-12,1e-8,1e-6	m^2/s
DTiCtaC	1e-12,1e-8,1e-6	m^2/s

STUDY SETTINGS

Description	Value
Sweep type	Specified combinations
Parameter name	{DTiC, DtaC, DTiCtaC}
Unit	{m^2/s, m^2/s, m^2/s}

PARAMETERS

Parameter name	Parameter value list	Parameter unit
DTiC	1e-12,1e-8,1e-6	m^2/s
DtaC	1e-12,1e-8,1e-6	m^2/s
DTiCtaC	1e-12,1e-8,1e-6	m^2/s

4 Results

4.1 DATASETS

4.1.1 Study 1/Solution 1

SOLUTION

Description	Value
Solution	Solution 1
Component	Save Point Geometry 1

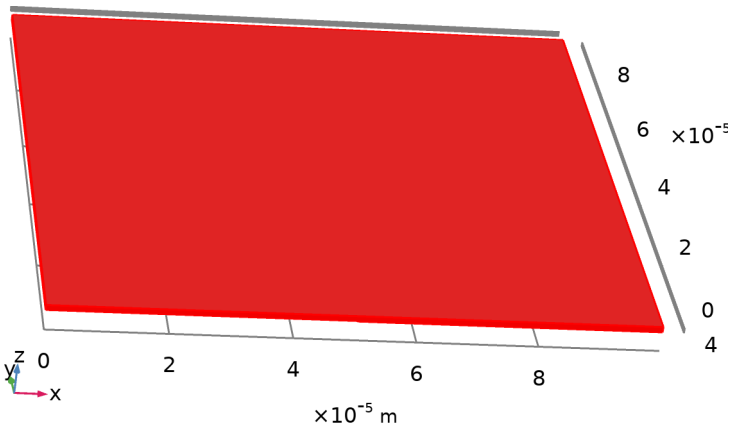

Dataset: Study 1/Solution 1

4.1.2 Study 1/Parametric Solutions 1

SOLUTION

Description	Value
Solution	Parametric Solutions 1
Component	Save Point Geometry 1

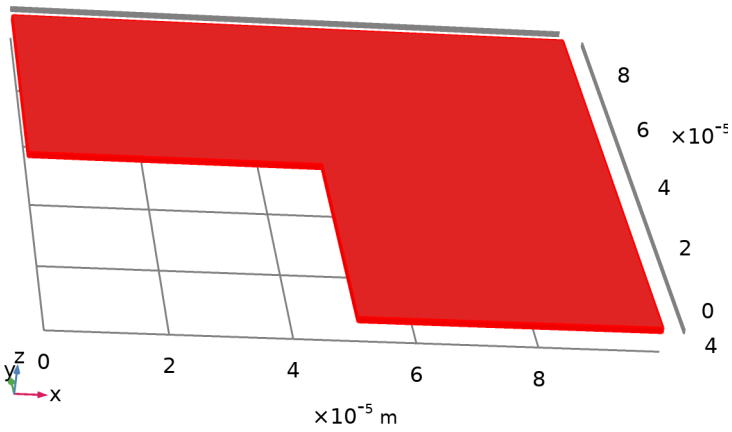

Dataset: Study 1/Parametric Solutions 1

4.1.3 Study 1/Parametric Solutions 2

SOLUTION

Description	Value
Solution	Parametric Solutions 2
Component	Save Point Geometry 1

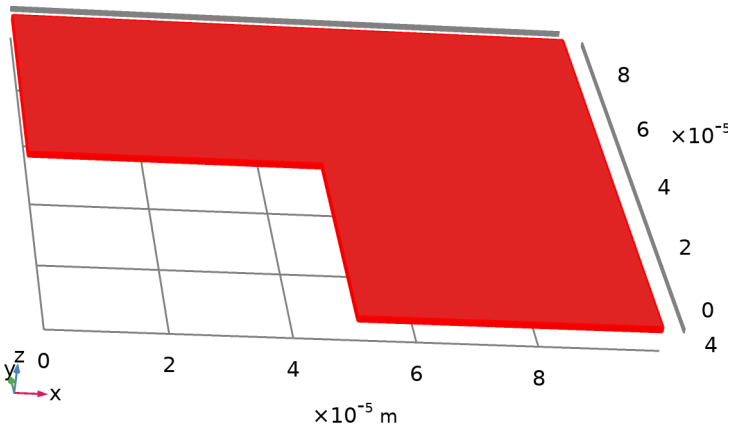

Dataset: Study 1/Parametric Solutions 2

4.1.4 Study 1/Parametric Solutions 3

SOLUTION

Description	Value
Solution	Parametric Solutions 3
Component	Save Point Geometry 1

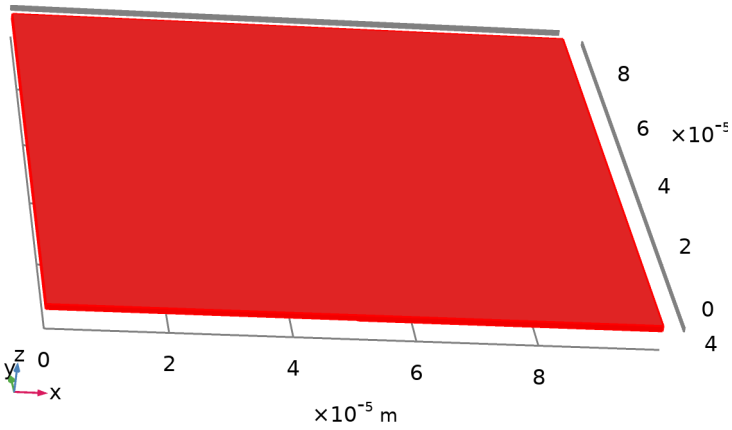

Dataset: Study 1/Parametric Solutions 3

4.1.5 Study 1/Parametric Solutions 4

SOLUTION

Description	Value
Solution	Parametric Solutions 4
Component	Save Point Geometry 1

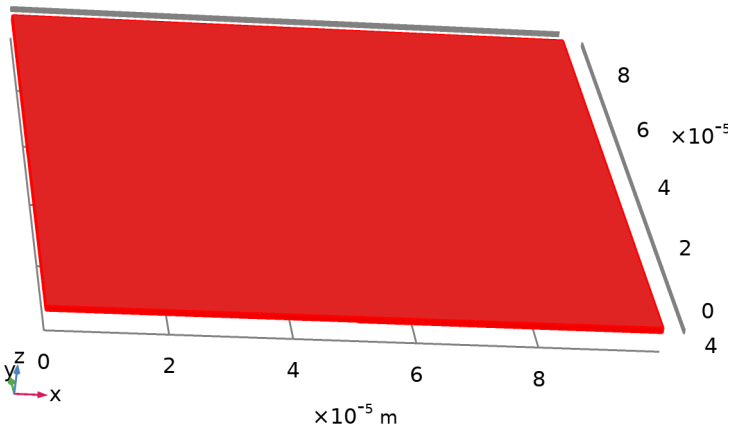

Dataset: Study 1/Parametric Solutions 4

4.1.6 Study 1/Parametric Solutions 5

SOLUTION

Description	Value
Solution	Parametric Solutions 5
Component	Save Point Geometry 1

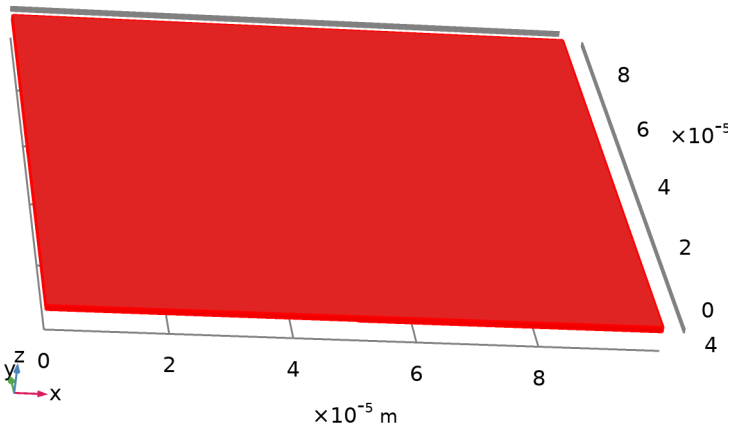

Dataset: Study 1/Parametric Solutions 5

4.2 PLOT GROUPS

4.2.1 3D Plot Group 3

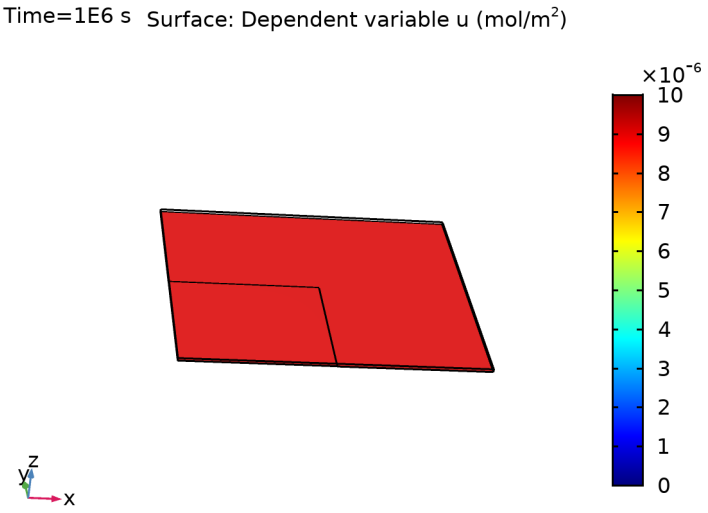

Surface: Dependent variable u (mol/m²)

4.2.2 1D Plot Group 4

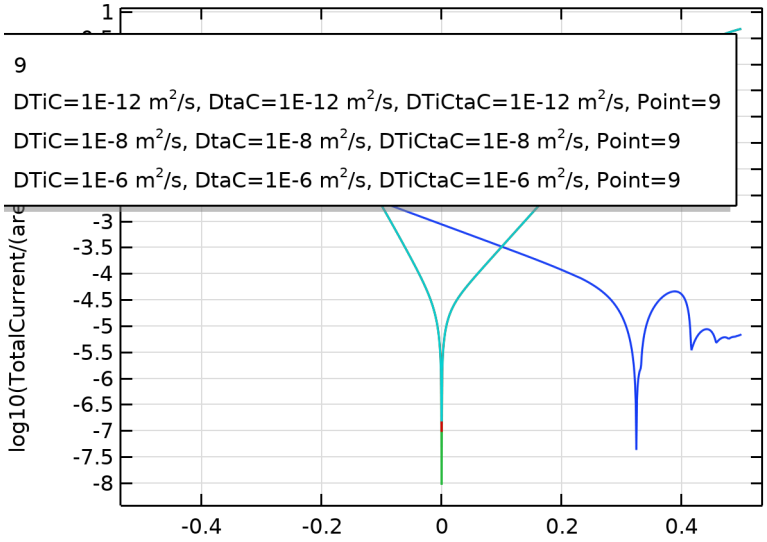

4.2.3 1D Plot Group 5

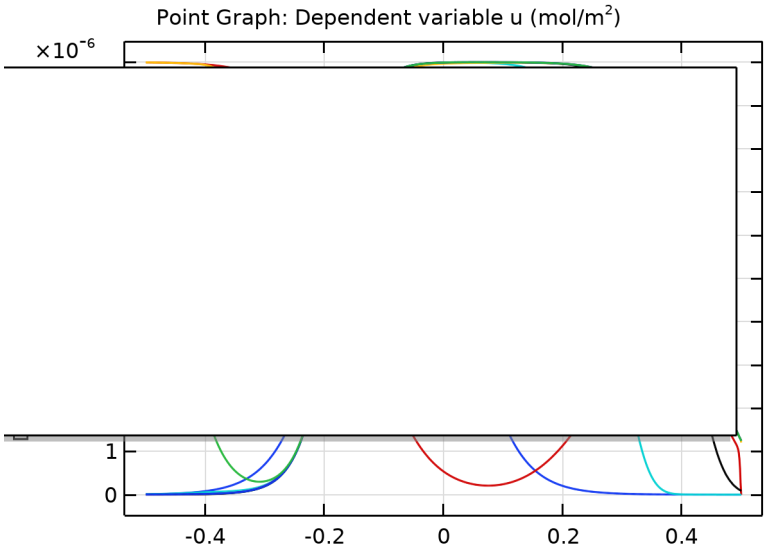

Point Graph: Dependent variable u (mol/m²)

4.2.4 1D Plot Group 6

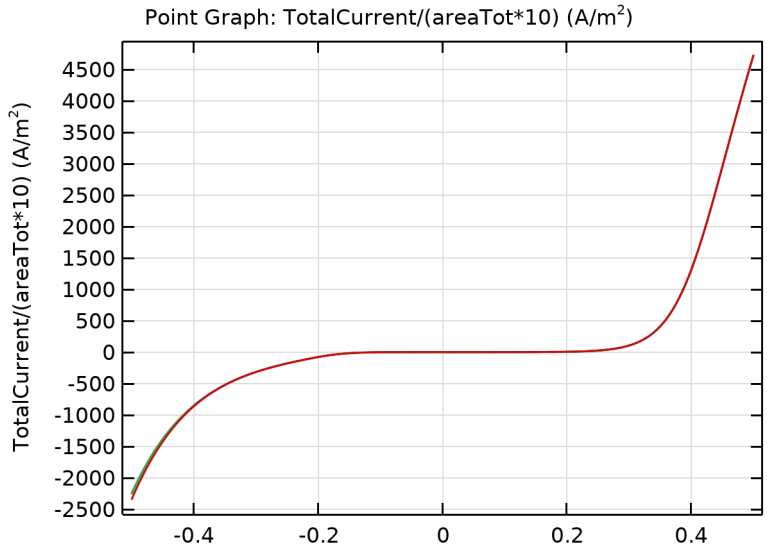

*Point Graph: TotalCurrent/(areaTot*10) (A/m²)*

4.2.5 Concentration, Streamline (tds)

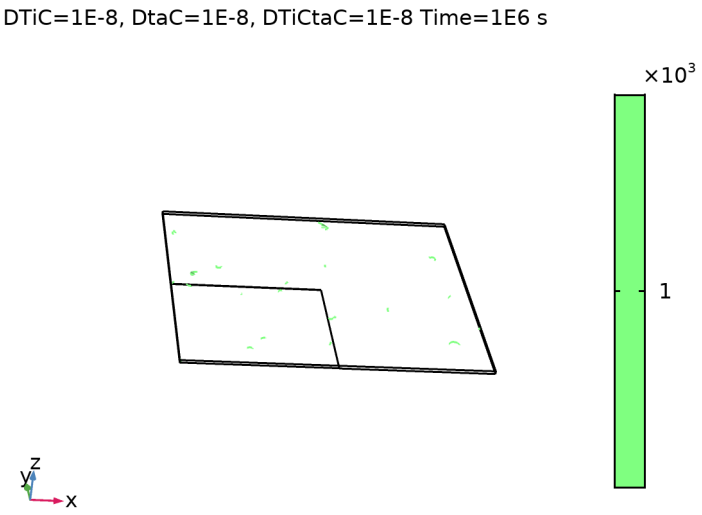

Streamline: Total flux Streamline Color: Concentration (mol/m³)

4.2.6 Concentration, Surface (tds)

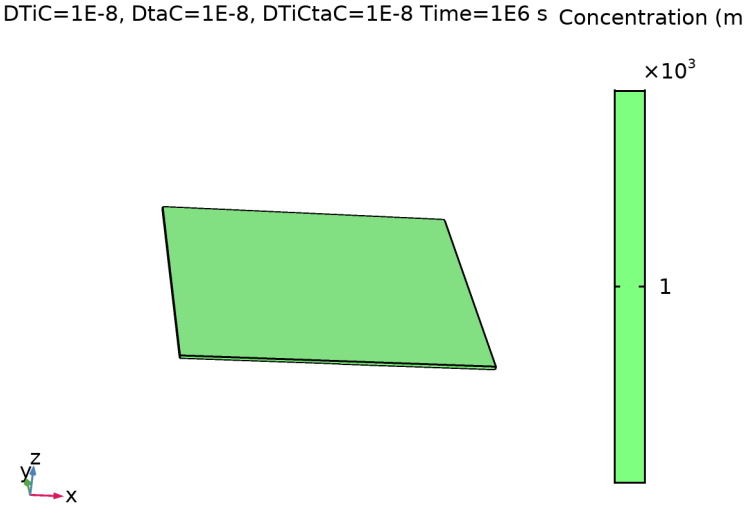

Concentration (mol/m³)

4.2.7 3D Plot Group 9

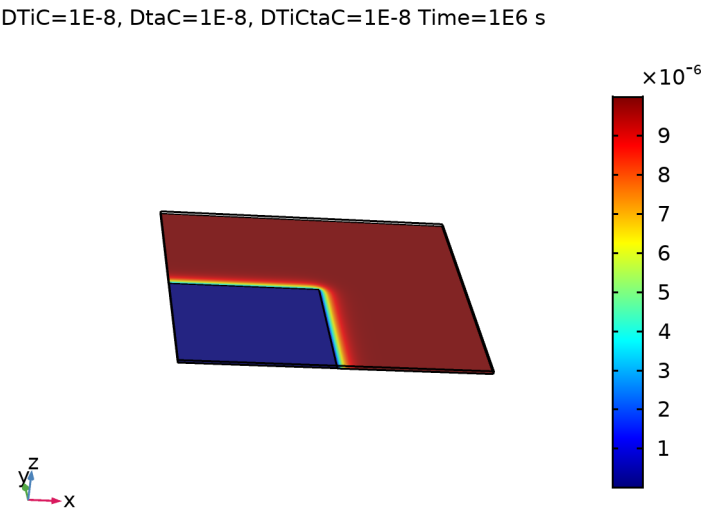

Surface: Dependent variable u (mol/m²)

4.2.8 Concentration, Streamline (tds) 1

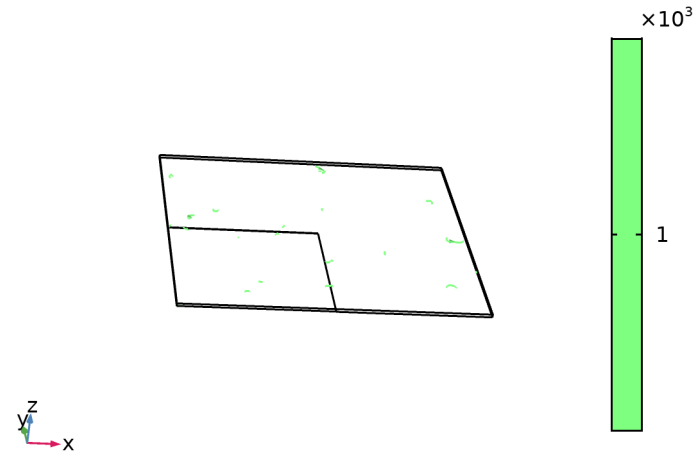

Streamline: Total flux Streamline Color: Concentration (mol/m³)

4.2.9 Concentration, Surface (tds) 1

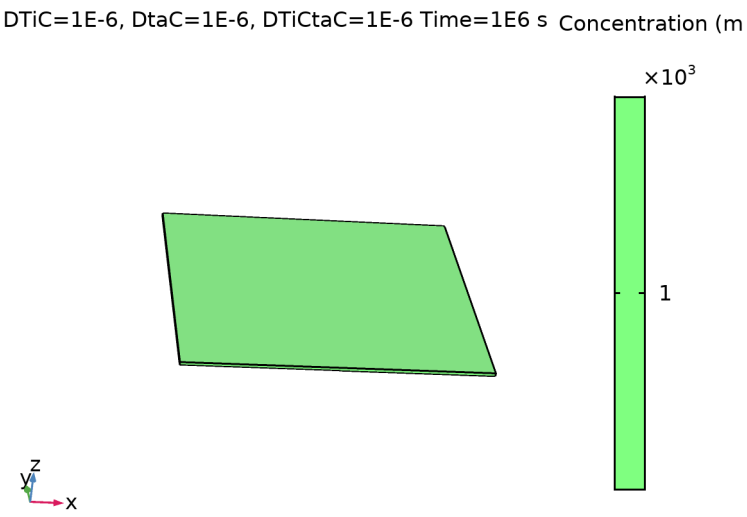

Concentration (mol/m³)

4.2.10 3D Plot Group 12

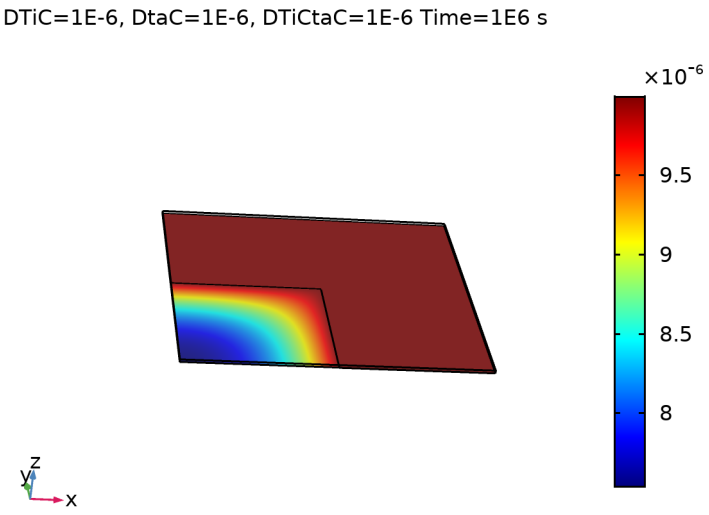

Surface: Dependent variable u (mol/m²)